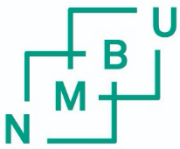

Norwegian University
of Life Sciences

Master's Thesis 2020 30 ECTS
Faculty of Science and Technology

Methods for the Performance Evaluation of GNSS Receivers: A Software Development Process

Bjørn-Eirik Roald
Geomatics

Acknowledgements

In concluding this thesis, I also conclude a five-year master's degree at The Norwegian University of Life Sciences, NMBU. This period of my life has left me with an even greater thirst for knowledge and understanding than when I first arrived at NMBU. Much of my growth through this time can be attributed to the support and friendship of my fellow students. However, equal credit must be given to the teachers of NMBU for my university education.

A special acknowledgement must be given to Ola Øvstedal and Jon Glenn Omholt Gjevestad. They have been inspiring teachers within the field of geodesy throughout my time at NMBU, and have been my mentors through this thesis. Thank you for countless hours of discussion, advice and help.

Abstract

Today's society relies heavily on the use of Global Navigation Satellite Systems (GNSS). As GNSS has developed, its use has been introduced into countless new sectors, many of these vital. As GNSS continues to become an integral part of society, overcoming its weaknesses becomes even more critical. This thesis focuses on a particular weakness, namely the performance of the GNSS receivers themselves.

Through this thesis, a computer software capable of evaluating the performance of GNSS receivers has been developed. Multiple metrics have been used in order to evaluate receiver performances. Among these are estimates of multipath, cycle slips and receiver clock jumps. As a means of illustrating the capabilities of this software, four data sets have been collected. These were collected using four significantly different receivers, but under comparable conditions. The receivers in question were Topcon Hiper VR, Trimble NETR5, Septentrio PolaRxS Pro and Emlid Reach RS2. The software analysis of these data sets are discussed and compared. Hence, a conclusion is made that the software succeeds in computing metrics capable of discerning receiver performances. Weaknesses and future development of the software are also discussed.

Sammendrag

Dagens samfunn er svært avhengige av satellittbaserte navigasjonssystemer (GNSS). Etter hvert som GNSS har utviklet seg har bruksområdene økt, og GNSS er derfor introdusert i utallige nye sektorer. Ettersom GNSS fortsetter å bli en mer integrert del av samfunnet blir det desto viktigere å overkomme dens svakheter. Denne oppgaven vil fokusere på en spesifikk svakhet ved GNSS, nemlig ytelsen til GNSS-mottakerne.

Gjennom arbeidet med denne oppgaven har det blitt utviklet en programvare i stand til å vurdere ytelsen til GNSS-mottakere. Forskjellige vurderingskriterier har blitt benyttet for å vurdere mottakernes ytelse. Blant disse er estimater for multipath, fasebrudd og mottakerens tidshopp. For å illustrere evnen til programvaren har fire datasett blitt innsamlet. Datasettene har blitt samlet inn ved hjelp av fire betydelig forskjellige mottakere, men under sammenlignbare forhold. Mottakerne som ble benyttet var Topcon Hiper VR, Trimble NETR5, Septentrio PolaRxS Pro og Emlid Reach RS2. Programvarens analyse av datasettene blir diskutert og sammenlignet. Derav dras konklusjonen at programvaren lykkes i å produsere verdier egnet til å vurdere mottakerytelse. Svakheter og fremtidig utvikling av programvaren blir også diskutert.

Contents

List of Figures

List of Tables

Abbreviations

CDMA Code-division multiple access

CS Commercial Service

DGNSS Differential GNSS

FDMA Frequency-division multiple access

FOC Full operational capability

GEO Geosynchronous equatorial orbit

GNSS Global Navigation Satellite System

GPS Global Positioning System

HAS High Accuracy Service

IGSO Inclined geosynchronous orbit

IP Ionospheric point

LLI Loss-of-lock indicator

MEO Medium Earth orbit

OS Open Service

PPS Precise Positioning Service

PRN Pseudo-random-noise

PRS Public Regulated Service

RMS Root mean square

SARS Search and Rescue Service

SPS Standard Positioning Service

TEC Total electron content

TVEC Total vertical electron content

Chapter 1: Introduction

Since the turn of the millennium, significant advancements have been made within many areas of technology. One such advancement that is mostly overlooked by the general population is within GNSS, more commonly known as GPS. However, as shall be made clear through this thesis, GNSS has made strides in the last two decades and has become an integral part of our daily lives. GNSS is being used more and more frequently and in new areas such as sports, location-based games, social networking as well as more dire areas such as agriculture, search and rescue and autonomous vehicles (European GNSS Agency 2019, p. 26, 34 and 50). Furthermore, traditional uses of GNSS, such as navigation and surveying, are still an integral part of society. As the use of GNSS increases, society becomes more and more dependant on GNSS and its continued success. However, as with most technology, GNSS contains its share of weaknesses, some of which will be detailed in this thesis.

One limiting factor of GNSS is the performance of the GNSS receivers themselves. With the global amount of GNSS receivers in use forecasted to increase from 6.4 billion in 2019 to 9.6 billion in 2029 (European GNSS Agency 2019, p. 7), and with receivers varying greatly in price, purpose and quality, the question of the reliability of individual GNSS receivers is a pressing one.

Problem Statement

In an attempt to bolster progress within the performance evaluation of individual GNSS receivers, the following problem statement has been proposed for this thesis.

Through the work of this thesis, an attempt shall be made to develop a computer software that may be used as a tool for evaluating the quality, or performance, of any GNSS receiver. The intent is for this software to require the least amount of work from the user, only requiring observation and navigation files. As a byproduct of developing this software, this thesis will also evaluate specific methods' and metrics' functionality in measuring the performance of GNSS receivers.

Thesis Structure

The main body of this thesis is comprised of six chapters, including the introduction. In addition, an appendix is also present. Each chapter outlines a different aspect of the thesis. To provide the reader with a guide concerning how this thesis should be read, a brief description of each chapter is presented.

Chapter 2 presents the theories and underlying concepts of this thesis. More fundamental principles are also explored so as to lay the foundation for this theory.

Chapter 3 presents the methods actually used in this thesis. This description includes methods of data collection, estimation methods, as well as the structure of the developed software.

Chapter 4 presents the results of the software analyses executed in this thesis. The majority of these results are relegated to Appendix A.

Chapter 5 discusses the results of chapter 4 and how they reflect on the capabilities of the developed software. Discussions of weaknesses and future development of this software are also included.

Chapter 6 summarises the main aspects of this thesis.

A note should be made concerning the length of Appendix A. A consideration was made to limit the amount of results in this appendix, in order to reduce its length. However, in the pursuit of presenting the full specter of results produced in this thesis, all of Appendix A was included.

Chapter 2: Theory

2.1 GNSS

Though it is expected that the reader has some previous acquaintance with the field of spatial positioning, it is prudent to present the general concept of GNSS as a means of spacial positioning.

2.1.1 Principles of GNSS Positioning

When considering the basics of how GNSS positioning functions, the reader should first consider a single satellite. At a point in time, t_0, this satellite is positioned at a point in orbit described by a geocentric position vector ρ^s. At the same point in time, there is a GNSS receiver on the surface of the earth with an unknown position vector ρ_r. The geometric range between satellite and receiver is therefore defined as

$$\rho = \|\rho^s - \rho_r\| \tag{2.1}$$

The above-mentioned situation is illustrated in Figure 2.1 from Hofmann-Wellenhof et al. (2008).

Given that the satellite positions are known, and the receiver does not move, it would require three known geometric ranges, such as (2.1), to solve for the three elements of ρ_r. However, the methods for measuring geometric ranges are not without errors.

One method of measuring geometric ranges between satellites and receivers is to observe the time it takes for the satellite signal transmitted at t_0 to reach the receiver at t_1. This method requires very precise clocks in both the satellite and receiver in order to accurately measure t_0 and t_1 in system time. In practice, only the satellites are equipped with oscillators accurate enough. The receivers use less expensive clocks and, as a result, measure t_1 with a slight offset from true system time. As a result, the observed ranges differ from the true geometric ranges, and are therefore called pseudoranges. As a result, the geometric range ρ and pseudorange R differ by a single correction, called a clock bias.

$$R = \rho + c\ \delta t_r \tag{2.2}$$

where δt_r is the clock bias, and c is the speed of light.

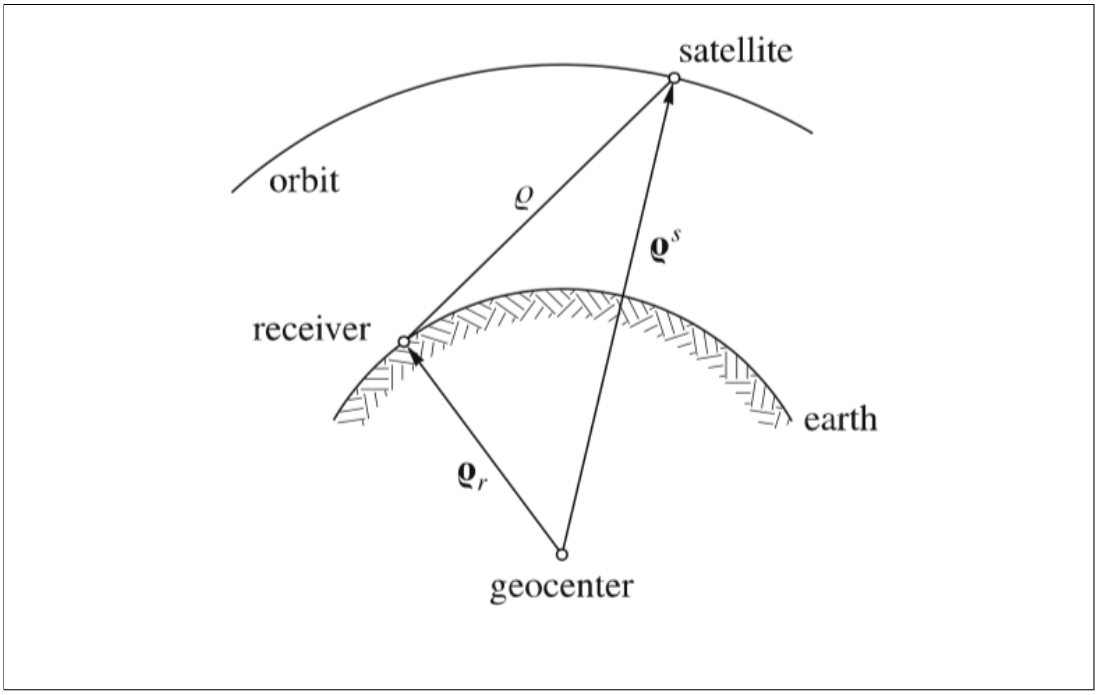

Figure 2.1: Principle geometry of satellite-based positioning (Hofmann-Wellenhof et al. 2008, p. 4)

This observation model makes it necessary to have four, not three, observations to solve for the four unknowns in the model. The models used for pseudoranges get more involved and include more variables when further errors, such as satellite clock biases, multipath and atmospheric effects, are included. Such models will be investigated at a later point.

2.1.2 Observation Types

Although a general model of pseudorange measurements was presented in equation 2.2, there are in fact multiple ways of measuring pseudoranges. The two that are the most relevant to GNSS positioning are code pseudoranges and phase pseudoranges. All current GNSS satellites allow for the use of both of these observation types. Each have their advantages and shortcomings, and these should therefore be explored.

Code Observations

The code observable is perhaps the simpler of the pseudorange measurements to understand. The signal transmitted from the satellite is encoded with a PRN code. This code contains, among other things, the transmission time. The receiver registers the time it receives the signal and then computes the travel time. As mentioned in section 2.1.1, there is an offset between the time registered by the receiver clock and system time. This offset results in a receiver clock bias, δt_r. However, even though satellites are equipped with very exact atomic clocks, they are not perfect. As a result, there is also a satellite clock bias, δt_s. As

such, the model for code pseudoranges from (2.2) is expanded to:

$$R = \rho + c(\delta t_r - \delta t_s) \tag{2.3}$$

As mentioned previously, this model may be expanded further when more errors are modeled.

The advantage of code pseudoranges, as opposed to phase pseudoranges, is that the estimate of ρ is unambiguous. This is true even when only the observations from a single epoch are available. This, as shall be seen later, is not true for phase observations.

The drawback to code observations, however, is the limited precision attained compared to using phase observations. Traditionally, the precision of code pseudoranges has been considered to be 1% of the chip length. This results in precisions between 3 m and 0.3 m, depending on which code observation is used (Hofmann-Wellenhof et al. 2008, p. 106). However today, with improved receiver hardware, a measurement resolution of 0.1% of the chip length can be achieved (Hofmann-Wellenhof et al. 2008, p. 197).

Phase Observations

The most accurate pseudoranges are those derived from carrier-phase observations. These pseudoranges may achieve millimeter precision. However, this precision comes at a cost. Unlike the code pseudoranges, phase pseudoranges are ambiguous, which may cause challenges.

The basis of the phase measurements is the beat phase, ϕ_r^s, between the satellite transmitted carrier wave and the receiver-generated reference carrier wave.

$$\phi_r^s = \phi^s - \phi_r \tag{2.4}$$

In (2.4), ϕ^s is the phase of the GNSS signal as it is transmitted, before propagating through the atmosphere. ϕ_r is the phase of the receiver reference carrier wave. These parameters can be modelled by

$$\begin{aligned} \phi^s &= f^s\ t - f^s \frac{\rho}{c} - \phi_0^s \\ \phi_r &= f_r\ t - \phi_{0r} \end{aligned} \tag{2.5}$$

The last terms of each model are the initial phases of each wave. These are unknown and must therefore be modelled. Furthermore, the term $f^s \frac{\rho}{c}$ is a correction for the oscillation of the carrier wave that occurs as it propagates through the atmosphere.

We can model the initial phases as if they were caused by clock biases in the satellite and receiver.

$$\begin{aligned} \phi_0^s &= -f^s\ \delta t_s \\ \phi_{r0} &= -f_r\ \delta t_r \end{aligned} \tag{2.6}$$

Although the frequencies f^s and f_r are not exactly equal in most cases, the error caused by this difference is in fact lower than the noise limit (Hofmann-Wellenhof et al. 2008, p. 107). The approximation $f^s = f_r = f$ is therefore made. As GLONASS utilizes FDMA (see section 2.2.2) this approximation is not acceptable for GLONASS observations.

Now, substituting (2.5) and (2.6) into (2.4) results in the following equation:

$$\phi_r^s = -f\ \frac{\rho}{c} - f\ \delta t \tag{2.7}$$

where $\delta t = \delta t_r - \delta t_s$.

How does this measurement work in practice? The GNSS receiver is turned on. It cannot measure the actual beat phase, but only the fraction of the last beat phase cycle. The remaining integer number of cycles, N, between the satellite and receiver remains unknown. As time passes without loss of signal, the receiver continues to measure the fractional beat phases of each epoch while also keeping track of the number of full cycles that have occurred since the first epoch. N remains unknown, but constant, so long as there is no loss of signal. At any point in time, t, the total beat phase is modeled by

$$\phi_r^s(t) = \Delta\phi_r^s + N \tag{2.8}$$

where $\Delta\phi_r^s$ is the measurable fractional phase which has also been augmented by the total number of cycles since the first epoch. By substituting (2.8) into (2.7), and denoting $\Phi = -\Delta\phi_r^s$, the model for phase pseudoranges is derived.

$$\Phi = \frac{1}{\lambda}\rho + \frac{c}{\lambda}\ \delta t + N \tag{2.9}$$

The unit of Φ in (2.9) is cycles. A similar model with units in distance is achieved by multiplying by the wavelength λ.

$$\Phi_{meters} = \rho + c\ \delta t + \lambda N \tag{2.10}$$

As previously mentioned, phase pseudoranges have superior precision to code pseudoranges. However, they have the disadvantage of their solutions being ambiguous. When comparing the models for code pseudoranges (2.3) and phase pseudoranges (2.10), the only difference is the integer ambiguity term, N. The ambiguity term must be estimated as its own variable. This is the primary challenge of phase observations and is called ambiguity resolution.

Ambiguity Resolution

The integer ambiguity N is a large portion of the phase pseudorange. Precisely estimating N is, therefore, a necessity if highly precise phase pseudoranges are to be attained. One aspect of the integer ambiguity that makes ambiguity resolution more accomplishable is its integer nature. As more observations are added iteratively with time to the model, the estimates of N will converge towards an integer value. Once convergence is confirmed, the estimate of N can be approximated to the integer value, and fixed. This "fixed" integer ambiguity can now be substituted into the model as a known parameter, allowing for very precise estimates of position.

This integer-fixed solution is often referred to as a fix solution. The solution preceding the resolution of the integer ambiguity is referred to as a float solution. When evaluating estimates of position on an epoch-by-epoch basis, float solutions show precisions scattered in the meter range. However, fix solutions show coordinate precision below 1 cm (Hofmann-Wellenhof et al. 2008, p. 202). Despite this, there are clear disadvantages to phase observations that lead to code observations still readily being used today.

First of these is the fact that acquiring a fix solution requires noticeably more observation epochs, compared to merely using code observations. This is because each satellite has its own integer ambiguity that must be fixed. This means more epochs, containing each satellite, are needed to fix all the ambiguities. In comparison, code observations can get solutions from a single epoch.

Another issue is that of "false fix". The situation where the integer-ambiguity is fixed to the wrong value is commonly referred to as false fix. As an error of only one cycle can result in errors in the decimeter range, false fix is a serious error. Furthermore, this error is not outright easy to detect when it occurs.

Cycle slips are another issue that is exclusively present in phase observations. These occur when a receiver loses the signal of a satellite for a period of time. As the receiver has not been able to register the fractional beat phases continuously, the integer value N will experience a jump in value. In other words, when the receiver loses lock with a satellite, the integer ambiguity of that satellite changes. This is referred to as a cycle slip. As a result, the user must detect all cycle-slips and re-fix the ambiguity for that satellite after every slip.

Lastly is the fact that the process of fixing the integer ambiguity is complicated in and of itself. When observing the phase model (2.10), it can be seen that N is not the only source of ambiguity. The clock biases of the satellite and receiver also result in ambiguities in the solution. However, where the integer ambiguity N is an integer by definition, the clock biases are not. The trouble in attempting to fix the integer ambiguity using equation 2.10 is that it is too difficult to separate the clock biases from the integer ambiguities. As a result, it can be said that the integer ambiguity in a way loses its integer characteristic. This makes a fix solution impossible. The solution is to use double differenced phase observations, also called short baselines. More detail about relative GNSS will be given in section 2.1.3.

2.1.3 Positioning Methods

A general overview of the different positioning methods most commonly used is presented in order to illustrate the defining differences between these methods. This also includes a certain amount of terminology.

Real-Time-Processing vs. Post-Processing

Two terms commonly used in the field of GNSS positioning are real-time processing and post-processing. Real-time processing implies that the results of the processing are available near instantaneously. The advantages of real-time GNSS is that the results are available to be used and evaluated in the field. This is, of course, completely essential for navigation purposes. Real-time GNSS is especially useful in the field of surveying as the quality of measurements can be evaluated in the field, and not after having returned to the workspace. Thus, time can be saved when having to re-do erroneous measurements. However, only broadcasted ephemeris, as described in section 2.6.1, are available to be used when using real-time GNSS. Furthermore, some measurement methods, such as traditional relative GNSS, are impossible to do in real time.

The alternative, post-processing, implies that the results are processed at a later time. This removes the advantages of knowing the results in the field and excludes its use for navigation-purposes. On the other hand, the user may use precise orbital information, as described in section 2.6.2, to attain the most precise results. Furthermore, post-processing allows for a much more thorough treatment of the data, which is often required in many high-precision applications.

Static vs. Kinematic

Two defining differences in methods of positioning is whether or not the observation period is static or kinematic. In other words, whether the receiver is standing still or moving. If the receiver is fixed in one position during the entire observation period, then all epochs share the same unknown position vector. The result is that all observations of the observation period contribute to estimating one position vector. If a receiver is allowed to complete a longer observation period, then the increased amount of observations would significantly increase the accuracy of the estimates. Static GNSS is also very useful in estimating other parameters, as there are fewer parameters involved in a static model.

In kinematic positioning, it is assumed that the receiver is in motion. There is, therefore, a new position vector for each observation epoch. This results in a lot more parameters to be estimated. The result is that the results are more prone to lower precision and errors.

Absolute GNSS

So far, the examples of GNSS positioning have concerned absolute positioning. In absolute positioning, as explained in section 2.1.1, a single GNSS receiver measures pseudoranges to a minimum of four satellites in order to determine its own position. The following models for code and phase pseudoranges were derived.

$$R = \rho + c(\delta t_r - \delta t_s) \qquad \text{(2.3 revisited)}$$

$$\Phi_{meters} = \rho + c(\delta t_r - \delta t_s) + \lambda N \qquad \text{(2.10 revisited)}$$

More complex models may be used that attempt to model other effects such as those of the ionosphere, as described in section 2.4.1, or the troposphere. The following are examples of such models.

$$\begin{aligned} R &= \rho + c(\delta t_r - \delta t_s) + I + T \\ \Phi_{meters} &= \rho + c(\delta t_r - \delta t_s) + \lambda N - I + T \end{aligned} \tag{2.11}$$

The ionospheric and tropospheric effects are denoted by I and T, respectively.

In absolute GNSS, all these parameters are estimated. The results are, as a result, less precise. Specific steps can be made to improve the results. Both broadcasted and precise orbital data can often include models for the satellite clock biases. Furthermore, there exist models that attempt to describe the effect of the ionosphere. Utilizing such models can improve the precision of the estimates. However, as described in section 2.1.2, attaining a fix solution using phase observations is not possible with absolute GNSS. Relative GNSS, however, makes a fix solution possible.

Relative GNSS

Relative GNSS is achieved when two receivers, placed in two locations, observe pseudoranges to the same satellites simultaneously. Furthermore, the coordinates of one of the receivers is known. This allows the user to create a double difference of the measurements. The following example will illustrate the effect.

Imagine two receivers, **A** and **B**, both measuring phase observations simultaneously to satellites **1** and **2**. The observation models for these observations would be

$$\Phi_A^1 = \rho_A^1 + c(\delta t_A - \delta t^1) + \lambda N_A^1 - I + T \tag{2.12}$$
$$\Phi_A^2 = \rho_A^2 + c(\delta t_A - \delta t^2) + \lambda N_A^2 - I + T \tag{2.13}$$
$$\Phi_B^1 = \rho_B^1 + c(\delta t_B - \delta t^1) + \lambda N_B^1 - I + T \tag{2.14}$$
$$\Phi_B^2 = \rho_B^2 + c(\delta t_B - \delta t^2) + \lambda N_B^2 - I + T \tag{2.15}$$

where the subscript indicates the receiver, and the superscript indicates the satellite.

In these models there is an approximation that the effects of the ionosphere and troposphere are equal on both receivers. While this is not true, the approximation may be made given that the receivers are in relatively close proximity to each other. By taking the differences between the observations of each receiver to a single satellite, the following single-differences are made.

$$\Delta\Phi_{AB}^1 = \Phi_B^1 - \Phi_A^1 = \Delta\rho_{AB}^1 + c\Delta t_{AB} + \lambda\Delta N_{AB}^1 \tag{2.16}$$
$$\Delta\Phi_{AB}^2 = \Phi_B^2 - \Phi_A^2 = \Delta\rho_{AB}^2 + c\Delta t_{AB} + \lambda\Delta N_{AB}^2 \tag{2.17}$$

The result of the single difference is an apparent, though only approximate, elimination of the parameters I and T. Furthermore, the satellite clock biases have been eliminated. By taking the difference of (2.16) and (2.17) the double-difference is derived.

$$\Delta\Phi_{AB}^{12} = \Delta\Phi_{AB}^2 - \Delta\Phi_{AB}^1 = \Delta\rho_{AB}^{12} + \lambda\Delta N_{AB}^{12} \tag{2.18}$$

The result of the double-difference is now clear. The effects of the ionosphere and troposphere have been strongly reduced, and the clock biases have been eliminated. This results in a simpler model with less parameters, which again improves the precision of the results. Furthermore, by removing the non-integer aspects of the ambiguity, meaning the clock biases, the integer ambiguity can now be fixed. Hence, a fix solution is possible.

It is worth mentioning that this form of static relative GNSS can only be achieved through post-processing. However, a variation of relative GNSS, which allows for real-time-processing, exists. This method is called Differential GNSS, or DGNSS. When implementing DGNSS, the observations from both receivers are not combined into one solution. Instead, the receiver with known coordinates, referred to as the base receiver, transmits correction data to the other receiver, referred to as a rover. Radio-waves are typically used for transmitting this data between base and rover. This allows a fix solution to be attained in real time.

2.1.4 GNSS Segments

The different GNSS systems are commonly divided into three segments. Each segment has a distinct function in the operation of the GNSS system. While all GNSS systems can be considered to have the same three segments, the segments themselves can vary from GNSS system to system. These differences shall be explored further in section 2.2. However, as the principle concept of the GNSS segments are the same for all GNSS, a description of each is included.

Space Segment

The space segment concerns itself with the equipment that operates in orbit, i.e. the satellites. The primary function of this segment is, therefore, to maintain a complete constellation of functional, up-to-date, and properly placed satellites. This last aspect is of great importance as it is essential that, as far as it is possible, any ground-based user can maintain a line of sight with at least four satellites simultaneously. The different GNSS systems vary in how they distribute the satellites in orbit, but all attempt to fulfill this goal. When a GNSS system maintains a full constellation of functional satellites, it is declared FOC, or "full operational capabilities". Another function of the space segment is to replace satellites that have reached the end of their life cycles. When new satellites are launched into orbit, they usually carry more advanced technology and often have longer life expectancies than the previous generation. These advancements in technology usually include more available services or improved atomic clocks.

Control Segment

The control segment, as the name indicates, is intended to control the entire GNSS system. This responsibility includes tracking the satellites in order to estimate satellite orbits and clock errors. As such, all ground antennas used to track the satellites are also considered

as part of the control segment. The control segment also uploads these estimates to the satellites themselves, so that they may be included in the broadcasted satellite message to receivers (see section 2.6.1). The precise orbital information is also produced by the control segment(see section 2.6.2).

User Segment

The user segment consists of all the different GNSS receivers utilized by users. These receivers can vary significantly in many aspects. Among the most relevant differences are which pseudoranges they can measure and which GNSS systems the receivers are compatible with. This is especially relevant today as newer GNSS systems such as Galileo and BeiDou are introduced, and as all GNSS systems introduce additional and more modern observation signals. Furthermore, as some GNSS services are restricted to military use, receivers are also divided into military and civilian receivers.

As more GNSS services become available, the dependence on GNSS increases, and the amount of different receivers grows to fulfill this demand. For instance, the development of smartphones has led to large portions of the population carrying GNSS receivers in their pockets.

2.2 State of GNSS Today

The state of GNSS is in constant development. That which a few decades ago consisted of only two systems, GPS and GLONASS, now consists of four: GPS, GLONASS, Galileo and BeiDou. Though these systems share core principles, they also differ greatly in certain aspects. Among these are the composition of their space and control segments, as well as the intended purpose of each system.

As the field of GNSS is always in a state of change, it is appropriate to give an overview of the current state of GNSS, at the time of writing. This is both in order to give an account of past developments within GNSS, as well as providing context for the methods used in this thesis.

2.2.1 GPS

Background

GPS, or "Global Positioning System", is perhaps the most recognized GNSS system in the world today. Developed by the United States of America from 1973, GPS became the first operational GNSS system. FOC was officially declared on July 17. 1995 (Hofmann-Wellenhof et al. 2008, p. 310). Initially, the primary goals of GPS were of a military nature. However, the civil use of the system has also been a goal since the beginning.

Focus on civil use has only increased with time. These somewhat conflicting goals have greatly affected the composition of the space and control segments of GPS.

Space Segment

The current GPS constellation consists of 31 active satellites distributed over six orbital planes (U.S. Coast Guard Navigation Center 2020). The six orbital planes have an inclination angle of 55 degrees to the equator. In addition to the 24 active satellites needed to provide complete coverage are spares that provide redundant observations. Figure 2.2 shows an overview of the distribution of the satellites over the different planes. The present constellation allows for a line of sight to at least four satellites at any position on Earth, even with a line of sight as low as 15 degrees.

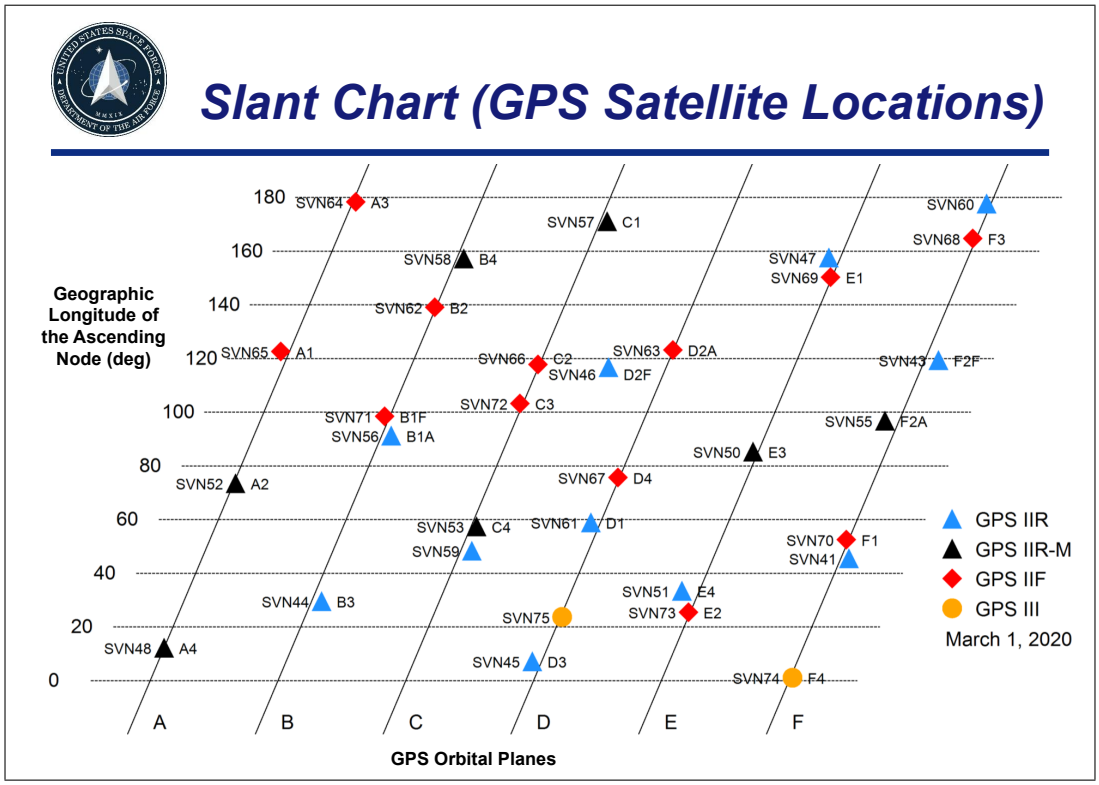

Figure 2.2: Depiction of GPS constellation with plane and slot distribution (U.S. Coast Guard Navigation Center 2020)

Figure 2.2 also shows the different satellite categories, or generations. The generations of GPS that have been developed so far are Block I, Block II, Block IIA, Block IIR, Block IIR-M, Block IIF and Block III. At the time of writing, no satellites from Block I, II or IIA are still in orbit (The National Coordination Office for Space Based Positioning 2020). The different blocks vary in many aspects such as expected lifespan, weight and functionality. However, the most relevant differences to discuss in this context is the changes to the available services. The current GPS signal plan will be explored in more detail in a later section. However, a brief overview of the changes from Block to Block in given.

Block IIR-M, first launched in 2005, introduced a second military signal and a first civil

signal on the second carrier frequency L2. As a result, GPS became compatible with civil dual-frequency receivers. This opened up for a potential major improvement in the accuracy of civil positioning.

Block IIF, first launched in 2010, introduced a third carrier frequency L5. A third civil code is transmitted on this frequency. The third carrier frequency allowed for more variations within dual inter-frequency linear combinations and also opened up for triple-frequency linear combinations.

Block III, first launched in 2018, introduced a new and improved civil signal on the first carrier frequency L1. The original legacy C/A civil signal on L1 remains, in order to maintain backward compatibility. Another major development of the third generation of GPS satellites is the removal of the selective availability functionality (The National Coordination Office for Space Based Positioning 2020). At the time of writing, only one Block III satellite is currently active, though two are in orbit.

Anti-Spoofing

GPS is divided into a civil segment, open for all to use, and a military segment restricted to all but authorised personnel. In order to allow for this restriction, two techniques are used to deny access to the complete GPS system from civilians. These are called anti-spoofing and selective availability. As selective availability has effectively been turned off since 2000, and is not included in the newest generation of GPS, it will not be discussed further.

Anti-spoofing, in the context of GPS, is the ability for signals restricted to military use to be encrypted. Originally this encryption was applied to the P-codes of the first and second carrier bands. However, when the second military signal was introduced in Block IIR-M, this was encrypted as well. A simple explanation of the encryption process is that the P-codes are encrypted with a secret W-code. To correctly decrypt the P-code, one must have knowledge of the W-code. The official purpose of anti-spoofing is to prevent military adversaries from sending out false, or "spoofed", GPS signals to the military. However, another effect of anti-spoofing is that civilians are not able to access the most precise pseudoranges. It also means that civilians are denied dual-frequency observations when measuring to satellites that predate Block IIR-M. However, it should be noted that more advanced geodetic GNSS receivers are able to estimate the W-code. This allows them to still track the encrypted signal, though with less than the full precision of the P-code.

Services

As mentioned previously, the services provided by GPS are divided into a military and a civilian segment. These services are more commonly known as the Standard Positioning Service, SPS, and the Precise Positioning Service, PPS. The difference between the two services is which pseudoranges are available.

SPS is available for civilian use. However, this means that the service does not provide access to the precise pseudorange P-codes, and more modern M-code. Previously, this meant

denying civilians the use of dual-frequency observations. However, after the introduction of the civilian L2C code on the L2 band and the civilian L5C code on the L5 band, this is no longer the case. This does not mean that SPS is no longer inferior to PPS. The precise P and M-codes are considered ten times more precise than the legacy C/A code, as the chip rate is ten times higher. Furthermore, as old GPS satellites are only replaced after their life cycles are over, it will still take some time until all GPS satellites provide dual-frequency observations to civilians. Lastly, some functions, like increased resistance to jamming, are still reserved to PPS alone.

CDMA

As GNSS satellites transmit multiple observation signals to receivers, the receiver must be able to distinguish different signals from one another. As different GPS satellites transmit on the same three frequencies, the solution is not straightforward. One solution, which is implemented by GPS, Galileo and BeiDou, is Code-Division Multiple Access (CDMA).

Satellites using CDMA each transmit their own Pseudo-Random Noise (PRN) code, encoded with observation and navigation data. Each PRN code is chosen so as to have very low cross-correlation with the others. In that way, a receiver knowing the PRN code of each satellite can extract the signal of a single satellite from the others. An advantage of CDMA is that the satellites all use the same frequencies. However, as the number of suitable PRN numbers is limited, so is the amount of satellites that can be used at the same time. However, this does not hinder any GNSS system from having enough active satellites to fill a full constellation.

Signal structure

As of Block IIF, GPS satellites transmit ranging codes on three distinct frequencies, or bands. These are named L1, L2 and L5. The frequencies and wavelengths of each of these bands are depicted in Table 2.1.

Band	**Frequency [MHz]**	**Wavelength [m]**
L1	1575.42	0.190
L2	1227.60	0.244
L5	1176.45	0.255

Table 2.1: GPS carrier frequency overview (Subirana et al. 2013, p. 23)

Each GPS band is encoded with multiple PRN codes. As mentioned previously, which codes are modulated onto each carrier band will vary from satellite to satellite, depending on which generation the satellite is part of. However, an overview of the different codes modulated onto the different GPS carrier bands is depicted in Table 2.2.

Table 2.2: GPS PRN code overview (Subirana et al. 2013, p. 23)

Carrier band	PRN code	Code rate [Mc/s]	Service
L1	C/A	1.023	SPS
	P	10.23	PPS
	M [1]	5.115	PPS
	L1C [2]	1.023	SPS
L2	P	10.23	PPS
	L2C [1]	1.023	SPS
	M [1]	5.115	PPS
L5	L5C [3]	10.23	SPS

[1] Available from Block IIR-M and onward.
[2] Available from Block III and onward.
[3] Available from Block IIF and onward.

2.2.2 GLONASS

Background

GLONASS is the Russian Federation's contribution to GNSS. The development of GLONASS was initialized in the mid-1970s by the former Soviet Union. After the fall of the Soviet Union, the development was continued by the Russian Federation. As with GPS, GLONASS is a military GNSS system with civilian services. FOC was officially announced in 1993, but only adequately achieved in 1996 (Hofmann-Wellenhof et al. 2008, p. 342). At this time, a single signal was available for civilian use. However, since then, a second has been introduced (Hofmann-Wellenhof et al. 2008, p. 343 and 358).

Space Segment

At the time of writing, the GLONASS satellite constellation consists of 24 active satellites distributed over three planes (*GLONASS CONSTELLATION STATUS* 2020). The inclination angle of the satellite orbits to the equator is 64.8 degrees (Hofmann-Wellenhof et al. 2008, p. 349). As with GPS, new generations of satellites are different from the preceding in many factors, such as weight and lifespan. However, the signal structure of the satellites is the aspect most relevant to this thesis. In addition to adding more carrier frequencies, a major development of GLONASS continues to be the gradual change from FDMA to CDMA. An overview of the most relevant changes introduced by the different GLONASS generations follows.

GLONASS-M, first launched in 2001, separates itself from the previous generation foremost by the increased lifetime, increased from three to seven years (Subirana et al. 2013, p. 11). Furthermore, GLONASS-M satellites were the first to transmit a civil signal on the G2 carrier band (Subirana et al. 2013, p. 11).

GLONASS-K1, first launched in 2011, is the first GLONASS generation to transmit a signal on the new CDMA band at 1202.025 MHz (Subirana et al. 2013, p. 11, 12 and 26). However, GLONASS-K1 is mostly a placeholder for GLONASS-K2, which brings even greater changes. First launched in 2019, the GLONASS-K2 satellites transmit on three CDMA carrier bands (Mirgorodskaya 2013, p. 18). In order to maintain backward compatibility, the satellites still transmit FDMA signals. However, as the GLONASS-K2 satellites eventually replace all older satellites, a full shift to CDMA is possible.

Services

Though not officially named as such, GLONASS also has two services that may be called the Standard Positioning Service (SPS) and the Precise Positioning Service (PPS). The advantages of GPS's PPS over that of SPS, as described in section 2.2.1, are in principle true for GLONASS as well. However, though PPS has not been officially released by the Russian government, it is not encrypted with anti-spoofing, such as the GPS PPS is (Hofmann-Wellenhof et al. 2008, p. 348). Furthermore, no selective availability function exists in GLONASS satellites. However, future anti-spoofing of the PPS is within the capabilities of GLONASS (Hofmann-Wellenhof et al. 2008, p. 348).

FDMA

GLONASS, unlike the rest of the current GNSS systems, did not originally utilize CDMA to separate satellite signals from each other. Instead, Frequency Division Multiple Access (FDMA) is utilized (Hofmann-Wellenhof et al. 2008, p. 357). The concept is slightly less complex to understand than CDMA. Each satellite has a set of fundamental frequencies. However, each satellite's frequencies are offset by an increment frequency, proportional to the channel number of the satellite. For a satellite with frequency channel k, an example frequency is described in general terms by

$$f_k = f_0 + k\,\Delta f \tag{2.19}$$

In theory, this would require a frequency channel k for each satellite. However, in order to reduce the number of frequencies used by GLONASS satellites, only the channels $k = -7, -6, -5, \ldots, 5, 6$ are used. This is made possible by having some satellites share channels. No difficulty arises from this, however, as any satellites sharing frequency channels are orbiting opposite sides of the Earth from one another. Hence, no receiver can receive signals from both satellites at the same time (Hofmann-Wellenhof et al. 2008, p. 356-357). As has been mentioned before, GLONASS satellites are gradually transitioning to CDMA, but this transition will take time.

Signal Structure

Since the first generation of GLONASS, satellites have transmitted on two frequencies, G1 and G2. These have the following frequencies (Hofmann-Wellenhof et al. 2008, p. 356).

$$\begin{aligned} f_{G1\_k} &= 1602 + k\,0.5625\ MHz \\ f_{G2\_k} &= 1246 + k\,0.4375\ MHz \end{aligned} \tag{2.20}$$

where k is the frequency channel of the satellite.

Furthermore, the later GLONASS-M satellites and those that follow transmit on a CDMA carrier band as well. This band will be referred to as G3C to indicate it's use of CDMA. With the arrival of the GLONASS-K2 satellites, two more CDMA carrier bands will be transmitted, now referred to as G1C and G2C. These use the following frequencies (Subirana et al. 2013, p. 26).

$$\begin{aligned} f_{G1C} &= 1600.995\ MHz \\ f_{G2C} &= 1248.060\ MHz \\ f_{G3C} &= 1202.025\ MHz \end{aligned} \tag{2.21}$$

Table 2.3: GLONASS observation signal overview (Subirana et al. 2013, 28)

Carrier Band	**Code name**	**Code rate [Mc/s]**	**Service**
G1	C/A	0.511	SPS
	P	5.11	PPS
G2	C/A	0.511	SPS
	P	5.11	PPS
G1C [1]	C/A	10.23	SPS
	P	[3]	PPS
G2C [1]	C/A	10.23	SPS
	P	[3]	PPS
G3C [2]	C/A	10.23	SPS

[1] Available from GLONASS-K2 and onward.
[2] Available from GLONASS-K1 and onward.
[3] Unknown

2.2.3 Galileo

Background

Galileo, named after the Italian astronomer Galileo Galilei, is a GNSS system developed and maintained by the European Union through the European GNSS Agency. Unlike the GPS and GLONASS, Galileo is intended mainly as a civilian system, as opposed to a military one. The motivation behind Galileo has been the development of a GNSS system independent of the other systems, while still being compatible with the last generation of GNSS, GPS and GLONASS. Though the system has been active since 2016, Galileo is expected to reach FOC in 2020 (Subirana et al. 2013, p. 13).

Space Segment

The intended Galileo satellite constellation contains 24 satellites in orbit, with an additional six spare satellites (European GNSS Agency 2020). These are distributed across three orbital planes with a 56-degree inclination angle to the equator. At the time of writing, 22 Galileo satellites are active (European GNSS Agency 2020). As FOC has yet to be achieved, there are no official plans regarding the next generation of Galileo satellites.

Services

Unlike the previous generation of GNSS, Galileo does not provide two services, but four. Each is intended to fulfill a specific user need. The four services are named: The Open Service (OS), High Accuracy Service (HAS), Public Regulated Service (PRS), and Search and Rescue Service (SARS).

The Open Service (OS) is free to use. This service is intended for the mass market that requires simple positioning. The service is provided through PRN codes modulated onto three different carrier frequencies, hence providing double-frequency and even triple-frequency observations (Subirana et al. 2013, p. 30).

The High Accuracy service (HAS) was originally developed under a different name and purpose. Originally called the Commercial Service (CS), CS was intended to provide a higher precision service to the commercial market. For a fee, it would provide decimeter accuracy. This would be a commercial service that would generate revenue for Galileo. However, in February 2018, it was announced that the service would instead go under the name HAS and would be a free service (Fernandez-Hernandez et al. 2018).

The Public Regulated Service (PRS) is an encrypted service intended only for authorised users. Though Galileo is not a military system meant to provide support to armed forces, it is meant to provide essential aid to authorised personnel such as law enforcement or national security agencies. As open GNSS services are considered vulnerable to misuse or interference, it is considered essential to have a robust service that will function even in a crisis. The PRS intends to fulfill this purpose. The performance of the PRS is envisioned to be comparable to the OS, with a more robust integrity (Hofmann-Wellenhof et al. 2008, p. 372).

The Search and Rescue Service (SARS) is intended to aid in search and rescue operations. This includes, among other things, detecting distress beacons (Subirana et al. 2013, p. 31).

Signal Structure

All Galileo satellites currently transmit on five carrier bands. The first three are named E1, E5 and E6. E5 is further subdivided into two carrier bands called E5a and E5b. As with GPS, Galileo uses CDMA as a multiple access method. Table 2.4 depicts the frequencies and wavelengths of these carrier bands.

Band	Frequency [MHz]	Wavelength [m]
E1	1575.420	0.190
E5	1191.795	0.252
E5a	1176.450	0.255
E5b	1207.140	0.248
E6	1278.750	0.234

Table 2.4: Galileo carrier frequency overview (Subirana et al. 2013, p. 32)

Onto each of the carrier bands signal components are modulated. For the E1 and E6 bands these components are referred to as A, B and C. The E5a and E5b bands only have two components each. These are referred to as I and Q, assumably to avoid confusion. Each component may be modulated with pseudoranges and satellite navigation data, or only with pseudoranges. Components modulated with both are referred to as data channels while the others are referred to as pilot channels. An overview of the different PRN codes transmitted by Galileo satellites, their channels and the services they provide is given in Table 2.5

Band	PRN code	Channel	Service	Code rate [Mc/s]
E1	E1A	data	PRS	2.558
	E1B	data	OS	1.023
	E1C	pilot	OS	1.023
E6	E6A	data	PRS	5.115
	E6B	data	HAS	5.115
	E6C	pilot	HAS	5.115
E5a	E5a-I	data	OS	10.23
	E5a-Q	pilot	OS	10.23
E5b	E5b-I	data	OS	10.23
	E5b-Q	pilot	OS	10.23

Table 2.5: Galieo PRN code overview (Subirana et al. 2013, p. 32)

2.2.4 BeiDou

Background

BeiDou is the GNSS system developed and maintained by The People's Republic of China. The decision to implement its own independent satellite navigation system was made by the Chinese government in 1993 (Hofmann-Wellenhof et al. 2008, p. 402). Since then, BeiDou has gone through two phases, BeiDou I and BeiDou II/COMPASS. The third generation will be finalized in 2020 when the system is expected to reach FOC (Subirana et al. 2013, p. 37). As with GPS and GLONASS, BeiDou is a military system that also supports civilian use.

Space Segment

The space segment of BeiDou is somewhat unorthodox, compared to the other GNSS systems. The satellite constellation does not comprise of only medium Earth orbit (MEO) satellites. Instead, there are three different orbit types used in the constellation. MEO satellites are distributed over three planes. These planes have an inclination angle of 56 degrees to the equator. When FOC is reached in 2020, there will be a total of 24 active MEO satellites, plus an additional three spares (Subirana et al. 2013, p. 13).

In addition, there will be five satellites in geosynchronous equatorial orbit (GEO), and three satellites in inclined geosynchronous orbits (IGSO) (Subirana et al. 2013, p. 13).

Services

In much the same way as has been done by GPS and GLONASS before it, BeiDou will provide two services. One will be an open service with standard accuracy. The other will ensure reliable and precise positioning for authorised users (Subirana et al. 2013, p. 35).

Signal Structure

Like GPS and Galileo, BeiDou utilizes CDMA to distinguish its satellite signals. As the signal structure of BeiDou II and III satellites are noticeably different, and as both types of satellite are in orbit at the time of writing, overviews of both are presented. Both BeiDou II and III transmit PRN codes on three carrier bands. The frequencies and wavelengths of the carrier bands of both BeiDou II and III are detailed in Tables 2.6 and 2.7.

Band	**Frequency [MHz]**	**Wavelength [m]**
B1	1561.098	0.192
B2	1207.14	0.248
B5	1268.52	0.236

Table 2.6: BeiDou II carrier frequency overview (Subirana et al. 2013, p. 36)

Band	**Frequency [MHz]**	**Wavelength [m]**
B1	1575.42	0.190
B2	1191.795	0.252
B5	1268.52	0.236

Table 2.7: BeiDou III carrier frequency overview (Subirana et al. 2013, p. 36)

An overview of the different PRN codes transmitted by BeiDou II and III satellites, their channels, and the services they provide is detailed in Tables 2.8 and 2.9. Note that once again, some PRN codes are denoted D for data, meaning they contain both pseudoranges and navigation data. The PRN codes denoted with P, for pilot, only contain pseudoranges.

Band	PRN code	Code rate [Mc/s]	Service
B1	B1-I	2.046	Open
	B1-Q	2.046	Authorised
B2	B2-I	2.046	Open
	B2-Q	10.23	Authorised
B3	B3	10.23	Authorised

Table 2.8: BeiDou II PRN code overview (Subirana et al. 2013, p. 36)

Band	PRN code	Code rate [Mc/s]	Service
B1	B1-C_D B1-C_P	1.023	Open
	B1	2.046	Authorised
B2	B2-a_D B2-a_P B2-b_D B2-b_P	10.23	Open
B3	B3	10.23	Authorised
	B3-A_D B3-A_P	2.5575	

Table 2.9: BeiDou III PRN code overview (Subirana et al. 2013, p. 36)

2.3 Linear Combinations

As discussed in section 2.2, all GNSS satellites currently broadcast pseudoranges on at least two carrier frequencies. This allows users to take advantage of inter-frequency linear combinations. These linear combinations come in different variations and may be used for a wide range of purposes. Among these combinations are those referred to as wide-lane, narrow-lane, geometry-free, and ionospheric-free linear combinations. As more and more satellites transmit civil pseudoranges on two or more frequencies, these linear combinations can be used to achieve better positioning in the mass market. Before describing the specific linear combinations utilized in this thesis, however, an investigation of linear combinations in more general terms is appropriate.

Following the overview given by Collins (1999), the general concept of inter-frequency combinations may be presented. The observation models for two phase pseudoranges on two distinct carrier frequencies are given.

$$\begin{aligned} \Phi_1[m] &= \rho + \lambda_1 N_1 - I_1 \\ \Phi_2[m] &= \rho + \lambda_2 M_2 - q^2 I_1 \end{aligned} \tag{2.22}$$

In (2.22), the variable q is such that $I_2 = q^2 I_1$. The actual value of q will be derived in section (2.4.1).

Using the general expression for any linear combination the following expression is born.

$$LC[m] = \alpha\Phi_1 + \beta\Phi_2 \tag{2.23}$$

By substituting in (2.22), a more expanded equation is derived.

$$LC[m] = \rho(\alpha + \beta) + \alpha\lambda_1 N_1 + \beta\lambda_2 N_2 - I(\alpha + \beta q^2) \tag{2.24}$$

If we impose certain constants on the linear combination, such as that ρ remains unchanged and the resultant ambiguity remains an integer, then (2.24) should be equated with

$$LC[m] = \rho + \lambda N - I\eta \tag{2.25}$$

hence giving

$$\alpha + \beta = 1 \tag{2.26}$$
$$\alpha\lambda_1 N_1 + \beta\lambda_2 N_2 = \lambda N \tag{2.27}$$
$$(\alpha + \beta q^2) = \eta \tag{2.28}$$

Rearranging equation 2.27 gives an equation for the combined ambiguity of the linear combination.

$$N = \frac{\alpha\lambda_1 N_1}{\lambda} + \frac{\alpha\lambda_2 N_2}{\lambda} \tag{2.29}$$

Equation 2.29 shows that, as N_1 and N_2 are integer values, for N to also be an integer then the following parameters must also be integers.

$$\begin{aligned} i &= \frac{\alpha\lambda_1}{\lambda} \\ j &= \frac{\beta\lambda_2}{\lambda} \end{aligned} \tag{2.30}$$

As presented in Collins (1999), the easiest way to make sure of this is to define i and j as integers and instead rearranging (2.30) to compute α and β.

$$\begin{aligned} \alpha &= \frac{i\lambda}{\lambda_1} \\ \beta &= \frac{j\lambda}{\lambda_2} \end{aligned} \tag{2.31}$$

By substituting (2.31) into (2.26) the resulting wavelength of the linear combination can be computed.

$$\lambda = \frac{\lambda_1\lambda_2}{i\lambda_1 + j\lambda_2} \tag{2.32}$$

Furthermore, by utilizing the relationship $\lambda = c/f$, the frequency of the linear combination can be given by

$$f = if_1 + jf_2 \tag{2.33}$$

The conclusion drawn is that by varying the frequencies, f_1 and f_2, and by selecting specific integer values of i and j, then linear combinations with the desired frequency f and wavelength λ can be created. In this way, certain useful combinations may be obtained. Many of these combinations, such as the "widelane" and "narrowlane" combinations, are commonly used. However, they are not directly used in this thesis and will, therefore, only be quickly introduced as examples of useful combinations.

The widelane combination is described in the context of GPS as being a linear combination with a resultant wavelength greater than the GPS L2 carrier band (Collins 1999, p. 1). However, this can be generalized to any linear combination with a significantly wide wavelengths. This is useful both in cycle-slip detection and in ambiguity fixing (Collins 1999, p. 3).

The narrowlane combination is the opposite of the widelane, being a combination with a significantly narrow wavelength. The result, as is thoroughly explored by Collins (1999), has the useful property of having reduced noise, compared to each individual component.

The linear combinations used in this thesis will be explored in section 2.4.

2.4 GNSS Signal Path Errors

An inherent weakness of GNSS positioning is that all GNSS signals must travel the inter-spanning distance between the satellite and receiver. The consequences of this are errors caused by signals not following the straight geometric line between satellite and receiver. Such errors are separated into two categories: Dispersive and neutral errors. Dispersive errors, as shall be explored further, are dependant on the frequency of the signals themselves. Examples of such errors are ionospheric delays and multipath. Neutral errors, such as the effect of the troposphere, are independent of the signal frequencies. Other errors that are not considered path errors, such as clock biases, may also be categorized as dispersive or neutral errors. These are all significant errors in the context of precise positioning. Much effort is, therefore, put into modeling these errors and eliminating them. However, only dispersive path errors will be explored further in this section. The reasoning behind this is that much of this thesis will be focused on estimating errors using inter-frequency linear combinations. This is mainly possible for dispersive errors.

2.4.1 The Ionosphere

The part of the atmosphere known as the ionosphere is located at an altitude of 50-1000 km (Hofmann-Wellenhof et al. 2008, p. 118). As the name indicates, the ionosphere is comprised of an ionized medium. As such, the ionosphere contains an amount of free electrons. The number of electrons in the ionosphere at any time will vary, as the ionizing radiation from the sun varies over a 24-hour cycle (Hofmann-Wellenhof et al. 2008, p. 65).

Another characteristic of the ionosphere is that it is dispersive. This means that the delay, caused by the ionosphere, upon a GNSS signal's propagation is dependant on the frequency of the signal itself (Hofmann-Wellenhof et al. 2008, p. 62). In order to properly understand this signal delay, it is important to consider the propagating velocity of signals passing through the ionosphere.

Group and Phase Velocities of GNSS Signals

The carrier waves emitted by GNSS satellites are, simply put, electromagnetic waves propagating through space. Given a signal with frequency f and wavelength λ, the velocity of its propagation will be given by

$$v_{ph} = \lambda f \tag{2.34}$$

This velocity is denoted as the phase velocity. While the carrier wave can be considered to be propagating with phase velocity, the code observations propagate with a "group velocity" (Hofmann-Wellenhof et al. 2008, p. 116). The group velocity is given by:

$$v_{gr} = -\frac{df}{d\lambda}\lambda^2 \tag{2.35}$$

The group velocity is defined as the velocity of the propagation of a group of waves, with slightly different frequencies (Hofmann-Wellenhof et al. 2008, p. 116).

Following the mathematical derivation of Hofmann-Wellenhof et al.(2008, p. 116–118), equations for the refractive indices of phase and group signals passing through the ionosphere are given.

$$n_{ph} = 1 + \frac{c_2}{f^2} \tag{2.36}$$

$$n_{gr} = 1 - \frac{c_2}{f^2} \tag{2.37}$$

where c_2 is not associated with the speed of light, but is simply a coefient independant of the frequency of the signal (Hofmann-Wellenhof et al. 2008, p. 118).

Seeber (2003, p. 54) gives an estimate for c_2 of $c_2 = -40.3N_e$. Where N_e denotes the electron density along the path of the signal's propagation.

As the electron density N_e cannot be negative, the following inequalities are deduced

$$\begin{aligned} n_{gr} &> n_{ph} \\ v_{gr} &< v_{ph} \end{aligned} \tag{2.38}$$

As a result of the differences in phase and group velocity, distinct phase and group delays occur when signals travel through the ionosphere. We also see that, as n_{ph} must be lower than 1, phase signals will experience an advancement while passing through the ionosphere. The observed phase pseudoranges will, therefore, be too short, compared to the true geometric distance. The opposite is true for the code observations, as n_{gr} must be greater than 1. It will be shown that the magnitude of the delays are the same, despite their signs being different.

Ionospheric Delay

To determine the magnitude of the ionospheric delay, we turn to Fermat's principle which states that the measured range s can be determined through

$$s = \int n \, ds \tag{2.39}$$

As the refractive index of vacuum is equal to 1, setting n=1 gives the geometric range between the satellite and receiver.

$$s_0 = \int ds_0 \tag{2.40}$$

The delay caused by the ionosphere will be the difference between the measured range and the geometric range. The ionospheric delay is therefore obtained through

$$\Delta^{Iono} = \int n \, ds - \int ds_0 \tag{2.41}$$

Though s and s_0 are by definition not the same, an approximation of the ionospheric delay can be obtained by approximating the first integral along the straight line of the geometric range. In other world, ds becomes ds_0. The phase refractive index from equation 2.36 is substituted for n. Seeber's estimate of c_2 is used. Furthermore, "total electron count" (TEC) is defined as

$$TEC = \int N_e \, ds_0 \tag{2.42}$$

Hence the following formula for the magnitude of the phase delay is given.

$$\begin{aligned}
\Delta_{ph}^{Iono} &= \int n \, ds_0 - \int ds_0 \\
&= \int (n-1) \, ds_0 \\
&= \int ((1 + \frac{c_2}{f^2}) - 1) \, ds_0 \\
&= \int \frac{c_2}{f^2} \, ds_0 \\
&= -\frac{40.3}{f^2} \int N_e \, ds_0 \\
&= -\frac{40.3}{f^2} \, TEC
\end{aligned} \tag{2.43}$$

Through a similar derivation as (2.43) it can be shown that the group delay has the same magnitude as the phase delay, but the opposite sign. The group ionospheric delay is hence given as

$$\Delta_{gr}^{Iono} = -\Delta_{ph}^{Iono} = \frac{40.3}{f^2} \, TEC \tag{2.44}$$

From equations 2.43 and 2.44 we can compute the ionospheric delay of a signal with frequency f. This, however, requires that we possess information about TEC along the signal path during the observations. While there are models that attempt to model TEC around the world (Hofmann-Wellenhof et al. 2008, p. 123), these can not estimate 100% of the ionospheric delay. However, other practical methods exist to estimate ionospheric delay.

Estimating Ionospheric Delay in Practice

As mentioned previously, there are major advantages to GNSS satellites broadcasting on at least two carrier frequencies. The greatest of these is that it allows us to use inter-frequency linear combinations. As a result of the dispersive nature of the ionosphere, such linear combinations allow us to estimate the ionospheric delay upon a signal. The mathematical principle of the linear combination used to estimate ionospheric delays in this thesis will now be presented.

The foundation of the derivation of this linear combination is the observation model of phase observations. The following model will be used.

$$\Phi_i = \rho + c(dt_r + dt_s) - I_i + T + m_i + N_i\lambda_i \tag{2.45}$$

Equation 2.45 is in the unit of distance. The following symbols are adopted:

Φ_i	Phase pseudorange measurement for carrier band i, converted to distance
ρ	Geometric distance between the satellite and GNSS receiver
c	Speed of light
dt_r	Receiver clock error
dt_s	Satellite clock error
I_i	Ionospheric group delay on carrier band i
T	Other, non-dispersive, atmospheric delays
m_i	Phase multipath effect on carrier band i
$N_i\lambda_i$	Integer ambiguity for carrier band i, converted to distance

Table 2.10: Symbol overview for phase observation model 2.45

Note that I_i is the group ionospheric delay in this case. This can be seen from the negative sign of this variable.

From rearranging equation 2.44 we can express TEC as a function of the ionospheric delay on the first band, I_1.

$$\begin{aligned} I_1 &= \frac{40.3}{{f_1}^2}\, TEC \\ I_1 {f_1}^2 &= 40.3\, TEC \end{aligned} \tag{2.46}$$

The same may be done for I_2.

$$I_2 {f_2}^2 = 40.3\, TEC \tag{2.47}$$

Equalling (2.46) and (2.47) gives a relationship between the ionospheric delay on carrier band 1 and 2.

$$\begin{aligned} I_1 {f_1}^2 &= I_2 {f_2}^2 \\ I_2 &= \frac{{f_1}^2}{{f_2}^2} I_1 \end{aligned} \tag{2.48}$$

By defining the variable α as

$$\alpha \equiv \frac{{f_1}^2}{{f_2}^2} \tag{2.49}$$

the following form of (2.48) is found

$$I_2 = \alpha I_1 \tag{2.50}$$

As can be seen from (2.50), given the ionospheric delay of one carrier band with frequency f_i, the delay of another band with frequency f_j can be found.

With α defined, an estimate for I_1 can be derived by looking at the difference $(\Phi_1 - \Phi_2)$.

$$\Phi_1 - \Phi_2 = I_2 - I_1 + m_1 - m_2 + N_1\lambda_1 - N_2\lambda_2 \tag{2.51}$$

By applying (2.50), I_2 is eliminated.

$$\begin{aligned}
\Phi_1 - \Phi_2 &= I_2 - I_1 && +m_1 - m_2 + N_1\lambda_1 - N_2\lambda_2 \\
\Phi_1 - \Phi_2 &= -(I_1 - I_2) && +m_1 - m_2 + N_1\lambda_1 - N_2\lambda_2 \\
\Phi_1 - \Phi_2 &= -(I_1 - \alpha I_1) && +m_1 - m_2 + N_1\lambda_1 - N_2\lambda_2 \\
\Phi_1 - \Phi_2 &= I_1(\alpha - 1) && +m_1 - m_2 + N_1\lambda_1 - N_2\lambda_2
\end{aligned} \tag{2.52}$$

By rearranging (2.52), the result is an equation for I_1.

$$I_1 = \frac{1}{\alpha - 1}(\Phi_1 - \Phi_2) - \frac{1}{\alpha - 1}(m_1 - m_2 + N_1\lambda_1 - N_2\lambda_2) \tag{2.53}$$

It is important to note that the linear combination (2.53) is only possible given two simultaneous phase observations with different frequencies.

In practice, equation 2.53 is not so simple to use. The last term of the equation is the source of the difficulty. As the phase multipath effects m_1 and m_2 are not explicitly known, these must be modeled in order to solve for I_1. Furthermore, the integer ambiguity terms $N_1\lambda_1$ and $N_2\lambda_2$ must be computed.

The practical solution used in this thesis has two parts. Firstly, the phase multipath effects are of a negligible magnitude, compared to the code multipath delays that will be explored later (Estey & Meertens 1999, p. 46). On account of this, the following approximation is made

$$\begin{aligned}
m_1 &\approx 0 \\
m_2 &\approx 0
\end{aligned} \tag{2.54}$$

Secondly, the integer ambiguity terms $N_1\lambda_1$ and $N_2\lambda_2$ are constant over sequential measurement epochs, given no cycle slips. These terms can therefore be eliminated by subtracting the I_1 estimate of the first epoch from all following estimates. The resulting estimates of I_1 are, therefore, all relative to the first estimate, and not absolute estimates.

In practice, however, a situation where no cycle slips occur is unlikely. After any cycle slip the integer ambiguity terms $N_1\lambda_1$ and $N_2\lambda_2$ will have new values. As such, all estimates of I_1 cannot simply be reduced by the I_1 estimate of the first epoch. They must instead be reduced by the I_1 estimate of the first epoch following the previous cycle slip. Method of determining during which epochs cycle slips have occurred will be covered section 2.4.3.

Mapping Ionospheric Delay to Zenith

As shown in equation 2.44, the ionospheric delay can be determined mainly through TEC. However, TEC depends on a range of factors. Among these are variations in radiation from the sun, either from daily, seasonal, or even longer cycles (Hofmann-Wellenhof et al. 2008, p. 66). Furthermore, the actual line of sight of the observation affects TEC. As a result, TEC will vary with the position of the GNSS receiver, and the elevation angle of the satellite. In order to compare the estimates of ionospheric delay of multiple signals from multiple satellites, it may be prudent to reduce the effects caused by the varying elevation angles. This may be achieved by using a mapping function to map the ionospheric delay to the zenith.

Figure 2.3, from Hofmann-Wellenhof et al. (2008), illustrates a simplified model of the ionospheric path delay. In this model, an approximation is made that all free-electrons are concentrated in an ionospheric layer of infinitesimal thickness. This layer is at an altitude of h_m. This layer also contains the "ionospheric point", IP, where the signal path crosses the ionospheric layer. The angles z_0 and z' are the zenith angles to the satellite from the observation point and the ionospheric point, respectively. z' can be calculated using the following trigonometric equation

$$z' = \arcsin\left(\frac{R_e}{R_e + h_m}\right) z_0 \tag{2.55}$$

where R_e is the mean radius of the Earth. An acceptable estimate of h_m is between 300 km and 400 km (Hofmann-Wellenhof et al. 2008, p. 121).

It may be useful to introduce the term "total vertical electron content", or TVEC. This is the TEC in the specific scenario where a satellite is at the zenith. Hofmann-Wellenhof et al. (2008) gives a modified form of equation 2.44 using TVEC, in place of TEC.

$$\Delta^{Iono} = \frac{1}{\cos(z')} \frac{40.3}{f^2}\, TVEC \tag{2.56}$$

With z' calculated, the ionospheric delay can be mapped to the zenith through

$$\Delta^{Iono}_{zenith} = \Delta^{Iono}_{slant} \cos(z') \tag{2.57}$$

where Δ^{Iono}_{slant} is the ionospheric delay before being mapped to the zenith, also called the slant delay.

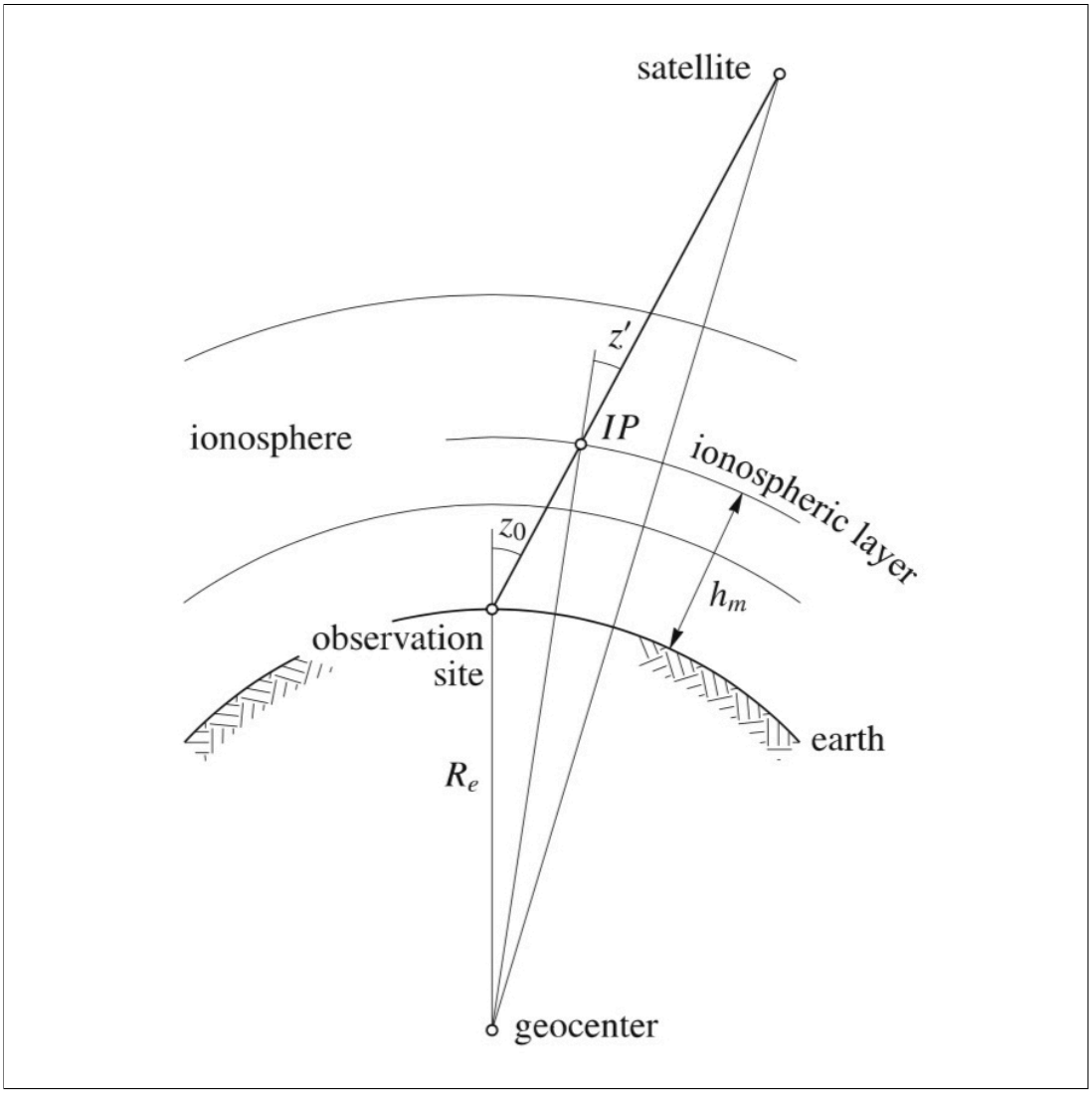

Figure 2.3: Geometry of zenith mapping of ionospheric delay. (Hofmann-Wellenhof et al. 2008, p. 121)

Ionosphere-free Linear Combination

Having appropriately described the ionospheric delay, the next task is to sufficiently eliminate the effect of the ionosphere upon observations. The most effective method of eliminating the ionospheric effect is to utilize an ionosphere-free linear combination. Once again the foundation of this derivation is the observation model for phase observations. In this specific case, the model for the first carrier band is used.

$$\Phi_1 = \rho + c(dt_r + dt_s) - I_1 + T + m_1 + N_1\lambda_1 \qquad \text{(2.45 revisited)}$$

By substituting in equation 2.53 for I_1 and moving terms related to the phase observations to the left side of the equation, we are left with the following.

$$\Phi_1 + \frac{(\Phi_1 - \Phi_2)}{\alpha - 1} = \rho + c(dt_r + dt_s) \frac{1}{\alpha - 1}[m_1 - m_2 + N_1 + N_1\lambda_1 - N_2\lambda_2] + T + m_1 + N_1\lambda_1 \quad (2.58)$$

This can be further organized by sorting together terms related to phase multipath effect and integer ambiguity together, respectively. Thus, one is left with the following ionosphere-free linear combination.

$$\Phi_1 + \frac{(\Phi_1 - \Phi_2)}{\alpha - 1} = \rho + c(dt_r + dt_s) + T + mp_{\Phi_1} + b_1 \tag{2.59}$$

where

$$\begin{aligned} mp_{\Phi_1} &\equiv m_1 + \frac{m_1 - m_2}{\alpha - 1} \\ b_1 &\equiv N_1\lambda_1 + \frac{N_1\lambda_1 - N_2\lambda_2}{\alpha - 1} \end{aligned} \tag{2.60}$$

Although equation 2.59 will be used in further derivations, by rearranging (2.59) to the following form it is more clearly shown to be an inter-frequency linear combination.

$$\frac{{f_1}^2}{{f_1}^2 - {f_2}^2}\Phi_1 - \frac{{f_2}^2}{{f_1}^2 - {f_2}^2}\Phi_2 = \rho + c(dt_r + dt_s) + T + mp_{\Phi_1} + b_1 \tag{2.61}$$

As is clearly seen in both (2.59) and (2.61), the ionosphere-free linear combination is dependant on there being two simultaneous phase range observations, Φ_1 and Φ_2, broadcasted on two carrier signals with distinct frequencies, f_1 and f_2.

2.4.2 The Multipath Effect

As mentioned previously, a weakness of GNSS positioning is that the transmitted signals must traverse the inter-spanning space between satellite and receiver. In the case where this signal arrives at the receiver by more than a single path, each received signal will present distances with offsets to one another. The effect of a GNSS signal arriving at a receiver by multiple paths is aptly named the multipath effect. Both code and phase observations are affected by the multipath effect. However, the effects upon phase observations are very low compared to the effects on code observation (Hofmann-Wellenhof et al. 2008, 160). In theory, a code observation may experience a multipath effect as big as 1.5 times the chip length of the observation. This would mean an effect of 450 meters for the C/A code of GPS. Figure 2.4 illustrates how a signal affected by the multipath effect may lead to two contradicting receiver positions.

The cause of multipath is often the presence of reflective surfaces, like buildings, cars or the ground, near the receiver (Subirana et al. 2013, p. 78). As every case of multipath is highly dependant on the time and location, no good models of multipath effects exist today. Basic geometry, however, tells us that more multipath effect should be expected from satellites with lower elevation angles. Furthermore, the effects of multipath can, as with the ionospheric delay, be estimated using inter-frequency linear combinations.

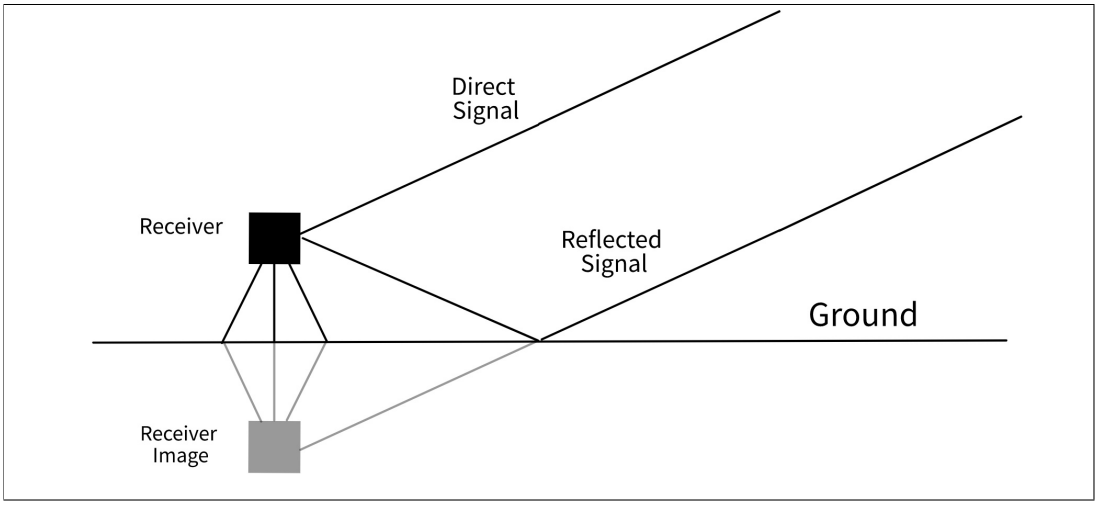

Figure 2.4: Geometry of multipath effect

Estimating Code Multipath in Practice

The foundation of deriving a linear combination for estimating the multipath effect on code observations is the observation model for a code observation.

$$R_i = \rho + c(dt_r + dt_s) + I_i + T + M_i \tag{2.62}$$

The following symbols are adopted:

R_i	Code pseudorange measurement for carrier band i
ρ	Geometric distance between the satellite and GNSS receiver
c	Speed of light
dt_r	Receiver clock error
dt_s	Satellite clock error
I_i	Ionospheric group delay on carrier band i
T	Other, non-dispersive, atmospheric delays
M_i	Code multipath delay on carrier band i

Table 2.11: Symbol overview for code observation model 2.62

By taking code observations corrected for ionospheric delay and subtracting the ionosphere-free phase observation of equation 2.59, the terms ρ, dt_r, dt_s, I_i and T are eliminated.

$$\begin{gathered} R_1 - I_1 - \Phi_1^{IF} = \\ [\rho + c(dt_r + dt_s) + I_1 + T + M_1] \; - \; I_1 - [\rho + c(dt_r + dt_s) + T + mp_{\Phi_1} + b_1] \end{gathered} \tag{2.63}$$

where Φ_1^{IF} is the ionosphere-free range observation from (2.59). As previously mentioned the terms ρ, dt_r, dt_s, I_i and T are eliminated leaving

$$R_1 - I_1 - \Phi_1^{IF} = M_1 - mp_{\Phi_1} - b_1 \tag{2.64}$$

Substituting in I_1 from (2.53), mp_{Φ_1} and b_1 from (2.60), and the left-hand side of (2.59) for Φ_1^{IF} fills out the equation.

$$R_1 - [\frac{\Phi_1 - \Phi_2}{\alpha - 1} - \frac{N_1\lambda_1 - N_2\lambda_2}{\alpha - 1} - \frac{m_1 - m_2}{\alpha - 1}] - [\Phi_1 + \frac{\Phi_1 - \Phi_2}{\alpha - 1}]$$

$$= M_1 - (m_1 + \frac{m_1 - m_2}{\alpha - 1}) - (N_1\lambda_1 + \frac{N_1\lambda_1 - N_2\lambda_2}{\alpha - 1}) \tag{2.65}$$

By sorting together terms related to integer ambiguity, phase multipath, Φ_1 and Φ_2, the following linear combination for estimating M_1 is attained:

$$M_1 = R_1 - \Phi_1(1 + \frac{2}{\alpha - 1}) + \Phi_2(\frac{2}{\alpha - 1}) + B_1 + MP_{\Phi_1} \tag{2.66}$$

where B_1 and MP_{Φ_1} are the terms related to integer ambiguity and phase multipath, respectively.

$$\begin{aligned} B_1 &\equiv N_1\lambda_1(1 + \frac{2}{\alpha - 1}) - N_2\lambda_2(\frac{2}{\alpha - 1}) \\ MP_{\Phi_1} &\equiv m_1(1 + \frac{2}{\alpha - 1}) - m_2(\frac{2}{\alpha - 1}) \end{aligned} \tag{2.67}$$

As was the case when estimating the ionospheric delay, these equations are not fully practical to implement. The terms B_1 and MP_{Φ_1} are unknown. This problem is solved in a similar way as with the ionospheric delay. As described in (2.54), m_1 and m_2 are of a negligible magnitude. As a consequence

$$MP_{\Phi_1} \approx 0 \tag{2.68}$$

The term B_1 is more complicated to handle. The terms remain constant from epoch to epoch, assuming no cycle slip on either of the carrier frequencies. When a cycle slip occurs for either of the carrier bands, B_1 gets a new value. In this thesis, this is solved by reducing every multipath estimate by the mean of all estimates from the previous cycle slip to the next. In this way, the estimates of multipath are actually only the estimates of multipath variation, centered around 0.

2.4.3 Cycle Slip Detection

As seen in sections 2.4.1 and 2.4.2, proper detection of cycle slips is key in estimating ionospheric delays and code multipath effects. This is because cycle slips must be detected in order to counteract the effect of cycle slips upon the estimates. Proper detection of cycle slips is also of interest as a measure of a receiver's ability to maintain continuous signal lock with satellites. This thesis has implemented two methods of detecting cycle slips. Both are explored below.

Rate of Change of Ionospheric Delay

Detecting cycle slips can, once again, be managed through the use of an inter-frequency linear combinations. Equation 2.53 from section 2.4.1, as shown below,

$$I_1 = \frac{1}{\alpha - 1}(\Phi_1 - \Phi_2) - \frac{1}{\alpha - 1}(m_1 - m_2 + N_1\lambda_1 - N_2\lambda_2) \qquad \text{(2.53 revisited)}$$

has previously been explained as having terms, $N_1\lambda_1$ and $N_2\lambda_2$, related to integer ambiguities. These terms will remain constant over sequential epochs as long as there is no cycle slip on either the first or second carrier band. As a result the variation with time of the ionospheric delays should remain low under normal ionospheric conditions. However, if the variation in ionospheric delay from one epoch to the next should exceed a defined limit, this would be an indication that a cycle slip has occurred for one or both of the carrier bands.

Estimates of the rate of change of the ionospheric delay, from one epoch to another, can be made through a simple equation.

$$[\frac{\Delta I_1}{\Delta t}]_j = [(I_1)_j - (I_1)_{j-1}]/(t_j - t_{j-1}) \qquad (2.69)$$

where t_j is the system time at epoch j.

A critical limit that is used by some software, such as TEQC, is 4 m/min, but other critical limits may be used (Estey & Meertens 1999, p. 46). The choice of critical limit should be considered in the context of receiver hardware quality and the local conditions during the observation periods. The reasoning behind this is that if there is increased noise, caused either by the receiver hardware or site conditions, the critical limit is more likely to be passed with no cycle slip occurring.

Another aspect that should be considered is the observation interval. Short observation intervals should be preferred as the noise accumulated over a short amount of time will still be small relative to a cycle slip. As an example, the reader should consider an observation interval of 1 second. Assuming a cycle slip of a single cycle occurs, the result would be a jump of 19 cm for the GPS L1 carrier wave. Using the critical limit of 4m/min, or 6.7 cm/s, this cycle slip would be detected. However, if the the observation interval was 30 second, that same cycle slip would not be detected, as $6.7cm/s * 30s = 201cm$.

A weakness of this method of slip detection is that it is not certain which of the bands has experienced a slip. It could be the first carrier band, the second, or both. In the context of correcting estimates of ionospheric delay and multipath, as described in sections 2.4.1 and 2.4.2, this flaw does not matter greatly. This is because the correction to the estimates are the same regardless of the source of the cycle slip. However, if the goal is to document the cycle slips of each individual carrier band, a different testing quantity must be used to achieve this.

Phase-Code Linear Combination

The observation models for code and phase pseudoranges are shown again. Recall that Φ_i is in units of distance, not cycles.

$$R_i = \rho + c(dt_r + dt_s) + I_i + T \qquad \text{(2.62 revisited)}$$

$$\Phi_i = \rho + c(dt_r + dt_s) - I_i + T + N_i\lambda_i \qquad \text{(2.45 revisited)}$$

By taking the difference of of the two, the following testing quantity is given.

$$\Phi_i - R_i = N_i\lambda_i - 2\,I_i \qquad (2.70)$$

If not for the ionospheric term in (2.70), the equation would give estimates of the integer ambiguity in units of distance. However, as the ionospheric term is time dependant, the estimates from (2.70) will vary from epoch to epoch, even with no cycle slip occurring. The ionospheric term could be modeled, or it could simply be neglected. Cycle slips can once again be detected by taking the differences in estimates from one epoch to another. As such, a fitting critical limit must be set to account for the variations of the ionospheric term, and the noise of the observations.

A weakness of this phase-code combination, compared to (2.53), is the noise level. This combination has a noise level in the range of five cycles (Hofmann-Wellenhof et al. 2008, p. 197). This is mainly due to the noise level of the code observation (Hofmann-Wellenhof et al. 2008, p. 197). In this thesis, an educated choice was made concerning the critical limit used for this method of slip detection. Code observations are expected to produce precisions approximately two orders of magnitude lower than those of phase observations. As such, the critical limit used for the phase-code combination was set as 100 times that of the ionospheric delay. However, as mentioned previously, such limits should be adjusted based on external conditions.

2.5 Receiver Clock Jumps

A phenomenon that may resemble a cycle slip in many ways, but which differs greatly in cause, is the phenomenon of receiver clock jumps. The errors caused by this receiver artefact is dealt with in this thesis, but clock jumps cannot be considered to be a signal path error. Hence, this topic is relegated here to its own section.

The cause of this effect is rooted in the limited precision of internal oscillators used in most GNSS receivers (Guo & Zhang 2014, p. 41). These receiver clocks slowly drift away from true system time. In an attempt to minimize the clock bias, the receiver attempts to re-synchronize with system time (Guo & Zhang 2014, p. 41). Though there are multiple ways this re-synchronization may be executed, a common method is for the receiver to introduce discrete jumps in the receivers time estimate. Often this correction occurs when the offset to true system time exceeds 1 millisecond (Guo & Zhang 2014, p. 41).

In a RINEX observation file (see section 2.7.1), the effect of such a "clock jump" may manifest itself in four different ways. Each of these four outcomes affects one or more of the observation time tag, the code observation, and the phase observation. An overview from Guo & Zhang (2014, p. 42) describes the four different outcomes of a clock jump (see Table 2.12).

Jump type	**Time tag**	**Code observation**	**Phase observation**
1	Jumpy	Smooth	Smooth
2	Jumpy	Jumpy	Smooth
3	Smooth	Jumpy	Smooth
4	Smooth	Jumpy	Jumpy

Table 2.12: Four types of receiver clock jumps (Guo & Zhang 2014, p. 42)

When the code observation, phase observation, or both are affected by a clock jump, the magnitude of the effects will depend on the magnitude of the clock jump. For a clock jump of 1 millisecond, code observation will experience a jump of $0.001s * c$ meters, where c is the speed of light in a vacuum (Guo & Zhang 2014, p. 43). The phase observations will, on the other hand, experience a jump of $0.001s * f$ cycles, where f is the frequency of the carrier signal. Another way the clock jumps differ from cycle slips is that a clock jump will effect observations from all satellites simultaneously. This characteristic makes it possible to detect clock jumps by simply looking for epochs where such a jump occurs for all satellites.

2.6 Orbit Determination of GNSS satellites

While much time has been spent on the topic of GNSS signals and their use, the end goal of GNSS is determining the position of a GNSS receiver. However, to do this requires more than the proper treatment of GNSS observations. It is also essential to correctly determine the satellites' positions at each observation time. It is only with both the satellite positions and the GNSS measurements that a receiver position may be determined (Hofmann-Wellenhof et al. 2008, p. 26).

As satellites travel in vacuum, there are few external forces, such as drag, acting on the satellites. The dominant forces acting upon the satellites are those of gravitation. The gravitational pull of nearby celestial objects such as the Moon, the Sun and of course the Earth are the primary forces determining the motion of a satellite in orbit. Solar radiation also applies some forces to a satellite. However, these forces are small relative to those of gravitation (Hofmann-Wellenhof et al. 2008, p. 35–36). As there is such a limited set of forces acting on orbiting satellites, it is possible to determine current satellite orbits, and predict future orbits. This results in the user not needing continuous satellite positions, but instead being able to predict satellite positions continuously from a discrete number of samples.

At the core of determining GNSS satellite orbits are the observations of reference stations located all across the Earth. A global network such as this has a much higher reliability

when it comes to accurately estimating satellite orbits. This network of reference stations that monitor satellite orbits are all part of the respective control-segments of each GNSS system (Hofmann-Wellenhof et al. 2008, p. 47). As there is a high correlation between errors in satellite orbits and errors in the estimated receiver position, the reliability of estimated satellite orbits is of utmost importance (Hofmann-Wellenhof et al. 2008, p. 26).

In essence, the problem of determining satellite positions is the inverse of determining receiver positions. Instead of working from known satellite coordinates and determining receiver coordinates from ranging observations, the receiver coordinates are known, and the satellite positions are determined.

Once satellite orbits are determined, they can be expressed to the user in different formats. Though these formats vary in many aspects, an important difference is regarding whether or not the orbits are available in real time, or if they are only available after the fact, i.e. for post-processing. Each format also requires a different set of algorithms in order to predict future or past satellite positions.

2.6.1 Broadcast Ephemeris

Broadcast ephemeris are, as the name suggests, broadcasted from satellite to receiver along with the observation message. The data related to the orbit of the satellite is called the navigation message (Hofmann-Wellenhof et al. 2008, p. 50). The major advantage of broadcasting the navigation message in real time is that the position of the receiver may be estimated in real time. This type of real-time positioning is, of course, a necessity when GNSS is used for navigation purposes, or other forms of real-time positioning.

As mentioned previously, it is the observations of reference stations on the Earth that allow the determination of these ephemerides. The most recent observations are used to determine the orbit of a satellite at certain reference times. After the computation of the ephemerides, they are broadcasted to the satellites so that it may further broadcast them to the receiver. With these reference orbits in hand, the user may extrapolate the orbit of the satellite at the time observation epochs (Hofmann-Wellenhof et al. 2008, p. 50).

The contents of the navigation message may vary from satellite to satellite. These variations result in different extrapolation methods.

Broadcasted Keplerian Parameters

The first, and currently most used, form of broadcasted orbital information is Keplerian parameters. This format is currently used by all GNSS systems, except for GLONASS. By providing the six Kepler parameters needed to describe a Kepler ellipse, the path of the satellite along this orbital ellipse is easy to predict. However, as a Kepler ellipse is only fully applicable in a two-body point mass system, these six parameters will not adequately describe the change of the satellite orbit over larger temporal distance. Effects of the previously mentioned solar radiation, the non-spherical nature of the Earth, and the gravitational pull of other celestial masses will result in the described Kepler ellipse

changing over time. Nine correction terms are, therefore, also broadcasted, along with the Kepler parameters (Subirana et al. 2013, p. 56).

These correction terms allow the extrapolation of orbits with higher temporal distance from the reference epoch. As a consequence, the reference epochs may have a longer interval when using Kepler parameters. A typical interval is three to four hours (Subirana et al. 2013, p. 33). However, the quantity of parameters, as seen in Table 2.13, results in the data size being greater for this kind of navigation message.

Parameter	**Explanation**
t_e	Reference epoch of ephemeris
$\sqrt{a}$	Square root of semi-major axis in $\sqrt{meters}$
e	Eccentricity
M_0	Mean anomaly at reference epoch
ω_0	Argument of perigee
i_0	Inclination
ℓ_0	Longitude of the node at weekly epoch t_0
$\dot{i}$	Rate of inclination angle
$\dot{\Omega}$	Rate of node's right ascension
C_{uc}, C_{us}	Cos and sine correction coefficients for ω_0
C_{rc}, C_{rs}	Cos and sine correction coefficients for geocentric distance
C_{ic}, C_{is}	Cos and sine correction coefficients for i_0

Table 2.13: Broadcasted ephemeris for GPS, Galileo and BeiDou. (Hofmann-Wellenhof et al. 2008, p. 51)

Broadcasted Position and Velocity Vectors

The other form of broadcast ephemeris, currently only used by GLONASS, is position and velocity vectors. This form of broadcast ephemeris only includes the position and velocity vectors of the satellites, along with the combined gravitational acceleration vector of the Moon and Sun (Subirana et al. 2013, p. 59). The parameters transmitted in the GLONASS navigation message are illustrated in Table 2.14. With less data describing the change of the orbit over time, satellite positions can not be extrapolated as far temporally as with Keplerian parameters. As a result, the navigation messages in this form are usually transmitted at a higher rate than other broadcast ephemerides. A common interval is 15 minute (Subirana et al. 2013, p. 59).

Parameter	Explanation
t_e	Reference epoch of ephemeris
$x(t_e)$	X coordinate at t_e
$y(t_e)$	Y coordinate at t_e
$z(t_e)$	Z coordinate at t_e
$v_x(t_e)$	X velocity component at t_e
$v_y(t_e)$	Y velocity component at t_e
$v_z(t_e)$	Z velocity component at t_e
$\ddot{X}(t_e)$	X component of Sun and Moon acceleration at t_e
$\ddot{Y}(t_e)$	Y component of Sun and Moon acceleration at t_e
$\ddot{Z}(t_e)$	Z component of Sun and Moon acceleration at t_e

Table 2.14: Broadcasted ephemeris for GLONASS (Subirana et al. 2013, p. 59)

2.6.2 Precise Ephemeris

The final form of orbital information available is precise ephemerides. This form separates itself from broadcasted ephemeris in that it is not available in real time. As such, the use of precise ephemerides are limited to post-processing. However, as the name indicated, precise ephemeris are the most accurate of the orbital information available (Hofmann-Wellenhof et al. 2008, p. 52). Precise orbital data may be presented in different file formats. The SP3 file format, however, is well documented and currently adopted by IGS. The Sp3 file format is explored further in section 2.7.2.

Currently, precise ephemeris are delivered by organizations like IGS and CDDIS for free (Subirana et al. 2013, p. 62). These organizations deliver various products of precise ephemeris. These vary in accuracy, completeness and latency, with the most accurate and complete products, like the IGS "final" product, taking up to 18 days to become available (Subirana et al. 2013, p. 63).

Lagrange Interpolation

A standard method of interpolating precise satellite positions is the Lagrange interpolating polynomial (Boulet 1991, p. 327). Although other interpolation methods exist, the Lagrange interpolation is a fast algorithm that is easily programmable. It allows the user to vary the amount of reference epochs in the series, by varying the order of the polynomial, and may be used for a series of unequally spaced epochs (Boulet 1991, p. 327).

In describing the Lagrange interpolation, the reading should consider an unknown function f(x). The user wishes to determine the function value f(X) at a specific point x=X. All the user has is a discrete set of n functional values f_i, where $i = 1, ..., n$. Each functional values has a corresponding x values, x_i, which surround the point of interest, X. These data points may also be known as nodes. One way to determine the f(X) is to determine

an n-1th order polynomial that passes through all the known data points. Figure 2.5a shows such a polynomial.

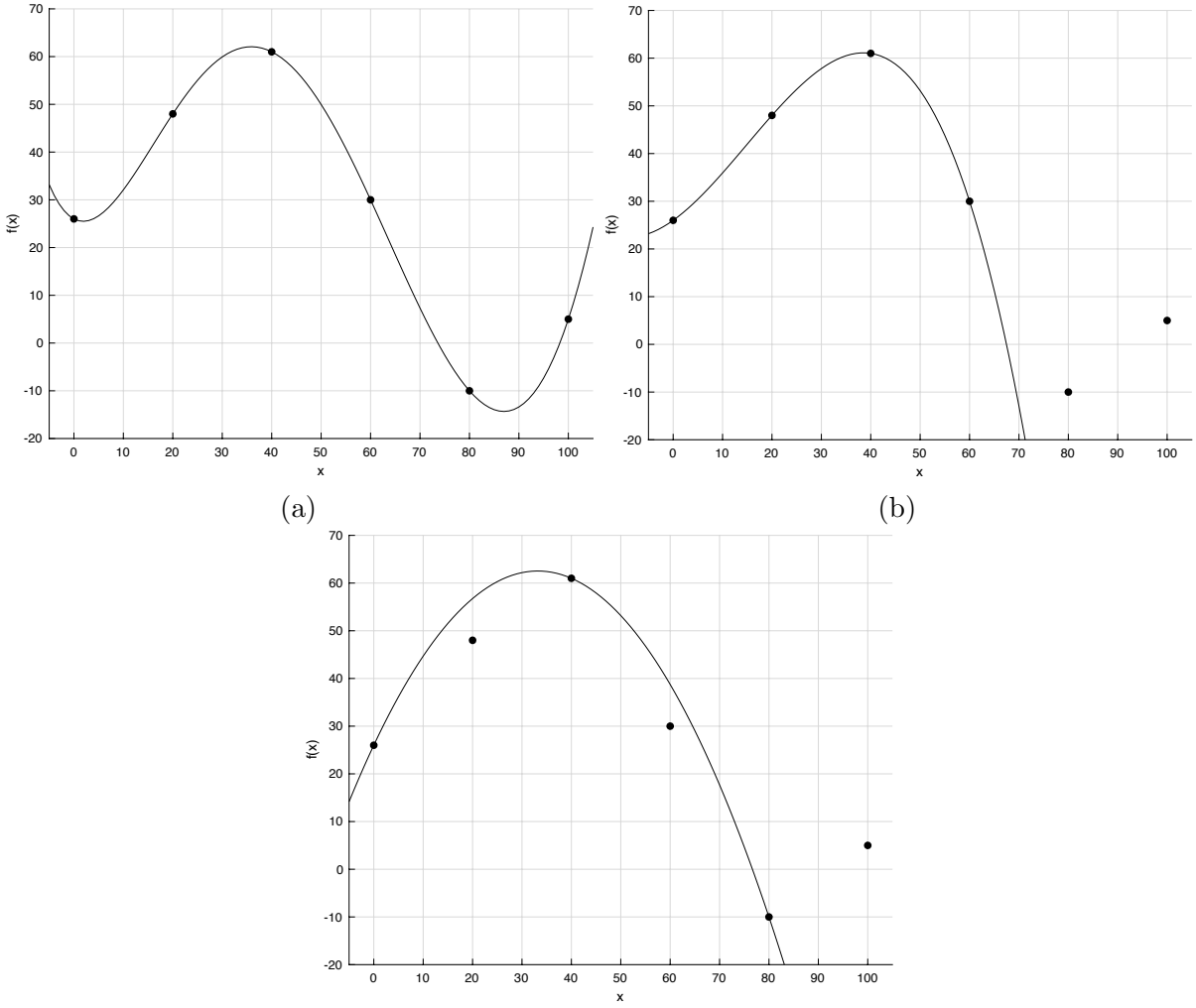

Figure 2.5: Visualization of Lagrange interpolation polynomials: (a) polynomial with six data points. (b) polynomial with only four out of six data points. (c) polynomial only fitted to nodes one, three and five

From Figure 2.5a it is clear that, having a polynomial such as this, the user may quite easily interpolate any functional value f(x) between the nodes. However, how well does the polynomial do at extrapolating points outside of the known nodes? Figure 2.5b shows a Lagrange polynomial that has been fit only to the first four known data points.

It is clear from Figure 2.5b that the polynomial is not fit to extrapolate functional values beyond the known nodes. However, how many nodes are required to interpolate satellite positions with enough accuracy?

Figure 2.5c shows a Lagrange polynomial that has only been fitted to some of the known nodes. From this, it is possible to see how limiting the number of nodes will reduce the interpolation accuracy, even for data points in between the nodes.

When considering Lagrange polynomials in the context of the interpolation of precise

orbital data, B.W. Remondi's studies showed that ten nodes would result in an accuracy of some decimeters, for epoch intervals of 30 minutes (Hofmann-Wellenhof et al. 2008, p. 53). He concluded in another study, in 1991, that 18 nodes could result in millimeter-level accuracy, even with 40 minutes epoch intervals (Hofmann-Wellenhof et al. 2008, p. 53).

The computation of a Lagrange polynomial is relatively simple to program, while being time-consuming if done by hand. Given n nodes with functional values f_i at x_i, the functional value of the n-1th order Lagrange polynomial, at x=X, is determined by the following algorithm (Boulet 1991, p. 327–328).

$$f(x = X) = \sum_{i=1}^{n} [\, f_i \prod_{\substack{j=1 \\ j \neq i}}^{n} \frac{X - x_j}{x_i - x_j}] \tag{2.71}$$

2.7 File Formats

The file formats used in this thesis are well documented. However, in the spirit of thoroughness, a short introduction of the file formats used in this thesis follows.

2.7.1 RINEX

Receiver Independent Exchange Format, or RINEX, is one of the most used file formats for the storage of GNSS data. The RINEX format includes three different ASCII file types: Observation files, navigation files, and meteorological files. The most commonly used RINEX file types, however, are the observation and navigation files (Hofmann-Wellenhof et al. 2008, p. 449).

The RINEX observation files mainly contain the measured carrier phases and code ranges. However, they also contain Doppler measurements, signal-to-noise ratios, and metadata (Hofmann-Wellenhof et al. 2008, p. 449). This metadata includes essential data, such as the observation period, time systems used, antenna offsets and observation types observed.

The RINEX navigation files mainly contain satellite ephemeris. However, RINEX navigation file can also contain information about satellite clock biases, as well as relativistic effects.

At the time of writing, the most recent version of RINEX is version 3.04. This version supports the following satellite systems, each with their own identifying code (International GNSS Service (IGS) 2018, p. A5):

- **G**: GPS
- **E**: Galileo
- **R**: GLONASS
- **C**: BeiDou
- **J**: QZSS
- **I**: IRNSS
- **S**: SBAS

RINEX 3 uses its own set of codes to describe specific observables. These consist of one letter, followed by a number and finally another letter. The first letter designates the type of the observation. RINEX 3 uses the following types (International GNSS Service (IGS) 2018, p. A7):

- C: Code pseudorange
- L: Phase pseudorange
- D: Doppler
- S: Signal strength
- I: Ionosphere phase delay
- X: Receiver channel numbers

The number in the second position of the observation code designates the carrier band. This number can be a number from zero to nine. However, as these carrier band numbers are used for all GNSS systems, the carrier band number five will reference different carrier bands depending on the GNSS system. Table 2.15 gives an overview of the designation of each RINEX band number:

RINEX band number	**GNSS system**	**Carrier band**
1	GPS Galileo GLONASS BeiDou	L1 E1 G1 B1
2	GPS GLONASS BeiDou	L2 G2 B1-2
4	GLONASS	G1a
5	GPS Galileo BeiDou	L5 E5a B2a
6	Galileo GLONASS BeiDou	E6 G2a B3
7	Galileo BeiDou	E5b B2b
8	Galileo BeiDou	E5(a+b) B2(a+b)

Table 2.15: RINEX 3 carrier band number designations (International GNSS Service (IGS) 2018, p. A7-A8)

The final letter of the observation code designates the "attribute" of the observation (International GNSS Service (IGS) 2018, p. A8). Though there are currently 14 different letters that may be used to designate the attribute, only the attributes that appear in the results of this thesis will be presented in Table 2.16. The rest can be found on page A8 of International GNSS Service (IGS) (2018). It should also be noted that an attribute code, such as X, will have different meanings for a single GNSS system, such as GPS, depending on the carrier band. This can be seen in Table 2.16.

Attribute code	GNSS system	Attribute
C	GPS GLONASS	C code-based
	Galileo	C channel
L	GPS L2C	L channel
	GPS	P channel
P	GPS GLONASS	P code-based
	BeiDou	Pilot channel
Q	GPS Galileo BeiDou	Q channel
W	GPS	Based on Z-tracking
X	Galileo	B+C channel
	GPS	M+L channel
	GPS	Y code based
	GPS Galileo BeiDou	I+Q channel
	GPS BeiDou	D+P channel

Table 2.16: RINEX 3 attribute code overview (International GNSS Service (IGS) 2018, p. A8)

2.7.2 SP3

A commonly used file format for precise orbital data is SP3. SP3 is an ASCII format used by IGS, among others, which may contain any combination of satellite positions, velocities, and satellite clock corrections (Hofmann-Wellenhof et al. 2008, p. 52). A typical interval for the reference epochs is 15 minutes, though shorter intervals may be found (Subirana et al. 2013, p. 62). For each epoch, the ephemeris of all satellites described in the SP3 file header are given. In essence, the velocity data is not necessary for orbit determination, as velocity may be derived from numerical derivations of position. Regardless, having precise position data at reference epochs before and after the observation epoch allows the user to interpolate the position in between reference epochs (see section 2.6.2). A full description of the SP3 file format can be found on the web page of the European Space Agency (see Hilla (2016)).

Chapter 3: Method

Developing a software for evaluating receiver performances required decisions regarding which mathematical estimation methods would be used, as well as how the computer software should be structured to utilize these methods. Furthermore, in order to produce results that could display the functionality of the software, a representative data set needed to be collected. Each of these aspects are explored in their own section of this chapter.

3.1 Estimation Methods

As most of the estimation methods used in the developed software have been thoroughly introduced in chapter 2, their presentation in this chapter will be brief. The intent is only to present which mathematical methods have been used, and to what purpose.

3.1.1 Lagrange Polynomial Interpolation

As will be discussed in section 3.2, satellite positions needed to be computed for observation epochs. Precise orbital data were used for this purpose, as opposed to broadcasted ephemeris. The reasoning behind this decision was of a practical nature. In order to interpolate the satellite positions of the relevant epochs, the Lagrange interpolation method, as described in 2.6.2, was utilized. As the satellite positions were only needed to determine satellite elevation angles, extreme precision was not needed. As such, a seventh order Lagrange polynomial was deemed sufficient.

3.1.2 Estimation of Ionospheric Delay

Ionospheric delays upon the satellite signals were computed for multiple reasons. Firstly, these estimates were to be used for cycle slip detection. These estimates were also of interest by themselves, as they would illustrate the periodic changes of ionospheric delay over longer time intervals. Equation 2.53 was chosen to create relative estimates of ionospheric delays. These estimates were corrected for the effects of cycle slips, as described in section 2.4.1. Hence the resulting estimates were relative and not absolute values.

In order to map the ionospheric delay to the zenith, equation 2.57 was used.

3.1.3 Estimation of Multipath Effect

One of the main metrics used to evaluate the performance of GNSS receivers would be the estimates of multipath effect on the code observations. Estimates of multipath were computed using equation 2.66. As with the estimates of ionospheric delay, these estimates were also corrected for the effects of cycle slips. However, these estimates were corrected with mean values, as described in section 2.4.2.

RMS values of the multipath estimates were computed in the software. These RMS values were computed using the following equation.

$$M_{RMS} = \sqrt{\frac{1}{N_{estimates}} \sum_{i=1}^{N_{sat}} \sum_{j=1}^{N_{epochs}} {M_{ij}}^2} \tag{3.1}$$

where M_{ij} denotes the estimated multipath effect of observation epoch j and satellite i.

Epochs with no observations, or those with cycle slips, were not included. Hence, $N_{estimates}$ denotes the amount of estimates included in the computation. Similar RMS values were calculated for each individual satellite. Equation 3.1 was utilized for this as well, but naturally, only estimates from a single satellite were included.

As the magnitude of the multipath effect is strongly correlated to the elevation angle of the satellite, weighted RMS values were also computed. The multipath estimates were weighted based on the satellite elevation angle of each epoch. The following weighting function was used.

$$w = \begin{cases} \frac{1}{4\sin^2\beta}, & if\ \beta < 30^\circ \\ 1, & otherwise \end{cases} \tag{3.2}$$

where β is the elevation angle of the satellite.

For elevation angles from 0 to 30 degrees, this function assigns weights from 0 to 1. Elevation angles above 30 degrees are all assigned the weight 1.

3.1.4 Cycle Slip Detection

The proper detection of cycle slips was of great importance. Cycle slips needed to be detected in order to correct for the effects of cycle slips on the multipath and ionospheric delay estimates. Furthermore, the receiver's tendency to experience cycle slips was another metric that would be used to evaluate the receiver performance. For the purpose of detecting cycle slips, two methods were utilized, for different purposes.

The first method utilized for cycle slip detection was observing the rate of change of the ionospheric delay, as shown in equation 2.69. As described in section 2.4.3, a cycle slip experience by one, or both, of the phase signals of equation 2.53 will result in a jump in

the ionospheric delay estimate. The advantage of using this method is its low noise level. As the phase observations contain little noise, the critical rate of change that indicate a cycle slip can be set very low, without being crossed because of noise alone. The default critical limit was set to 4 meters/minute, as suggested by Estey & Meertens (1999, p. 46). However, the user is also allowed to define the limit to be used. A weakness of this method is that it does not specify which of the phase signals experienced a slip. The slips detected by this method are, therefore, only used to correct the estimates of multipath and ionospheric delay.

The second method utilized for cycle slips detection is the phase-code combination shown in equation 2.70. The advantage of this method is that it will detect a cycle slip on a single phase observation. This, therefore, allows for determining how many slips occur for each individual phase signal. However, as has been mentioned in 2.4.3, the inclusion of the code pseudorange results in much more noise. The result is that this method is not as sensitive as the first method of slip detection. The default critical limit was set to 400 m/min, but the user can also choose this value.

3.2 Software Structure

The main body of this thesis has been the development of a software capable of executing performance evaluations of GNSS receivers. As a result, a presentation of this software is appropriate. The program, officially named "**GNSS_Receiver_QC_2020**", was developed in MATLAB. The primary goal of the development process was to create a program that would produce a performance analysis with the least amount of work required from the user. However, a secondary goal was also that the functions comprising **GNSS_Receiver_QC_2020** could be used independently. Figure 3.1 shows the overall structure of the program, and the dependencies of the different functions. The following presentation will be divided into the main segments of **GNSS_Receiver_QC_2020**. This is in an attempt to present the independent segments comprising the program, and in doing so, also presenting the overall structure of the program.

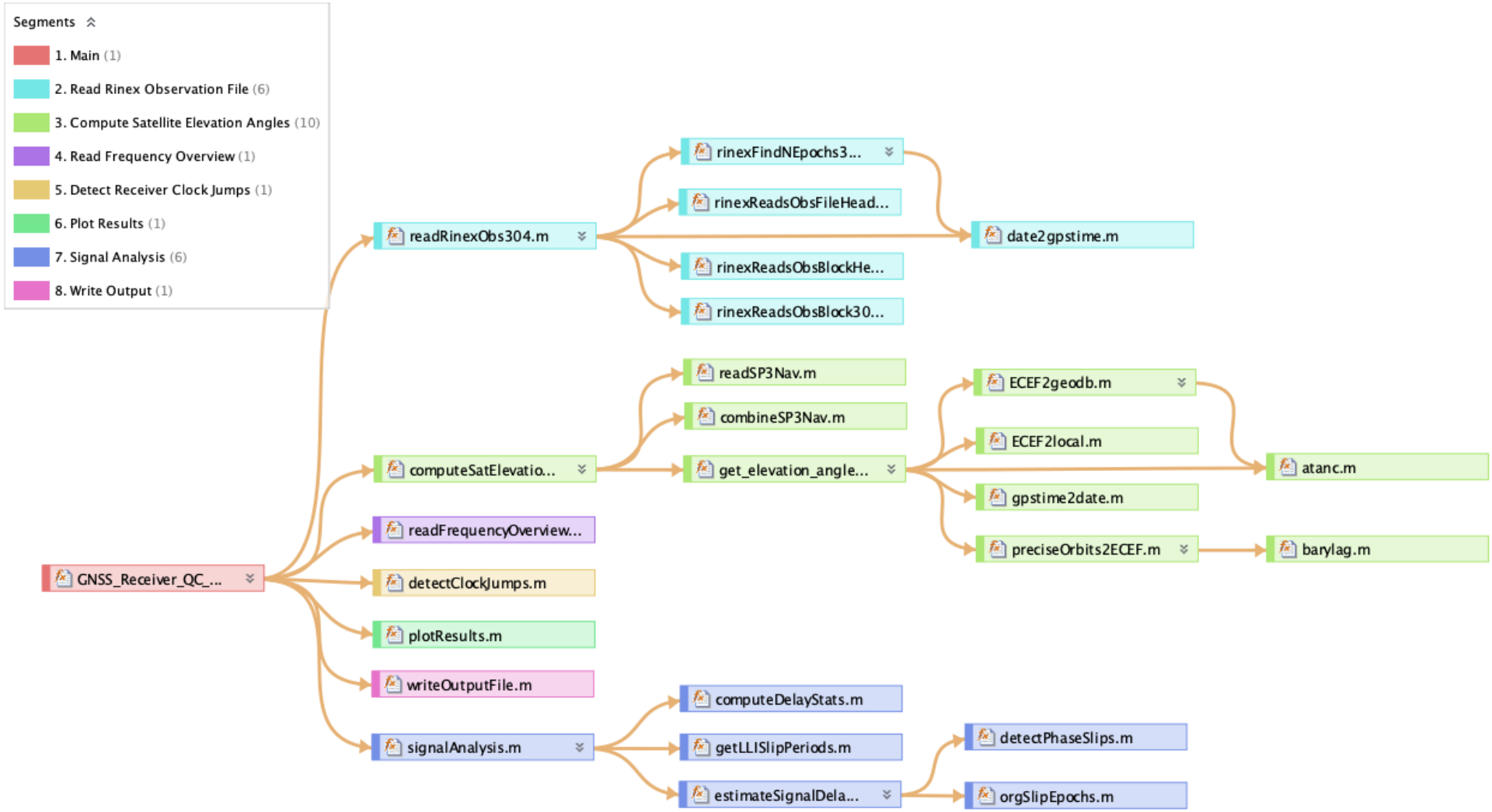

Figure 3.1: **GNSS_Receiver_QC_2020** function dependencies

3.2.1 Reading RINEX Observation Files

In order for the software to function for a wide variety of receivers, it needed to be able to read GNSS observations from RINEX observation files. The software analysis needed to include all four GNSS systems. As RINEX 3 greatly improves upon RINEX 2 in handling multiple GNSS systems, the program was developed to read RINEX 3 files from version 3.02 and onward. The segment of **GNSS_Receiver_QC_2020** that reads RINEX 3 observation files is executed through the function "**readRinexObs304**".

readRinexObs304 reads and stores the following information from the header of a RINEX 3 observation file:

- GNSS systems present
- Observation types present
- Observation interval
- Time of first observation epoch
- Time of last observation epoch
- GLONASS frequency channel of each satellite
- Marker name
- Receiver type
- RINEX version
- RINEX converting software
- Antenna offset
- Approximate position of receiver
- Number of leap seconds

readRinexObs304 reads and stores the following information from the main body of a RINEX 3 observation file:

- Epoch time tags
- GNSS observations: Phase, code, Doppler and signal strength
- "Loss-of-lock" indicators
- "Signal strength" indicators

It should be possible to use **readRinexObs304** for the purpose of reading RINEX 3 observation files in other contexts. The user is, therefore, given a range of different input arguments to specify the desired content to be returned from **readRinexObs304**. The following aspects are possible for the user to affect:

- Which GNSS systems that should be included
- Which carrier bands that should be included
- What kind of observations should be included: Phase, code, Doppler or signal strength

This allows the user some level of flexibility to use the function for purposes other than **GNSS_Receiver_QC_2020** alone.

3.2.2 Computing Satellite Elevation Angles

The software needed to be able to compute the satellite elevation angles at each observation epoch. This mostly came down to computing the satellite positions of each observation epoch. This segment of **GNSS_Receiver_QC_2020** was executed through the function "**computeSatElevations**".

As has been mention in section 3.1.1, precise orbital data were used, more specifically the SP3 format. As such, **computeSatElevations** needed to be able to read SP3 files. As SP3c and SP3d are better suited to describe multiple GNSS systems than older versions, the program was developed to read these formats. The Lagrange interpolation method requires a certain amount of nodes before and after each observation epoch. However, as most SP3 files are limited to a 24 hour period, this would cause problems when observation periods approached the limits of the SP3 files. As a result, the program needed to be able to read data from multiple SP3 files. In the end, the user has the choice of inputting one, two, or three SP3 files as needed. **computeSatElevations** is capable of combining the data of all SP3 files inputted so that observation periods can surpass 24 hours in length.

With the approximate position of the receiver known from the RINEX observation header and the satellite positions computed through Lagrange interpolation, elevation angles of satellites could be computed. This was achieved by projecting the vector between satellite and receiver onto a tangent plane. Following this, the arctangent of the horizontal North-East vector and the Up vector is computed. Thus, the elevation angle is acquired.

3.2.3 Reading Frequency Overview

As changes in technology are often rapid, some effort was put into making the program modifiable in some aspects. One such aspect was the frequencies of the RINEX designated carrier bands. The RINEX format is well planned out in advance. However, the fifth RINEX carrier band, which currently refers to the E5a carrier band for Galileo, could be re-designated at a later time. Although this is unlikely to happen, this should ideally be simple to correct for. Furthermore, as new carrier signals are introduced, these will need to be designated band numbers in the RINEX format.

As such, the frequencies of each RINEX designated carrier band, for each GNSS system, are read from a text file. This file also contains the increment frequencies for GLONASS signals. If changes to the RINEX signal plan were to occur, this text file is all that must be modified.

3.2.4 Analysing Combinations of Observation Signals

The analysis segment of the **GNSS_Receiver_QC_2020** was developed to compute estimates capable of producing the metrics needed to evaluate receiver performance. The methods utilized to make these estimates are presented in section 3.1. This segment of the software is executed through the **signalAnalysis** function. The analysis is executed

for each observation signal and is, as a result, quite extensive. The estimates produced in each analysis are the following:

- Estimates of multipath effects on code observation signal, corrected for cycle slips
- Estimates of ionospheric effect on observation signal, corrected for cycle slips
- Epochs with cycle slips on observation signal, detected using methods from section 3.1
- Epochs with cycle slips on observation signal, detected using "Loss-of-lock" Indicators (LLI) from RINEX observation file

Other practical data is also stored, such as the epochs where the current observation signal is tracked.

The final task of **signalAnalysis** is to compute statistical metrics concerning the estimates in the analysis. These statistics are stored in a MATLAB structure so they may be easily accessed in the source code, as well as displayed in the output file. As the metrics computed in this process are introduced in section 3.2.7, they will not be explored further here.

One last aspect of the analysis segment that should be explored: How was the secondary observation signal, to be used in the linear combinations of the analysis, chosen? An observation signal transmitted on one carrier band may be combined with another observation signal transmitted on a different carrier band. This leaves the question of which combination is the "best". In the end, this question was resolved by executing an analysis using all valid combinations, one after the other. After this process, the combination that produced the most estimates of multipath effect was chosen as the "best". Though this "brute force" method is not the most elegant and computationally fast, the analysis segment is still a relatively small part of the computation time of **GNSS_Receiver_QC_2020**.

3.2.5 Detection of Receiver Clock Jumps

A receiver's tendency to experience receiver clock jumps may be considered a measure of the receivers clock's tendency to drift. As a result, detecting a receiver's clock jumps and the interval between clock jumps, was implemented in **GNSS_Receiver_QC_2020**. This task was executed by the function **detectClockJumps**. This function detects any observation epoch where all code observation of all tracked satellites experienced significant jump simultaneously. These epochs, along with the epoch where the observation time tag jumps, are considered epochs where receiver clock jumps have occurred.

3.2.6 Plotting Results

The plotting of the computed estimates was implemented for multiple reasons. First of all, it allows for a quick visual control that no abnormal or unexpected results, such as undetected cycle slips, have occurred. Furthermore, the resulting graphs allow for a more

visual comparison of the results of the different analyses. As the user may not be interested in visual plots, the user has the choice, through an input argument, whether or not the results should be plotted. The plotting is executed by the function "**plotResults**". For each signal processed, the following plots are created:

- Multipath estimates of the primary code observation versus time
- Multipath estimates of the primary code observation versus satellite elevation angle
- Ionospheric delay estimates of the primary observation signal, versus time
- Ionospheric delay estimates of the primary observation signal mapped to the zenith, versus time

By plotting the multipath estimates versus elevation angles, the user can focus on the multipath effects that are not primarily caused by very low elevation angles. As the estimates of multipath sometimes include outliers, the y-axis of the multipath plots are cropped. The y limits are set to the mean of estimates $\pm$ 7 standard deviations. However, to preserve the actual perspective of the data, both the cropped and uncropped graphs are saved.

Although the ionospheric delay does not necessarily indicate a great deal about a receiver's performance, it does provide a visualization of the periodic effects of ionization in the ionosphere, which may be of interest to some users. Hence, it is also plotted through **plotResults**.

3.2.7 Producing Output Files

The software is well documented, allowing users to work with the source code itself. However, a goal for the development process was for the software to return a detailed but understandable output file to the user. Balancing the amount of detail with the need to create a compact output file was, therefore, crucial. As a result, the user is required to input four booleans to the software. These specify which aspects should be included in the output file or not. These four aspects, in addition to the header, comprise the five segments of the output file. These segments are shown below. Explanations of each segment follow.

- Header
- Completeness overview
- Compressed results overview
- Detailed results overview
- Information concerning "Loss-of-lock" indicators (LLI).

Header

The main function of the header segment of the output file is to provide metadata about the rest of the file. This information includes:

- RINEX observation filename
- RINEX version of observation file
- Program used to convert raw data to RINEX format
- Marker name
- Receiver type
- Date of first observation epoch
- Date of last observation epoch
- Observation interval
- Amount of receiver clock jumps that have occurred in the observation period
- Average time interval between clock jumps, with respective standard deviation
- The critical limits used for cycle slip detection, for both the ionospheric delay and the phase-code combination
- Which GNSS systems that are included in the output file

Note that as most of this data is extracted directly from the header of the RINEX observation file, its accuracy is dependant on the accuracy of the RINEX header. The header also gives an overview of which segments of the output file the user has elected to include. Lastly, some RINEX files do not include LLI. As such, the inclusion of this information will automatically be turned off if LLI are missing. This is regardless of the user's inputted booleans. In this case, a message will be produced in the header, informing the user of the change.

Completeness Overview

The purpose of the completeness overview segment is to provide context for the user regarding what satellites are included in the analysis. As this overview is on a satellite to satellite basis, it also allows the user to see which observation signals the receiver has tracked from each satellite. For increased ease of use, the information is sorted by GNSS systems and carrier bands.

Compressed Results Overview

The purpose of the compressed results overview is to give the user a compact overview of the performance metrics. In order to remain as readable as possible, this segment does not give information on a satellite to satellite basis. Instead, the values are compounded from all satellites. Furthermore, the values are sorted by GNSS system and presented for each observation signal processed. The following values are presented for each observation signal:

- RMS of multipath estimates
- Weighted RMS of multipath estimates
- Amount of cycle slip periods
- Amount of cycle slip periods, and elevation angles above 10 degrees
- Amount of cycle slip periods, and elevation angles below 10 degrees
- Amount of cycle slip periods, where elevation angles were not computed
- Ratio of number of cycle slip periods and observation epochs

Although the compressed results overview allows the user to get an overview quickly, it does not present the variations from one satellite to another. One satellite might have produced inferior results because of poor conditions, while other satellites may not. This would not show itself clearly in the compressed results overview.

Detailed Results Overview

The function of the detailed results overview is to allow the user to dig deeper into the results, on a satellite to satellite basis. This allows the user to look at variations caused by aspects such as differences in satellite generation, satellite elevation angles, and number of estimates made. This amount of detail leads to a much less compressed overview. As a result, the data is presented in several tables, with one table for each observation signal. Each row holds data concerning one satellite. This allows for comparisons of different satellites. For each satellite in the table, the following information is given:

- Satellite ID (PRN for all GNSS systems excluding GLONASS)
- Number of observation epochs with current observation signal
- Number of epochs with estimates of multipath on code observation
- RMS of multipath estimates
- Weighted RMS of multipath estimates
- Average satellite elevation angle of observation epochs

- Total number of cycle slip periods
- Ratio of number of cycle slip periods and observation epochs
- Number of cycle slip periods distributed over elevation angle of slip epoch
  - 0 - 10 degrees
  - 10 - 20 degrees
  - 20 - 30 degrees
  - 30 - 40 degrees
  - 40 - 50 degrees
  - Above 50 degrees
  - Elevation angle not computed for slip epoch

Information Concerning "Loss-of-lock Indicators"

Information concerning LLI is not displayed in its own segment of the output file. Instead, if the user desires this information, it is included as an expansion to the detailed results overview. In this case, the following values are presented not only from the software analysis, but also from the LLI analysis.

- Total number of cycle slip periods
- Ratio of number of cycle slip periods and observation epochs
- Number of cycle slip periods distributed over elevation angle of slip epoch
  - 0 - 10 degrees
  - 10 - 20 degrees
  - 20 - 30 degrees
  - 30 - 40 degrees
  - 40 - 50 degrees
  - Above 50 degrees
  - Elevation angle not computed for slip epoch

Lastly, these values are also presented for the epochs where the software and LLI analyses coincide.

As mentioned previously, if no LLI are present in the RINEX observation file, this information will automatically be excluded, regardless of the input parameters of the user.

3.3 Data Collection Protocol

The purpose of this thesis has not been to draw a conclusion concerning the quality of any specific receiver. However, in order to evaluate the capabilities of the developed software, a presentation of some analyses results is needed. An observation data set is therefore needed. This leaves questions regarding the protocol for collecting this data set. A description of this protocol follows.

3.3.1 Presentation of the Receivers

A decision was made concerning which GNSS receivers were to be used. In order to gather dissimilar data sets, the receivers should be equally dissimilar. These receivers were therefore chosen to differ in manufacturing brand, original production year, antenna type, and price. Hence, these variations should ideally present themselves in the analysis results.

The four receivers chosen were:

- Topcon Hiper VR
- Septentrio PolaRxS Pro
- Trimble NETR5
- Emlid Reach RS2

Table 3.1 illustrates some of the notable differences between the receivers. The range in production years is 13 years. In the perspective of GNSS advancement, this is a long time. As a result, the Trimble receiver, being the oldest, tracks neither Galileo nor BeiDou satellites.

Another significant difference to note is the price tag of each receiver. The Emlid receiver comes in at a considerably lower price than the rest. A consequence of this seems to be the receiver's lack of ability to decode encrypted observation codes, such as the P-code of GPS. In other words, this receiver will only have access to civil signals. A problem that arises from this is that there are considerably fewer satellites that have civil observation signals on two carrier bands. As a result, this receiver will have considerably less satellites that produce inter-frequency linear combinations. This includes the ionosphere-free linear combination, which greatly increases precision.

It is also worth mentioning that two of the receivers (Topcon and Emlid) come with built-in antennas. While these "all-in-one" solutions are convenient, such antennas are inferior in many ways to the calibrated external antennas the other receivers are equipped with. This difference should be considered when discussing the results.

Receiver Name	Prod. Year	Approx. Price [USD]	GNSS Systems Tracked	Anti-Spoofing Tracking	Antenna Type
Hiper VR	2019	12.000	All	Yes	Built In
PolaRxS	2010	17.000	All	Yes	External
NETR5	2006	7.000	GPS & GLONASS	Yes	External
Reach RS2	2019	1900	All	No	Built In

Table 3.1: Comparison of receivers used in data collection. Approximate prices from Blinken AS (2020), Norgeodesi AS (2020) and NavSys AS (2020)

It is important to note that the approximate prices displayed in Table 3.1 are only meant as guiding values. As suppliers of such high-end receivers can provide a wide range of packages, the prices will vary accordingly. Such differences in packaged may include differences in which GNSS systems are tracked, the number of carrier frequencies tracked, antennas provided as well as a range of different functions. The guiding prices are for the receivers alone, not including external antennas. The reader must, therefore, also bear in mind that a calibrated high-end antenna, such as a "choke-ring" antenna, may cost approximately 5.000 USD (Norgeodesi AS 2020).

Furthermore, prices provided by suppliers may also vary based on the volume of the purchase, as well as service and support deals that are included in the price. As such, it is often the case that it is the expertise of the supplier that the buyer, is in, part paying for.

3.3.2 Description of Setup and Logging

In order for the analyses results from each receiver to be as comparable to each other as possible, all four receivers were set up to track satellites for the same 24 hour period. They were placed on the same roof with little to no obstruction to their lines of sight. The receivers were set to sample at a rate of 1 Hz, except for the Emlid receiver. The Emlid receiver was set to 5 Hz, but this was reduced to 1 Hz in preprocessing. They were also set to track all GNSS systems and observables available to the receiver. The physical setup of the four receivers is captured in Figure 3.2.

(a)

(b)

(c)

Figure 3.2: Receiver setup for the four receivers used in data collection: (a) Topcon receiver to the left. Trimble antenna to the right. (b) Emlid receiver. (c) Septentrio receiver antenna

3.3.3 Preprocessing

Before the observation data collected could be processed using **GNSS_Receiver_QC_2020**, some preprocessing was necessary. First of this preprocessing was the conversion from the receiver-dependant observation file formats to the RINEX 3 format. As each receiver produced an observation file in its own format, four different conversion software were needed. The different conversion software used were:

- Topcon: TPS2RIN
- Septentrio: sbf2rin
- Trimble: cnvtToRINEX
- Emlid: CONVBIN Emlid

After converted the observation files to the RINEX format, some of the receivers produced multiple RINEX files, splitting them at the start of the new day. These were spliced together and then trimmed so all would contain the same 24 hour period. The Emlid observation file was also altered so as to have a sample rate of 1 Hz, not 5 Hz. By this process, four RINEX 3 observation files, with the same observation period and sample rate, were created. The process of splicing, trimming, and otherwise altering the RINEX 3 observation file was executed in the software GFZRNX. This software is a free software developed by the German Research Centre for Geosciences.

Chapter 4: Results

After the preprocessing detailed in section 3.3.3, a full analyses using the software **GNSS_Receiver_QC_2020** was executed. All four 24 hour observation files were processed. All GNSS systems were included, as well as all available observation signals. Furthermore, the default critical limits were used to detect cycle slips. As stated in section 3.1.4, the default limits are 4 m/min and 400 m/min for the ionospheric delay and phase-code combination, respectively. Thus, both output files and plotted figures were produced. Given the amount of information produced in each analysis, only certain aspects of the results will be presented in this chapter. The remaining results will be relegated to Appendix A.

4.1 Topcon Hiper VR

The following results were produced from the analysis of the Topcon observation data. These include sections from the output file, as well as plotted results.

4.1.1 Header

The following is the header of the output file from the Topcon analysis.

```
GNSS Receiver Quality Check 2020
Software version: 1.00
Last software version release: 02/06/2020

Software developed by Bjørn-Eirik Roald
Norwegian University of Life Sciences(NMBU)

RINEX observation filename:      FLO300XXX_R_20200901200_01D_01S_MO.rnx
RINEX version:                   3.04
RINEX converting program:        TPS2RIN 11.5
Marker name:                     FLO3
Receiver type:                   TPS HIPER_VR
Date of observation start:       2020/3/30 12:20:0.00
Date of observation end:         2020/3/31 12:19:59.00
Observation interval [seconds]:  1
Number of receiver clock jumps:  62
Average clock jumps interval:    00:23:14 (std: 42.97 seconds)

Critical cycle slip limits [m/s]:
- Ionospheric delay:             0.067
- Phase-code combination:        6.667

GNSS systems presents in RINEX observation file:
- BeiDou
- Galileo
- GPS
- GLONASS


NOTE: As there were no "Loss-of-Lock" indicators in RINEX observation file,
no information concerining "Loss-of-Lock" indicators is included in output file

User-specified contend included in output file
- Include overview of observations for each satellite:          Yes
- Include compact summary of analysis estimates:               Yes
- Include detailed summary of analysis
   estimates, including for each individual satellite:         Yes
- Include information about "Loss-of-Lock"
   indicators in detailed summary:                             No
```

Figure 4.1: Topcon analysis output file: Header

4.1.2 Completeness Overview

The following tables are from the observation completeness section of the output file from the Topcon analysis.

GPS Observation overview

PRN	L1 Observations	L2 Observations	L5 Observations
G1	C1C,C1W	C2W,C2X	C5X
G2	C1C,C1W	C2W	
G3	C1C,C1W	C2W,C2X	C5X
G4	C1C,C1W	C2W,C2X	C5X
G5	C1C,C1W	C2W,C2X	
G6	C1C,C1W	C2W,C2X	C5X
G7	C1C,C1W	C2W,C2X	
G8	C1C,C1W	C2W,C2X	C5X
G9	C1C,C1W	C2W,C2X	C5X
G10	C1C,C1W	C2W,C2X	C5X
G11	C1C,C1W	C2W	
G12	C1C,C1W	C2W,C2X	
G13	C1C,C1W	C2W	
G14	C1C,C1W	C2W	
G15	C1C,C1W	C2W,C2X	
G16	C1C,C1W	C2W	
G17	C1C,C1W	C2W,C2X	
G19	C1C,C1W	C2W	
G20	C1C,C1W	C2W	
G21	C1C,C1W	C2W	
G22	C1C,C1W	C2W	
G24	C1C,C1W	C2W,C2X	C5X
G25	C1C,C1W	C2W,C2X	C5X
G26	C1C,C1W	C2W,C2X	C5X
G27	C1C,C1W	C2W,C2X	C5X
G28	C1C,C1W	C2W	
G29	C1C,C1W	C2W,C2X	
G30	C1C,C1W	C2W,C2X	C5X
G31	C1C,C1W	C2W,C2X	
G32	C1C,C1W	C2W,C2X	C5X

Figure 4.2: Topcon analysis output file: GPS observation overview

Galileo Observation overview

PRN	E1 Observations	E5a Observations	E6 Observations	E5b Observations	G5(a+b) Observations
E1	C1X	C5X		C7X	C8X
E2	C1X	C5X		C7X	C8X
E3	C1X	C5X		C7X	C8X
E4	C1X	C5X		C7X	C8X
E5	C1X	C5X		C7X	C8X
E7	C1X	C5X		C7X	C8X
E8	C1X	C5X		C7X	C8X
E9	C1X	C5X		C7X	C8X
E11	C1X	C5X		C7X	C8X
E12	C1X	C5X		C7X	C8X
E13	C1X	C5X		C7X	C8X
E14	C1X	C5X		C7X	C8X
E15	C1X	C5X		C7X	C8X
E18	C1X	C5X		C7X	C8X
E20	C1X	C5X			
E21	C1X	C5X		C7X	C8X
E24	C1X	C5X		C7X	C8X
E25	C1X	C5X		C7X	C8X
E26	C1X	C5X		C7X	C8X
E27	C1X	C5X		C7X	C8X
E30	C1X	C5X		C7X	C8X

Figure 4.3: Topcon analysis output file: Galileo observation overview

GLONASS Observation overview

Sat ID	Frequency Channel	G1 Observations	G2 Observations	G3 Observations	G1a Observations	G2a Observations
R1	1	C1C,C1P	C2C,C2P			
R2	-4	C1C,C1P	C2C,C2P			
R3	5	C1C,C1P	C2C,C2P			
R4	6	C1C,C1P	C2C,C2P			
R5	1	C1C,C1P	C2C,C2P			
R6	-4	C1C,C1P	C2P			
R7	5	C1C,C1P	C2C,C2P			
R8	6	C1C,C1P	C2C,C2P			
R9	-2	C1C,C1P	C2C,C2P			
R10	-7	C1C,C1P	C2P			
R11	0	C1C,C1P	C2C,C2P			
R12	-1	C1C,C1P	C2C,C2P			
R13	-2	C1C,C1P	C2C,C2P			
R14	-7	C1C,C1P	C2C,C2P			
R15	0	C1C,C1P	C2C,C2P			
R16	-1	C1C,C1P	C2C,C2P			
R17	4	C1C,C1P	C2C,C2P			
R18	-3	C1C,C1P	C2C,C2P			
R19	3	C1C,C1P	C2C,C2P			
R20	2	C1C,C1P	C2C,C2P			
R21	4	C1C,C1P	C2C,C2P			
R22	-3	C1C,C1P	C2C,C2P			
R23	3	C1C,C1P	C2C,C2P			
R24	2	C1C,C1P	C2C,C2P			

Figure 4.4: Topcon analysis output file: GLONASS observation overview

BeiDou Observation overview

PRN	B1 Observations	E1-2 Observations	B2a Observations	B3 Observations	B2b Observations	B2(a+b) Observations
C5		C2X			C7X	
C6		C2X			C7X	
C7		C2X			C7X	
C8		C2X			C7X	
C9		C2X			C7X	
C10		C2X			C7X	
C11		C2X			C7X	
C12		C2X			C7X	
C13		C2X			C7X	
C14		C2X			C7X	
C16		C2X			C7X	
C19		C2X			C7X	
C20		C2X			C7X	
C21		C2X			C7X	
C22		C2X			C7X	
C23		C2X			C7X	
C25		C2X			C7X	
C27		C2X				
C28		C2X			C7X	
C29		C2X			C7X	
C30		C2X			C7X	
C32		C2X				
C33		C2X				
C34		C2X				
C35		C2X				
C36		C2X				
C37		C2X				

Figure 4.5: Topcon analysis output file: BeiDou observation overview

4.1.3 Compressed Results Overview

The following tables are from the compressed results overview section of the output file from the Topcon analysis.

GPS ANALYSIS SUMMARY

	C1C	C1W	C2W	C2X	C5X
RMS multipath[meters]	0.320	0.482	0.448	0.452	0.369
Weighted RMS multipath[meters]	0.181	0.246	0.213	0.266	0.201
N ambiguity slips periods	32	366	405	151	101
N slip periods, elevation angle > 10 degrees	1	73	77	25	20
N slip periods, elevation angle < 10 degrees	31	293	328	126	81
N slip periods, elevation angle not computed	0	0	0	0	0
Ratio of N slip periods/N obs epochs [%]	0.002	0.018	0.020	0.011	0.011

Figure 4.6: Topcon analysis output file: GPS compressed results overview

GALILEO ANALYSIS SUMMARY

	C1X	C5X	C7X	C8X
RMS multipath[meters]	0.486	0.262	0.232	0.176
Weighted RMS multipath[meters]	0.312	0.180	0.168	0.115
N ambiguity slips periods	13	45	34	95
N slip periods, elevation angle > 10 degrees	6	14	14	52
N slip periods, elevation angle < 10 degrees	7	25	20	43
N slip periods, elevation angle not computed	0	6	0	0
Ratio of N slip periods/N obs epochs [%]	0.001	0.003	0.003	0.007

Figure 4.7: Topcon analysis output file: Galileo compressed results overview

GLONASS ANALYSIS SUMMARY

	C1C	C1P	C2C	C2P
RMS multipath[meters]	0.743	0.441	1.108	0.335
Weighted RMS multipath[meters]	0.416	0.294	0.524	0.223
N ambiguity slips periods	75	219	230	254
N slip periods, elevation angle > 10 degrees	32	80	83	88
N slip periods, elevation angle < 10 degrees	24	78	105	101
N slip periods, elevation angle not computed	19	61	42	65
Ratio of N slip periods/N obs epochs [%]	0.004	0.013	0.014	0.015

Figure 4.8: Topcon analysis output file: GLONASS compressed results overview

BEIDOU ANALYSIS SUMMARY

	C2X	C7X
RMS multipath[meters]	0.501	0.494
Weighted RMS multipath[meters]	0.312	0.323
N ambiguity slips periods	14	83
N slip periods, elevation angle > 10 degrees	0	56
N slip periods, elevation angle < 10 degrees	14	27
N slip periods, elevation angle not computed	0	0
Ratio of N slip periods/N obs epochs [%]	0.001	0.009

Figure 4.9: Topcon analysis output file: BeiDou compressed results overview

4.1.4 Detailed Results Overview

The following are some of the tables included in the detailed results overview section of the output file from the Topcon analysis. Only the GPS results are presented in this section. The tables presented have also been cropped to increase readability. All the results from this section of the output file can be seen in Appendix A.1.4.

PRN	n C1C Observations	n Epochs with Multipath Estimates	RMS Multipath [meters]	Weighted RMS Multipath [meters]	Average Sat. Elevation Angle [degrees]	n Slip Periods	Slip/Obs Ratio [%]
G1	54689	29228	0.314	0.184	38.383	3	0.005
G2	86400	34513	0.283	0.199	29.646	0	0.000
G3	86400	30381	0.296	0.152	39.074	0	0.000
G4	54289	30593	0.413	0.157	37.626	1	0.002
G5	64815	32303	0.310	0.192	30.661	1	0.002
G6	86400	33189	0.302	0.207	30.648	1	0.001
G7	53755	31764	0.293	0.157	35.672	0	0.000
G8	54763	31260	0.360	0.213	33.957	0	0.000
G9	56180	29989	0.285	0.153	39.003	0	0.000
G10	65200	32588	0.507	0.185	33.386	1	0.002
G11	54474	27505	0.309	0.174	36.406	2	0.004
G12	86400	30794	0.251	0.128	38.843	0	0.000
G13	61072	29355	0.325	0.161	37.390	2	0.003
G14	86400	32857	0.281	0.201	31.452	0	0.000
G15	63730	31151	0.325	0.195	31.717	4	0.006
G16	54132	31738	0.443	0.239	32.290	1	0.002
G17	53310	33834	0.268	0.189	30.650	0	0.000
G19	86400	33132	0.274	0.192	30.853	0	0.000
G20	65086	31292	0.300	0.192	32.114	2	0.003
G21	63485	31734	0.318	0.185	36.713	1	0.002
G22	86400	29517	0.248	0.126	39.533	1	0.001
G24	86400	29210	0.305	0.162	37.552	3	0.003
G25	86400	29808	0.277	0.153	39.296	0	0.000
G26	54377	31466	0.364	0.206	32.439	0	0.000
G27	55273	29316	0.328	0.190	37.576	0	0.000
G28	53576	31996	0.309	0.196	34.147	0	0.000
G29	86400	31306	0.291	0.141	38.153	0	0.000
G30	54353	30546	0.316	0.152	37.471	3	0.006
G31	86400	33121	0.279	0.182	29.822	0	0.000
G32	86400	34213	0.283	0.196	29.583	6	0.007

Figure 4.10: Topcon analysis output file: GPS C1C signal, detailed results overview. Table has been cropped. For full table, see Figure A.1.10

PRN	n C1W Observations	n Epochs with Multipath Estimates	RMS Multipath [meters]	Weighted RMS Multipath [meters]	Average Sat. Elevation Angle [degrees]	n Slip Periods	Slip/Obs Ratio [%]
G1	54686	29204	0.415	0.209	38.419	12	0.022
G2	86400	34513	0.457	0.291	29.732	15	0.017
G3	86400	30381	0.458	0.202	39.110	11	0.013
G4	54281	30592	0.468	0.218	37.645	3	0.006
G5	64813	32302	0.397	0.243	30.667	2	0.003
G6	86400	33189	0.417	0.280	30.665	6	0.007
G7	53747	31762	0.432	0.204	35.796	18	0.033
G8	54760	31260	0.509	0.295	33.978	7	0.013
G9	56173	29987	0.518	0.196	39.039	4	0.007
G10	65191	32586	0.638	0.258	33.415	7	0.011
G11	54453	27502	0.572	0.230	36.648	27	0.050
G12	86400	30781	0.430	0.184	38.949	15	0.017
G13	60982	29350	0.683	0.241	37.558	27	0.044
G14	86400	32845	0.468	0.303	31.475	4	0.005
G15	63631	31151	0.414	0.250	31.763	8	0.013
G16	54095	31735	0.542	0.307	32.340	9	0.017
G17	53304	33834	0.372	0.233	30.662	5	0.009
G19	86400	33132	0.423	0.275	30.915	13	0.015
G20	65078	31288	0.539	0.292	32.271	28	0.043
G21	63464	31729	0.519	0.239	36.853	15	0.024
G22	86400	29511	0.494	0.183	39.786	28	0.032
G24	86400	29209	0.441	0.185	37.611	14	0.016
G25	86400	29804	0.443	0.209	39.371	14	0.016
G26	54363	31459	0.492	0.264	32.511	13	0.024
G27	55259	29317	0.446	0.227	37.638	11	0.020
G28	53566	31995	0.578	0.299	34.263	17	0.032
G29	86400	31306	0.463	0.182	38.170	4	0.005
G30	54347	30546	0.502	0.208	37.491	7	0.013
G31	86400	33121	0.393	0.248	29.833	3	0.003
G32	86400	34213	0.432	0.285	29.643	19	0.022

Figure 4.11: Topcon analysis output file: GPS C1W signal, detailed results overview. Table has been cropped. For full table, see Figure A.1.11

PRN	n C2X Observations	n Epochs with Multipath Estimates	RMS Multipath [meters]	Weighted RMS Multipath [meters]	Average Sat. Elevation Angle [degrees]	n Slip Periods	Slip/Obs Ratio [%]
G1	54685	29153	0.406	0.223	38.525	6	0.011
G3	86400	30370	0.420	0.220	39.123	10	0.012
G4	54279	30589	0.406	0.239	37.650	3	0.006
G5	64809	32223	0.461	0.289	30.721	4	0.006
G6	86400	33159	0.441	0.307	30.687	9	0.010
G7	53753	31826	0.467	0.242	35.741	8	0.015
G8	54756	31198	0.490	0.278	34.037	10	0.018
G9	56173	29982	0.519	0.321	39.045	4	0.007
G10	65050	32496	0.587	0.284	33.495	3	0.005
G12	86400	30911	0.394	0.208	38.874	9	0.010
G15	63577	31085	0.516	0.284	31.815	7	0.011
G17	53303	33833	0.408	0.300	30.664	3	0.006
G24	86400	29131	0.396	0.216	37.702	14	0.016
G25	86400	29835	0.450	0.248	39.345	11	0.013
G26	54370	31434	0.506	0.278	32.547	11	0.020
G27	55265	29276	0.431	0.241	37.680	10	0.018
G29	86400	31294	0.413	0.239	38.180	6	0.007
G30	54343	30546	0.406	0.237	37.489	5	0.009
G31	86400	33034	0.447	0.299	29.894	4	0.005
G32	86400	34219	0.407	0.302	29.642	14	0.016

Figure 4.12: Topcon analysis output file: GPS C2X signal, detailed results overview. Table has been cropped. For full table, see Figure A.1.13

PRN	n C2W Observations	n Epochs with Multipath Estimates	RMS Multipath [meters]	Weighted RMS Multipath [meters]	Average Sat. Elevation Angle [degrees]	n Slip Periods	Slip/Obs Ratio [%]
G1	54686	29206	0.362	0.168	38.418	12	0.022
G2	86400	34511	0.416	0.232	29.736	14	0.016
G3	86400	30381	0.404	0.164	39.111	10	0.012
G4	54280	30593	0.455	0.212	37.646	3	0.006
G5	64813	32300	0.360	0.208	30.667	4	0.006
G6	86400	33189	0.392	0.242	30.665	6	0.007
G7	53747	31762	0.413	0.181	35.791	22	0.041
G8	54759	31260	0.422	0.220	33.979	7	0.013
G9	56173	29988	0.418	0.165	39.039	4	0.007
G10	65191	32588	0.613	0.213	33.415	9	0.014
G11	54457	27490	0.591	0.209	36.656	34	0.062
G12	86400	30779	0.380	0.142	38.951	17	0.020
G13	60973	29349	0.609	0.233	37.556	28	0.046
G14	86400	32848	0.491	0.292	31.476	4	0.005
G15	63678	31150	0.402	0.215	31.762	12	0.019
G16	54097	31737	0.546	0.261	32.340	10	0.018
G17	53304	33834	0.327	0.214	30.663	3	0.006
G19	86400	33132	0.410	0.224	30.916	15	0.017
G20	65074	31290	0.509	0.258	32.275	28	0.043
G21	63477	31729	0.523	0.226	36.843	23	0.036
G22	86400	29507	0.465	0.177	39.787	32	0.037
G24	86400	29202	0.380	0.160	37.611	18	0.021
G25	86400	29807	0.423	0.178	39.370	13	0.015
G26	54363	31463	0.452	0.224	32.513	14	0.026
G27	55260	29314	0.372	0.177	37.639	10	0.018
G28	53566	31993	0.554	0.269	34.269	18	0.034
G29	86400	31306	0.385	0.168	38.170	8	0.009
G30	54347	30546	0.434	0.183	37.491	7	0.013
G31	86400	33121	0.388	0.218	29.833	3	0.003
G32	86400	34213	0.363	0.226	29.645	17	0.020

Figure 4.13: Topcon analysis output file: GPS C2W signal, detailed results overview. Table has been cropped. For full table, see Figure A.1.12

PRN	n C5X Observations	n Epochs with Multipath Estimates	RMS Multipath [meters]	Weighted RMS Multipath [meters]	Average Sat. Elevation Angle [degrees]	n Slip Periods	Slip/Obs Ratio [%]
G1	54687	29255	0.576	0.172	38.423	10	0.018
G3	86400	30381	0.286	0.176	39.110	10	0.012
G4	54281	30599	0.291	0.167	37.641	2	0.004
G6	86400	33189	0.343	0.229	30.664	6	0.007
G8	54760	31261	0.376	0.247	33.978	7	0.013
G9	56174	29994	0.305	0.212	39.033	4	0.007
G10	65195	32611	0.529	0.181	33.401	3	0.005
G24	86400	29241	0.316	0.164	37.575	15	0.017
G25	86400	29846	0.319	0.171	39.334	11	0.013
G26	54374	31531	0.357	0.229	32.463	6	0.011
G27	55266	29340	0.351	0.218	37.613	12	0.022
G30	54347	30554	0.306	0.167	37.482	5	0.009
G32	86400	34288	0.311	0.237	29.590	10	0.012

Figure 4.14: Topcon analysis output file: GPS C5X signal, detailed results overview. Table has been cropped. For full table, see Figure A.1.14

4.1.5 Plotted Results

The following are some of the plotted results from the Topcon analysis. Only the graphs concerning the same observation signals presented in section 4.1.4 are included. All plotted results from the Topcon analysis can be seen in Appendix A.1.5.

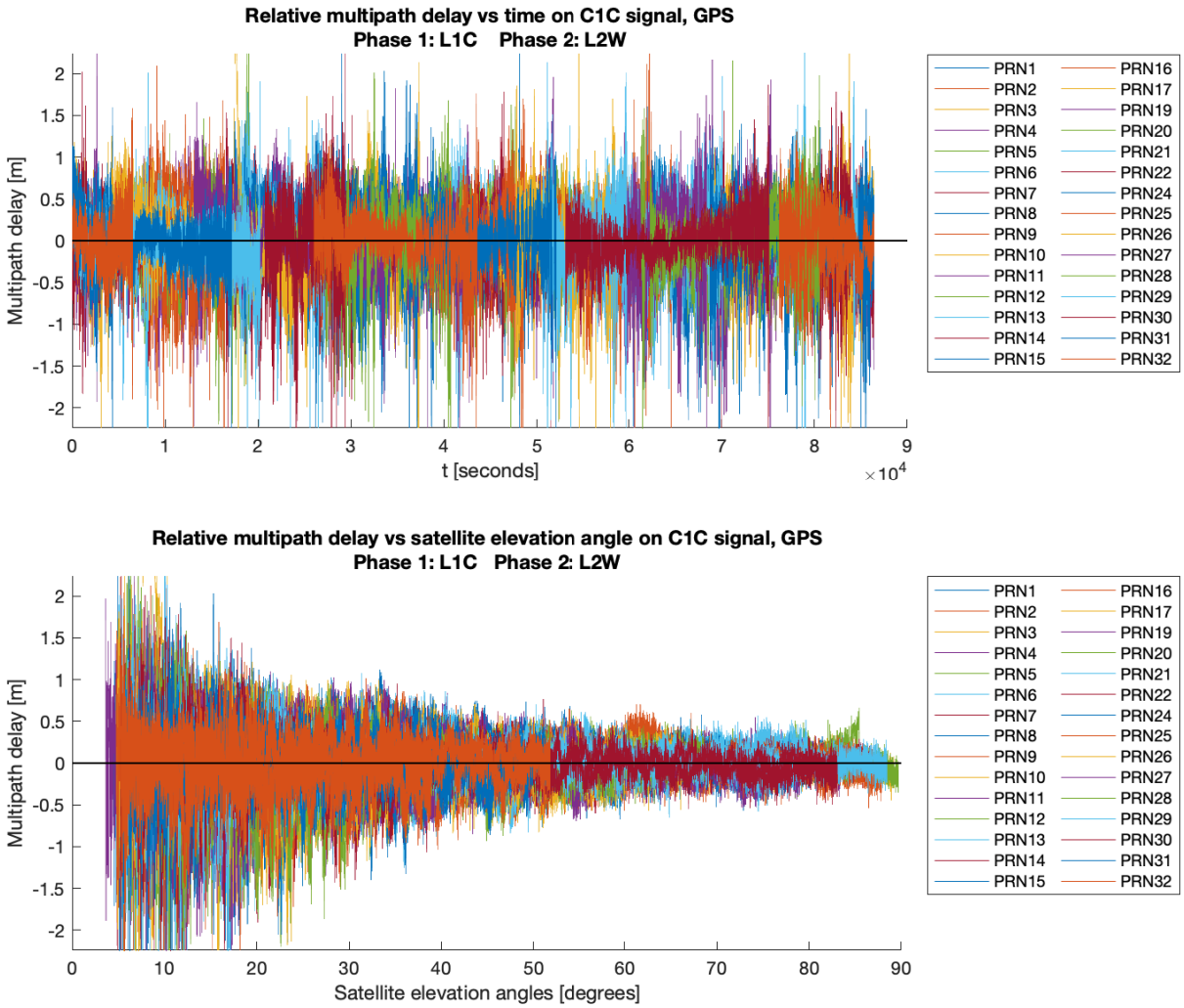

Figure 4.15: Topcon analysis results graph: GPS C1C signal, multipath effect vs. time and vs. satellite elevation angle. Graph has been cropped along y axis.

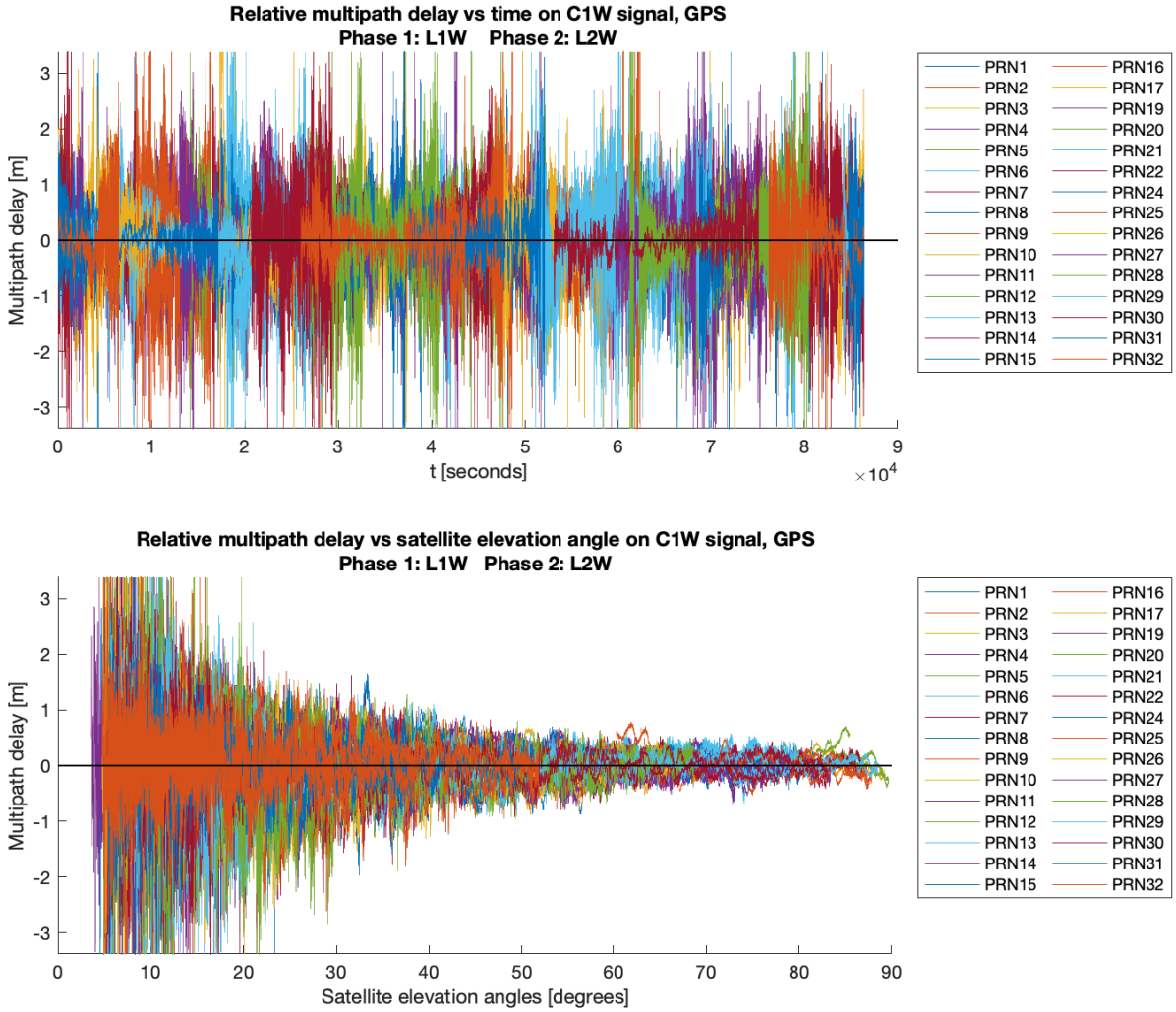

Figure 4.16: Topcon analysis results graph: GPS C1W signal, multipath effect vs. time and vs. satellite elevation angle. Graph has been cropped along y axis.

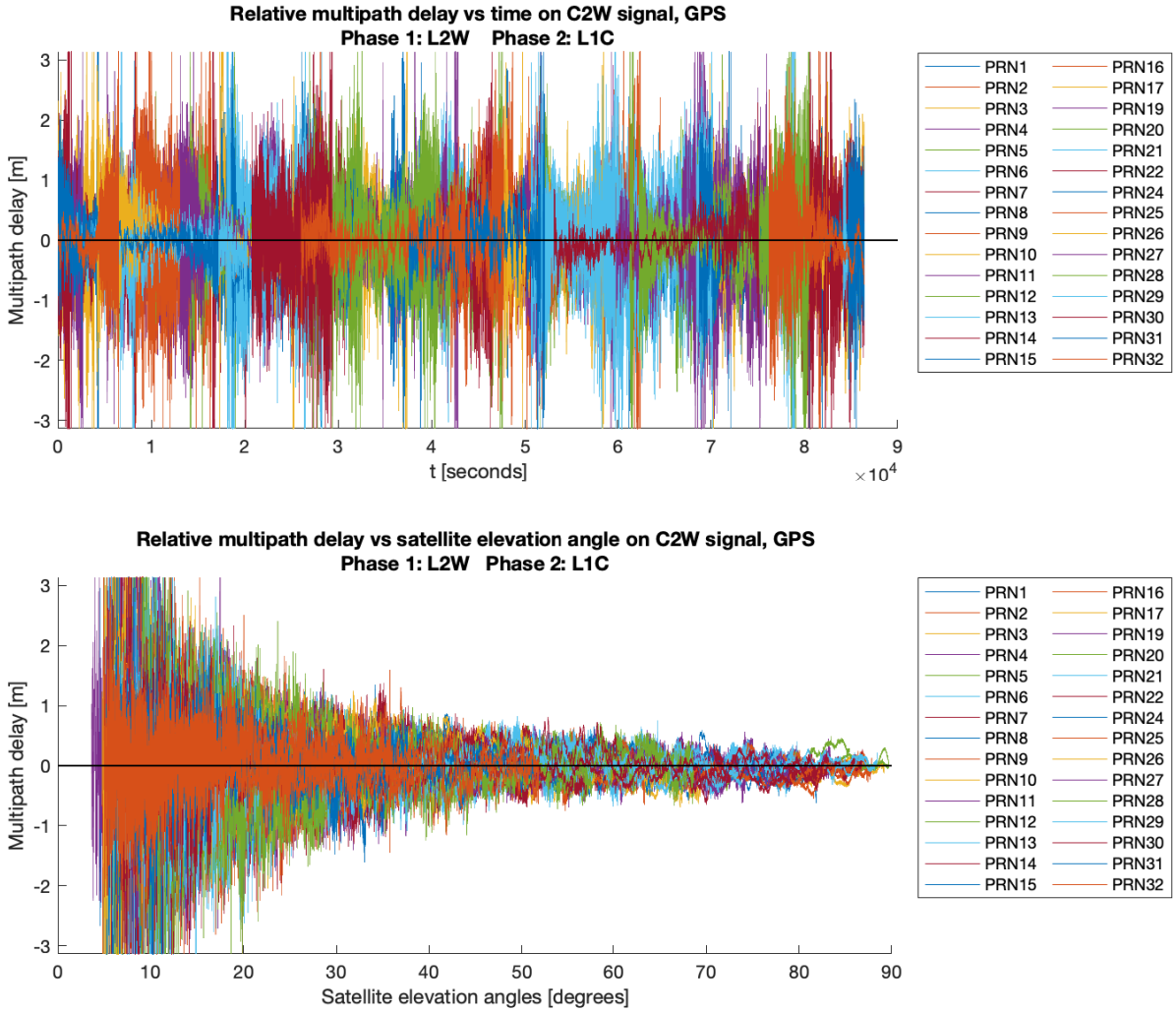

Figure 4.17: Topcon analysis results graph: GPS C2W signal, multipath effect vs. time and vs. satellite elevation angle. Graph has been cropped along y axis.

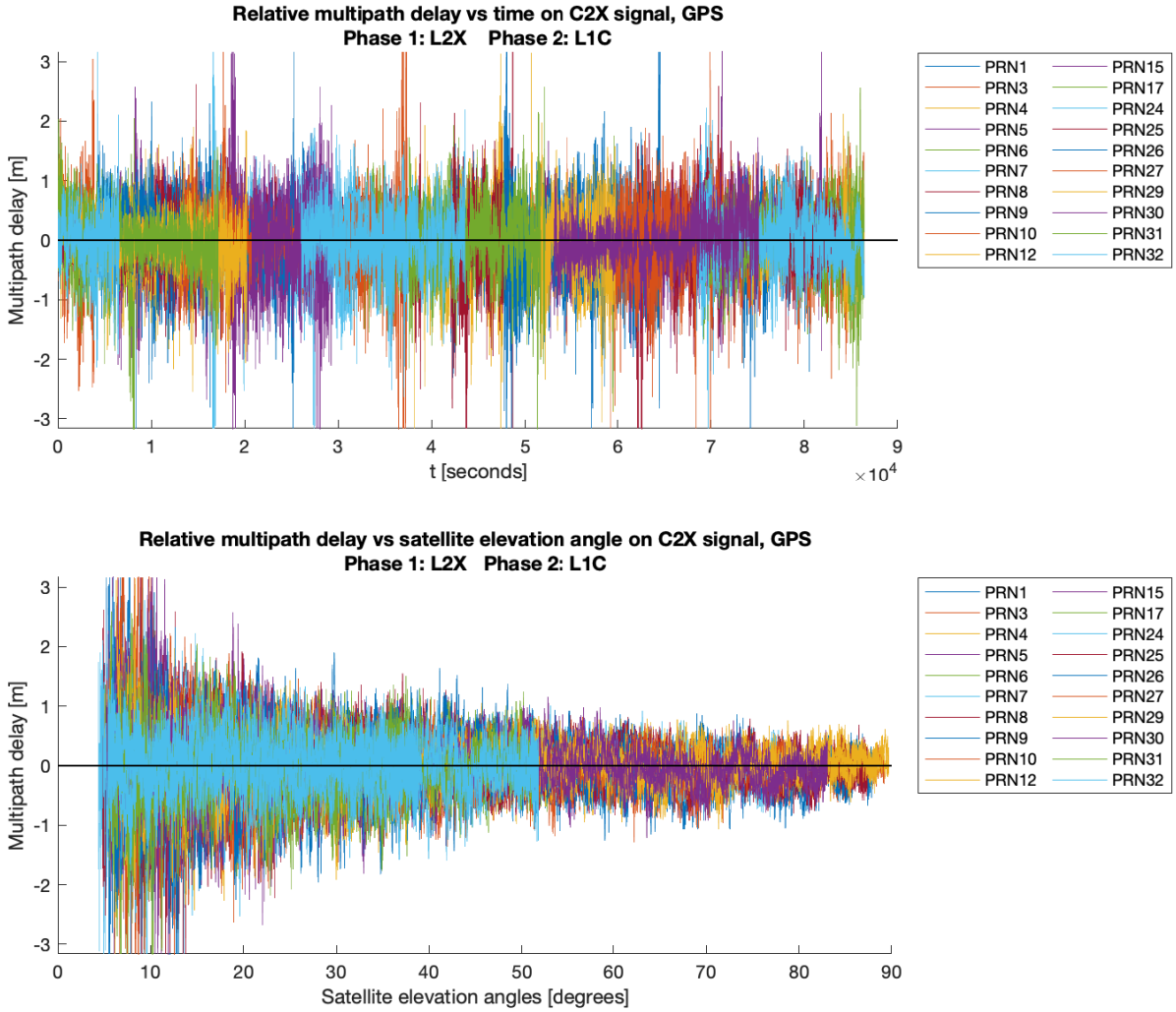

Figure 4.18: Topcon analysis results graph: GPS C2X signal, multipath effect vs. time and vs. satellite elevation angle. Graph has been cropped along y axis.

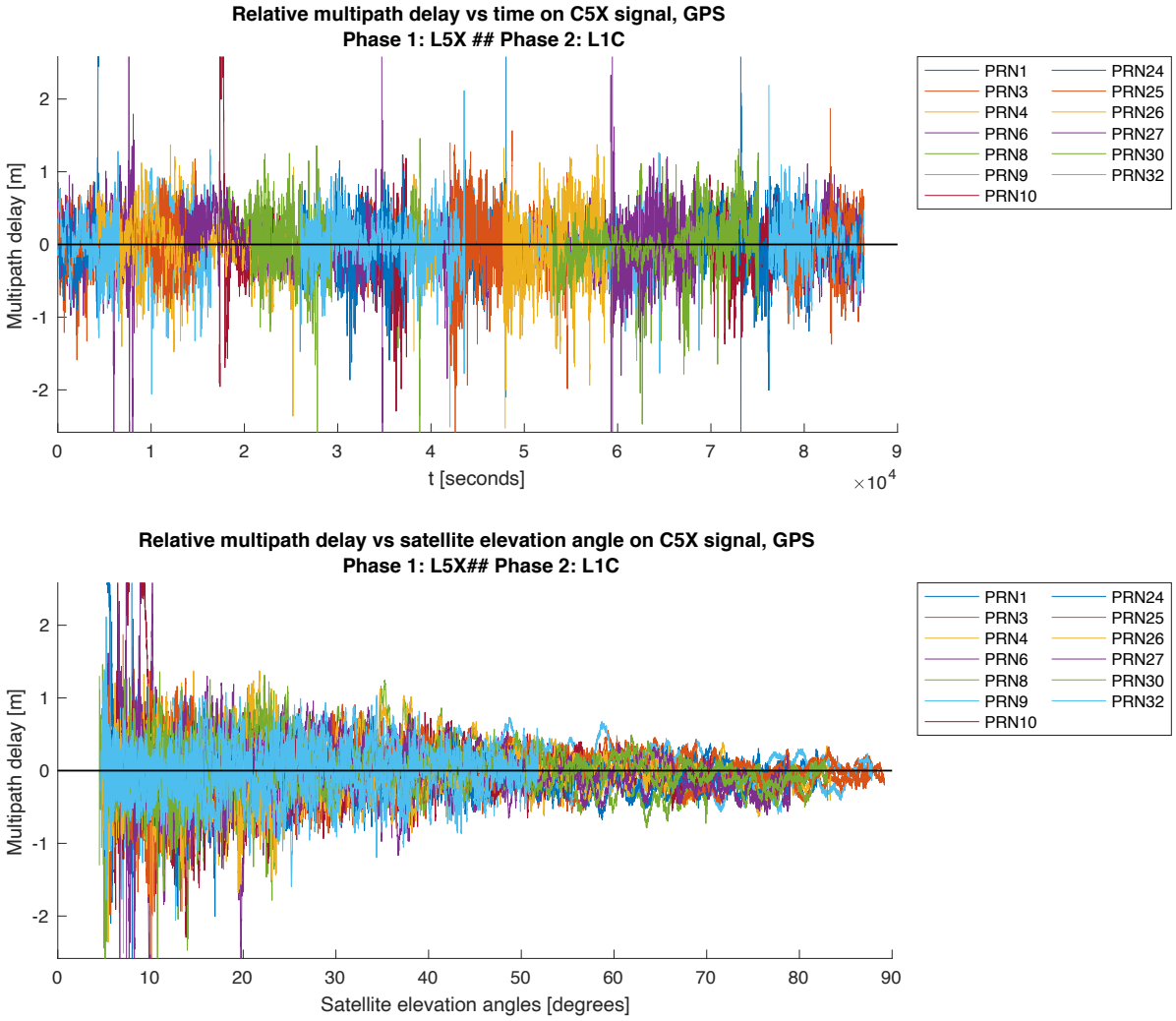

Figure 4.19: Topcon analysis results graph: GPS C5X signal, multipath effect vs. time and vs. satellite elevation angle. Graph has been cropped along y axis.

4.2 Emlid Reach RS2

The following section is dedicated to presenting the results produced from the analysis of the Emlid observation data. These include sections of the output file and plotted results. However, in order to maintain some compactness, some of the results have been relegated to Appendix A.2.

4.2.1 Header

The following is the header of the output file from the Emlid analysis.

```
GNSS Receiver Quality Check 2020
Software version: 1.00
Last software version release: 02/06/2020

Software developed by Bjørn-Eirik Roald
Norwegian University of Life Sciences(NMBU)

RINEX observation filename:      FLO300XXX_R_20200901220_01D_01S_MO.rnx
RINEX version:                   3.04
RINEX converting program:        CONVBIN 2.4.3 Emlid
Marker name:                     FLO3
Receiver type:                   Emlid Reach RS2
Date of observation start:       2020/3/30 12:20:7.99
Date of observation end:         2020/3/31 12:19:59.99
Observation interval [seconds]:  1
Number of receiver clock jumps:  28
Average clock jumps interval:    00:50:57 (std: 1210.85 seconds)

Critical cycle slip limits [m/s]:
- Ionospheric delay:             0.067
- Phase-code combination:        6.667

GNSS systems presents in RINEX observation file:
- BeiDou
- Galileo
- GPS
- GLONASS


User-specified contend included in output file
- Include overview of observations for each satellite:          Yes
- Include compact summary of analysis estimates:                Yes
- Include detailed summary of analysis
   estimates, including for each individual satellite:          Yes
- Include information about "Loss-of-Lock"
   indicators in detailed summary:                              No
```

Figure 4.20: Emlid analysis output file: Header

4.2.2 Completeness Overview

To see the observation completeness overview of the output file produced from the Emlid analysis, see Appendix A.2.2.

4.2.3 Compressed Results Overview

The following tables are from the compressed results overview section of the output file from the Emlid analysis.

GPS ANALYSIS SUMMARY

	C1C	C2X
RMS multipath[meters]	0.464	0.578
Weighted RMS multipath[meters]	0.398	0.499
N ambiguity slips periods	7437	14742
N slip periods, elevation angle > 10 degrees	4954	13441
N slip periods, elevation angle < 10 degrees	2483	1301
N slip periods, elevation angle not computed	0	0
Ratio of N slip periods/N obs epochs [%]	0.333	1.002

Figure 4.21: Emlid analysis output file: GPS compressed results overview

GALILEO ANALYSIS SUMMARY

	C1X	C7X
RMS multipath[meters]	0.735	0.448
Weighted RMS multipath[meters]	0.572	0.386
N ambiguity slips periods	4963	6204
N slip periods, elevation angle > 10 degrees	3401	5142
N slip periods, elevation angle < 10 degrees	1216	1062
N slip periods, elevation angle not computed	346	0
Ratio of N slip periods/N obs epochs [%]	0.313	0.408

Figure 4.22: Emlid analysis output file: Galileo compressed results overview

GLONASS ANALYSIS SUMMARY

	C1C	C2C
RMS multipath[meters]	0.527	0.796
Weighted RMS multipath[meters]	0.455	0.654
N ambiguity slips periods	2740	12615
N slip periods, elevation angle > 10 degrees	1451	8654
N slip periods, elevation angle < 10 degrees	654	650
N slip periods, elevation angle not computed	635	3311
Ratio of N slip periods/N obs epochs [%]	0.158	0.803

Figure 4.23: Emlid analysis output file: GLONASS compressed results overview

BEIDOU ANALYSIS SUMMARY

	C2I	C7I
RMS multipath[meters]	0.531	0.347
Weighted RMS multipath[meters]	0.446	0.290
N ambiguity slips periods	3142	2544
N slip periods, elevation angle > 10 degrees	2213	1744
N slip periods, elevation angle < 10 degrees	929	800
N slip periods, elevation angle not computed	0	0
Ratio of N slip periods/N obs epochs [%]	0.214	0.461

Figure 4.24: Emlid analysis output file: BeiDou compressed results overview

4.2.4 Detailed Results Overview

To see the observation detailed results overview of the output file produced from the Emlid analysis, see Appendix A.2.4.

4.2.5 Plotted Results

To see the plotted result graphs produced from the Emlid analysis, see Appendix A.2.5.

4.3 Septentrio PolaRxS Pro

The following section is dedicated to presenting the results produced from the analysis of the Septentrio observation data. These include sections of the output file and plotted results. However, in order to maintain some compactness, the actual results have been relegated to Appendix A.3. The following will instead be references to sections of Appendix A.3.

4.3.1 Header

To see the header of the output file produced from the Septentrio analysis, see Appendix A.3.1.

4.3.2 Completeness Overview

To see the observation completeness overview of the output file produced from the Septentrio analysis, see Appendix A.3.2.

4.3.3 Compressed Results Overview

To see the observation compressed results overview of the output file produced from the Septentrio analysis, see Appendix A.3.3.

4.3.4 Detailed Results Overview

To see the observation detailed results overview of the output file produced from the Septentrio analysis, see Appendix A.3.4.

4.3.5 Plotted Results

To see the plotted result graphs produced from the Septentrio analysis, see Appendix A.3.5.

4.4 Trimble NETR5

The following section is dedicated to presenting the results produced from the analysis of the Trimble observation data. These include sections of the output file and plotted results. However, in order to maintain some compactness, the actual results have been relegated to Appendix A.4. The following will instead be references to sections of Appendix A.4.

4.4.1 Header

To see the header of the output file produced from the Trimble analysis, see Appendix A.4.1.

4.4.2 Completeness Overview

To see the observation completeness overview of the output file produced from the Trimble analysis, see Appendix A.4.2.

4.4.3 Compressed Results Overview

To see the observation compressed results overview of the output file produced from the Trimble analysis, see Appendix A.4.3.

4.4.4 Detailed Results Overview

To see the observation detailed results overview of the output file produced from the Trimble analysis, see Appendix A.4.4.

4.4.5 Plotted Results

To see the plotted result graphs produced from the Trimble analysis, see Appendix A.4.5.

4.5 Results Comparison: Topcon vs. Emlid

The following table is a comparison of results from the Topcon analysis and the Emlid analysis. Note that only the results concerning the observation signals the receivers have in common are included. Hence, BeiDou is not included at all.

Parameter	**GNSS system**	**Obs. signal**	**Topcon Hiper VR**	**Emlid Reach RS2**
Receiver clock jump			62	28
Average clock jump interval [hh:mm:ss] (standard dev. [s])			00:23:14 (42.97 s)	00:50:57 (1210.85 s)
Multipath RMS [m]	GPS	C1C	0.320	0.464
		C2X	0.452	0.578
	Galileo	C1X	0.486	0.735
		C7X	0.232	0.448
	GLONASS	C1C	0.743	0.527
		C2C	1.108	0.796
Weighted multipath RMS [m]	GPS	C1C	0.181	0.398
		C2X	0.266	0.499
	Galileo	C1X	0.312	0.572
		C7X	0.168	0.386
	GLONASS	C1C	0.416	0.455
		C2C	0.524	0.654
N slip periods	GPS	C1C	32	7437
		C2X	151	14742
	Galileo	C1X	13	4963
		C7X	34	6204
	GLONASS	C1C	75	2740
		C2C	230	12615
N slip periods elevation angle $> 10^{\circ}$	GPS	C1C	1	4954
		C2X	25	13441
	Galileo	C1X	6	3401
		C7X	14	5142
	GLONASS	C1C	32	1451
		C2C	83	8654
N slip periods elevation angle $< 10^{\circ}$	GPS	C1C	31	2483
		C2X	126	1301
	Galileo	C1X	7	1216
		C7X	20	1062
	GLONASS	C1C	24	654
		C2C	105	650
Ratio N slip periods/ obs. epochs [%]	GPS	C1C	0.002	0.333
		C2X	0.011	1.002
	Galileo	C1X	0.001	0.313
		C7X	0.003	0.408
	GLONASS	C1C	0.004	0.158
		C2C	0.014	0.803

Table 4.1: Analysis results comparison: Topcon Hiper VR vs. Emlid Reach RS2

Chapter 5: Discussion

5.1 Results Discussion

The purpose of this thesis has not been to evaluate the performance of one or more specific GNSS receivers. However, discussing the results of chapter 4 may yield answers concerning the capabilities of **GNSS_Receiver_QC_2020**. The following will, therefore, be a discussion of the strengths and weaknesses of the software, as seen from the results of chapter 4.

5.1.1 Results Comparison: Topcon Hiper VR vs. Emlid Reach RS2

Certain expectations exist concerning the performances of the receivers compared to one another. As a result, a comparison of the analysis results of two receivers may confirm such expectations. By doing so, the capabilities of **GNSS_Receiver_QC_2020** may be demonstrated.

The receiver Emlid Reach RS2 is in many ways comparable to the Topcon Hiper VR receiver. Both are compact receivers with a built-in antenna intended for use in the field. However, they differ greatly in price. A natural expectation would, therefore, be that the Topcon receiver would perform better than the Emlid receiver, when compared under equal conditions. The following comparison will, therefore, be between the analysis results of these two receivers. Many of the metrics discussed are summarized in Table 4.1.

Metric 1: Multipath Estimates

The first metric used to compare the two receivers will be the estimates of multipath RMS. For all observation signals, except two, the Topcon receiver produces lower RMS values. However, for the two GLONASS observations, the Emlid receiver produces lower RMS values. Though most of the RMS values indicate that the Topcon receiver performs better, there is no clear consensus. However, when comparing the RMS values that have been weighted based on satellite elevation angles, all values are in favour of the Topcon receiver. This observation is interesting for two reasons. Firstly it further confirms the better performance of the Topcon receiver. Secondly, it illustrates the value of using weighted estimates in order to achieve unbiased comparisons.

Metric 2: Cycle slips

The second metric to be compared will be the number of cycle slips. Concerning this metric, there is no doubt that the Topcon receiver outperforms the Emlid receiver. The amount of cycle slips for the Emlid receiver is two orders of magnitude higher than those of the Topcon receiver, for every observation signal. This is also true when comparing the ratio between the number of cycle slips and the number of observation epochs. It is not the intention of this thesis to speculate about the causes of different performances. However, it should be pointed out that it is probable that the difference between the two receivers' ability to maintain signal lock can be traced back to the differences in receiver antennas. However, as both of these receivers are sold as a combined receiver-antenna package, comparing them as a whole is not considered to be unjust.

The number of cycle slips at higher and lower elevation angles should also be discussed. This will be a measure of the receivers' ability to maintain continuous signal lock at higher elevation angles. It should be noted that the cutoff angle used in Table 4.1 is 10 degrees. There will, therefore, naturally be considerably more observation epochs with elevation angles greater than 10 degrees than lower. As a result, a direct comparison of the two groups may not be entirely suitable. However, it is expected that the majority of cycle slips occur at the lower elevation angles.

When first observing the amount of Topcon cycle slips below and above 10 degrees, a clear correlation is observed. For all observation signals, there are more cycle slips below 10 degrees than above. This is despite the unbalanced nature of the 10 degree divide that was noted previously. The opposite is true for the cycle slips of the Emlid receiver. When observing the more detailed Emlid result overviews in Appendix A.2.4, it is clear that a great deal of cycle slips with elevation angles above 10 degrees occur in the 10-20 degree range. However, there are still considerable amounts of cycle slips occurring with elevation angles greater than 30 degrees, or even greater than 50 degrees. This all seems to be indicating a lesser ability in the Emlid receiver to maintain signal lock at higher elevation angles, compared to the Topcon receiver.

Metric 3: Receiver Clock Jumps

The next metric to be compared will be the amount of receiver clock jumps that have occurred. This could be considered as a measure of the rate to which the receiver clocks tend to drift. In this aspect, the Emlid receiver outperforms the Topcon receiver for the first time, having fewer clock jumps and a longer average time interval between jumps. However, the standard deviation of the time between clock jumps should also be considered. It can be seen that while the Topcon receiver's intervals have a standard deviation of 42.97 seconds, the Emlid receiver shows a standard deviation of 1210.85 seconds. This seems to indicate that while the clock jumps of the Topcon receiver are consistently space, those of the Emlid receiver are sporadic. No definite conclusion is drawn concerning which receiver performs better in this aspect.

Metric 4: Plotted Multipath Graphs

The primary purpose of plotting multipath estimates vs. satellite elevation angles is to determine how much of the estimated multipath effect can be traced to lower elevation angles. In other words, how well does a receiver do at reducing multipath at higher elevation angles?

When observing the plotted multipath estimates from the Topcon analyses (see section 4.1.5), there is a clear correlation between increased elevation angles and lower estimates of multipath. This can be seen from the sideways cone shape of the graph. In other words, this means that above certain elevation angles, the Topcon receiver will perform better at limiting multipath. This alone does not mean that the Topcon receiver performs well in general with regards to multipath. It does, however, indicate that the higher estimates of multipath can be attributed in parts to lower elevation angles.

When observing the plotted multipath estimates from the Emlid analyses (see Appendix A.2.5), there is considerably less correlation visible. This is especially clear in Figures A.2.15 and A.2.16. It should be noted that these graphs have been cropped along the y-axis, making it difficult to see the most extreme values of some of these plots. Nevertheless, from a visual standpoint, it does seem that the graphs indicate that less of the multipath effect experienced by the Emlid receiver can be attributed to lower elevation angles. This is at least compared to the Topcon receiver.

Conclusion From Results Comparison

Based on the metrics compared in section 5.1.1, the natural conclusion to draw is that the performance of the Topcon receiver was superior to that of the Emlid receiver. A stated previously, the intention of this comparison has not been to rank these receivers. However, the comparison has shown that the results produced by the software can be used to evaluate the performance of a GNSS receiver. While the metrics above have illustrated some strengths of this software, weaknesses of the software should also be discussed.

5.1.2 Areas of Weakness

The following section details weaknesses in the software as it stands today. These weaknesses were derived from the results of chapter 4.

Lack of Overall Quality Evaluation

Both the results in the output file and the plotted results illustrate many characteristics of a GNSS receiver. However, reaching a definite conclusion concerning the "absolute quality" of a receiver requires a certain amount of proficiency and competence from the user. By this, it is meant that the values presented in the output file may have little meaning to

users that are not well versed in the field of GNSS. In this respect, the software fails at providing the user with a complete verdict of the receiver quality.

Evaluation of Signal Continuity

The detection of cycle slips may illustrate the tendency of a receiver to experience cycle slips. However, the user may be more interested in the receiver's ability to maintain continuous signal tracking. In this aspect, the software fails somewhat, as it fails to show the distribution of cycle slips over time. For example: A receiver could experience many short periods of signal loss over a short time. However, it may still have very long periods of continuous tracking before and after. By only presenting the number of cycle slips, this nuance is not shown.

Sensitivity of Cycle slip Detection

The method of detecting cycle slips through observing the change in the ionospheric delay is quite sensitive, given the low noise to signal ratio. However, as this method does not distinguish which signal experiences the slip, it could not be utilized to compute the number of cycle slips for each individual signal. Instead, the phase-code linear combination was used for this purpose. While this combination will distinguish which signal experiences a cycle slip, it does suffer from more noise than the previously mentioned ionosphere combination. The result is a less sensitive detection method. Exactly how detrimental this reduced sensitivity may be is not entirely clear from the results of this thesis.

Missing Navigation Data

Though information concerning the elevation angles of the satellites is available in the output file, there are satellites for which this is not the case. This is as a result of certain satellites not being included in the SP3 file. For these satellites, the user is not given information about the elevation angles of cycle slips. Furthermore, the weighted RMS estimates of multipath are not available for these satellites, given that they are weighted based on the elevation angles. Lastly, these satellites are excluded from plotted graphs that require elevation angles, such as the multipath vs. elevation angle graphs.

5.2 Aspects To Improve Upon

When examining the results of chapter 4, as well as the weaknesses discussed in section 5.1.2, certain aspects that could be improved upon have come to light. These may be aspects of the final product that are missing entirely, or which were undertaken in a less than ideal way. A presentation of such aspects therefore follows.

5.2.1 Use of Precise Orbital Data

The decision to use precise orbital data in order to determine satellite elevation angles ended up having some drawbacks. The most notable of these is the lack of orbital data for all satellites. The consequences of this were detailed in section 5.1.2.

The SP3 format, while being excellent in many aspects, can vary a great deal in content. An example of aspects that may vary are which GNSS systems and satellites are included, as well as the sample interval. The somewhat variable nature of SP3 files leaves more room for mistakes by the user of **GNSS_Receiver_QC_2020**. For example, a user may provide multiple SP3 files with different sample intervals. Another example is that the user might input two SP3 files that are not from consecutive days. Though the program was, in part, developed to at least warn the user of such errors, it is not rigorously tested in this fashion.

In general, using broadcasted orbital data would possibly have been a better choice. Doing so would solve the problem of missing satellites, as well as making the process somewhat easier for the user. It would require separate algorithms for determining GLONASS satellite positions, on account of the differences in broadcasted information. However, this would have been a minor inconvenience.

5.2.2 Choice of Critical Limits

The methods used for the detection of cycle slips required a choice of critical limits. This choice could have deserved more thought and experimentation. Though the default critical limit used for the detection of slips through changes in the ionospheric delay followed the suggestions of Estey & Meertens (1999, p. 46), no such suggestion existed for the phase-code combination. This limit was set, roughly, based on the indicated noise level of Hofmann-Wellenhof et al. (2008, p.197). However, the uncertainty of this limit meant that some experimentation with other limits should perhaps have been done.

5.2.3 Presentation of Plotted Results

The plotted results were saved separately and were not part of the output file. In the spirit of producing a single output file containing all of the results, these graphs could have been included in the output file itself. In order to accommodate images, this would have required a more complex output file format than a simple text file, such as a pdf file.

5.2.4 Use of MATLAB

A quick note should be made of the disadvantage of using MATLAB as the programming language of this software. Great effort was put into developing a computationally fast software. However, the result is still a software that will process a 24-hour observation file, containing most GNSS systems and observation types, in approximately 2 hours. If a

compile-language such as C++ had been utilized, the result would undoubtedly have been a computationally faster product.

5.2.5 Robustness

Though robustness was a focus during the development of this software, there are still unexpected occurrences which may cause the software to throw errors. This mainly includes errors in the RINEX observation file. Accidental changes to the observation file, or errors caused by the conversion software, may both cause the software to fail. Many such errors are dealt with by the software directly. Otherwise, they lead to the software informing the user about the cause of the problem. However, there is still much that can be done to improve the robustness of the software.

5.3 Future Development

As the project period of this thesis comes to an end, there remain many aspects where the software could be developed further. These aspects include improving functionalities that already exist, as well as expanding the software in new directions. A presentation of possible future development follows.

5.3.1 Utilization of Additional Linear Combinations

As the framework for computing linear combinations has already been put in place, a natural next step would be to expand the software to be able to compute other linear combinations. This could hence be used to aid in research concerning other linear combinations. This development would, in turn, lead to a more generalized software that could be used as a tool for other purposes than only receiver performance evaluation.

One linear combination that could also contribute to better detection of cycle slips would be the widelane linear combination (see section 2.3). Having more redundant methods for cycle slip detection would also allow for evaluation concerning which of these methods succeed the most, and in what ways.

5.3.2 Development of a "Quality Index"

One criticism of the final product of this thesis, as described in section 5.1.2, is that it does not provide a conclusive verdict of the receiver quality. One improvement that would help in this manner is a "quality index". Such an index could combine all the quality metrics presented in the output file into a single numeric value. In this way, the user would receive a more conclusive verdict of the receiver performance. Given the number of aspects that may vary from one receiver to another, developing such a generalized index would be challenging. However, it would quite possibly be worth the effort.

5.3.3 Visualization of Signal Continuity

As noted in section 5.1.2, the results in the output file do not provide the user with an idea of the receiver's ability to maintain continuous signal tracking. A visualization of the distribution of the cycle slips over time could aid in evaluating this ability. Another metric that could be of use in this aspect would be the average time interval between cycle slips.

5.3.4 Processing "Signal Strength" Observations

Though the function **readRinexObs304**, used for reading RINEX observation file, does in fact have the ability to read the "signal strength" observation type, these observation are not actually utilized in **GNSS_Receiver_QC_2020**. A possible future development could be to compare the change in signal strength to, among other things, the tendency of cycle slips. This could be paired with the visualization suggestion in section 5.3.3.

Chapter 6: Conclusion

Through the work of this thesis, a computer software named **GNSS_Receiver_QC_2020** was developed to evaluate the performance of GNSS receivers. This software was developed to be as autonomous as possible, with little work required from the user. Furthermore, four data sets were collected using four different receivers. These were collected simultaneously and in comparable conditions. As such, the results produced from the software analyses of these data sets could be compared.

By comparing the results of two of the receivers, a definite conclusion concerning which receiver performed better was reached. This conclusion also coincided with the expectations derived from the price tag of the receivers. Hence, it was argued that the developed software succeeds in evaluating the performance of GNSS receivers. However, weaknesses of the current software were also discussed, as well as possible future development.

By developing a software for the evaluation of GNSS receiver performance, a contribution has been made to the continued use of *reliable* GNSS.

References

Blinken AS (2020), Private Communication.

Boulet, D. (1991), *Methods of orbit determination for the microcomputer*, Willmann-Bell, Inc, Richmond, Va.

Collins, J. P. (1999), An overview of gps inter-frequency carrier phase combinations. unpublished.

Estey, L. H. & Meertens, C. M. (1999), 'Teqc: The multi-purpose toolkit for gps/glonass data', *GPS Solutions* **3**(1), 42–49.

European GNSS Agency (2019), *GNSS market report*, Publications Office of the European Union, Luxembourg.

European GNSS Agency (2020), 'Constellation information'.
URL: *https://www.gsc-europa.eu/system-service-status/constellation-information*

Fernandez-Hernandez, I., Vecchione, G., Díaz-Pulido, F., Jeannot, M., Valentaite, G., Blasi, R., Reyes, J. & Simón, J. (2018), Galileo high accuracy: A programme and policy perspective.

GLONASS CONSTELLATION STATUS (2020).
URL: *https://www.glonass-iac.ru/en/GLONASS/*

Guo, F. & Zhang, X. (2014), 'Real-time clock jump compensation for precise point positioning', *GPS Solutions* **18**(1), 41–50.
URL: *https://doi.org/10.1007/s10291-012-0307-3*

Hilla, S. (2016), *The Extended Standard Product 3 Orbit Format (SP3-d).*
URL: *https://gssc.esa.int/library/*

Hofmann-Wellenhof, B., Lichtenegger, H. & Wasle, E. (2008), *GNSS – Global Navigation Satellite Systems*, Springer Vienna.

International GNSS Service (IGS) (2018), *RINEX The Receiver Independent Exchange Format Version 3.04.*
URL: *https://kb.igs.org/hc/en-us/articles/201096516-IGS-Formats*

Mirgorodskaya, T. (2013), Glonass government policy, status and modernization plans, *in* 'Proceedings of international global navigation satellite systems (IGNSS) symposium, Golden Coast', pp. 16–18.

NavSys AS (2020), Private Communication.

Norgeodesi AS (2020), Private Communication.

Seeber, G. (2003), *Satellite geodesy*, Walter de Gruyter, Berlin New York.

Subirana, J., Zornoza, J. M. J. & Heràandez-Pajares, M. (2013), *GNSS Data Processing, Vol. I: Fundamentals and Algorithms*, ESA Communications.

The National Coordination Office for Space Based Positioning (2020), 'Space segment'. **URL:** *https://www.gps.gov/systems/gps/space/III*

U.S. Coast Guard Navigation Center (2020), 'Gps constellation status for 03/26/2020'. **URL:** *https://www.navcen.uscg.gov/?Do=constellationstatus*

Appendix

Appendix A: Analyses Results

As was explained in Chapter 1, a considered was made to limit the amount of results in this appendix, as it is very long. However, in the pursuit of presenting the full specter of results produced in this thesis, the decision was made to include the full contents of Appendix A.

A.1 Topcon Hiper VR

A.1.1 Header

```
GNSS Receiver Quality Check 2020
Software version: 1.00
Last software version release: 02/06/2020

Software developed by Bjørn-Eirik Roald
Norwegian University of Life Sciences(NMBU)

RINEX observation filename:      FLO300XXX_R_20200901200_01D_01S_MO.rnx
RINEX version:                   3.04
RINEX converting program:        TPS2RIN 11.5
Marker name:                     FLO3
Receiver type:                   TPS HIPER_VR
Date of observation start:       2020/3/30 12:20:0.00
Date of observation end:         2020/3/31 12:19:59.00
Observation interval [seconds]:  1
Number of receiver clock jumps:  62
Average clock jumps interval:    00:23:14 (std: 42.97 seconds)

Critical cycle slip limits [m/s]:
- Ionospheric delay:             0.067
- Phase-code combination:        6.667

GNSS systems presents in RINEX observation file:
- BeiDou
- Galileo
- GPS
- GLONASS


NOTE: As there were no "Loss-of-Lock" indicators in RINEX observation file,
no information concerining "Loss-of-Lock" indicators is included in output file

User-specified contend included in output file
- Include overview of observations for each satellite:          Yes
- Include compact summary of analysis estimates:               Yes
- Include detailed summary of analysis
   estimates, including for each individual satellite:         Yes
- Include information about "Loss-of-Lock"
   indicators in detailed summary:                             No
```

Figure A.1.1: Topcon analysis output file: Header

A.1.2 Observation Overview

GPS Observation overview

PRN	L1 Observations	L2 Observations	L5 Observations
G1	C1C,C1W	C2W,C2X	C5X
G2	C1C,C1W	C2W	
G3	C1C,C1W	C2W,C2X	C5X
G4	C1C,C1W	C2W,C2X	C5X
G5	C1C,C1W	C2W,C2X	
G6	C1C,C1W	C2W,C2X	C5X
G7	C1C,C1W	C2W,C2X	
G8	C1C,C1W	C2W,C2X	C5X
G9	C1C,C1W	C2W,C2X	C5X
G10	C1C,C1W	C2W,C2X	C5X
G11	C1C,C1W	C2W	
G12	C1C,C1W	C2W,C2X	
G13	C1C,C1W	C2W	
G14	C1C,C1W	C2W	
G15	C1C,C1W	C2W,C2X	
G16	C1C,C1W	C2W	
G17	C1C,C1W	C2W,C2X	
G19	C1C,C1W	C2W	
G20	C1C,C1W	C2W	
G21	C1C,C1W	C2W	
G22	C1C,C1W	C2W	
G24	C1C,C1W	C2W,C2X	C5X
G25	C1C,C1W	C2W,C2X	C5X
G26	C1C,C1W	C2W,C2X	C5X
G27	C1C,C1W	C2W,C2X	C5X
G28	C1C,C1W	C2W	
G29	C1C,C1W	C2W,C2X	
G30	C1C,C1W	C2W,C2X	C5X
G31	C1C,C1W	C2W,C2X	
G32	C1C,C1W	C2W,C2X	C5X

Figure A.1.2: Topcon analysis output file: GPS observation overview

Galileo Observation overview

PRN	E1 Observations	E5a Observations	E6 Observations	E5b Observations	G5(a+b) Observations
E1	C1X	C5X		C7X	C8X
E2	C1X	C5X		C7X	C8X
E3	C1X	C5X		C7X	C8X
E4	C1X	C5X		C7X	C8X
E5	C1X	C5X		C7X	C8X
E7	C1X	C5X		C7X	C8X
E8	C1X	C5X		C7X	C8X
E9	C1X	C5X		C7X	C8X
E11	C1X	C5X		C7X	C8X
E12	C1X	C5X		C7X	C8X
E13	C1X	C5X		C7X	C8X
E14	C1X	C5X		C7X	C8X
E15	C1X	C5X		C7X	C8X
E18	C1X	C5X		C7X	C8X
E20	C1X	C5X			
E21	C1X	C5X		C7X	C8X
E24	C1X	C5X		C7X	C8X
E25	C1X	C5X		C7X	C8X
E26	C1X	C5X		C7X	C8X
E27	C1X	C5X		C7X	C8X
E30	C1X	C5X		C7X	C8X

Figure A.1.3: Topcon analysis output file: Galileo observation overview

GLONASS Observation overview

Sat ID	Frequency Channel	G1 Observations	G2 Observations	G3 Observations	G1a Observations	G2a Observations
R1	1	C1C,C1P	C2C,C2P			
R2	-4	C1C,C1P	C2C,C2P			
R3	5	C1C,C1P	C2C,C2P			
R4	6	C1C,C1P	C2C,C2P			
R5	1	C1C,C1P	C2C,C2P			
R6	-4	C1C,C1P	C2P			
R7	5	C1C,C1P	C2C,C2P			
R8	6	C1C,C1P	C2C,C2P			
R9	-2	C1C,C1P	C2C,C2P			
R10	-7	C1C,C1P	C2P			
R11	0	C1C,C1P	C2C,C2P			
R12	-1	C1C,C1P	C2C,C2P			
R13	-2	C1C,C1P	C2C,C2P			
R14	-7	C1C,C1P	C2C,C2P			
R15	0	C1C,C1P	C2C,C2P			
R16	-1	C1C,C1P	C2C,C2P			
R17	4	C1C,C1P	C2C,C2P			
R18	-3	C1C,C1P	C2C,C2P			
R19	3	C1C,C1P	C2C,C2P			
R20	2	C1C,C1P	C2C,C2P			
R21	4	C1C,C1P	C2C,C2P			
R22	-3	C1C,C1P	C2C,C2P			
R23	3	C1C,C1P	C2C,C2P			
R24	2	C1C,C1P	C2C,C2P			

Figure A.1.4: Topcon analysis output file: GLONASS observation overview

BeiDou Observation overview

PRN	B1 Observations	E1-2 Observations	B2a Observations	B3 Observations	B2b Observations	B2(a+b) Observations
C5		C2X			C7X	
C6		C2X			C7X	
C7		C2X			C7X	
C8		C2X			C7X	
C9		C2X			C7X	
C10		C2X			C7X	
C11		C2X			C7X	
C12		C2X			C7X	
C13		C2X			C7X	
C14		C2X			C7X	
C16		C2X			C7X	
C19		C2X			C7X	
C20		C2X			C7X	
C21		C2X			C7X	
C22		C2X			C7X	
C23		C2X			C7X	
C25		C2X			C7X	
C27		C2X				
C28		C2X			C7X	
C29		C2X			C7X	
C30		C2X			C7X	
C32		C2X				
C33		C2X				
C34		C2X				
C35		C2X				
C36		C2X				
C37		C2X				

Figure A.1.5: Topcon analysis output file: BeiDou observation overview

A.1.3 Compressed Results Overview

GPS ANALYSIS SUMMARY

	C1C	C1W	C2W	C2X	C5X
RMS multipath[meters]	0.320	0.482	0.448	0.452	0.369
Weighted RMS multipath[meters]	0.181	0.246	0.213	0.266	0.201
N ambiguity slips periods	32	366	405	151	101
N slip periods, elevation angle > 10 degrees	1	73	77	25	20
N slip periods, elevation angle < 10 degrees	31	293	328	126	81
N slip periods, elevation angle not computed	0	0	0	0	0
Ratio of N slip periods/N obs epochs [%]	0.002	0.018	0.020	0.011	0.011

Figure A.1.6: Topcon analysis output file: GPS compressed results overview

GALILEO ANALYSIS SUMMARY

	C1X	C5X	C7X	C8X
RMS multipath[meters]	0.486	0.262	0.232	0.176
Weighted RMS multipath[meters]	0.312	0.180	0.168	0.115
N ambiguity slips periods	13	45	34	95
N slip periods, elevation angle > 10 degrees	6	14	14	52
N slip periods, elevation angle < 10 degrees	7	25	20	43
N slip periods, elevation angle not computed	0	6	0	0
Ratio of N slip periods/N obs epochs [%]	0.001	0.003	0.003	0.007

Figure A.1.7: Topcon analysis output file: Galileo compressed results overview

GLONASS ANALYSIS SUMMARY

	C1C	C1P	C2C	C2P
RMS multipath[meters]	0.743	0.441	1.108	0.335
Weighted RMS multipath[meters]	0.416	0.294	0.524	0.223
N ambiguity slips periods	75	219	230	254
N slip periods, elevation angle > 10 degrees	32	80	83	88
N slip periods, elevation angle < 10 degrees	24	78	105	101
N slip periods, elevation angle not computed	19	61	42	65
Ratio of N slip periods/N obs epochs [%]	0.004	0.013	0.014	0.015

Figure A.1.8: Topcon analysis output file: GLONASS compressed results overview

BEIDOU ANALYSIS SUMMARY

	C2X	C7X
RMS multipath[meters]	0.501	0.494
Weighted RMS multipath[meters]	0.312	0.323
N ambiguity slips periods	14	83
N slip periods, elevation angle > 10 degrees	0	56
N slip periods, elevation angle < 10 degrees	14	27
N slip periods, elevation angle not computed	0	0
Ratio of N slip periods/N obs epochs [%]	0.001	0.009

Figure A.1.9: Topcon analysis output file: BeiDou compressed results overview

A.1.4 Detailed Results Overview

GPS

PRN	n C1C Observations	n Epochs with Multipath Estimates	RMS Multipath [meters]	Weighted RMS Multipath [meters]	Average Sat. Elevation Angle [degrees]	n Slip Periods	Slip/Obs Ratio [%]	n Slip Periods Elevation Angle 0–10 degrees	n Slip Periods Elevation Angle 10–20 degrees	n Slip Periods Elevation Angle 20–30 degrees	n Slip Periods Elevation Angle 30–40 degrees	n Slip Periods Elevation Angle 40–50 degrees	n Slip Periods Elevation Angle >50 degrees	n Slip Periods Elevation Angle NaN degrees
G1	54689	29228	0.314	0.184	38.383	3	0.005	3	0	0	0	0	0	0
G2	86400	34513	0.283	0.199	29.646	0	0.000	0	0	0	0	0	0	0
G3	86400	30381	0.296	0.152	39.074	0	0.000	0	0	0	0	0	0	0
G4	54289	30593	0.413	0.157	37.626	1	0.002	1	0	0	0	0	0	0
G5	64815	32303	0.310	0.192	30.661	1	0.002	1	0	0	0	0	0	0
G6	86400	33189	0.302	0.207	30.648	1	0.001	1	0	0	0	0	0	0
G7	53755	31764	0.293	0.157	35.672	0	0.000	0	0	0	0	0	0	0
G8	54763	31260	0.360	0.213	33.957	0	0.000	0	0	0	0	0	0	0
G9	56180	29989	0.285	0.153	39.003	0	0.000	0	0	0	0	0	0	0
G10	65200	32588	0.507	0.185	33.386	1	0.002	1	0	0	0	0	0	0
G11	54474	27505	0.309	0.174	36.406	2	0.004	1	1	0	0	0	0	0
G12	86400	30794	0.251	0.128	38.843	0	0.000	0	0	0	0	0	0	0
G13	61072	29355	0.325	0.161	37.390	2	0.003	2	0	0	0	0	0	0
G14	86400	32857	0.281	0.201	31.452	0	0.000	0	0	0	0	0	0	0
G15	63730	31151	0.325	0.195	31.717	4	0.006	4	0	0	0	0	0	0
G16	54132	31738	0.443	0.239	32.290	1	0.002	1	0	0	0	0	0	0
G17	53310	33834	0.268	0.189	30.650	0	0.000	0	0	0	0	0	0	0
G19	86400	33132	0.274	0.192	30.853	0	0.000	0	0	0	0	0	0	0
G20	65086	31292	0.300	0.192	32.114	2	0.003	2	0	0	0	0	0	0
G21	63485	31734	0.318	0.185	36.713	1	0.002	1	0	0	0	0	0	0
G22	86400	29517	0.248	0.126	39.533	1	0.001	1	0	0	0	0	0	0
G24	86400	29210	0.305	0.162	37.552	3	0.003	3	0	0	0	0	0	0
G25	86400	29808	0.277	0.153	39.296	0	0.000	0	0	0	0	0	0	0
G26	54377	31466	0.364	0.206	32.439	0	0.000	0	0	0	0	0	0	0
G27	55273	29316	0.328	0.190	37.576	0	0.000	0	0	0	0	0	0	0
G28	53576	31996	0.309	0.196	34.147	0	0.000	0	0	0	0	0	0	0
G29	86400	31306	0.291	0.141	38.153	0	0.000	0	0	0	0	0	0	0
G30	54353	30546	0.316	0.152	37.471	3	0.006	3	0	0	0	0	0	0
G31	86400	33121	0.279	0.182	29.822	0	0.000	0	0	0	0	0	0	0
G32	86400	34213	0.283	0.196	29.583	6	0.007	6	0	0	0	0	0	0

Figure A.1.10: Topcon analysis output file: GPS C1C signal, detailed results overview

PRN	n C1W Observations	n Epochs with Multipath Estimates	RMS Multipath [meters]	Weighted RMS Multipath [meters]	Average Sat. Elevation Angle [degrees]	n Slip Periods	Slip/Obs Ratio [%]	n Slip Periods Elevation Angle 0–10 degrees	n Slip Periods Elevation Angle 10–20 degrees	n Slip Periods Elevation Angle 20–30 degrees	n Slip Periods Elevation Angle 30–40 degrees	n Slip Periods Elevation Angle 40–50 degrees	n Slip Periods Elevation Angle >50 degrees	n Slip Periods Elevation Angle NaN degrees
G1	54686	29204	0.415	0.209	38.419	12	0.022	11	1	0	0	0	0	0
G2	86400	34513	0.457	0.291	29.732	15	0.017	15	0	0	0	0	0	0
G3	86400	30381	0.458	0.202	39.110	11	0.013	11	0	0	0	0	0	0
G4	54281	30592	0.468	0.218	37.645	3	0.006	2	1	0	0	0	0	0
G5	64813	32302	0.397	0.243	30.667	2	0.003	2	0	0	0	0	0	0
G6	86400	33189	0.417	0.280	30.665	6	0.007	3	3	0	0	0	0	0
G7	53747	31762	0.432	0.204	35.796	18	0.033	17	1	0	0	0	0	0
G8	54760	31260	0.509	0.295	33.978	7	0.013	2	5	0	0	0	0	0
G9	56173	29987	0.518	0.196	39.039	4	0.007	2	2	0	0	0	0	0
G10	65191	32586	0.638	0.258	33.415	7	0.011	7	0	0	0	0	0	0
G11	54453	27502	0.572	0.230	36.648	27	0.050	12	15	0	0	0	0	0
G12	86400	30781	0.430	0.184	38.949	15	0.017	11	4	0	0	0	0	0
G13	60982	29350	0.683	0.241	37.558	27	0.044	11	16	0	0	0	0	0
G14	86400	32845	0.468	0.303	31.475	4	0.005	4	0	0	0	0	0	0
G15	63631	31151	0.414	0.250	31.763	8	0.013	7	1	0	0	0	0	0
G16	54095	31735	0.542	0.307	32.340	9	0.017	8	1	0	0	0	0	0
G17	53304	33834	0.372	0.233	30.662	5	0.009	5	0	0	0	0	0	0
G19	86400	33132	0.423	0.275	30.915	13	0.015	13	0	0	0	0	0	0
G20	65078	31288	0.539	0.292	32.271	28	0.043	28	0	0	0	0	0	0
G21	63464	31729	0.519	0.239	36.853	15	0.024	9	6	0	0	0	0	0
G22	86400	29511	0.494	0.183	39.786	28	0.032	25	3	0	0	0	0	0
G24	86400	29209	0.441	0.185	37.611	14	0.016	12	2	0	0	0	0	0
G25	86400	29804	0.443	0.209	39.371	14	0.016	13	1	0	0	0	0	0
G26	54363	31459	0.492	0.264	32.511	13	0.024	12	1	0	0	0	0	0
G27	55259	29317	0.446	0.227	37.638	11	0.020	8	3	0	0	0	0	0
G28	53566	31995	0.578	0.299	34.263	17	0.032	12	5	0	0	0	0	0
G29	86400	31306	0.463	0.182	38.170	4	0.005	2	2	0	0	0	0	0
G30	54347	30546	0.502	0.208	37.491	7	0.013	7	0	0	0	0	0	0
G31	86400	33121	0.393	0.248	29.833	3	0.003	3	0	0	0	0	0	0
G32	86400	34213	0.432	0.285	29.643	19	0.022	19	0	0	0	0	0	0

Figure A.1.11: Topcon analysis output file: GPS C1W signal, detailed results overview

PRN	n C2W Observations	n Epochs with Multipath Estimates	RMS Multipath [meters]	Weighted RMS Multipath [meters]	Average Sat. Elevation Angle [degrees]	n Slip Periods	Slip/Obs Ratio [%]	n Slip Periods Elevation Angle 0–10 degrees	n Slip Periods Elevation Angle 10–20 degrees	n Slip Periods Elevation Angle 20–30 degrees	n Slip Periods Elevation Angle 30–40 degrees	n Slip Periods Elevation Angle 40–50 degrees	n Slip Periods Elevation Angle >50 degrees	n Slip Periods Elevation Angle NaN degrees
G1	54686	29206	0.362	0.168	38.418	12	0.022	11	1	0	0	0	0	0
G2	86400	34511	0.416	0.232	29.736	14	0.016	14	0	0	0	0	0	0
G3	86400	30381	0.404	0.164	39.111	10	0.012	10	0	0	0	0	0	0
G4	54280	30593	0.455	0.212	37.646	3	0.006	2	1	0	0	0	0	0
G5	64813	32300	0.360	0.208	30.667	4	0.006	3	1	0	0	0	0	0
G6	86400	33189	0.392	0.242	30.665	6	0.007	3	3	0	0	0	0	0
G7	53747	31762	0.413	0.181	35.791	22	0.041	21	1	0	0	0	0	0
G8	54759	31260	0.422	0.220	33.979	7	0.013	2	5	0	0	0	0	0
G9	56173	29988	0.418	0.165	39.039	4	0.007	2	2	0	0	0	0	0
G10	65191	32588	0.613	0.213	33.415	9	0.014	9	0	0	0	0	0	0
G11	54457	27490	0.591	0.209	36.656	34	0.062	17	17	0	0	0	0	0
G12	86400	30779	0.380	0.142	38.951	17	0.020	16	1	0	0	0	0	0
G13	60973	29349	0.609	0.233	37.556	28	0.046	8	20	0	0	0	0	0
G14	86400	32848	0.491	0.292	31.476	4	0.005	4	0	0	0	0	0	0
G15	63678	31150	0.402	0.215	31.762	12	0.019	11	1	0	0	0	0	0
G16	54097	31737	0.546	0.261	32.340	10	0.018	9	1	0	0	0	0	0
G17	53304	33834	0.327	0.214	30.663	3	0.006	3	0	0	0	0	0	0
G19	86400	33132	0.410	0.224	30.916	15	0.017	15	0	0	0	0	0	0
G20	65074	31290	0.509	0.258	32.275	28	0.043	28	0	0	0	0	0	0
G21	63477	31729	0.523	0.226	36.843	23	0.036	18	5	0	0	0	0	0
G22	86400	29507	0.465	0.177	39.787	32	0.037	29	3	0	0	0	0	0
G24	86400	29202	0.380	0.160	37.611	18	0.021	16	2	0	0	0	0	0
G25	86400	29807	0.423	0.178	39.370	13	0.015	11	2	0	0	0	0	0
G26	54363	31463	0.452	0.224	32.513	14	0.026	13	1	0	0	0	0	0
G27	55260	29314	0.372	0.177	37.639	10	0.018	8	2	0	0	0	0	0
G28	53566	31993	0.554	0.269	34.269	18	0.034	14	4	0	0	0	0	0
G29	86400	31306	0.385	0.168	38.170	8	0.009	4	4	0	0	0	0	0
G30	54347	30546	0.434	0.183	37.491	7	0.013	7	0	0	0	0	0	0
G31	86400	33121	0.388	0.218	29.833	3	0.003	3	0	0	0	0	0	0
G32	86400	34213	0.363	0.226	29.645	17	0.020	17	0	0	0	0	0	0

Figure A.1.12: Topcon analysis output file: GPS C2W signal, detailed results overview

PRN	n C2X Observations	n Epochs with Multipath Estimates	RMS Multipath [meters]	Weighted RMS Multipath [meters]	Average Sat. Elevation Angle [degrees]	n Slip Periods	Slip/Obs Ratio [%]	n Slip Periods Elevation Angle 0–10 degrees	n Slip Periods Elevation Angle 10–20 degrees	n Slip Periods Elevation Angle 20–30 degrees	n Slip Periods Elevation Angle 30–40 degrees	n Slip Periods Elevation Angle 40–50 degrees	n Slip Periods Elevation Angle >50 degrees	n Slip Periods Elevation Angle NaN degrees
G1	54685	29153	0.406	0.223	38.525	6	0.011	5	1	0	0	0	0	0
G3	86400	30370	0.420	0.220	39.123	10	0.012	10	0	0	0	0	0	0
G4	54279	30589	0.406	0.239	37.650	3	0.006	2	1	0	0	0	0	0
G5	64809	32223	0.461	0.289	30.721	4	0.006	4	0	0	0	0	0	0
G6	86400	33159	0.441	0.307	30.687	9	0.010	6	3	0	0	0	0	0
G7	53753	31826	0.467	0.242	35.741	8	0.015	7	1	0	0	0	0	0
G8	54756	31198	0.490	0.278	34.037	10	0.018	5	5	0	0	0	0	0
G9	56173	29982	0.519	0.321	39.045	4	0.007	2	2	0	0	0	0	0
G10	65050	32496	0.587	0.284	33.495	3	0.005	3	0	0	0	0	0	0
G12	86400	30911	0.394	0.208	38.874	9	0.010	7	2	0	0	0	0	0
G15	63577	31085	0.516	0.284	31.815	7	0.011	6	1	0	0	0	0	0
G17	53303	33833	0.408	0.300	30.664	3	0.006	3	0	0	0	0	0	0
G24	86400	29131	0.396	0.216	37.702	14	0.016	12	2	0	0	0	0	0
G25	86400	29835	0.450	0.248	39.345	11	0.013	9	2	0	0	0	0	0
G26	54370	31434	0.506	0.278	32.547	11	0.020	10	1	0	0	0	0	0
G27	55265	29276	0.431	0.241	37.680	10	0.018	8	2	0	0	0	0	0
G29	86400	31294	0.413	0.239	38.180	6	0.007	4	2	0	0	0	0	0
G30	54343	30546	0.406	0.237	37.489	5	0.009	5	0	0	0	0	0	0
G31	86400	33034	0.447	0.299	29.894	4	0.005	4	0	0	0	0	0	0
G32	86400	34219	0.407	0.302	29.642	14	0.016	14	0	0	0	0	0	0

Figure A.1.13: Topcon analysis output file: GPS C2X signal, detailed results overview

PRN	n C5X Observations	n Epochs with Multipath Estimates	RMS Multipath [meters]	Weighted RMS Multipath [meters]	Average Sat. Elevation Angle [degrees]	n Slip Periods	Slip/Obs Ratio [%]	n Slip Periods Elevation Angle 0–10 degrees	n Slip Periods Elevation Angle 10–20 degrees	n Slip Periods Elevation Angle 20–30 degrees	n Slip Periods Elevation Angle 30–40 degrees	n Slip Periods Elevation Angle 40–50 degrees	n Slip Periods Elevation Angle >50 degrees	n Slip Periods Elevation Angle NaN degrees
G1	54687	29255	0.576	0.172	38.423	10	0.018	9	1	0	0	0	0	0
G3	86400	30381	0.286	0.176	39.110	10	0.012	10	0	0	0	0	0	0
G4	54281	30599	0.291	0.167	37.641	2	0.004	1	1	0	0	0	0	0
G6	86400	33189	0.343	0.229	30.664	6	0.007	3	3	0	0	0	0	0
G8	54760	31261	0.376	0.247	33.978	7	0.013	2	5	0	0	0	0	0
G9	56174	29994	0.305	0.212	39.033	4	0.007	2	2	0	0	0	0	0
G10	65195	32611	0.529	0.181	33.401	3	0.005	3	0	0	0	0	0	0
G24	86400	29241	0.316	0.164	37.575	15	0.017	13	2	0	0	0	0	0
G25	86400	29846	0.319	0.171	39.334	11	0.013	9	2	0	0	0	0	0
G26	54374	31531	0.357	0.229	32.463	6	0.011	5	1	0	0	0	0	0
G27	55266	29340	0.351	0.218	37.613	12	0.022	9	3	0	0	0	0	0
G30	54347	30554	0.306	0.167	37.482	5	0.009	5	0	0	0	0	0	0
G32	86400	34288	0.311	0.237	29.590	10	0.012	10	0	0	0	0	0	0

Figure A.1.14: Topcon analysis output file: GPS C5X signal, detailed results overview

Galileo

PRN	n C1X Observations	n Epochs with Multipath Estimates	RMS Multipath [meters]	Weighted RMS Multipath [meters]	Average Sat. Elevation Angle [degrees]	n Slip Periods	Slip/Obs Ratio [%]	n Slip Periods Elevation Angle 0–10 degrees	n Slip Periods Elevation Angle 10–20 degrees	n Slip Periods Elevation Angle 20–30 degrees	n Slip Periods Elevation Angle 30–40 degrees	n Slip Periods Elevation Angle 40–50 degrees	n Slip Periods Elevation Angle >50 degrees	n Slip Periods Elevation Angle NaN degrees
E1	66038	42395	0.429	0.298	36.805	0	0.000		0		0	0	0	0
E2	86400	17735	0.579	0.240	21.317	0	0.000		0		0	0	0	0
E3	69360	29708	0.516	0.380	25.413	0	0.000		0		0	0	0	0
E4	67887	34092	0.400	0.225	39.810	0	0.000		0		0	0	0	0
E5	72196	32811	0.586	0.325	27.532	0	0.000		0		0	0	0	0
E7	49575	27317	0.395	0.239	38.051	0	0.000		0		0	0	0	0
E8	65592	25599	0.526	0.299	30.060	0	0.000		0		0	0	0	0
E9	71583	33126	0.468	0.295	33.657	2	0.003	2	0		0	0	0	0
E11	86356	22171	0.546	0.334	24.926	0	0.000	0	0		0	0	0	0
E12	50940	28675	0.445	0.330	33.617	1	0.002	1	0		0	0	0	0
E13	68585	38539	0.454	0.271	39.899	1	0.001	1	0		0	0	0	0
E14	86018	470	0.271	0.130	26.088	0	0.000	0	0		0	0	0	0
E15	70970	36077	0.432	0.265	38.194	1	0.001	1	0		0	0	0	0
E18	55102	912	2.817	2.809	34.514	6	0.011	0	0		0	0	6	0
E20	55944	0	NaN	NaN	NaN	0	0.000	0	0		0	0	0	0
E21	65799	43852	0.446	0.304	34.899	0	0.000	0	0		0	0	0	0
E24	57280	28676	0.526	0.260	39.001	0	0.000	0	0		0	0	0	0
E25	52540	18545	0.507	0.220	21.625	0	0.000	0	0		0	0	0	0
E26	67650	40456	0.439	0.275	38.866	1	0.001	1	0		0	0	0	0
E27	63238	39051	0.442	0.336	38.071	0	0.000	0	0		0	0	0	0
E30	55789	28729	0.464	0.266	37.656	1	0.002	1	0		0	0	0	0

Figure A.1.15: Topcon analysis output file: Galileo C1X signal, detailed results overview

PRN	n C5X Observations	n Epochs with Multipath Estimates	RMS Multipath [meters]	Weighted RMS Multipath [meters]	Average Sat. Elevation Angle [degrees]	n Slip Periods	Slip/Obs Ratio [%]	n Slip Periods Elevation Angle 0–10 degrees	n Slip Periods Elevation Angle 10–20 degrees	n Slip Periods Elevation Angle 20–30 degrees	n Slip Periods Elevation Angle 30–40 degrees	n Slip Periods Elevation Angle 40–50 degrees	n Slip Periods Elevation Angle >50 degrees	n Slip Periods Elevation Angle NaN degrees
E1	66038	42398	0.250	0.187	36.805	2	0.003	1	1	0	0	0	0	0
E2	86400	17734	0.263	0.116	21.317	3	0.003	3	0	0	0	0	0	0
E3	69360	29709	0.306	0.237	25.413	0	0.000	0	0	0	0	0	0	0
E4	67887	34088	0.211	0.140	39.811	1	0.001	0	1	0	0	0	0	0
E5	72193	32809	0.277	0.165	27.533	0	0.000	0	0	0	0	0	0	0
E7	49575	27317	0.211	0.141	38.051	1	0.002	1	0	0	0	0	0	0
E8	65592	25595	0.266	0.148	30.062	4	0.006	4	0	0	0	0	0	0
E9	71583	33132	0.246	0.158	33.657	3	0.004	3	0	0	0	0	0	0
E11	86356	22173	0.289	0.174	24.926	1	0.001	0	1	0	0	0	0	0
E12	50940	28679	0.226	0.170	33.617	0	0.000	0	0	0	0	0	0	0
E13	68585	38538	0.210	0.126	39.899	1	0.001	1	0	0	0	0	0	0
E14	86018	466	0.213	0.078	26.122	1	0.001	1	0	0	0	0	0	0
E15	70970	36079	0.218	0.124	38.194	1	0.001	1	0	0	0	0	0	0
E18	55102	911	2.149	2.113	34.517	12	0.022	1	1	2	0	1	7	0
E20	18254	0	NaN	NaN	NaN	6	0.033	0	0	0	0	0	0	6
E21	65799	43854	0.220	0.154	34.899	0	0.000	0	0	0	0	0	0	0
E24	57280	28677	0.259	0.129	39.001	0	0.000	0	0	0	0	0	0	0
E25	52540	18542	0.269	0.106	21.625	0	0.000	0	0	0	0	0	0	0
E26	67650	40458	0.224	0.150	38.867	3	0.004	3	0	0	0	0	0	0
E27	63238	39049	0.273	0.204	38.071	1	0.002	1	0	0	0	0	0	0
E30	55789	28655	0.272	0.135	37.717	5	0.009	5	0	0	0	0	0	0

Figure A.1.16: Topcon analysis output file: Galileo C5X signal, detailed results overview

PRN	n C7X Observations	n Epochs with Multipath Estimates	RMS Multipath [meters]	Weighted RMS Multipath [meters]	Average Sat. Elevation Angle [degrees]	n Slip Periods	Slip/Obs Ratio [%]	n Slip Periods Elevation Angle 0–10 degrees	n Slip Periods Elevation Angle 10–20 degrees	n Slip Periods Elevation Angle 20–30 degrees	n Slip Periods Elevation Angle 30–40 degrees	n Slip Periods Elevation Angle 40–50 degrees	n Slip Periods Elevation Angle >50 degrees	n Slip Periods Elevation Angle NaN degrees
E1	66038	42395	0.220	0.173	36.807	2	0.003	2	0	0	0	0	0	0
E2	86400	17735	0.240	0.104	21.317	4	0.005	4	0	0	0	0	0	0
E3	69359	29707	0.250	0.183	25.413	1	0.001	1	0	0	0	0	0	0
E4	67887	34090	0.205	0.140	39.810	1	0.001	0	1	0	0	0	0	0
E5	72196	32810	0.247	0.148	27.532	0	0.000	0	0	0	0	0	0	0
E7	49575	27317	0.176	0.128	38.051	2	0.004	2	0	0	0	0	0	0
E8	65592	25596	0.208	0.135	30.060	2	0.003	2	0	0	0	0	0	0
E9	71583	33126	0.199	0.146	33.657	2	0.003	2	0	0	0	0	0	0
E11	86356	22171	0.256	0.167	24.926	0	0.000	0	0	0	0	0	0	0
E12	50940	28676	0.173	0.131	33.617	0	0.000	0	0	0	0	0	0	0
E13	68584	38537	0.208	0.138	39.900	1	0.001	1	0	0	0	0	0	0
E14	86017	470	0.080	0.043	25.975	2	0.002	0	1	0	0	0	1	0
E15	70969	36077	0.213	0.118	38.195	1	0.001	1	0	0	0	0	0	0
E18	55102	908	2.220	2.220	34.440	11	0.020	0	0	0	1	1	9	0
E21	65799	43852	0.188	0.138	34.899	0	0.000	0	0	0	0	0	0	0
E24	57280	28675	0.206	0.101	39.001	0	0.000	0	0	0	0	0	0	0
E25	52540	18544	0.220	0.100	21.625	0	0.000	0	0	0	0	0	0	0
E26	67650	40456	0.219	0.153	38.867	3	0.004	3	0	0	0	0	0	0
E27	63238	39050	0.213	0.165	38.071	0	0.000	0	0	0	0	0	0	0
E30	55789	28710	0.226	0.126	37.656	2	0.004	2	0	0	0	0	0	0

Figure A.1.17: Topcon analysis output file: Galileo C7X signal, detailed results overview

PRN	n C8X Observations	n Epochs with Multipath Estimates	RMS Multipath [meters]	Weighted RMS Multipath [meters]	Average Sat. Elevation Angle [degrees]	n Slip Periods	Slip/Obs Ratio [%]	n Slip Periods Elevation Angle 0–10 degrees	n Slip Periods Elevation Angle 10–20 degrees	n Slip Periods Elevation Angle 20–30 degrees	n Slip Periods Elevation Angle 30–40 degrees	n Slip Periods Elevation Angle 40–50 degrees	n Slip Periods Elevation Angle >50 degrees	n Slip Periods Elevation Angle NaN degrees
E1	66038	42396	0.178	0.141	36.807	2	0.003	2	0	0	0	0	0	0
E2	86400	17728	0.191	0.087	21.322	6	0.007	5	1	0	0	0	0	0
E3	69360	29706	0.217	0.161	25.413	2	0.003	2	0	0	0	0	0	0
E4	67886	34090	0.167	0.113	39.811	1	0.001	0	1	0	0	0	0	0
E5	72196	32811	0.206	0.116	27.533	3	0.004	2	1	0	0	0	0	0
E7	49575	27309	0.142	0.094	38.055	3	0.006	3	0	0	0	0	0	0
E8	65589	25590	0.165	0.107	30.068	4	0.006	4	0	0	0	0	0	0
E9	71582	33131	0.167	0.121	33.659	6	0.008	6	0	0	0	0	0	0
E11	86355	22173	0.213	0.127	24.927	3	0.003	1	2	0	0	0	0	0
E12	50939	28674	0.143	0.106	33.619	1	0.002	1	0	0	0	0	0	0
E13	68582	38537	0.168	0.109	39.902	1	0.001	1	0	0	0	0	0	0
E14	86018	468	0.068	0.039	26.085	16	0.019	2	6	3	1	2	2	0
E15	70970	36078	0.169	0.088	38.196	3	0.004	3	0	0	0	0	0	0
E18	55102	900	0.228	0.191	34.660	33	0.060	2	8	7	2	2	12	0
E21	65798	43852	0.153	0.106	34.900	1	0.002	1	0	0	0	0	0	0
E24	57279	28675	0.176	0.088	39.005	3	0.005	1	2	0	0	0	0	0
E25	52540	18543	0.182	0.078	21.627	2	0.004	2	0	0	0	0	0	0
E26	67649	40452	0.178	0.121	38.872	1	0.001	1	0	0	0	0	0	0
E27	63238	39044	0.183	0.138	38.076	1	0.002	1	0	0	0	0	0	0
E30	55789	28650	0.178	0.094	37.726	3	0.005	3	0	0	0	0	0	0

Figure A.1.18: Topcon analysis output file: Galileo C8X signal, detailed results overview

GLONASS

Sat ID	Frequency Channel	n C1C Observations	n Epochs with Multipath Estimates	RMS Multipath [meters]	Weighted RMS Multipath [meters]	Average Sat. Elevation Angle [degrees]	n Slip Periods	Slip/Obs Ratio [%]	n Slip Periods Elevation Angle 0–10 degrees	n Slip Periods Elevation Angle 10–20 degrees	n Slip Periods Elevation Angle 20–30 degrees	n Slip Periods Elevation Angle 30–40 degrees	n Slip Periods Elevation Angle 40–50 degrees	n Slip Periods Elevation Angle >50 degrees	n Slip Periods Elevation Angle NaN degrees
R1	1	81836	30241	0.483	NaN	NaN	3	0.004		0	0	0	0	0	3
R2	−4	58384	30689	0.465	NaN	NaN	3	0.005		0	0	0	0	0	3
R3	5	60586	31624	0.552	NaN	NaN	2	0.003		0	0	0	0	0	2
R4	6	62059	32204	0.425	NaN	NaN	3	0.005		0	0	0	0	0	3
R5	1	81974	32386	0.389	NaN	NaN	3	0.004		0	0	0	0	0	3
R6	−4	85980	0	NaN	NaN	NaN	5	0.006		0	0	0	0	0	5
R7	5	86400	35281	0.470	0.295	54.579	0	0.000		0	0	0	0	0	0
R8	6	85683	34445	0.636	0.352	35.394	2	0.002		0	2	0	0	0	0
R9	−2	83384	33794	0.447	0.297	31.866	2	0.002		1	0	0	0	0	0
R10	−7	50015	0	NaN	NaN	NaN	0	0.000		0	0	0	0	0	0
R11	0	49799	30025	0.448	0.280	33.848	1	0.002		1	0	0	0	0	0
R12	−1	50238	30058	0.505	0.288	35.823	6	0.012		6	0	0	0	0	0
R13	−2	50467	24413	0.844	0.575	42.927	7	0.014		0	4	3	0	0	0
R14	−7	83395	34585	0.501	0.227	35.308	2	0.002		2	0	0	0	0	0
R15	0	86400	37169	0.338	0.219	42.085	1	0.001		1	0	0	0	0	0
R16	−1	86400	35191	0.780	0.362	42.289	2	0.002		0	1	1	0	0	0
R17	4	86400	36852	1.585	0.298	39.793	5	0.006		4	1	0	0	0	0
R18	−3	86400	36631	0.375	0.269	38.420	1	0.001		1	0	0	0	0	0
R19	3	82103	27588	0.990	0.642	41.246	9	0.011		2	5	2	0	0	0
R20	2	55387	24739	1.588	1.151	42.622	9	0.016		1	2	6	0	0	0
R21	4	54179	30357	0.498	0.305	37.882	0	0.000		0	0	0	0	0	0
R22	−3	52366	29999	0.397	0.264	37.181	1	0.002		1	0	0	0	0	0
R23	3	82636	31896	1.282	0.304	33.604	3	0.004		1	2	0	0	0	0
R24	2	86400	35454	0.519	0.347	34.953	5	0.006		3	2	0	0	0	0

Figure A.1.19: Topcon analysis output file: GLONASS C1C signal, detailed results overview

Sat ID	Frequency Channel	n C1P Observations	n Epochs with Multipath Estimates	RMS Multipath [meters]	Weighted RMS Multipath [meters]	Average Sat. Elevation Angle [degrees]	n Slip Periods	Slip/Obs Ratio [%]	n Slip Periods Elevation Angle 0–10 degrees	n Slip Periods Elevation Angle 10–20 degrees	n Slip Periods Elevation Angle 20–30 degrees	n Slip Periods Elevation Angle 30–40 degrees	n Slip Periods Elevation Angle 40–50 degrees	n Slip Periods Elevation Angle >50 degrees	n Slip Periods Elevation Angle NaN degrees
R1	1	81835	30200	0.451	NaN	NaN	10	0.012	0	0	0	0	0	0	10
R2	−4	58382	30688	0.409	NaN	NaN	8	0.014	0	0	0	0	0	0	8
R3	5	60586	31600	0.443	NaN	NaN	9	0.015	0	0	0	0	0	0	9
R4	6	62057	32197	0.438	NaN	NaN	9	0.015	0	0	0	0	0	0	9
R5	1	81974	32384	0.423	NaN	NaN	9	0.011	0	0	0	0	0	0	9
R6	−4	85980	0	NaN	NaN	NaN	14	0.016	0	0	0	0	0	0	14
R7	5	86400	35281	0.469	0.280	54.582	2	0.002	1	0	0	0	0	0	1
R8	6	85683	34396	0.550	0.314	35.412	3	0.004	0	0	3	0	0	0	0
R9	−2	83383	33794	0.374	0.259	31.872	6	0.007	3	3	0	0	0	0	0
R10	−7	50014	0	NaN	NaN	NaN	1	0.002	0	0	0	0	0	0	1
R11	0	49799	30021	0.423	0.306	33.848	4	0.008	4	0	0	0	0	0	0
R12	−1	50157	30039	0.456	0.305	35.846	10	0.020	10	0	0	0	0	0	0
R13	−2	50467	24314	0.420	0.309	43.037	19	0.038	3	7	9	0	0	0	0
R14	−7	83395	34581	0.450	0.243	35.312	11	0.013	11	0	0	0	0	0	0
R15	0	86400	37169	0.395	0.237	42.088	5	0.006	5	0	0	0	0	0	0
R16	−1	86400	35185	0.451	0.315	42.297	7	0.008	1	4	2	0	0	0	0
R17	4	86400	36697	0.406	0.292	39.933	16	0.019	13	3	0	0	0	0	0
R18	−3	86400	36631	0.382	0.280	38.420	1	0.001	1	0	0	0	0	0	0
R19	3	82093	27331	0.387	0.311	41.480	27	0.033	5	15	6	0	1	0	0
R20	2	54760	24683	0.421	0.307	42.683	22	0.040	2	6	14	0	0	0	0
R21	4	54178	30357	0.511	0.300	37.883	1	0.002	1	0	0	0	0	0	0
R22	−3	52364	29993	0.444	0.263	37.190	4	0.008	4	0	0	0	0	0	0
R23	3	82636	31827	0.477	0.317	33.653	13	0.016	9	4	0	0	0	0	0
R24	2	86400	35425	0.474	0.353	34.976	8	0.009	5	3	0	0	0	0	0

Figure A.1.20: Topcon analysis output file: GLONASS C1P signal, detailed results overview

Sat ID	Frequency Channel	n C2C Observations	n Epochs with Multipath Estimates	RMS Multipath [meters]	Weighted RMS Multipath [meters]	Average Sat. Elevation Angle [degrees]	n Slip Periods	Slip/Obs Ratio [%]	n Slip Periods Elevation Angle 0–10 degrees	n Slip Periods Elevation Angle 10–20 degrees	n Slip Periods Elevation Angle 20–30 degrees	n Slip Periods Elevation Angle 30–40 degrees	n Slip Periods Elevation Angle 40–50 degrees	n Slip Periods Elevation Angle >50 degrees	n Slip Periods Elevation Angle NaN degrees
R1	1	81835	30241	0.705	NaN	NaN	8	0.010	0	0	0	0	0	0	8
R2	−4	58382	30688	0.428	NaN	NaN	8	0.014	0	0	0	0	0	0	8
R3	5	60586	31624	0.997	NaN	NaN	5	0.008	0	0	0	0	0	0	5
R4	6	62057	32202	0.379	NaN	NaN	8	0.013	0	0	0	0	0	0	8
R5	1	81974	32386	0.400	NaN	NaN	9	0.011	0	0	0	0	0	0	9
R7	5	86400	35281	0.430	0.263	54.582	5	0.006	1	0	0	0	0	0	4
R8	6	85683	34445	1.108	0.616	35.394	1	0.001	0	0	1	0	0	0	0
R9	−2	83383	33791	0.545	0.266	31.878	10	0.012	7	3	0	0	0	0	0
R11	0	49777	30024	0.732	0.260	33.908	4	0.008	4	0	0	0	0	0	0
R12	−1	50238	30049	0.392	0.264	35.839	11	0.022	11	0	0	0	0	0	0
R13	−2	50467	24408	1.321	0.780	42.941	21	0.042	4	8	9	0	0	0	0
R14	−7	83395	34585	0.498	0.253	35.311	9	0.011	9	0	0	0	0	0	0
R15	0	86400	37169	0.363	0.237	42.098	9	0.010	8	1	0	0	0	0	0
R16	−1	86400	35189	0.559	0.360	42.290	6	0.007	1	3	2	0	0	0	0
R17	4	86400	36851	3.052	0.375	39.816	19	0.022	16	3	0	0	0	0	0
R18	−3	86400	36631	0.377	0.251	38.424	1	0.001	0	1	0	0	0	0	0
R19	3	82103	27584	2.420	1.579	41.255	25	0.030	4	15	5	0	1	0	0
R20	2	55386	24732	0.936	0.641	42.638	22	0.040	2	7	13	0	0	0	0
R21	4	54178	30357	0.421	0.260	37.900	2	0.004	2	0	0	0	0	0	0
R22	−3	52364	29999	0.425	0.276	37.206	7	0.013	7	0	0	0	0	0	0
R23	3	82633	31894	1.795	0.438	33.630	17	0.021	14	3	0	0	0	0	0
R24	2	86400	35453	0.610	0.385	35.057	23	0.027	15	8	0	0	0	0	0

Figure A.1.21: Topcon analysis output file: GLONASS C2C signal, detailed results overview

Sat ID	Frequency Channel	n C2P Observations	n Epochs with Multipath Estimates	RMS Multipath [meters]	Weighted RMS Multipath [meters]	Average Sat. Elevation Angle [degrees]	n Slip Periods	Slip/Obs Ratio [%]	n Slip Periods Elevation Angle 0–10 degrees	n Slip Periods Elevation Angle 10–20 degrees	n Slip Periods Elevation Angle 20–30 degrees	n Slip Periods Elevation Angle 30–40 degrees	n Slip Periods Elevation Angle 40–50 degrees	n Slip Periods Elevation Angle >50 degrees	n Slip Periods Elevation Angle NaN degrees
R1	1	81835	30183	0.419	NaN	NaN	9	0.011	0	0	0	0	0	0	9
R2	−4	58352	30713	0.320	NaN	NaN	6	0.010	0	0	0	0	0	0	6
R3	5	60586	31603	0.308	NaN	NaN	9	0.015	0	0	0	0	0	0	9
R4	6	62057	32209	0.292	NaN	NaN	9	0.015	0	0	0	0	0	0	9
R5	1	81974	32385	0.307	NaN	NaN	8	0.010	0	0	0	0	0	0	8
R6	−4	53204	0	NaN	NaN	NaN	11	0.021	0	0	0	0	0	0	11
R7	5	86400	35309	0.336	0.201	54.582	3	0.003	1	0	0	0	0	0	2
R8	6	85683	34432	0.294	0.180	35.398	2	0.002	0	0	2	0	0	0	0
R9	−2	83383	33749	0.328	0.205	31.907	12	0.014	9	3	0	0	0	0	0
R10	−7	45787	0	NaN	NaN	NaN	11	0.024	0	0	0	0	0	0	11
R11	0	49799	30039	0.279	0.209	33.895	3	0.006	3	0	0	0	0	0	0
R12	−1	50157	30023	0.338	0.205	35.871	10	0.020	10	0	0	0	0	0	0
R13	−2	50467	24318	0.399	0.257	43.034	21	0.042	3	10	8	0	0	0	0
R14	−7	83395	34570	0.344	0.185	35.322	11	0.013	11	0	0	0	0	0	0
R15	0	86400	37178	0.294	0.173	42.088	7	0.008	6	1	0	0	0	0	0
R16	−1	86400	35185	0.418	0.293	42.297	6	0.007	2	2	2	0	0	0	0
R17	4	86400	36591	0.261	0.210	40.037	21	0.024	18	3	0	0	0	0	0
R18	−3	86400	36638	0.282	0.188	38.420	1	0.001	1	0	0	0	0	0	0
R19	3	82103	27368	0.290	0.211	41.444	29	0.035	6	16	6	0	1	0	0
R20	2	54760	24716	0.335	0.241	42.644	23	0.042	2	5	16	0	0	0	0
R21	4	54178	30369	0.342	0.200	37.886	4	0.007	4	0	0	0	0	0	0
R22	−3	52364	29984	0.322	0.216	37.229	4	0.008	4	0	0	0	0	0	0
R23	3	82623	31774	0.427	0.277	33.715	19	0.023	14	5	0	0	0	0	0
R24	2	86400	35429	0.387	0.294	35.074	15	0.017	7	8	0	0	0	0	0

Figure A.1.22: Topcon analysis output file: GLONASS C2P signal, detailed results overview

BeiDou

PRN	n C2X Observations	n Epochs with Multipath Estimates	RMS Multipath [meters]	Weighted RMS Multipath [meters]	Average Sat. Elevation Angle [degrees]	n Slip Periods	Slip/Obs Ratio [%]	n Slip Periods Elevation Angle 0–10 degrees	n Slip Periods Elevation Angle 10–20 degrees	n Slip Periods Elevation Angle 20–30 degrees	n Slip Periods Elevation Angle 30–40 degrees	n Slip Periods Elevation Angle 40–50 degrees	n Slip Periods Elevation Angle >50 degrees	n Slip Periods Elevation Angle NaN degrees
C5	1307	162	0.709	0.186	14.840	0	0.000	0	0	0	0	0	0	0
C6	27632	27631	0.537	0.331	24.584	0	0.000	0	0	0	0	0	0	0
C7	26520	26515	0.617	0.333	23.042	0	0.000	0	0	0	0	0	0	0
C8	86400	21157	0.553	0.376	28.093	0	0.000	0	0	0	0	0	0	0
C9	35419	35418	0.435	0.300	31.038	0	0.000	0	0	0	0	0	0	0
C10	34664	34658	0.462	0.314	29.830	2	0.006	2	0	0	0	0	0	0
C11	63801	28400	0.547	0.309	39.598	0	0.000	0	0	0	0	0	0	0
C12	86400	26988	0.529	0.299	28.502	0	0.000	0	0	0	0	0	0	0
C13	86400	35189	0.391	0.262	31.938	0	0.000	0	0	0	0	0	0	0
C14	70246	33968	0.492	0.319	27.558	2	0.003	2	0	0	0	0	0	0
C16	30275	30274	0.481	0.297	26.415	0	0.000	0	0	0	0	0	0	0
C19	63346	0	NaN	NaN	38.898	1	0.002	1	0	0	0	0	0	0
C20	57920	0	NaN	NaN	41.316	0	0.000	0	0	0	0	0	0	0
C21	67912	0	NaN	NaN	30.420	1	0.001	1	0	0	0	0	0	0
C22	65839	0	NaN	NaN	35.846	0	0.000	0	0	0	0	0	0	0
C23	54048	0	NaN	NaN	35.146	1	0.002	1	0	0	0	0	0	0
C25	82347	0	NaN	NaN	18.941	0	0.000	0	0	0	0	0	0	0
C27	3027	0	NaN	NaN	26.405	0	0.000	0	0	0	0	0	0	0
C28	62725	0	NaN	NaN	39.625	1	0.002	1	0	0	0	0	0	0
C29	57489	0	NaN	NaN	32.471	0	0.000	0	0	0	0	0	0	0
C30	59920	0	NaN	NaN	33.801	0	0.000	0	0	0	0	0	0	0
C32	86400	0	NaN	NaN	43.650	0	0.000	0	0	0	0	0	0	0
C33	69350	0	NaN	NaN	29.098	1	0.001	1	0	0	0	0	0	0
C34	61482	0	NaN	NaN	35.594	0	0.000	0	0	0	0	0	0	0
C35	49449	0	NaN	NaN	33.399	0	0.000	0	0	0	0	0	0	0
C36	58071	0	NaN	NaN	36.502	4	0.007	4	0	0	0	0	0	0
C37	55483	0	NaN	NaN	33.448	1	0.002	1	0	0	0	0	0	0

Figure A.1.23: Topcon analysis output file: BeiDou C2X signal, detailed results overview

PRN	n C7X Observations	n Epochs with Multipath Estimates	RMS Multipath [meters]	Weighted RMS Multipath [meters]	Average Sat. Elevation Angle [degrees]	n Slip Periods	Slip/Obs Ratio [%]	n Slip Periods Elevation Angle 0–10 degrees	n Slip Periods Elevation Angle 10–20 degrees	n Slip Periods Elevation Angle 20–30 degrees	n Slip Periods Elevation Angle 30–40 degrees	n Slip Periods Elevation Angle 40–50 degrees	n Slip Periods Elevation Angle >50 degrees	n Slip Periods Elevation Angle NaN degrees
C5	1307	162	0.147	0.038	14.840	1	0.077	0	1	0	0	0	0	0
C6	27632	27631	0.526	0.361	24.584	0	0.000	0	0	0	0	0	0	0
C7	26520	26515	0.552	0.319	23.042	3	0.011	3	0	0	0	0	0	0
C8	86400	21157	0.451	0.333	28.093	0	0.000	0	0	0	0	0	0	0
C9	35419	35418	0.465	0.302	31.038	0	0.000	0	0	0	0	0	0	0
C10	34664	34658	0.505	0.326	29.830	3	0.009	3	0	0	0	0	0	0
C11	63801	28398	0.459	0.290	39.598	0	0.000	0	0	0	0	0	0	0
C12	86400	26988	0.533	0.284	28.502	0	0.000	0	0	0	0	0	0	0
C13	86400	35189	0.485	0.325	31.938	0	0.000	0	0	0	0	0	0	0
C14	70246	33967	0.439	0.317	27.558	3	0.004	3	0	0	0	0	0	0
C16	30275	30274	0.520	0.370	26.415	0	0.000	0	0	0	0	0	0	0
C19	57322	0	NaN	NaN	35.322	9	0.016	2	3	0	0	1	3	0
C20	53474	0	NaN	NaN	30.437	16	0.030	4	6	1	0	1	4	0
C21	56114	0	NaN	NaN	35.288	9	0.016	2	1	3	0	0	3	0
C22	60816	0	NaN	NaN	25.643	6	0.010	2	3	0	0	0	1	0
C23	49772	0	NaN	NaN	32.496	10	0.020	2	2	1	1	1	3	0
C25	1	0	NaN	NaN	8.679	0	0.000	0	0	0	0	0	0	0
C28	24444	0	NaN	NaN	38.892	6	0.025	1	1	0	1	1	2	0
C29	45999	0	NaN	NaN	34.959	7	0.015	3	1	1	1	0	1	0
C30	54597	0	NaN	NaN	41.120	10	0.018	2	1	2	0	1	4	0

Figure A.1.24: Topcon analysis output file: BeiDou C7X signal, detailed results overview

A.1.5 Plotted Results

GPS

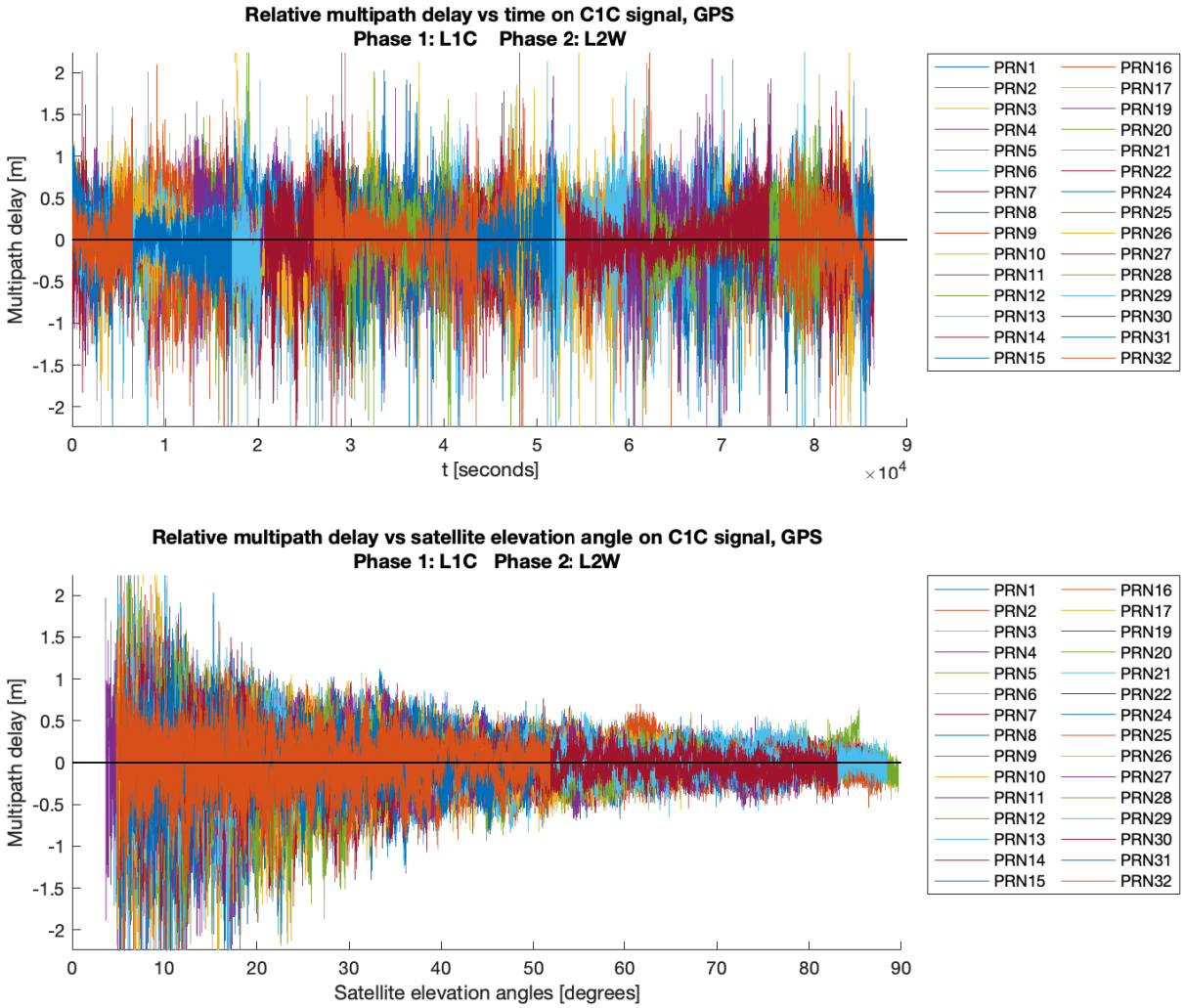

Figure A.1.25: Topcon analysis results graph: GPS C1C signal, multipath effect vs. time and vs. satellite elevation angle. Graph has been cropped along y axis.

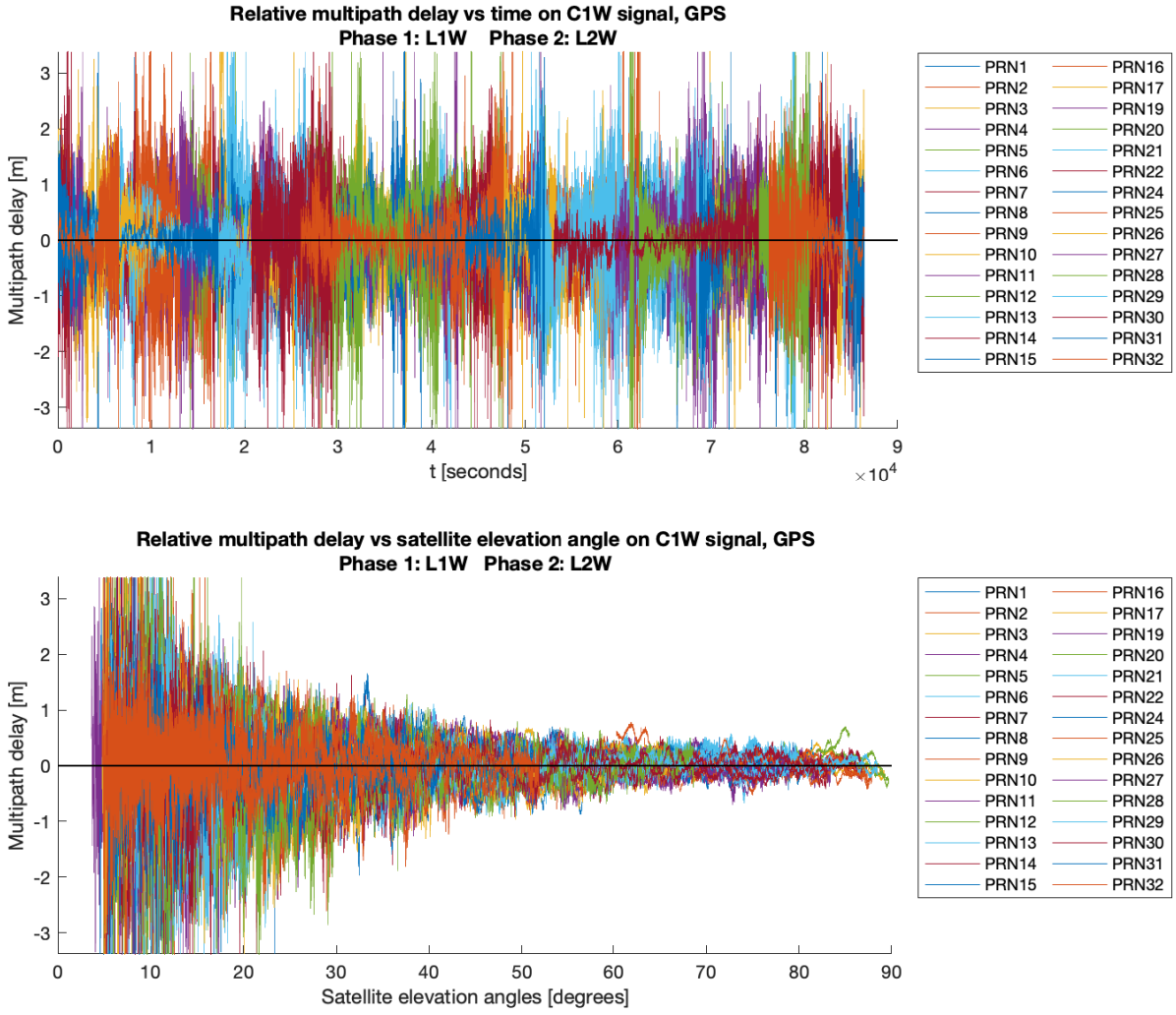

Figure A.1.26: Topcon analysis results graph: GPS C1W signal, multipath effect vs. time and vs. satellite elevation angle. Graph has been cropped along y axis.

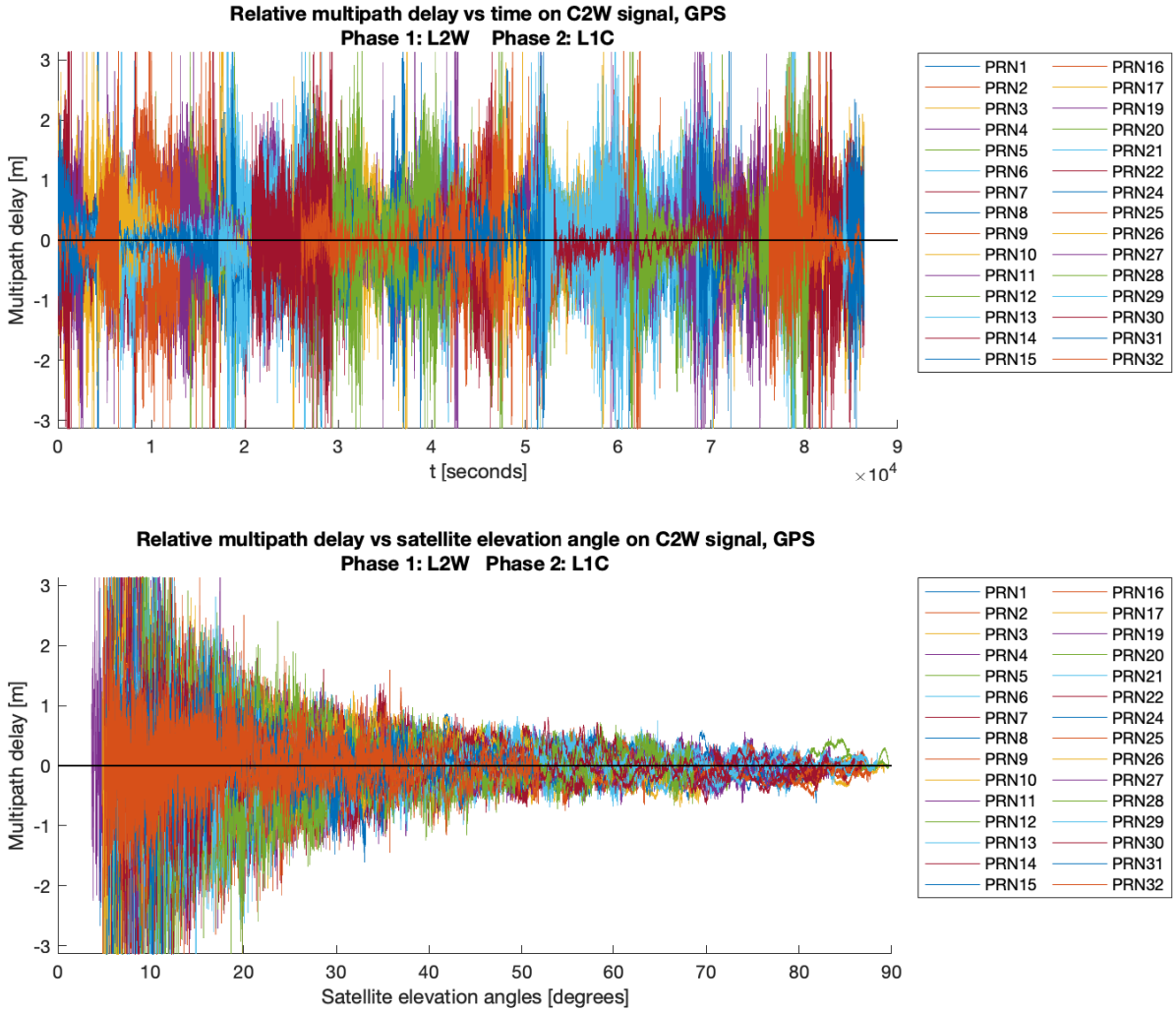

Figure A.1.27: Topcon analysis results graph: GPS C2W signal, multipath effect vs. time and vs. satellite elevation angle. Graph has been cropped along y axis.

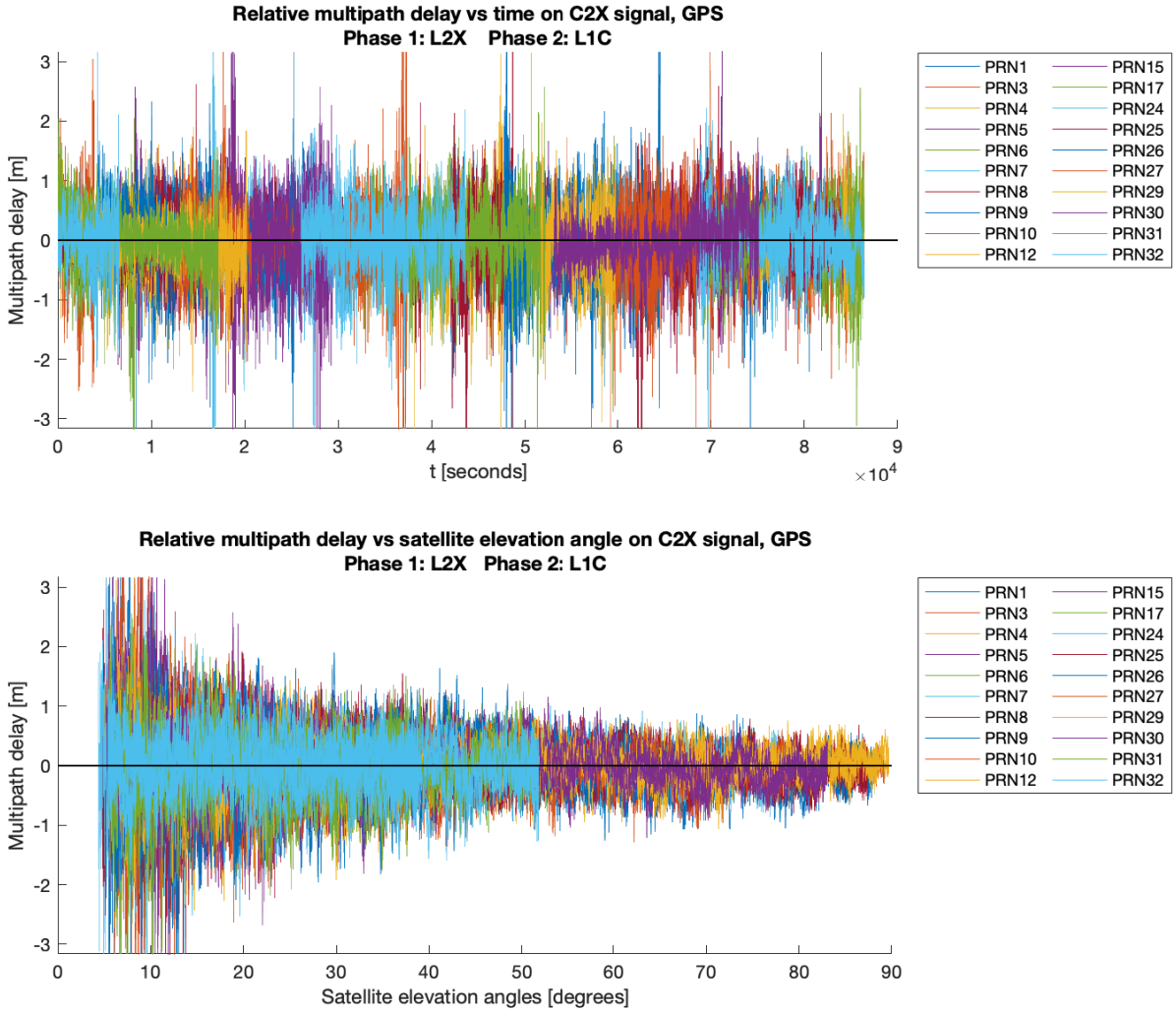

Figure A.1.28: Topcon analysis results graph: GPS C2X signal, multipath effect vs. time and vs. satellite elevation angle. Graph has been cropped along y axis.

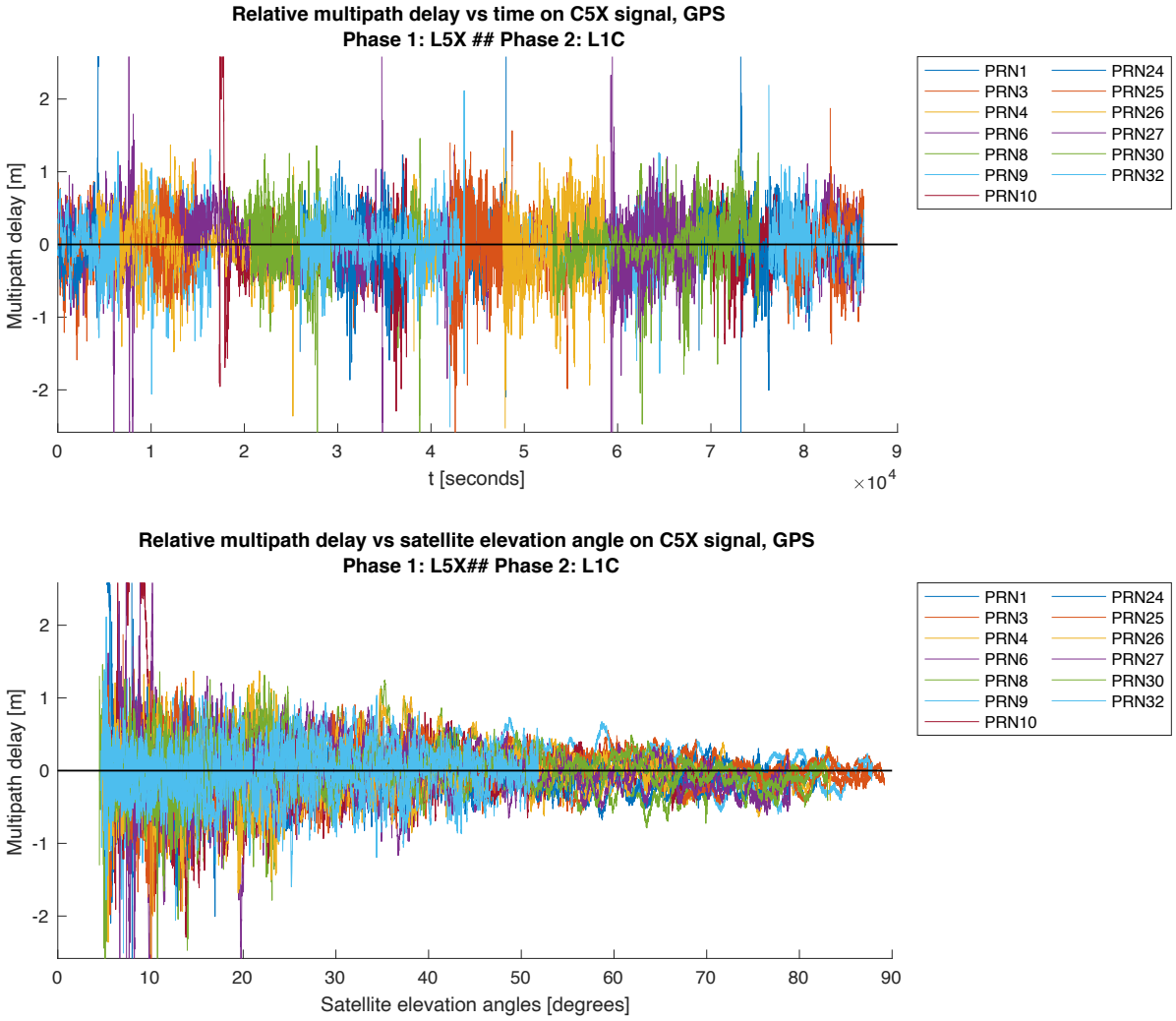

Figure A.1.29: Topcon analysis results graph: GPS C5X signal, multipath effect vs. time and vs. satellite elevation angle. Graph has been cropped along y axis.

Galileo

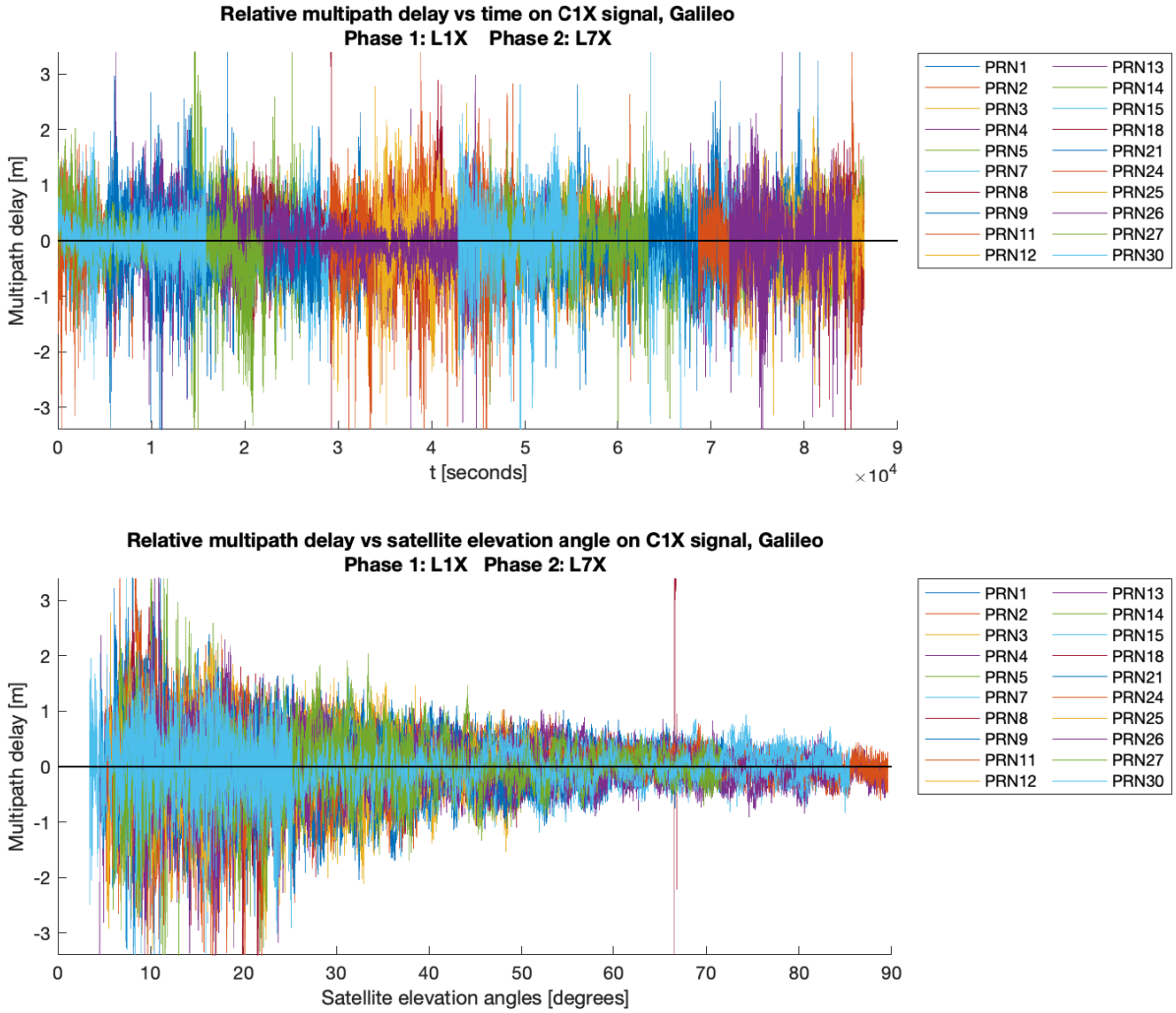

Figure A.1.30: Topcon analysis results graph: Galileo C1X signal, multipath effect vs. time and vs. satellite elevation angle. Graph has been cropped along y axis.

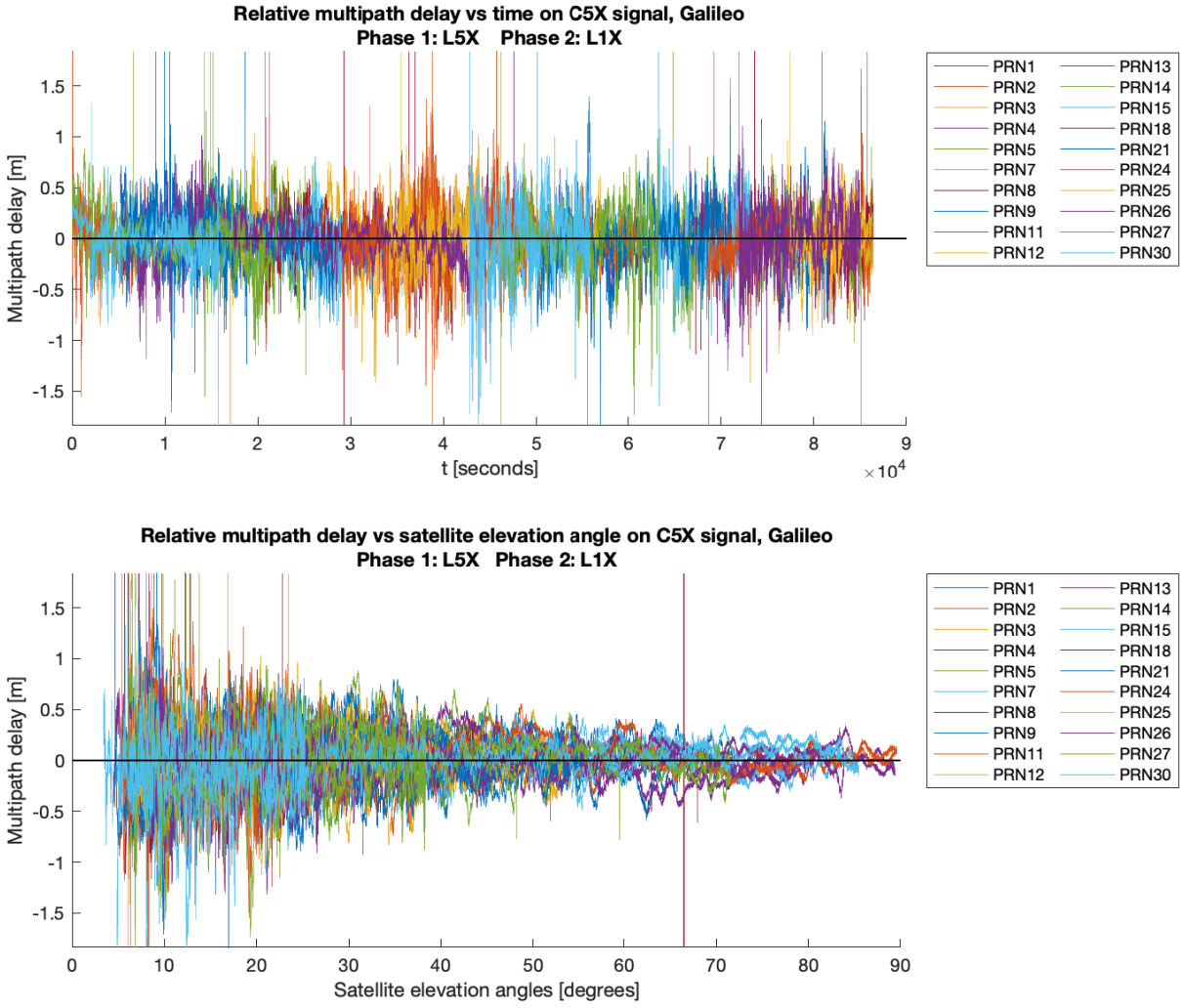

Figure A.1.31: Topcon analysis results graph: Galileo C5X signal, multipath effect vs. time and vs. satellite elevation angle. Graph has been cropped along y axis.

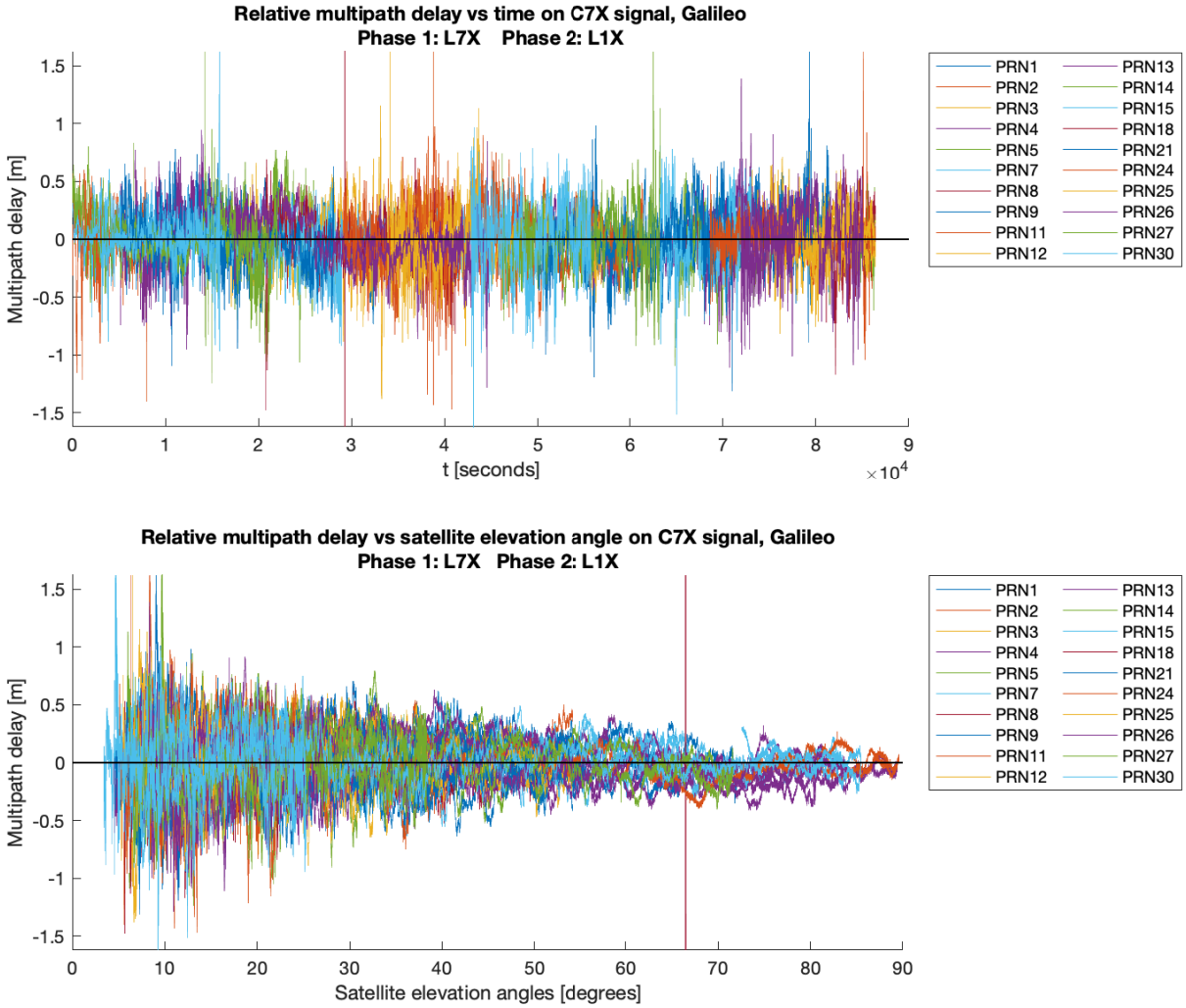

Figure A.1.32: Topcon analysis results graph: Galileo C7X signal, multipath effect vs. time and vs. satellite elevation angle. Graph has been cropped along y axis.

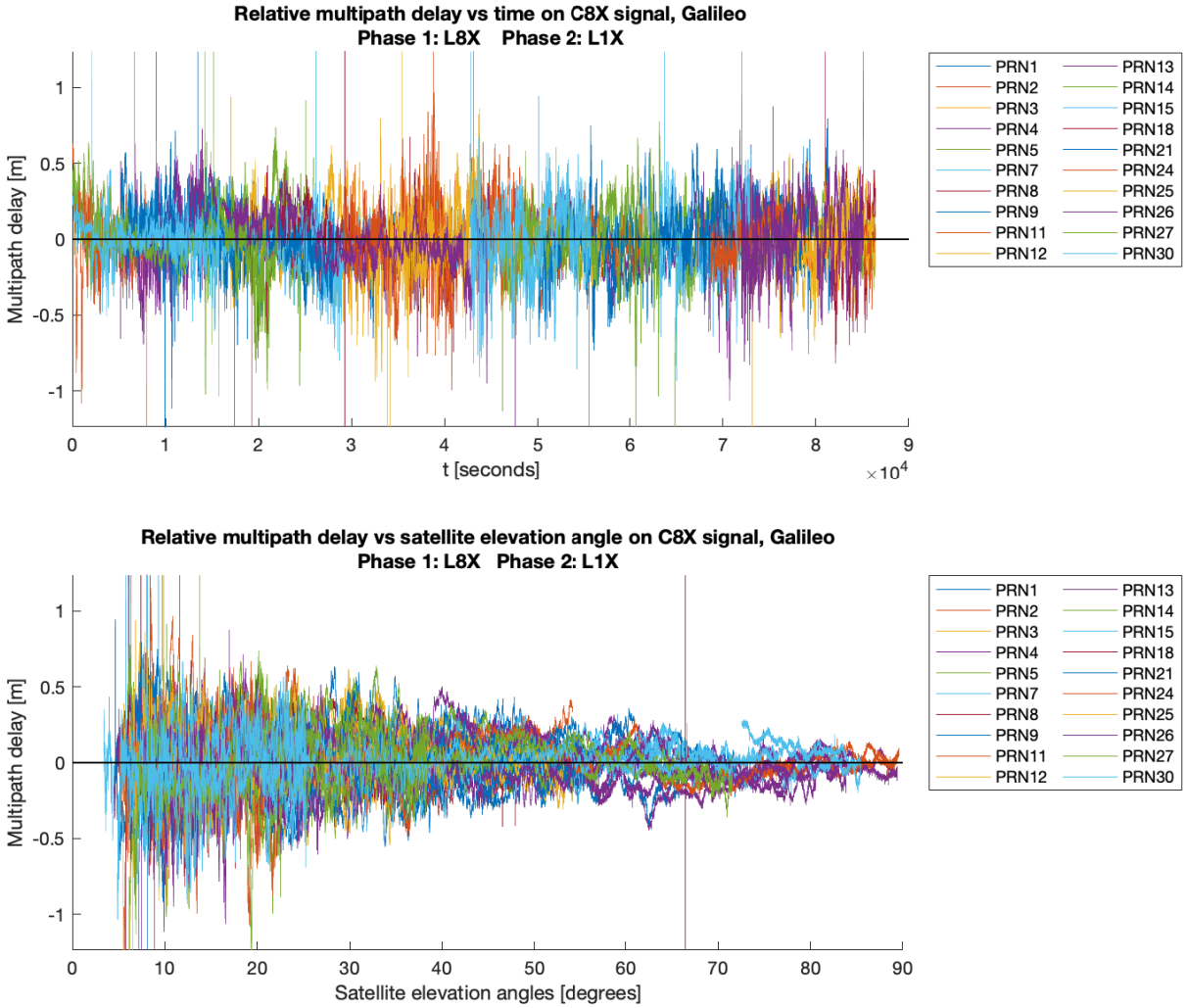

Figure A.1.33: Topcon analysis results graph: Galileo C8X signal, multipath effect vs. time and vs. satellite elevation angle. Graph has been cropped along y axis.

GLONASS

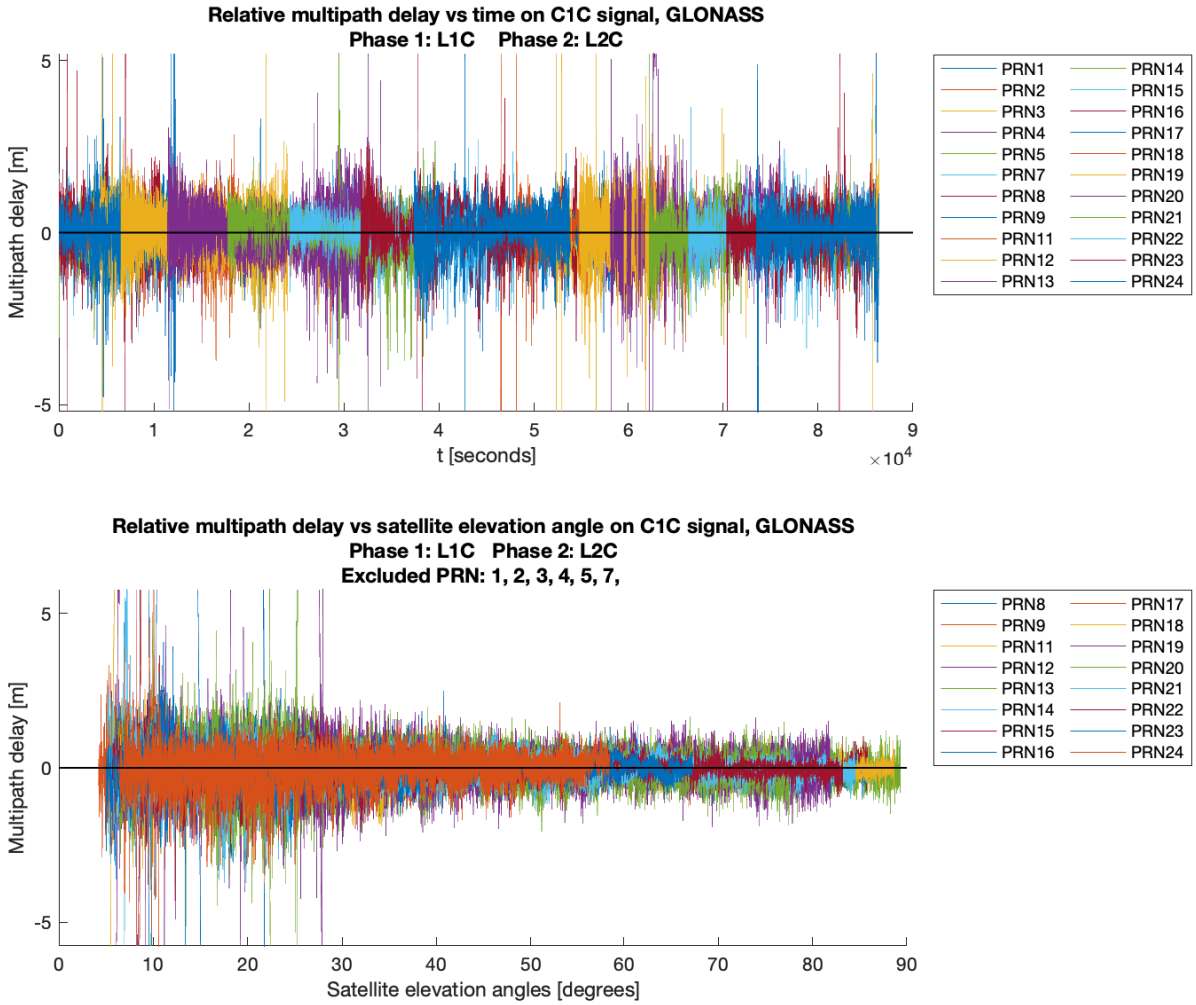

Figure A.1.34: Topcon analysis results graph: GLONASS C1C signal, multipath effect vs. time and vs. satellite elevation angle. Graph has been cropped along y axis.

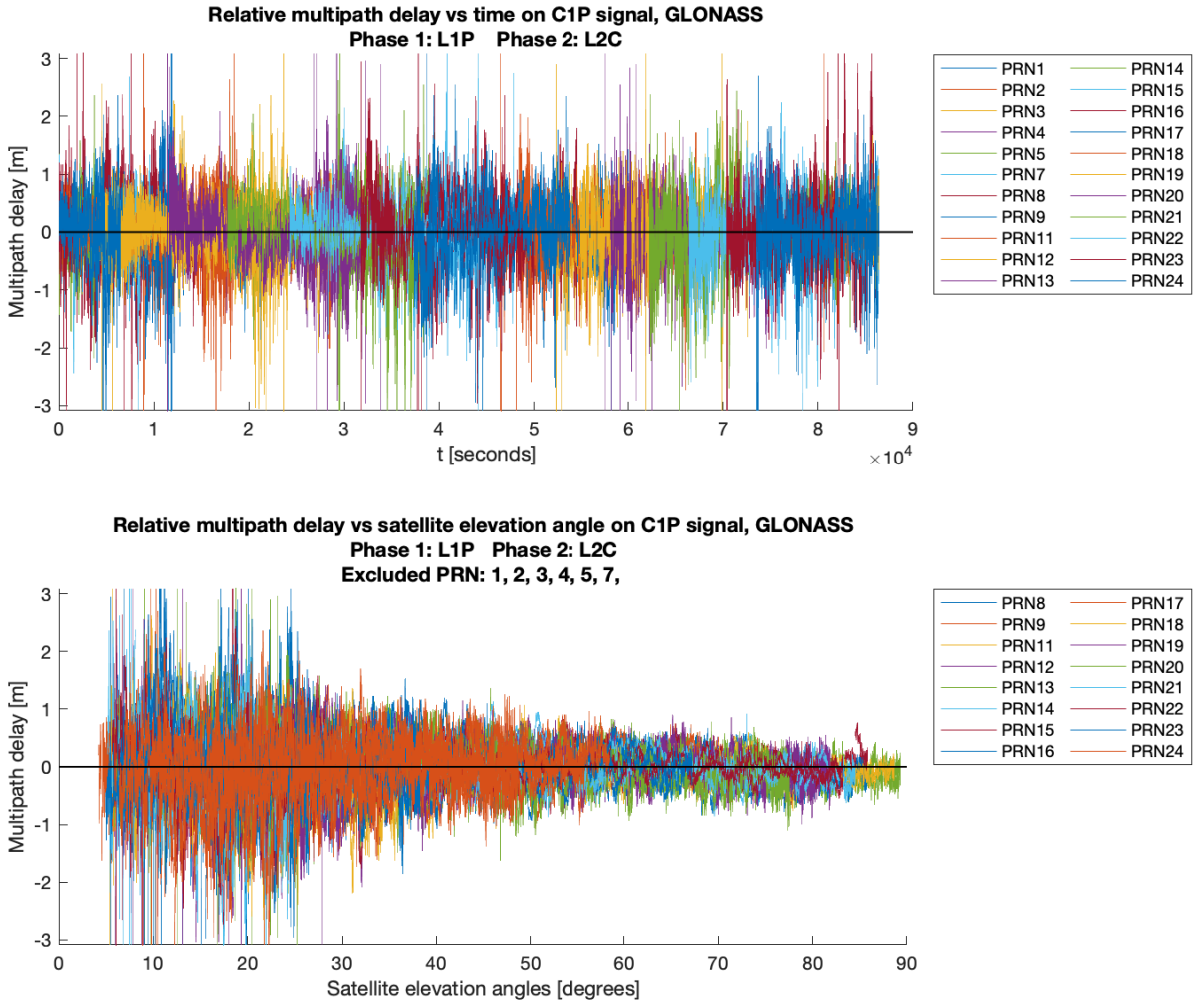

Figure A.1.35: Topcon analysis results graph: GLONASS C1P signal, multipath effect vs. time and vs. satellite elevation angle. Graph has been cropped along y axis.

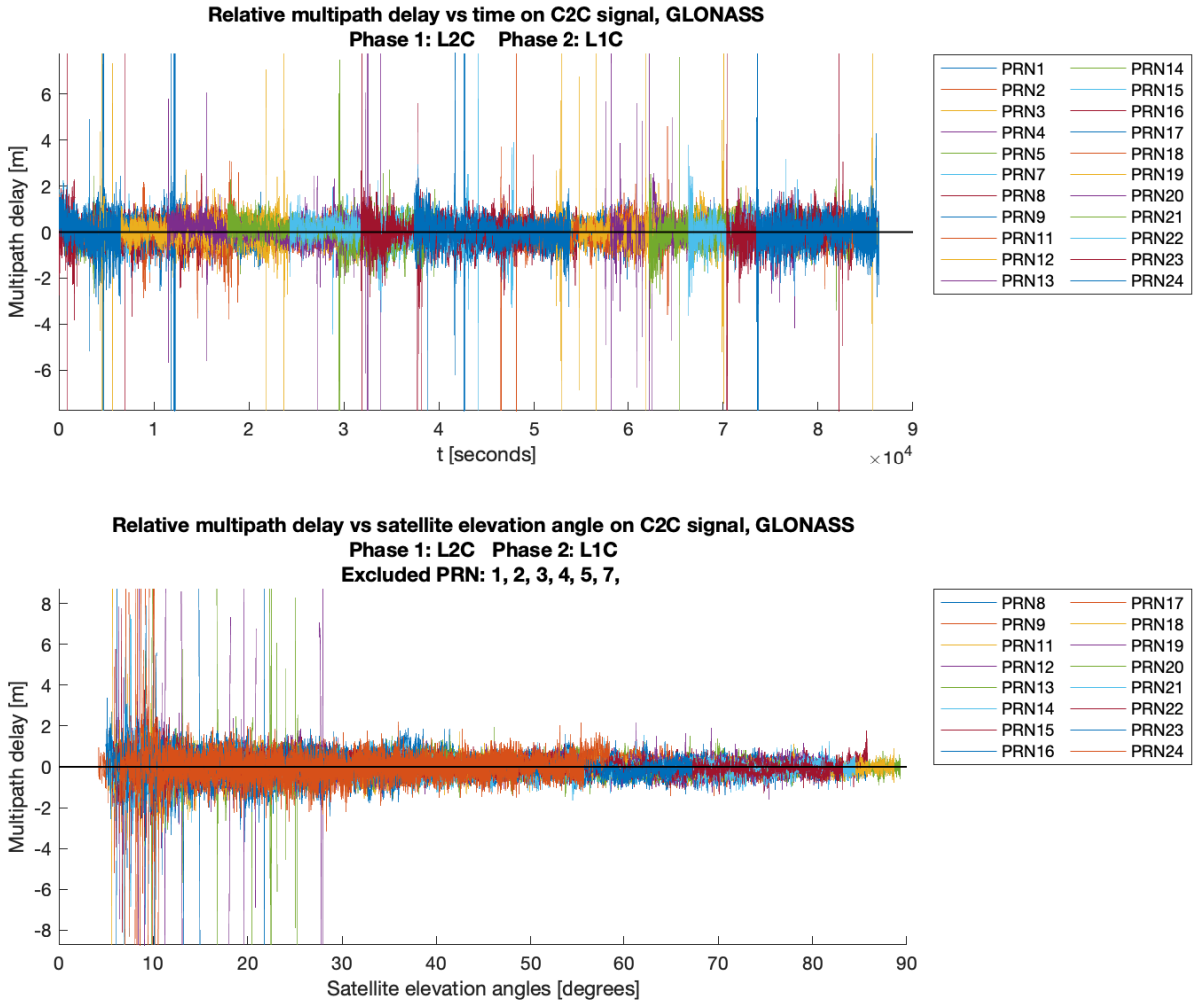

Figure A.1.36: Topcon analysis results graph: GLONASS C2C signal, multipath effect vs. time and vs. satellite elevation angle. Graph has been cropped along y axis.

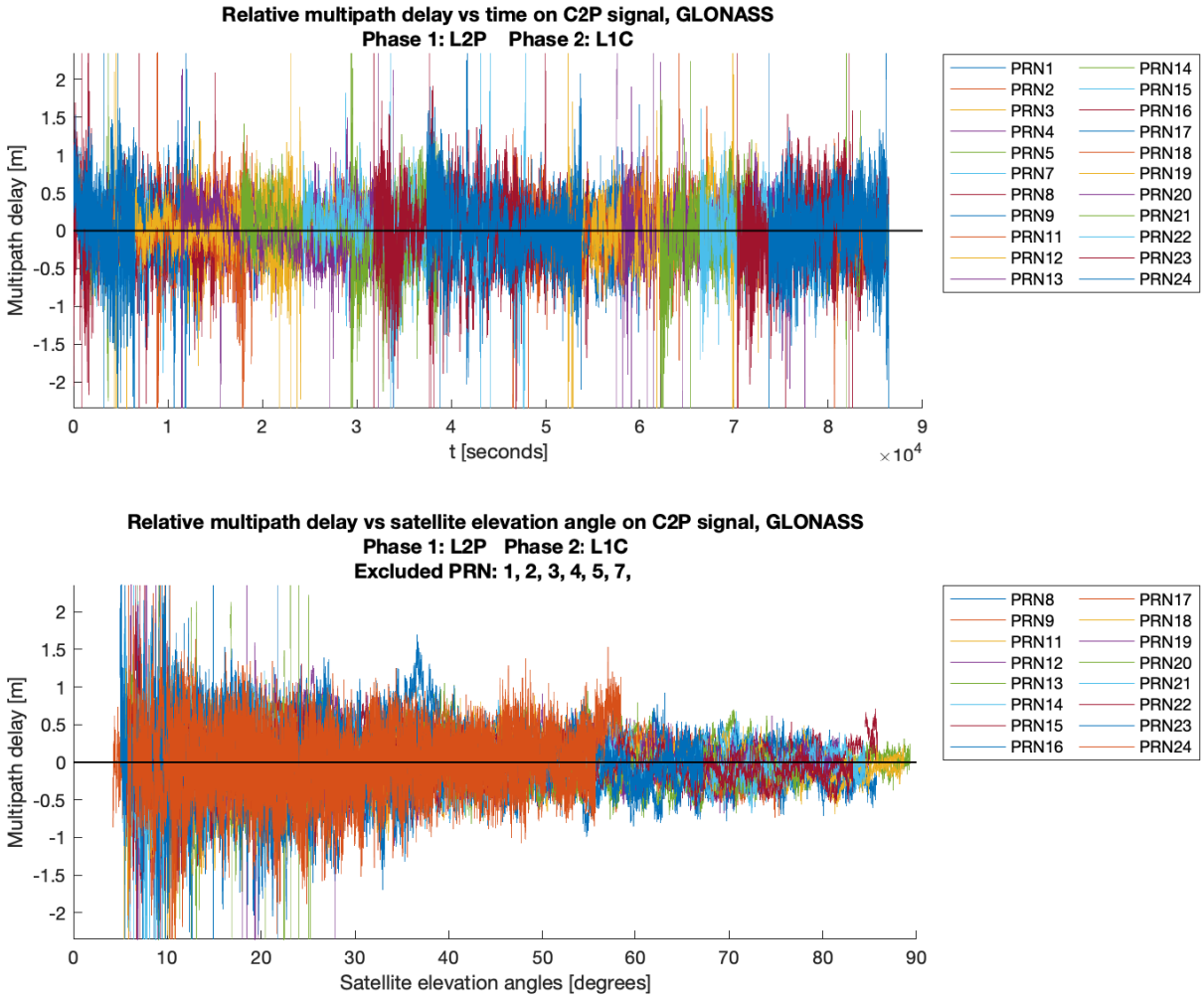

Figure A.1.37: Topcon analysis results graph: GLONASS C2P signal, multipath effect vs. time and vs. satellite elevation angle. Graph has been cropped along y axis.

BeiDou

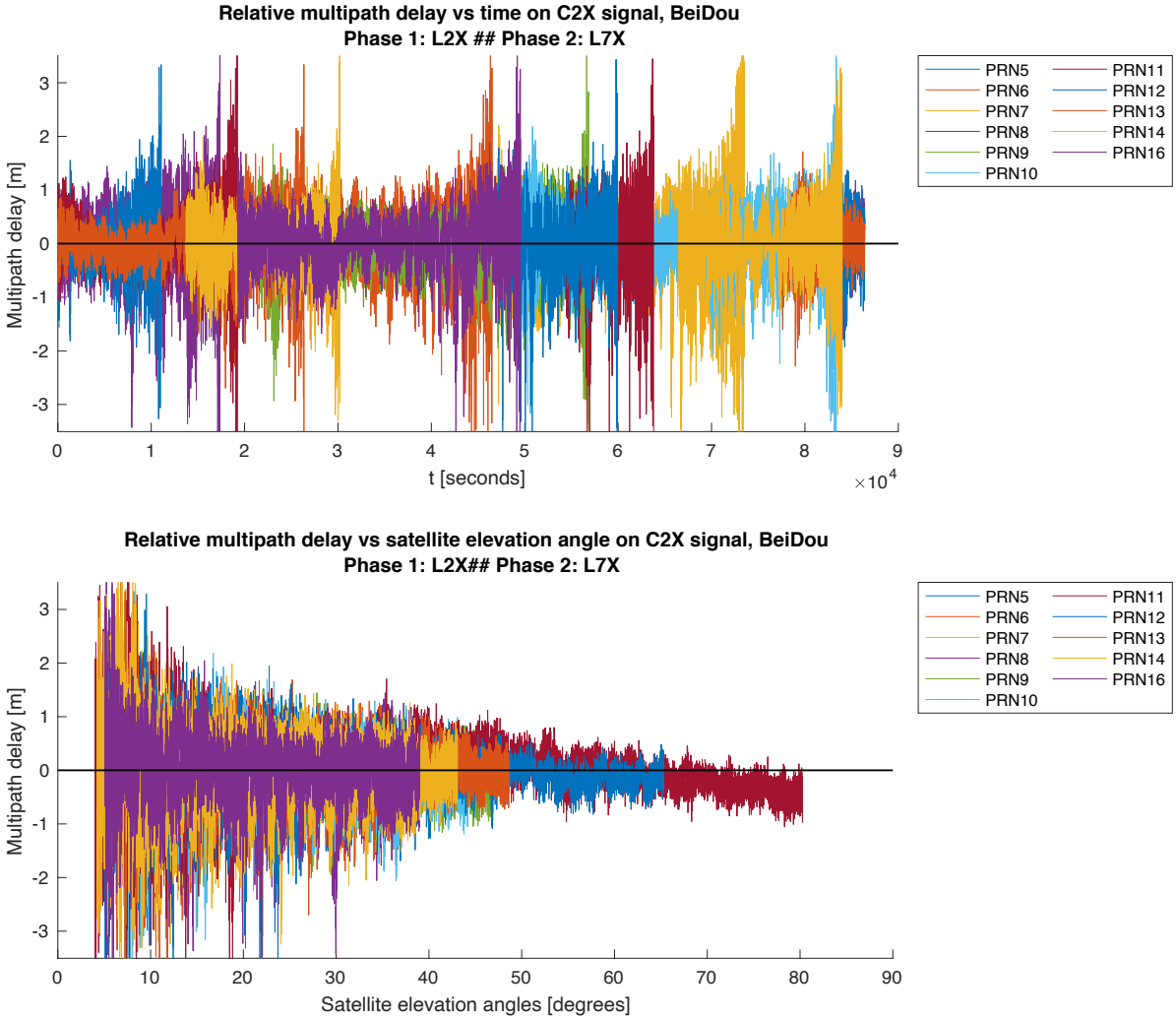

Figure A.1.38: Topcon analysis results graph: BeiDou C2X signal, multipath effect vs. time and vs. satellite elevation angle. Graph has been cropped along y axis.

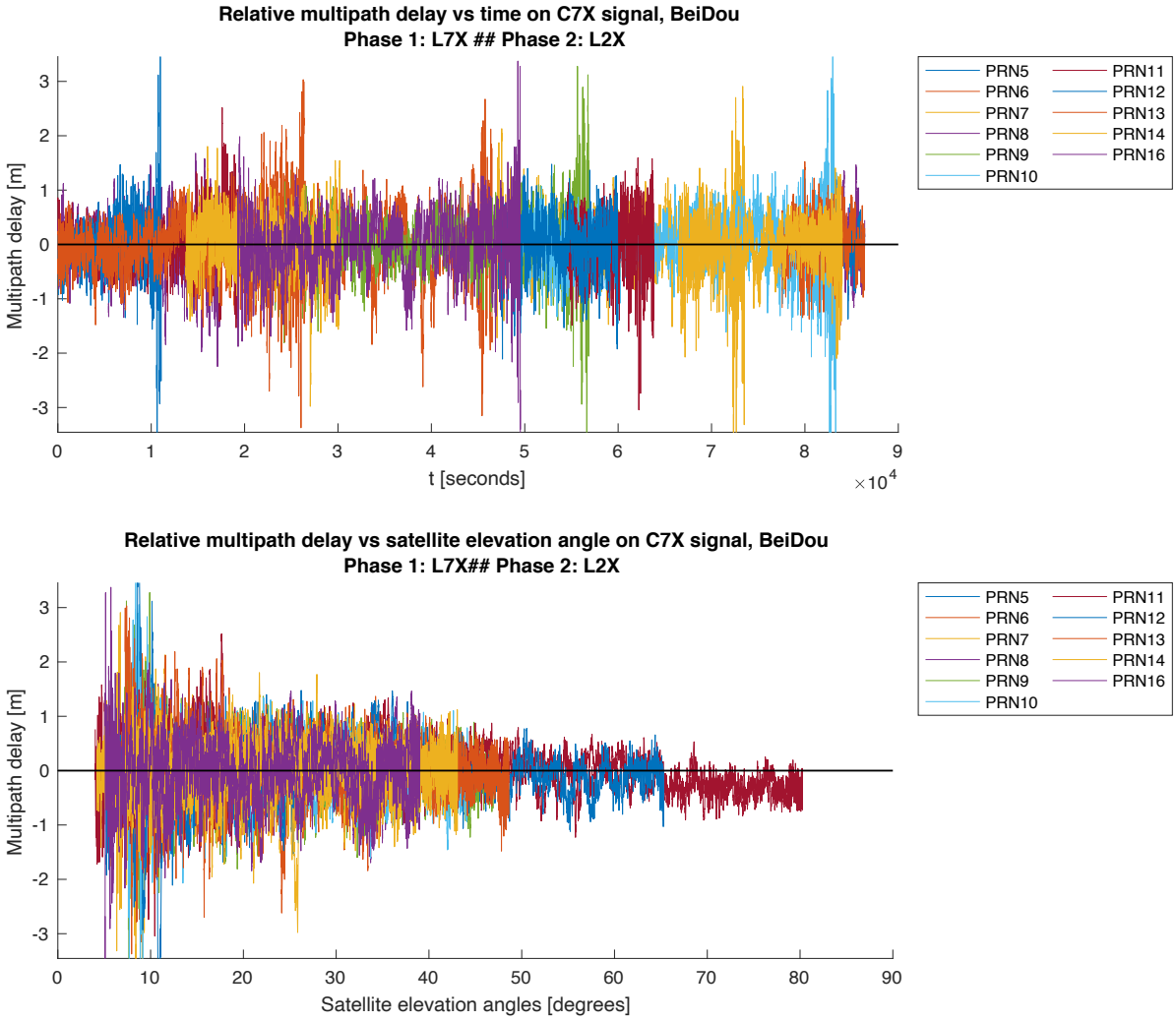

Figure A.1.39: Topcon analysis results graph: BeiDou C7X signal, multipath effect vs. time and vs. satellite elevation angle. Graph has been cropped along y axis.

A.2 Emlid Reach RS2

A.2.1 Header

```
GNSS Receiver Quality Check 2020
Software version: 1.00
Last software version release: 02/06/2020

Software developed by Bjørn-Eirik Roald
Norwegian University of Life Sciences(NMBU)

RINEX observation filename:      FLO300XXX_R_20200901220_01D_01S_MO.rnx
RINEX version:                   3.04
RINEX converting program:        CONVBIN 2.4.3 Emlid
Marker name:                     FLO3
Receiver type:                   Emlid Reach RS2
Date of observation start:       2020/3/30 12:20:7.99
Date of observation end:         2020/3/31 12:19:59.99
Observation interval [seconds]:  1
Number of receiver clock jumps:  28
Average clock jumps interval:    00:50:57 (std: 1210.85 seconds)

Critical cycle slip limits [m/s]:
- Ionospheric delay:             0.067
- Phase-code combination:        6.667

GNSS systems presents in RINEX observation file:
- BeiDou
- Galileo
- GPS
- GLONASS


User-specified contend included in output file
- Include overview of observations for each satellite:          Yes
- Include compact summary of analysis estimates:                Yes
- Include detailed summary of analysis
   estimates, including for each individual satellite:          Yes
- Include information about "Loss-of-Lock"
   indicators in detailed summary:                              No
```

Figure A.2.1: Emlid analysis output file: Header

A.2.2 Observation Overview

GPS Observation overview

PRN	L1 Observations	L2 Observations	L5 Observations
G1	C1C	C2X	
G2	C1C		
G3	C1C	C2X	
G4	C1C	C2X	
G5	C1C	C2X	
G6	C1C	C2X	
G7	C1C	C2X	
G8	C1C	C2X	
G9	C1C	C2X	
G10	C1C	C2X	
G11	C1C		
G12	C1C	C2X	
G13	C1C		
G14	C1C		
G15	C1C	C2X	
G16	C1C		
G17	C1C	C2X	
G18	C1C	C2X	
G19	C1C		
G20	C1C		
G21	C1C		
G22	C1C		
G23	C1C		
G24	C1C	C2X	
G25	C1C	C2X	
G26	C1C	C2X	
G27	C1C	C2X	
G28	C1C		
G29	C1C	C2X	
G30	C1C	C2X	
G31	C1C	C2X	
G32	C1C	C2X	

Figure A.2.2: Emlid analysis output file: GPS observation overview

Galileo Observation overview

PRN	E1 Observations	E5a Observations	E6 Observations	E5b Observations	G5(a+b) Observations
E1	C1X			C7X	
E2	C1X			C7X	
E3	C1X			C7X	
E4	C1X			C7X	
E5	C1X			C7X	
E7	C1X			C7X	
E8	C1X			C7X	
E9	C1X			C7X	
E11	C1X			C7X	
E12	C1X			C7X	
E13	C1X			C7X	
E14	C1X			C7X	
E15	C1X			C7X	
E18	C1X			C7X	
E20	C1X				
E21	C1X			C7X	
E24	C1X			C7X	
E25	C1X			C7X	
E26	C1X			C7X	
E27	C1X			C7X	
E30	C1X			C7X	
E31	C1X			C7X	
E33	C1X			C7X	
E36	C1X			C7X	

Figure A.2.3: Emlid analysis output file: Galileo observation overview

GLONASS Observation overview

Sat ID	Frequency Channel	G1 Observations	G2 Observations	G3 Observations	G1a Observations	G2a Observations
R1	1	C1C	C2C			
R2	-4	C1C	C2C			
R3	5	C1C	C2C			
R4	6	C1C	C2C			
R5	1	C1C	C2C			
R6	-4	C1C				
R7	5	C1C	C2C			
R8	6	C1C	C2C			
R9	-2	C1C	C2C			
R10	-7	C1C				
R11	0	C1C	C2C			
R12	-1	C1C	C2C			
R13	-2	C1C	C2C			
R14	-7	C1C	C2C			
R15	0	C1C	C2C			
R16	-1	C1C	C2C			
R17	4	C1C	C2C			
R18	-3	C1C	C2C			
R19	3	C1C	C2C			
R20	2	C1C	C2C			
R21	4	C1C	C2C			
R22	-3	C1C	C2C			
R23	3	C1C	C2C			
R24	2	C1C	C2C			

Figure A.2.4: Emlid analysis output file: GLONASS observation overview

BeiDou Observation overview

PRN	B1 Observations	E1-2 Observations	B2a Observations	B3 Observations	B2b Observations	B2(a+b) Observations
C6		C2I			C7I	
C7		C2I			C7I	
C8		C2I			C7I	
C9		C2I			C7I	
C10		C2I			C7I	
C11		C2I			C7I	
C12		C2I			C7I	
C13		C2I			C7I	
C14		C2I			C7I	
C16		C2I			C7I	
C19		C2I				
C20		C2I				
C21		C2I				
C22		C2I				
C23		C2I				
C24		C2I				
C25		C2I				
C26		C2I				
C27		C2I				
C28		C2I				
C29		C2I				
C30		C2I				
C32		C2I				
C33		C2I				
C34		C2I				
C35		C2I				
C36		C2I				
C37		C2I				

Figure A.2.5: Emlid analysis output file: BeiDou observation overview

A.2.3 Compressed Results Overview

GPS ANALYSIS SUMMARY

	C1C	C2X
RMS multipath[meters]	0.464	0.578
Weighted RMS multipath[meters]	0.398	0.499
N ambiguity slips periods	7437	14742
N slip periods, elevation angle > 10 degrees	4954	13441
N slip periods, elevation angle < 10 degrees	2483	1301
N slip periods, elevation angle not computed	0	0
Ratio of N slip periods/N obs epochs [%]	0.333	1.002

Figure A.2.6: Emlid analysis output file: GPS compressed results overview

GALILEO ANALYSIS SUMMARY

	C1X	C7X
RMS multipath[meters]	0.735	0.448
Weighted RMS multipath[meters]	0.572	0.386
N ambiguity slips periods	4963	6204
N slip periods, elevation angle > 10 degrees	3401	5142
N slip periods, elevation angle < 10 degrees	1216	1062
N slip periods, elevation angle not computed	346	0
Ratio of N slip periods/N obs epochs [%]	0.313	0.408

Figure A.2.7: Emlid analysis output file: Galileo compressed results overview

GLONASS ANALYSIS SUMMARY

	C1C	C2C
RMS multipath[meters]	0.527	0.796
Weighted RMS multipath[meters]	0.455	0.654
N ambiguity slips periods	2740	12615
N slip periods, elevation angle > 10 degrees	1451	8654
N slip periods, elevation angle < 10 degrees	654	650
N slip periods, elevation angle not computed	635	3311
Ratio of N slip periods/N obs epochs [%]	0.158	0.803

Figure A.2.8: Emlid analysis output file: GLONASS compressed results overview

BEIDOU ANALYSIS SUMMARY

	C2I	C7I
RMS multipath[meters]	0.531	0.347
Weighted RMS multipath[meters]	0.446	0.290
N ambiguity slips periods	3142	2544
N slip periods, elevation angle > 10 degrees	2213	1744
N slip periods, elevation angle < 10 degrees	929	800
N slip periods, elevation angle not computed	0	0
Ratio of N slip periods/N obs epochs [%]	0.214	0.461

Figure A.2.9: Emlid analysis output file: BeiDou compressed results overview

A.2.4 Detailed Results Overview

GPS

PRN	n C1C Observations	n Epochs with Multipath Estimates	RMS Multipath [meters]	Weighted RMS Multipath [meters]	Average Sat. Elevation Angle [degrees]	n Slip Periods	Slip/Obs Ratio [%]	n Slip Periods Elevation Angle 0–10 degrees	n Slip Periods Elevation Angle 10–20 degrees	n Slip Periods Elevation Angle 20–30 degrees	n Slip Periods Elevation Angle 30–40 degrees	n Slip Periods Elevation Angle 40–50 degrees	n Slip Periods Elevation Angle >50 degrees	n Slip Periods Elevation Angle NaN degrees
G1	56288	17918	0.420	0.409	37.763	360	0.640	79	271	10	0	0	0	0
G2	86393	0	NaN	NaN	29.213	63	0.073	47	16	0	0	0	0	0
G3	86379	21804	0.483	0.437	39.852	491	0.568	97	394	0	0	0	0	0
G4	55021	21852	0.503	0.426	37.239	202	0.367	52	150	0	0	0	0	0
G5	65417	21075	0.493	0.451	30.983	108	0.165	73	35	0	0	0	0	0
G6	86393	28948	0.682	0.440	30.546	103	0.119	55	48	0	0	0	0	0
G7	54330	19009	0.342	0.326	35.109	147	0.271	84	63	0	0	0	0	0
G8	54426	21837	0.413	0.382	33.583	254	0.467	101	141	12	0	0	0	0
G9	56094	21269	0.486	0.422	39.379	476	0.849	198	278	0	0	0	0	0
G10	65546	25398	0.574	0.464	33.492	78	0.119	49	29	0	0	0	0	0
G11	55359	0	NaN	NaN	36.336	326	0.589	95	227	4	0	0	0	0
G12	86393	18261	0.363	0.335	39.511	519	0.601	96	423	0	0	0	0	0
G13	61968	0	NaN	NaN	37.338	424	0.684	92	318	14	0	0	0	0
G14	86393	0	NaN	NaN	31.241	182	0.211	53	129	0	0	0	0	0
G15	64353	16939	0.393	0.375	32.005	187	0.291	60	107	20	0	0	0	0
G16	54236	0	NaN	NaN	32.572	126	0.232	30	95	1	0	0	0	0
G17	86312	22902	0.360	0.342	30.057	51	0.059	38	4	9	0	0	0	0
G18	64973	27017	0.452	0.381	34.135	164	0.252	60	101	3	0	0	0	0
G19	86393	0	NaN	NaN	30.790	119	0.138	72	43	4	0	0	0	0
G20	65737	0	NaN	NaN	32.407	224	0.341	102	109	13	0	0	0	0
G21	64086	0	NaN	NaN	36.986	120	0.187	29	91	0	0	0	0	0
G22	86390	0	NaN	NaN	39.664	468	0.542	113	355	0	0	0	0	0
G23	54436	0	NaN	NaN	38.355	70	0.129	17	53	0	0	0	0	0
G24	86393	17951	0.462	0.436	38.272	292	0.338	60	196	36	0	0	0	0
G25	86393	20269	0.349	0.306	39.204	418	0.484	117	301	0	0	0	0	0
G26	54600	21726	0.418	0.374	32.775	180	0.330	118	59	3	0	0	0	0
G27	55575	19273	0.406	0.384	36.994	346	0.623	68	274	4	0	0	0	0
G28	54216	0	NaN	NaN	33.980	290	0.535	93	181	16	0	0	0	0
G29	86393	18911	0.395	0.361	38.237	202	0.234	61	141	0	0	0	0	0
G30	55115	19887	0.639	0.522	37.260	195	0.354	47	148	0	0	0	0	0
G31	86393	22764	0.373	0.329	29.534	112	0.130	96	16	0	0	0	0	0
G32	86393	27649	0.406	0.364	29.582	140	0.162	131	9	0	0	0	0	0

Figure A.2.10: Emlid analysis output file: GPS C1C signal, detailed results overview

	n C2X	n Epochs with	RMS	Weighted RMS	Average Sat.		Slip/Obs	n Slip Periods	n Slip Periods	n Slip Periods	n Slip Periods	n Slip Periods	n Slip Periods	n Slip Periods
PRN	Observations	Multipath Estimates	Multipath [meters]	Multipath [meters]	Elevation Angle [degrees]	n Slip Periods	Ratio [%]	Elevation Angle 0–10 degrees	Elevation Angle 10–20 degrees	Elevation Angle 20–30 degrees	Elevation Angle 30–40 degrees	Elevation Angle 40–50 degrees	Elevation Angle >50 degrees	Elevation Angle NaN degrees
G1	55470	17918	0.610	0.583	38.268	456	0.822	30	252	101	22	8	43	0
G3	86393	21804	0.538	0.484	40.787	296	0.343	81	90	93	32	0	0	0
G4	54264	21851	0.763	0.655	37.596	583	1.074	99	416	43	25	0	0	0
G5	64454	21074	0.667	0.586	31.354	1041	1.615	60	320	515	128	5	13	0
G6	86393	28948	0.570	0.476	30.407	446	0.516	84	167	121	74	0	0	0
G7	53868	19008	0.529	0.422	35.932	1082	2.009	51	485	355	96	37	58	0
G8	54428	21837	0.518	0.448	33.762	734	1.349	50	357	302	24	1	0	0
G9	55664	21269	0.661	0.597	40.154	216	0.388	34	65	92	24	1	0	0
G10	64744	25397	0.654	0.491	33.839	525	0.811	45	292	179	9	0	0	0
G12	86393	18261	0.587	0.526	41.900	702	0.813	22	138	194	127	48	173	0
G15	63902	16937	0.597	0.505	32.395	1394	2.181	52	505	453	62	33	289	0
G17	86333	22902	0.433	0.378	30.227	1169	1.354	78	289	478	253	71	0	0
G18	64499	27017	0.526	0.433	34.316	463	0.718	89	272	72	30	0	0	0
G24	86393	17950	0.507	0.478	37.672	413	0.478	43	222	100	23	0	25	0
G25	86393	20269	0.478	0.438	40.714	456	0.528	100	172	79	29	31	45	0
G26	52594	21726	0.585	0.498	33.295	863	1.641	54	460	337	10	2	0	0
G27	54969	19272	0.522	0.472	36.777	610	1.110	11	465	68	57	0	9	0
G29	86393	18911	0.526	0.498	39.241	706	0.817	97	291	138	97	36	47	0
G30	54303	19887	0.698	0.619	37.763	708	1.304	60	424	86	127	1	10	0
G31	86393	22762	0.490	0.397	29.778	1322	1.530	99	387	298	281	50	207	0
G32	86393	27646	0.566	0.457	29.760	557	0.645	62	263	154	66	12	0	0

Figure A.2.11: Emlid analysis output file: GPS C2X signal, detailed results overview

Galileo

PRN	n C1X Observations	n Epochs with Multipath Estimates	RMS Multipath [meters]	Weighted RMS Multipath [meters]	Average Sat. Elevation Angle [degrees]	n Slip Periods	Slip/Obs Ratio [%]	n Slip Periods Elevation Angle 0–10 degrees	n Slip Periods Elevation Angle 10–20 degrees	n Slip Periods Elevation Angle 20–30 degrees	n Slip Periods Elevation Angle 30–40 degrees	n Slip Periods Elevation Angle 40–50 degrees	n Slip Periods Elevation Angle >50 degrees	n Slip Periods Elevation Angle NaN degrees
E1	66572	39659	0.713	0.587	35.601	189	0.284	69	115	5	0	0	0	0
E2	86393	11200	0.807	0.548	20.686	232	0.269	41	191	0	0	0	0	0
E3	69263	24747	0.662	0.536	25.577	184	0.266	98	86	0	0	0	0	0
E4	69696	25859	0.706	0.586	37.379	619	0.888	63	541	15	0	0	0	0
E5	72794	27964	0.702	0.453	27.343	132	0.181	42	83	7	0	0	0	0
E7	50097	23708	0.786	0.687	37.574	113	0.226	50	37	26	0	0	0	0
E8	65751	22565	0.852	0.633	29.171	160	0.243	104	52	4	0	0	0	0
E9	71792	24571	0.825	0.658	33.021	412	0.574	43	369	0	0	0	0	0
E11	86393	13437	0.420	0.347	23.659	229	0.265	47	173	9	0	0	0	0
E12	51864	24495	0.656	0.535	32.747	86	0.166	55	25	5	1	0	0	0
E13	69051	33260	0.750	0.570	39.219	223	0.323	70	153	0	0	0	0	0
E14	86393	13489	0.884	0.529	23.586	105	0.122	28	77	0	0	0	0	0
E15	71163	25757	0.819	0.649	38.691	475	0.667	105	370	0	0	0	0	0
E18	54763	23601	0.785	0.526	32.865	77	0.141	34	43	0	0	0	0	0
E20	58572	0	NaN	NaN	NaN	346	0.591	0	0	0	0	0	0	346
E21	66357	40726	0.661	0.551	34.314	88	0.133	55	33	0	0	0	0	0
E24	57169	24898	0.599	0.431	38.744	107	0.187	32	75	0	0	0	0	0
E25	52135	9939	0.662	0.418	21.350	461	0.884	22	439	0	0	0	0	0
E26	68806	35371	0.688	0.510	37.687	192	0.279	30	153	9	0	0	0	0
E27	63411	35857	0.796	0.673	37.517	75	0.118	49	26	0	0	0	0	0
E30	55495	22331	0.879	0.688	37.811	197	0.355	53	130	14	0	0	0	0
E31	64965	35060	0.793	0.635	39.541	83	0.128	35	48	0	0	0	0	0
E33	60727	34096	0.632	0.555	38.067	66	0.109	39	27	0	0	0	0	0
E36	65951	22007	0.699	0.488	25.533	112	0.170	52	55	5	0	0	0	0

Figure A.2.12: Emlid analysis output file: Galileo C1X signal, detailed results overview

PRN	n C7X Observations	n Epochs with Multipath Estimates	RMS Multipath [meters]	Weighted RMS Multipath [meters]	Average Sat. Elevation Angle [degrees]	n Slip Periods	Slip/Obs Ratio [%]	n Slip Periods Elevation Angle 0–10 degrees	n Slip Periods Elevation Angle 10–20 degrees	n Slip Periods Elevation Angle 20–30 degrees	n Slip Periods Elevation Angle 30–40 degrees	n Slip Periods Elevation Angle 40–50 degrees	n Slip Periods Elevation Angle >50 degrees	n Slip Periods Elevation Angle NaN degrees
E1	66522	39659	0.387	0.355	36.908	202	0.304	84	94	13	6	5	0	0
E2	86393	11200	0.355	0.257	22.739	458	0.530	92	366	0	0	0	0	0
E3	69174	24747	0.316	0.268	27.326	199	0.288	7	179	11	2	0	0	0
E4	69168	25858	0.510	0.476	40.811	488	0.706	33	424	18	7	0	6	0
E5	72475	27964	0.361	0.276	28.609	206	0.284	19	163	22	0	2	0	0
E7	49564	23708	0.387	0.345	40.263	156	0.315	16	75	54	5	3	3	0
E8	65640	22567	0.386	0.290	31.041	192	0.293	25	158	5	3	0	1	0
E9	70769	24571	0.600	0.515	36.256	469	0.663	53	399	16	1	0	0	0
E11	86393	13437	0.211	0.178	26.338	457	0.529	100	232	86	39	0	0	0
E12	51700	24495	0.318	0.270	33.807	289	0.559	88	105	38	31	11	16	0
E13	68606	33260	0.572	0.485	41.168	432	0.630	84	341	3	2	1	1	0
E14	86391	13489	0.341	0.220	25.995	126	0.146	23	95	8	0	0	0	0
E15	71198	25757	0.636	0.537	42.556	495	0.695	46	448	0	0	0	1	0
E18	54226	23601	0.506	0.431	33.862	127	0.234	23	91	13	0	0	0	0
E21	65415	40726	0.424	0.370	35.761	180	0.275	60	64	45	5	1	5	0
E24	56945	24898	0.387	0.316	41.565	174	0.306	43	122	6	0	0	3	0
E25	51494	9938	0.334	0.242	24.621	387	0.752	7	375	4	0	1	0	0
E26	67654	35371	0.459	0.418	39.606	281	0.415	41	157	74	1	2	6	0
E27	62982	35857	0.532	0.416	39.681	99	0.157	23	59	7	9	0	1	0
E30	55070	22331	0.468	0.429	41.563	209	0.380	15	147	46	0	1	0	0
E31	64893	35060	0.519	0.487	42.256	154	0.237	38	81	32	1	1	1	0
E33	60472	34095	0.406	0.373	39.052	155	0.256	44	64	25	15	3	4	0
E36	65937	22007	0.280	0.214	26.752	269	0.408	98	136	35	0	0	0	0

Figure A.2.13: Emlid analysis output file: Galileo C7X signal, detailed results overview

GLONASS

Sat ID	Frequency Channel	n C1C Observations	n Epochs with Multipath Estimates	RMS Multipath [meters]	Weighted RMS Multipath [meters]	Average Sat. Elevation Angle [degrees]	n Slip Periods	Slip/Obs Ratio [%]	n Slip Periods Elevation Angle 0–10 degrees	n Slip Periods Elevation Angle 10–20 degrees	n Slip Periods Elevation Angle 20–30 degrees	n Slip Periods Elevation Angle 30–40 degrees	n Slip Periods Elevation Angle 40–50 degrees	n Slip Periods Elevation Angle >50 degrees	n Slip Periods Elevation Angle NaN degrees
R1	1	82185	12054	0.299	NaN	NaN	120	0.146	0	0	0	0	0	0	120
R2	-4	58949	26919	0.428	NaN	NaN	79	0.134	0	0	0	0	0	0	79
R3	5	60829	22334	0.419	NaN	NaN	47	0.077	0	0	0	0	0	0	47
R4	6	62408	28462	0.576	NaN	NaN	63	0.101	0	0	0	0	0	0	63
R5	1	82214	28919	0.558	NaN	NaN	34	0.041	0	0	0	0	0	0	34
R6	-4	86393	0	NaN	NaN	NaN	184	0.213	0	0	0	0	0	0	184
R7	5	86393	29129	0.493	0.427	53.872	54	0.063	11	0	0	0	0	0	43
R8	6	85894	26874	0.617	0.525	34.977	152	0.177	69	83	0	0	0	0	0
R9	-2	83433	31542	0.652	0.469	31.442	96	0.115	55	41	0	0	0	0	0
R10	-7	50313	0	NaN	NaN	NaN	65	0.129	0	0	0	0	0	0	65
R11	0	50186	27572	0.499	0.405	32.966	29	0.058	22	7	0	0	0	0	0
R12	-1	50546	24435	0.581	0.534	35.763	49	0.097	27	22	0	0	0	0	0
R13	-2	51245	2419	0.239	0.171	37.704	455	0.888	62	267	99	27	0	0	0
R14	-7	83409	29153	0.695	0.556	35.160	63	0.076	27	36	0	0	0	0	0
R15	0	86393	31903	0.447	0.370	41.350	58	0.067	43	15	0	0	0	0	0
R16	-1	86393	22272	0.364	0.340	40.545	109	0.126	50	51	7	0	0	1	0
R17	4	86393	33008	0.458	0.404	39.270	37	0.043	27	10	0	0	0	0	0
R18	-3	86393	32113	0.655	0.591	38.146	85	0.098	30	51	0	3	1	0	0
R19	3	82268	20181	0.521	0.458	38.527	291	0.354	36	127	106	16	6	0	0
R20	2	57849	24389	0.528	0.421	37.586	291	0.503	42	201	48	0	0	0	0
R21	4	55379	20318	0.394	0.341	36.735	38	0.069	24	14	0	0	0	0	0
R22	-3	52535	26409	0.532	0.453	36.740	65	0.124	22	43	0	0	0	0	0
R23	3	82823	16314	0.354	0.343	32.842	108	0.130	52	56	0	0	0	0	0
R24	2	86393	3	0.079	0.079	34.096	168	0.194	55	112	1	0	0	0	0

Figure A.2.14: Emlid analysis output file: GLONASS C1C signal, detailed results overview

Sat ID	Frequency Channel	n C2C Observations	n Epochs with Multipath Estimates	RMS Multipath [meters]	Weighted RMS Multipath [meters]	Average Sat. Elevation Angle [degrees]	n Slip Periods	Slip/Obs Ratio [%]	n Slip Periods Elevation Angle 0–10 degrees	n Slip Periods Elevation Angle 10–20 degrees	n Slip Periods Elevation Angle 20–30 degrees	n Slip Periods Elevation Angle 30–40 degrees	n Slip Periods Elevation Angle 40–50 degrees	n Slip Periods Elevation Angle >50 degrees	n Slip Periods Elevation Angle NaN degrees
R1	1	55691	12054	0.727	NaN	NaN	1255	2.254	0	0	0	0	0	0	1255
R2	−4	58580	26919	0.769	NaN	NaN	298	0.509	0	0	0	0	0	0	298
R3	5	60692	22334	0.665	NaN	NaN	1089	1.794	0	0	0	0	0	0	1089
R4	6	62385	28462	0.811	NaN	NaN	162	0.260	0	0	0	0	0	0	162
R5	1	81994	28914	0.825	NaN	NaN	244	0.298	0	0	0	0	0	0	244
R7	5	86393	29129	0.816	0.602	54.391	583	0.675	45	77	23	7	0	168	263
R8	6	85368	26874	0.830	0.647	35.856	495	0.580	63	207	129	25	2	69	0
R9	−2	83412	31542	0.824	0.543	31.575	93	0.111	36	56	1	0	0	0	0
R11	0	49847	27572	0.793	0.578	33.255	164	0.329	50	89	19	6	0	0	0
R12	−1	50058	24435	0.875	0.782	37.302	231	0.461	24	141	66	0	0	0	0
R13	−2	51193	2417	0.326	0.258	39.379	1588	3.102	17	184	510	138	269	470	0
R14	−7	83218	29148	0.912	0.698	36.107	346	0.416	65	255	22	3	0	1	0
R15	0	86393	31903	0.790	0.641	41.825	396	0.458	44	261	79	6	0	6	0
R16	−1	86393	22272	0.666	0.619	41.623	1255	1.453	12	186	311	75	43	628	0
R17	4	86393	33007	0.761	0.676	40.261	205	0.237	48	56	77	16	2	6	0
R18	−3	86393	32113	0.808	0.675	39.282	148	0.171	21	94	29	0	0	4	0
R19	3	82049	20177	0.766	0.707	38.370	1150	1.402	37	197	400	110	55	351	0
R20	2	57876	24389	0.925	0.791	37.445	315	0.544	41	144	41	10	0	79	0
R21	4	55210	20318	0.730	0.635	37.141	1057	1.915	68	254	363	57	113	202	0
R22	−3	52368	26409	0.792	0.592	37.304	174	0.332	38	107	29	0	0	0	0
R23	3	82479	16314	0.662	0.594	34.768	1348	1.634	33	146	319	338	134	378	0
R24	2	86314	3	0.097	0.097	37.772	19	0.022	8	0	0	0	11	0	0

Figure A.2.15: Emlid analysis output file: GLONASS C2C signal, detailed results overview

PRN	n C2I Observations	n Epochs with Multipath Estimates	RMS Multipath [meters]	Weighted RMS Multipath [meters]	Average Sat. Elevation Angle [degrees]	n Slip Periods	Slip/Obs Ratio [%]	n Slip Periods Elevation Angle 0–10 degrees	n Slip Periods Elevation Angle 10–20 degrees	n Slip Periods Elevation Angle 20–30 degrees	n Slip Periods Elevation Angle 30–40 degrees	n Slip Periods Elevation Angle 40–50 degrees	n Slip Periods Elevation Angle >50 degrees	n Slip Periods Elevation Angle NaN degrees
C6	28315	23897	0.511	0.419	24.591	129	0.456	73	20	36	0	0	0	0
C7	25942	22283	0.529	0.426	23.352	99	0.382	38	15	46	0	0	0	0
C8	86393	25047	0.499	0.438	26.826	101	0.117	42	55	4	0	0	0	0
C9	35743	32897	0.505	0.431	31.102	52	0.145	35	3	14	0	0	0	0
C10	34845	31927	0.572	0.491	29.660	119	0.342	77	13	29	0	0	0	0
C11	52531	15215	0.563	0.407	23.289	137	0.261	26	111	0	0	0	0	0
C12	86393	21809	0.526	0.407	30.733	102	0.118	27	56	19	0	0	0	0
C13	86393	30450	0.537	0.485	31.028	136	0.157	133	0	3	0	0	0	0
C14	68628	29448	0.540	0.442	29.072	56	0.082	25	29	2	0	0	0	0
C16	30754	24654	0.529	0.468	26.153	131	0.426	84	42	5	0	0	0	0
C19	60747	0	NaN	NaN	45.361	307	0.505	19	288	0	0	0	0	0
C20	55297	0	NaN	NaN	48.027	50	0.090	44	5	0	0	1	0	0
C21	66683	0	NaN	NaN	32.383	88	0.132	13	69	6	0	0	0	0
C22	65313	0	NaN	NaN	38.412	175	0.268	6	169	0	0	0	0	0
C23	53488	0	NaN	NaN	39.510	79	0.148	16	63	0	0	0	0	0
C24	86393	0	NaN	NaN	36.424	50	0.058	21	29	0	0	0	0	0
C25	86393	0	NaN	NaN	31.992	181	0.210	21	155	5	0	0	0	0
C26	55948	0	NaN	NaN	44.178	383	0.685	27	356	0	0	0	0	0
C27	60491	0	NaN	NaN	38.145	197	0.326	34	163	0	0	0	0	0
C28	58939	0	NaN	NaN	42.344	398	0.675	46	352	0	0	0	0	0
C29	56325	0	NaN	NaN	34.652	12	0.021	12	0	0	0	0	0	0
C30	59732	0	NaN	NaN	35.847	78	0.131	28	50	0	0	0	0	0
C32	49821	0	NaN	NaN	46.992	14	0.028	14	0	0	0	0	0	0
C33	5499	0	NaN	NaN	17.123	24	0.436	24	0	0	0	0	0	0
C34	61418	0	NaN	NaN	41.920	32	0.052	32	0	0	0	0	0	0
C35	459	0	NaN	NaN	55.318	0	0.000	0	0	0	0	0	0	0
C36	48109	0	NaN	NaN	43.827	10	0.021	10	0	0	0	0	0	0
C37	3121	0	NaN	NaN	13.653	2	0.064	2	0	0	0	0	0	0

Figure A.2.16: Emlid analysis output file: BeiDou C2I signal, detailed results overview

PRN	n C7I Observations	n Epochs with Multipath Estimates	RMS Multipath [meters]	Weighted RMS Multipath [meters]	Average Sat. Elevation Angle [degrees]	n Slip Periods	Slip/Obs Ratio [%]	n Slip Periods Elevation Angle 0–10 degrees	n Slip Periods Elevation Angle 10–20 degrees	n Slip Periods Elevation Angle 20–30 degrees	n Slip Periods Elevation Angle 30–40 degrees	n Slip Periods Elevation Angle 40–50 degrees	n Slip Periods Elevation Angle >50 degrees	n Slip Periods Elevation Angle NaN degrees
C6	28504	23893	0.445	0.387	25.006	309	1.084	113	109	66	21	0	0	0
C7	26840	22283	0.283	0.199	23.444	234	0.872	37	143	45	9	0	0	0
C8	86393	25047	0.288	0.250	26.847	259	0.300	153	83	18	5	0	0	0
C9	36682	32896	0.299	0.238	30.704	188	0.513	71	65	30	15	7	0	0
C10	35853	31927	0.486	0.446	29.534	277	0.773	123	96	32	18	8	0	0
C11	63889	15215	0.317	0.224	40.467	147	0.230	24	122	0	0	0	1	0
C12	86393	21809	0.332	0.274	30.134	87	0.101	38	39	10	0	0	0	0
C13	86393	30448	0.311	0.252	32.525	471	0.545	88	237	106	30	10	0	0
C14	69971	29448	0.318	0.250	28.037	171	0.244	46	119	5	1	0	0	0
C16	30766	24654	0.295	0.226	27.451	401	1.303	107	157	104	33	0	0	0

Figure A.2.17: Emlid analysis output file: BeiDou C7I signal, detailed results overview

A.2.5 Plotted Results

GPS

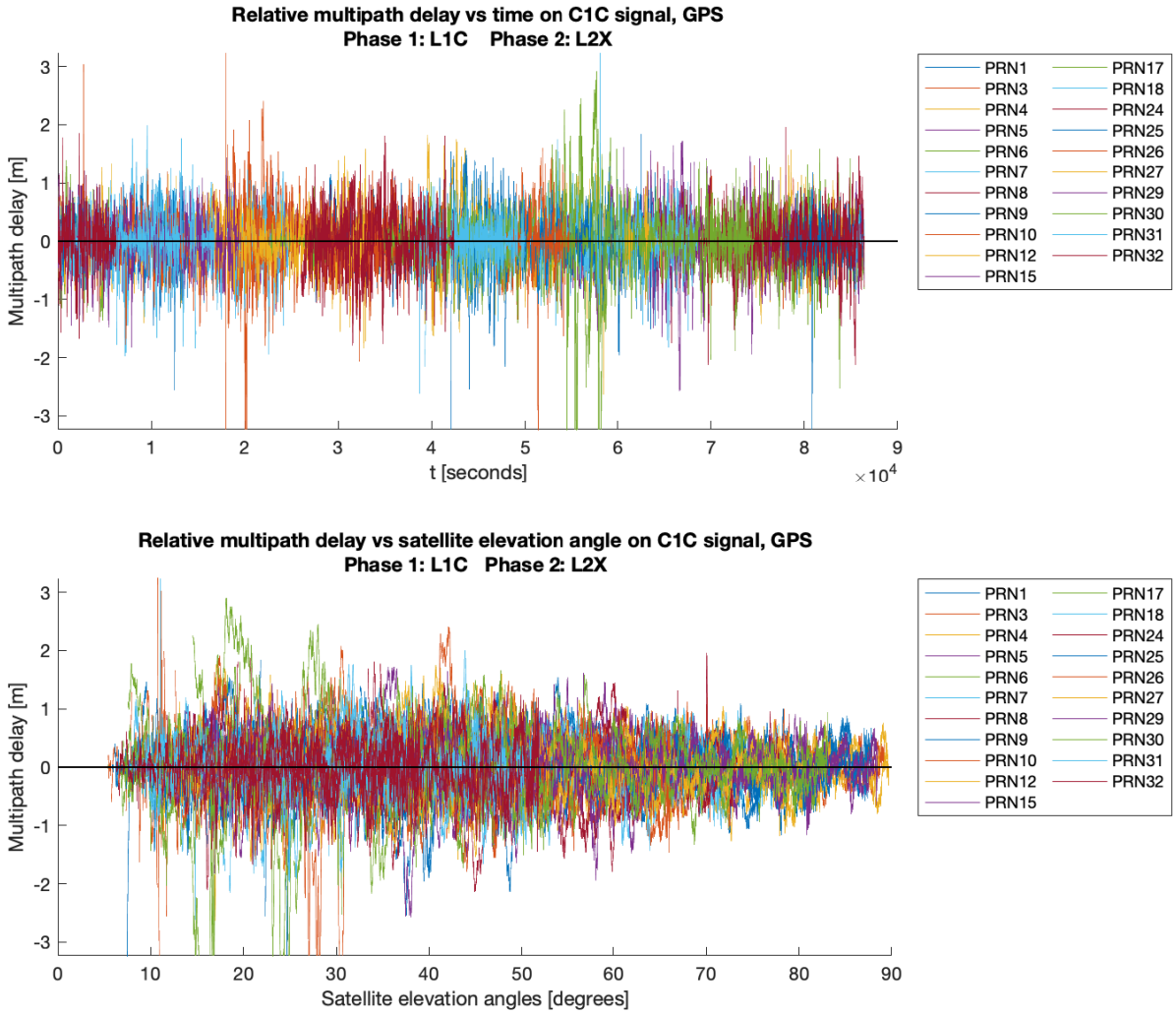

Figure A.2.18: Emlid analysis results graph: GPS C1C signal, multipath effect vs. time and vs. satellite elevation angle. Graph has been cropped along y axis.

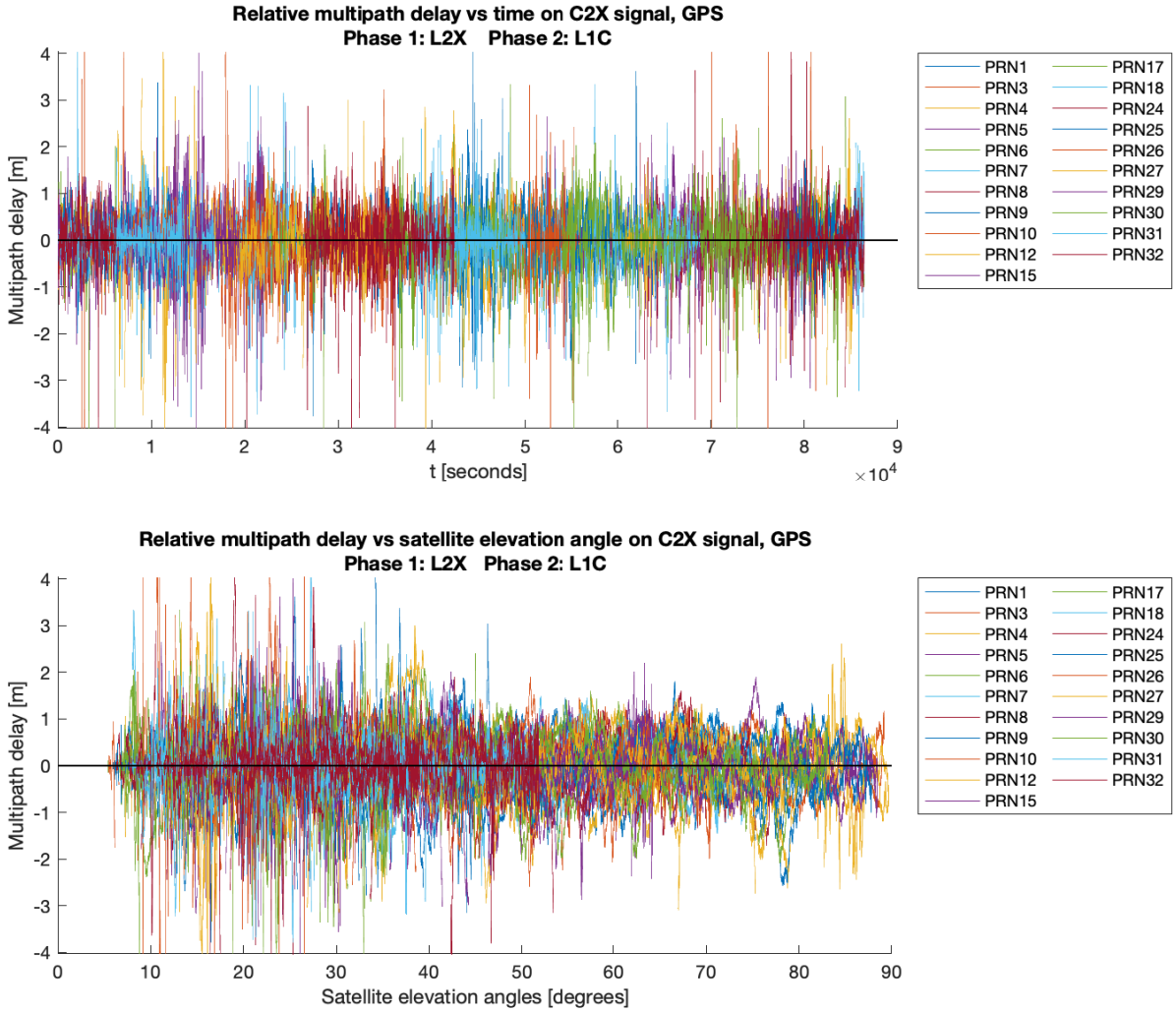

Figure A.2.19: Emlid analysis results graph: GPS C2X signal, multipath effect vs. time and vs. satellite elevation angle. Graph has been cropped along y axis.

Galileo

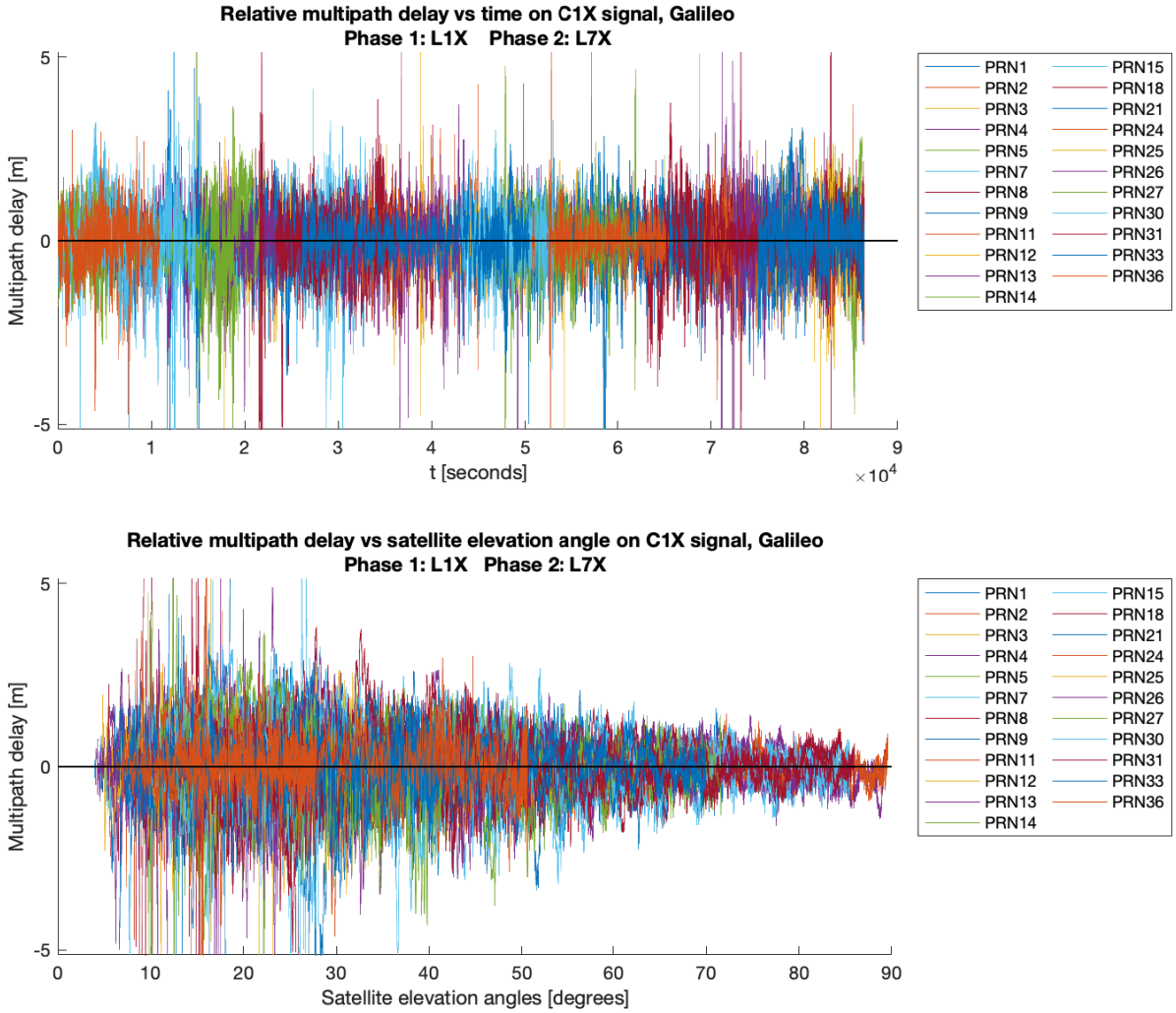

Figure A.2.20: Emlid analysis results graph: Galileo C1X signal, multipath effect vs. time and vs. satellite elevation angle. Graph has been cropped along y axis.

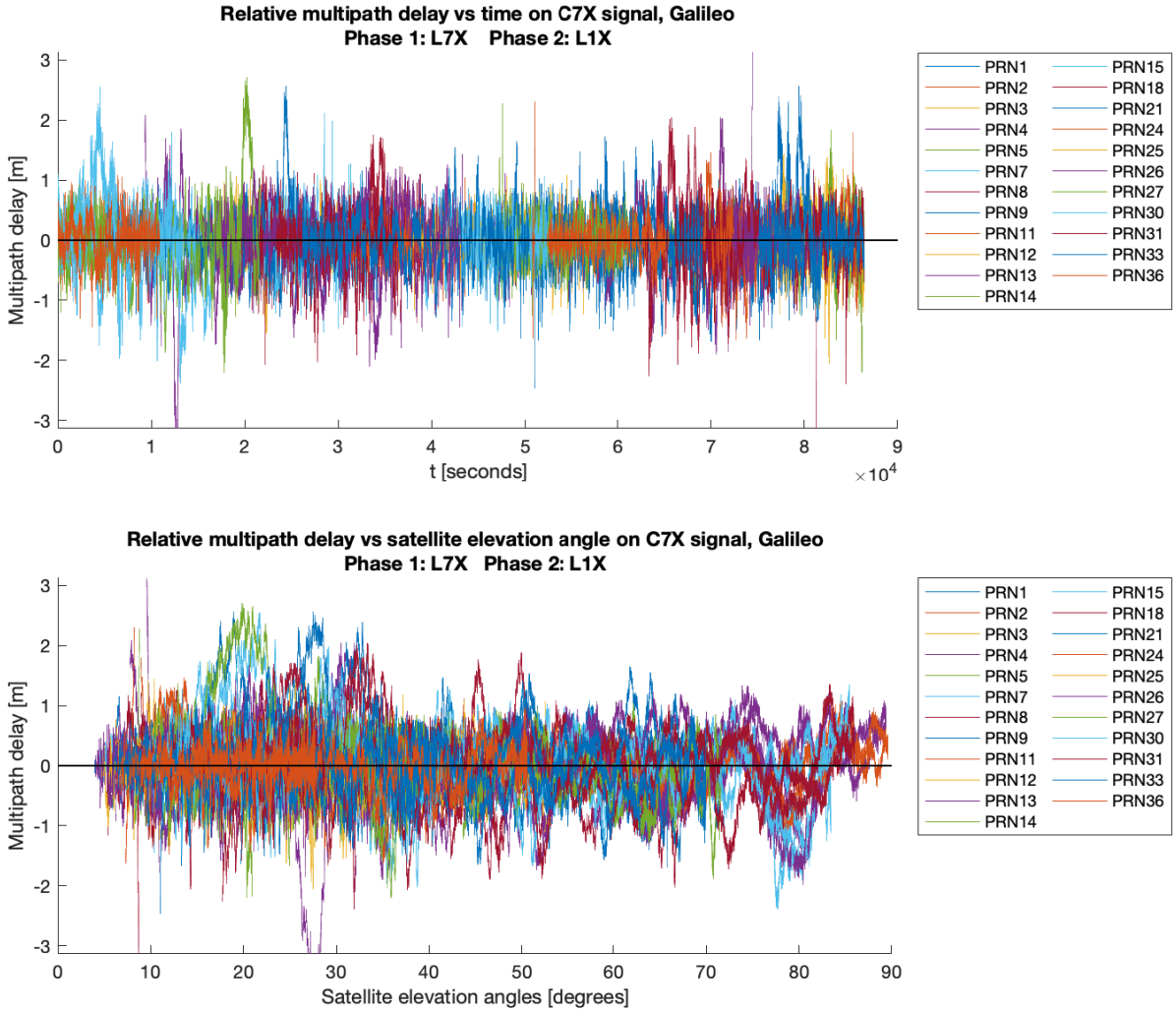

Figure A.2.21: Emlid analysis results graph: Galileo C7X signal, multipath effect vs. time and vs. satellite elevation angle. Graph has been cropped along y axis.

GLONASS

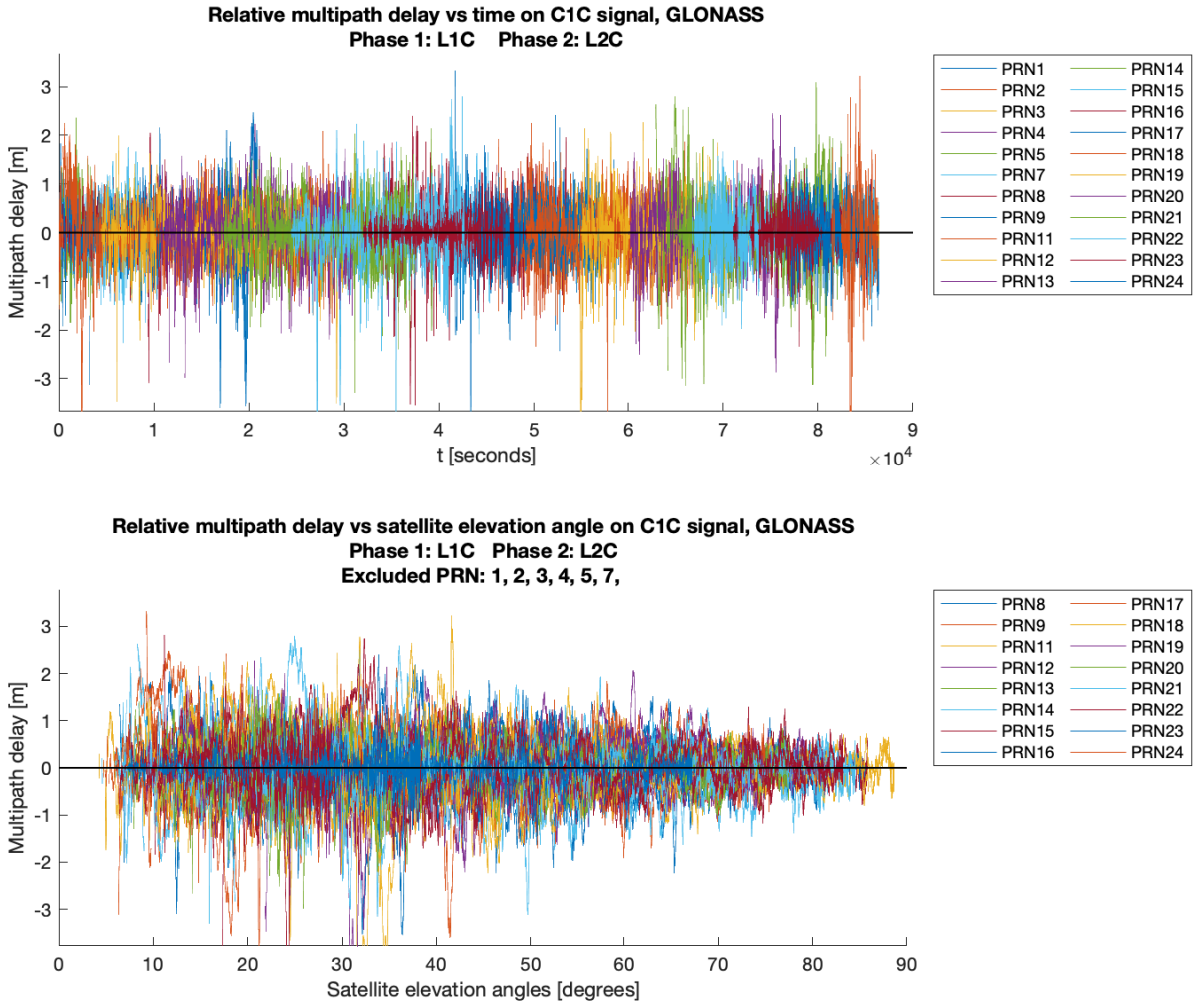

Figure A.2.22: Emlid analysis results graph: GLONASS C1C signal, multipath effect vs. time and vs. satellite elevation angle. Graph has been cropped along y axis.

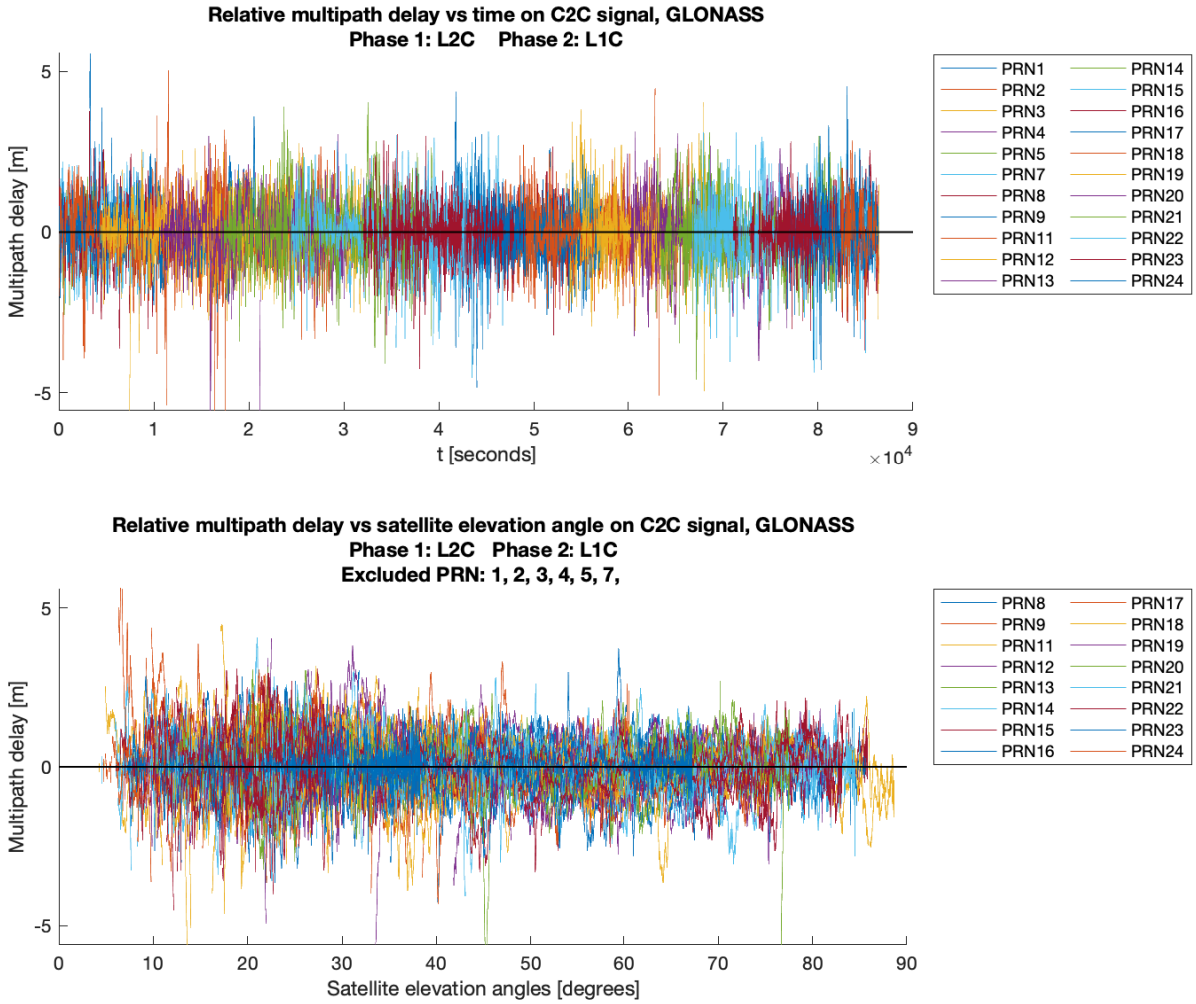

Figure A.2.23: Emlid analysis results graph: GLONASS C2C signal, multipath effect vs. time and vs. satellite elevation angle. Graph has been cropped along y axis.

BeiDou

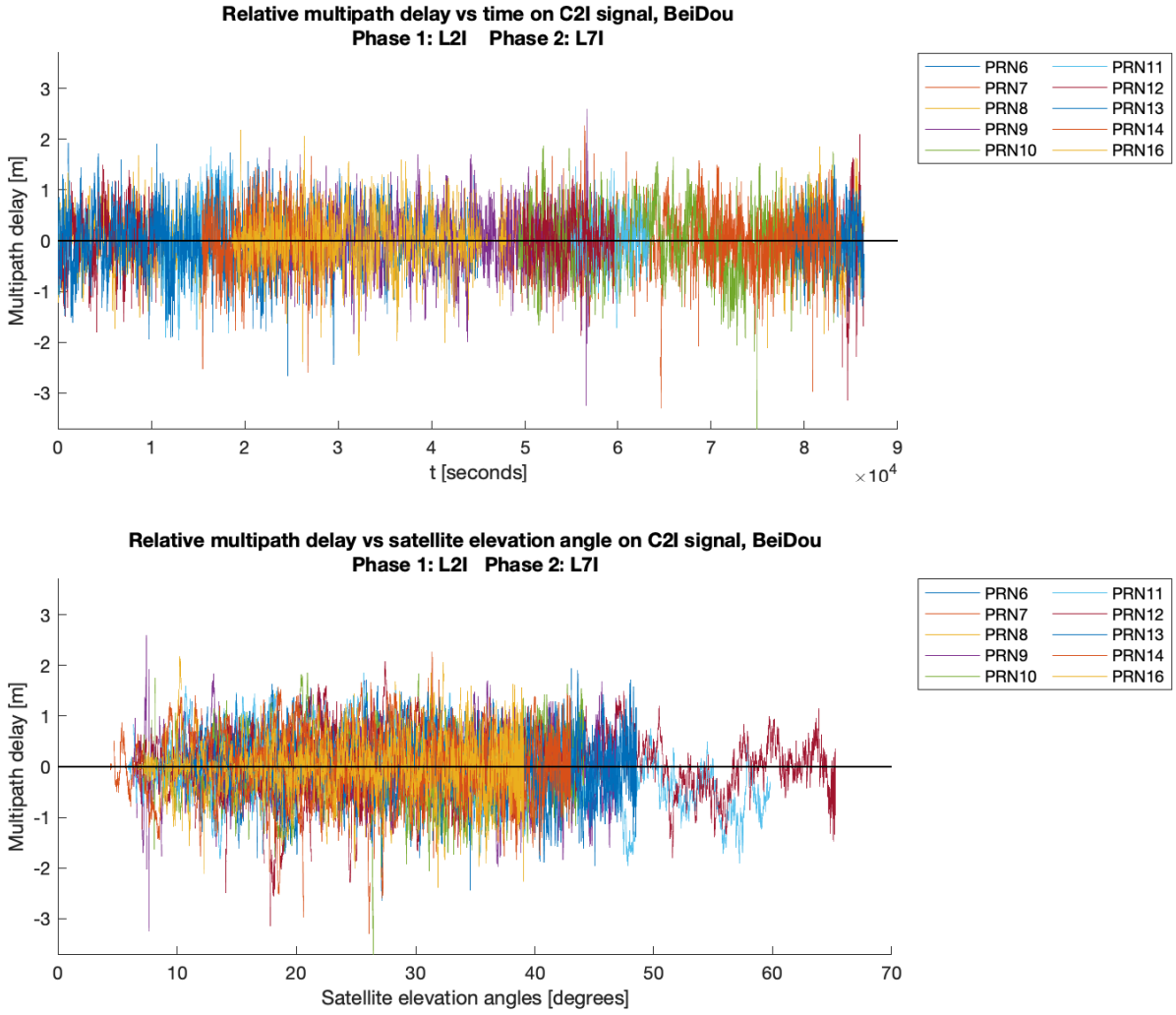

Figure A.2.24: Emlid analysis results graph: BeiDou C2I signal, multipath effect vs. time and vs. satellite elevation angle. Graph has been cropped along y axis.

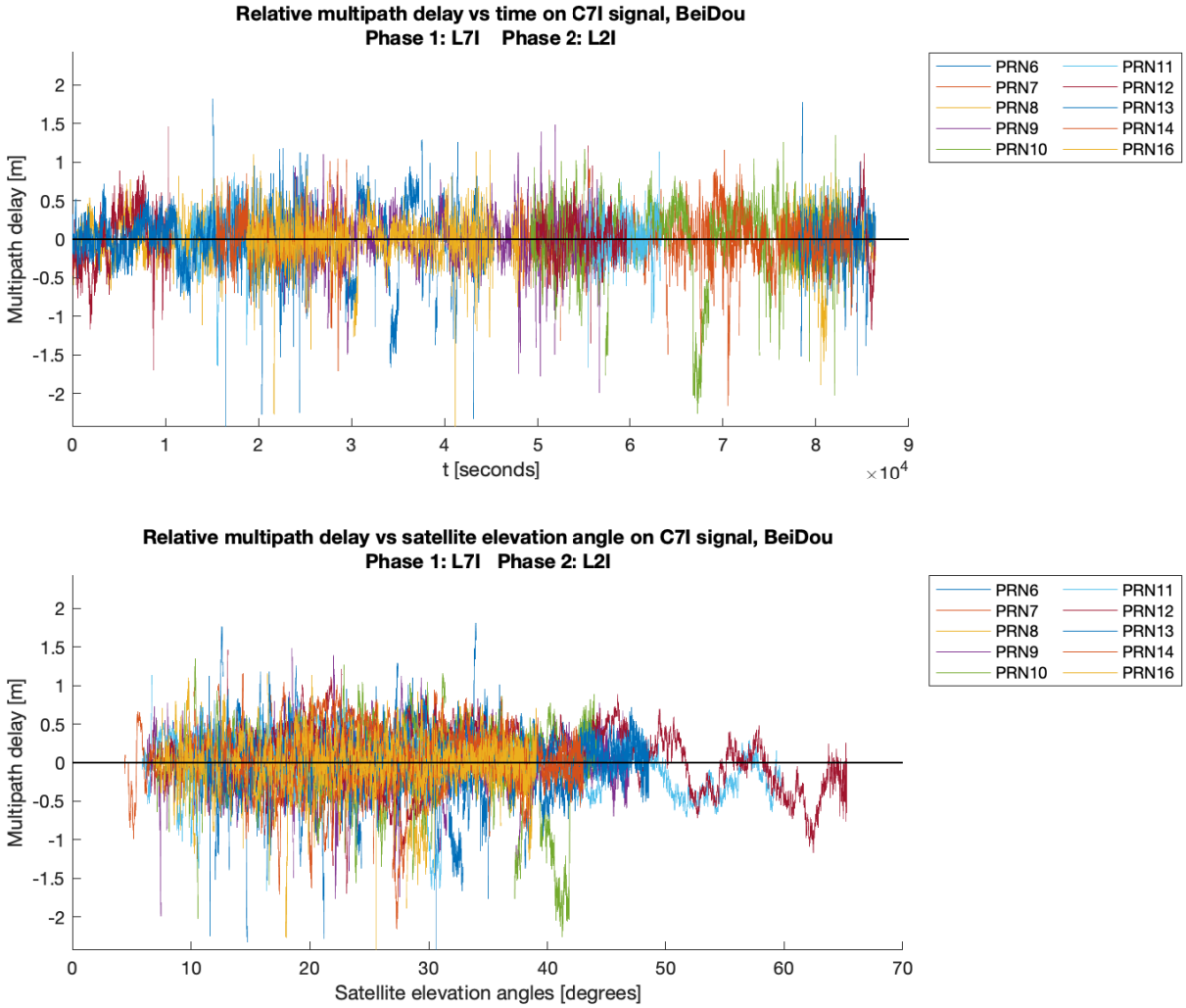

Figure A.2.25: Emlid analysis results graph: BeiDou C7I signal, multipath effect vs. time and vs. satellite elevation angle. Graph has been cropped along y axis.

A.3 Septentrio PolaRxS Pro

A.3.1 Header

```
GNSS Receiver Quality Check 2020
Software version: 1.00
Last software version release: 02/06/2020

Software developed by Bjørn-Eirik Roald
Norwegian University of Life Sciences(NMBU)

RINEX observation filename:      FLO300XXX_R_20200901200_01D_01S_MO.rnx
RINEX version:                   3.04
RINEX converting program:        sbf2rin-13.4.3
Marker name:                     FLO3
Receiver type:                   SEPT POLARXS
Date of observation start:       2020/3/30 12:20:0.00
Date of observation end:         2020/3/31 12:19:59.00
Observation interval [seconds]:  1
Number of receiver clock jumps:  5
Average clock jumps interval:    04:18:06 (std: 19.82 seconds)

Critical cycle slip limits [m/s]:
- Ionospheric delay:             0.067
- Phase-code combination:        6.667

GNSS systems presents in RINEX observation file:
- BeiDou
- Galileo
- GPS
- GLONASS


User-specified contend included in output file
- Include overview of observations for each satellite:          Yes
- Include compact summary of analysis estimates:                Yes
- Include detailed summary of analysis
   estimates, including for each individual satellite:          Yes
- Include information about "Loss-of-Lock"
   indicators in detailed summary:                              No
```

Figure A.3.1: Septentrio analysis output file: Header

A.3.2 Observation Overview

GPS Observation overview

PRN	L1 Observations	L2 Observations	L5 Observations
G1	C1C	C2L,C2W	C5Q
G2	C1C	C2W	
G3	C1C	C2L,C2W	C5Q
G4	C1C	C2L,C2W	C5Q
G5	C1C	C2L,C2W	
G6	C1C	C2L,C2W	C5Q
G7	C1C	C2L,C2W	
G8	C1C	C2L,C2W	C5Q
G9	C1C	C2L,C2W	C5Q
G10	C1C	C2L,C2W	C5Q
G11	C1C	C2W	
G12	C1C	C2L,C2W	
G13	C1C	C2W	
G14	C1C	C2W	
G15	C1C	C2L,C2W	
G16	C1C	C2W	
G17	C1C	C2L,C2W	
G18	C1C	C2W	
G19	C1C	C2W	
G20	C1C	C2W	
G21	C1C	C2W	
G22	C1C	C2W	
G23	C1C	C2W	
G24	C1C	C2L,C2W	C5Q
G25	C1C	C2L,C2W	C5Q
G26	C1C	C2L,C2W	C5Q
G27	C1C	C2L,C2W	C5Q
G28	C1C	C2W	
G29	C1C	C2L,C2W	
G30	C1C	C2L,C2W	C5Q
G31	C1C	C2L,C2W	
G32	C1C	C2L,C2W	C5Q

Figure A.3.2: Septentrio analysis output file: GPS observation overview

Galileo Observation overview

PRN	E1 Observations	E5a Observations	E6 Observations	E5b Observations	G5(a+b) Observations
E1	C1C	C5Q			
E2	C1C	C5Q			
E3	C1C	C5Q			
E4	C1C	C5Q			
E5	C1C	C5Q			
E7	C1C	C5Q			
E8	C1C	C5Q			
E9	C1C	C5Q			
E11	C1C	C5Q			
E12	C1C	C5Q			
E13	C1C	C5Q			
E14	C1C	C5Q			
E15	C1C	C5Q			
E18	C1C	C5Q			
E20	C1C				
E21	C1C	C5Q			
E24	C1C	C5Q			
E25	C1C	C5Q			
E26	C1C	C5Q			
E27	C1C	C5Q			
E30	C1C	C5Q			
E31	C1C	C5Q			

Figure A.3.3: Septentrio analysis output file: Galileo observation overview

GLONASS Observation overview

Sat ID	Frequency Channel	G1 Observations	G2 Observations	G3 Observations	G1a Observations	G2a Observations
R1	1	C1C	C2C			
R2	-4	C1C	C2C			
R3	5	C1C	C2C			
R4	6	C1C	C2C			
R5	1	C1C	C2C			
R6	-4	C1C				
R7	5	C1C	C2C			
R8	6	C1C	C2C			
R9	-2	C1C	C2C			
R10	-7	C1C				
R11	0	C1C	C2C			
R12	-1	C1C	C2C			
R13	-2	C1C	C2C			
R14	-7	C1C	C2C			
R15	0	C1C	C2C			
R16	-1	C1C	C2C			
R17	4	C1C	C2C			
R18	-3	C1C	C2C			
R19	3	C1C	C2C			
R20	2	C1C	C2C			
R21	4	C1C	C2C			
R22	-3	C1C	C2C			
R23	3	C1C	C2C			
R24	2	C1C	C2C			

Figure A.3.4: Septentrio analysis output file: GLONASS observation overview

BeiDou Observation overview

PRN	B1 Observations	E1-2 Observations	B2a Observations	B3 Observations	B2b Observations	B2(a+b) Observations
C5		C2I			C7I	
C12		C2I			C7I	
C13		C2I			C7I	
C19		C2I				
C21		C2I				
C22		C2I				
C24		C2I				

Figure A.3.5: Septentrio analysis output file: BeiDou observation overview

A.3.3 Compressed Results Overview

GPS ANALYSIS SUMMARY

	C1C	C2L	C2W	C5Q
RMS multipath[meters]	0.318	0.360	0.320	0.239
Weighted RMS multipath[meters]	0.151	0.177	0.174	0.128
N ambiguity slips periods	723	378	743	224
N slip periods, elevation angle > 10 degrees	63	22	74	6
N slip periods, elevation angle < 10 degrees	660	356	669	218
N slip periods, elevation angle not computed	0	0	0	0
Ratio of N slip periods/N obs epochs [%]	0.035	0.028	0.036	0.027

Figure A.3.6: Septentrio analysis output file: GPS compressed results overview

GALILEO ANALYSIS SUMMARY

	C1C	C5Q
RMS multipath[meters]	0.272	0.213
Weighted RMS multipath[meters]	0.139	0.105
N ambiguity slips periods	69	65
N slip periods, elevation angle > 10 degrees	11	6
N slip periods, elevation angle < 10 degrees	57	59
N slip periods, elevation angle not computed	1	0
Ratio of N slip periods/N obs epochs [%]	0.005	0.005

Figure A.3.7: Septentrio analysis output file: Galileo compressed results overview

GLONASS ANALYSIS SUMMARY

	C1C	C2C
RMS multipath[meters]	0.545	0.475
Weighted RMS multipath[meters]	0.306	0.294
N ambiguity slips periods	1221	883
N slip periods, elevation angle > 10 degrees	95	57
N slip periods, elevation angle < 10 degrees	782	637
N slip periods, elevation angle not computed	344	189
Ratio of N slip periods/N obs epochs [%]	0.070	0.056

Figure A.3.8: Septentrio analysis output file: GLONASS compressed results overview

BEIDOU ANALYSIS SUMMARY

	C2I	C7I
RMS multipath[meters]	0.432	0.290
Weighted RMS multipath[meters]	0.184	0.157
N ambiguity slips periods	30	25
N slip periods, elevation angle > 10 degrees	15	10
N slip periods, elevation angle < 10 degrees	15	15
N slip periods, elevation angle not computed	0	0
Ratio of N slip periods/N obs epochs [%]	0.030	0.037

Figure A.3.9: Septentrio analysis output file: BeiDou compressed results overview

A.3.4 Detailed Results Overview

GPS

PRN	n C1C Observations	n Epochs with Multipath Estimates	RMS Multipath [meters]	Weighted RMS Multipath [meters]	Average Sat. Elevation Angle [degrees]	n Slip Periods	Slip/Obs Ratio [%]	n Slip Periods Elevation Angle 0–10 degrees	n Slip Periods Elevation Angle 10–20 degrees	n Slip Periods Elevation Angle 20–30 degrees	n Slip Periods Elevation Angle 30–40 degrees	n Slip Periods Elevation Angle 40–50 degrees	n Slip Periods Elevation Angle >50 degrees	n Slip Periods Elevation Angle NaN degrees
G1	55986	29458	0.285	0.134	37.136	16	0.029	12	4	0	0	0	0	0
G2	86400	30801	0.234	0.147	31.366	39	0.045	39	0	0	0	0	0	0
G3	86400	29347	0.332	0.168	39.006	62	0.072	52	10	0	0	0	0	0
G4	54642	30763	0.395	0.165	36.847	4	0.007	4	0	0	0	0	0	0
G5	64773	31749	0.348	0.152	30.765	29	0.045	29	0	0	0	0	0	0
G6	86400	33129	0.331	0.158	30.437	29	0.034	29	0	0	0	0	0	0
G7	54899	30973	0.336	0.143	35.591	13	0.024	12	1	0	0	0	0	0
G8	54946	30651	0.244	0.131	34.062	6	0.011	6	0	0	0	0	0	0
G9	55581	28178	0.357	0.147	40.084	16	0.029	16	0	0	0	0	0	0
G10	65343	31452	0.250	0.146	33.964	9	0.014	9	0	0	0	0	0	0
G11	50922	23189	0.270	0.139	39.389	13	0.026	3	10	0	0	0	0	0
G12	86400	31000	0.343	0.139	38.110	28	0.032	26	2	0	0	0	0	0
G13	61297	28756	0.262	0.139	36.649	54	0.088	45	9	0	0	0	0	0
G14	86400	31830	0.246	0.157	31.557	42	0.049	42	0	0	0	0	0	0
G15	62740	29384	0.260	0.132	32.552	14	0.022	14	0	0	0	0	0	0
G16	53936	31709	0.284	0.140	32.011	13	0.024	13	0	0	0	0	0	0
G17	86400	32530	0.257	0.147	31.018	39	0.045	39	0	0	0	0	0	0
G18	10	3	0.132	0.017	10.165	0	0.000	0	0	0	0	0	0	0
G19	86400	32402	0.268	0.157	30.805	30	0.035	30	0	0	0	0	0	0
G20	64869	30553	0.294	0.172	32.237	26	0.040	26	0	0	0	0	0	0
G21	64208	32414	0.545	0.152	35.503	20	0.031	20	0	0	0	0	0	0
G22	86400	27977	0.367	0.141	40.405	25	0.029	16	9	0	0	0	0	0
G23	11	5	0.086	0.026	15.845	0	0.000	0	0	0	0	0	0	0
G24	86400	28993	0.266	0.131	36.522	63	0.073	63	0	0	0	0	0	0
G25	86400	27272	0.293	0.153	41.363	8	0.009	4	4	0	0	0	0	0
G26	54538	30699	0.296	0.142	32.589	21	0.039	21	0	0	0	0	0	0
G27	55850	29681	0.274	0.126	36.563	8	0.014	5	3	0	0	0	0	0
G28	53578	31341	0.256	0.168	33.892	25	0.047	15	10	0	0	0	0	0
G29	86400	30239	0.394	0.177	38.351	30	0.035	30	0	0	0	0	0	0
G30	54577	30344	0.423	0.154	37.172	10	0.018	9	1	0	0	0	0	0
G31	51775	30398	0.324	0.184	30.859	13	0.025	13	0	0	0	0	0	0
G32	86400	31899	0.281	0.162	30.524	18	0.021	18	0	0	0	0	0	0

Figure A.3.10: Septentrio analysis output file: GPS C1C signal, detailed results overview

	n C2L	n Epochs with	RMS	Weighted RMS	Average Sat.		Slip/Obs	n Slip Periods	n Slip Periods	n Slip Periods	n Slip Periods	n Slip Periods	n Slip Periods	n Slip Periods
PRN	Observations	Multipath Estimates	Multipath [meters]	Multipath [meters]	Elevation Angle [degrees]	n Slip Periods	Ratio [%]	Elevation Angle 0–10 degrees	Elevation Angle 10–20 degrees	Elevation Angle 20–30 degrees	Elevation Angle 30–40 degrees	Elevation Angle 40–50 degrees	Elevation Angle >50 degrees	Elevation Angle NaN degrees
G1	55040	28050	0.329	0.166	38.035	10	0.018	9	1	0	0	0	0	0
G3	86400	26556	0.396	0.154	42.468	62	0.072	53	9	0	0	0	0	0
G4	54666	30606	0.352	0.149	37.115	3	0.005	3	0	0	0	0	0	0
G5	64546	30774	0.418	0.207	31.432	26	0.040	26	0	0	0	0	0	0
G6	86400	32802	0.338	0.176	30.463	21	0.024	21	0	0	0	0	0	0
G7	54103	30220	0.435	0.196	36.410	6	0.011	6	0	0	0	0	0	0
G8	54634	28222	0.310	0.160	35.630	2	0.004	1	1	0	0	0	0	0
G9	55277	27492	0.328	0.148	40.379	13	0.024	12	1	0	0	0	0	0
G10	65085	30495	0.309	0.170	34.646	9	0.014	8	1	0	0	0	0	0
G12	86400	29054	0.399	0.176	39.136	27	0.031	25	2	0	0	0	0	0
G15	61337	28158	0.364	0.190	33.355	11	0.018	11	0	0	0	0	0	0
G17	86216	32384	0.352	0.205	31.402	40	0.046	39	1	0	0	0	0	0
G24	86400	28929	0.326	0.149	36.933	65	0.075	65	0	0	0	0	0	0
G25	86400	26596	0.401	0.169	41.105	6	0.007	3	3	0	0	0	0	0
G26	54197	30369	0.335	0.159	32.835	20	0.037	19	1	0	0	0	0	0
G27	55675	29628	0.330	0.152	36.644	7	0.013	7	0	0	0	0	0	0
G29	59974	25589	0.361	0.193	42.868	11	0.018	10	1	0	0	0	0	0
G30	53719	28874	0.375	0.164	38.894	11	0.020	11	0	0	0	0	0	0
G31	51612	30037	0.367	0.230	31.003	12	0.023	12	0	0	0	0	0	0
G32	86400	31052	0.345	0.186	31.007	16	0.019	15	1	0	0	0	0	0

Figure A.3.11: Septentrio analysis output file: GPS C2L signal, detailed results overview

PRN	n C2W Observations	n Epochs with Multipath Estimates	RMS Multipath [meters]	Weighted RMS Multipath [meters]	Average Sat. Elevation Angle [degrees]	n Slip Periods	Slip/Obs Ratio [%]	n Slip Periods Elevation Angle 0–10 degrees	n Slip Periods Elevation Angle 10–20 degrees	n Slip Periods Elevation Angle 20–30 degrees	n Slip Periods Elevation Angle 30–40 degrees	n Slip Periods Elevation Angle 40–50 degrees	n Slip Periods Elevation Angle >50 degrees	n Slip Periods Elevation Angle NaN degrees
G1	55284	29456	0.299	0.151	38.212	11	0.020	9	2	0	0	0	0	0
G2	86400	30798	0.313	0.212	32.035	43	0.050	41	2	0	0	0	0	0
G3	86400	29342	0.293	0.154	40.168	62	0.072	52	10	0	0	0	0	0
G4	54273	30756	0.358	0.154	37.469	4	0.007	4	0	0	0	0	0	0
G5	64614	31749	0.366	0.188	31.048	31	0.048	31	0	0	0	0	0	0
G6	86400	33127	0.398	0.232	30.715	29	0.034	29	0	0	0	0	0	0
G7	53708	30967	0.350	0.160	36.489	13	0.024	13	0	0	0	0	0	0
G8	54286	30649	0.275	0.148	34.491	3	0.006	2	1	0	0	0	0	0
G9	55106	28173	0.296	0.162	40.956	14	0.025	12	2	0	0	0	0	0
G10	64785	31448	0.319	0.180	34.322	9	0.014	8	1	0	0	0	0	0
G11	50316	23179	0.210	0.135	40.458	15	0.030	4	11	0	0	0	0	0
G12	86400	30989	0.317	0.145	38.778	31	0.036	28	3	0	0	0	0	0
G13	60054	28747	0.281	0.160	38.199	51	0.085	45	6	0	0	0	0	0
G14	86400	31823	0.302	0.190	32.176	45	0.052	44	1	0	0	0	0	0
G15	61996	29379	0.295	0.170	33.124	11	0.018	11	0	0	0	0	0	0
G16	53627	31695	0.295	0.172	32.395	15	0.028	15	0	0	0	0	0	0
G17	86211	32520	0.278	0.184	31.581	40	0.046	39	1	0	0	0	0	0
G18	4	3	0.014	0.002	10.188	0	0.000	0	0	0	0	0	0	0
G19	86400	32393	0.365	0.196	31.487	34	0.039	34	0	0	0	0	0	0
G20	64387	30543	0.313	0.192	32.768	26	0.040	26	0	0	0	0	0	0
G21	63937	32395	0.359	0.152	36.280	23	0.036	21	2	0	0	0	0	0
G22	86400	27967	0.292	0.158	41.575	31	0.036	20	11	0	0	0	0	0
G23	7	5	0.031	0.009	15.843	0	0.000	0	0	0	0	0	0	0
G24	86400	28987	0.266	0.151	37.849	65	0.075	65	0	0	0	0	0	0
G25	86400	27265	0.281	0.161	42.090	8	0.009	5	3	0	0	0	0	0
G26	54079	30692	0.279	0.158	33.187	22	0.041	21	1	0	0	0	0	0
G27	55094	29676	0.291	0.144	37.453	10	0.018	6	4	0	0	0	0	0
G28	52896	31333	0.312	0.200	34.852	23	0.043	13	10	0	0	0	0	0
G29	86400	30239	0.369	0.163	39.169	31	0.036	30	1	0	0	0	0	0
G30	54159	30342	0.381	0.158	37.695	12	0.022	11	1	0	0	0	0	0
G31	51059	30398	0.332	0.219	31.517	14	0.027	14	0	0	0	0	0	0
G32	86400	31897	0.380	0.206	31.119	17	0.020	16	1	0	0	0	0	0

Figure A.3.12: Septentrio analysis output file: GPS C2W signal, detailed results overview

PRN	n C5Q Observations	n Epochs with Multipath Estimates	RMS Multipath [meters]	Weighted RMS Multipath [meters]	Average Sat. Elevation Angle [degrees]	n Slip Periods	Slip/Obs Ratio [%]	n Slip Periods Elevation Angle 0–10 degrees	n Slip Periods Elevation Angle 10–20 degrees	n Slip Periods Elevation Angle 20–30 degrees	n Slip Periods Elevation Angle 30–40 degrees	n Slip Periods Elevation Angle 40–50 degrees	n Slip Periods Elevation Angle >50 degrees	n Slip Periods Elevation Angle NaN degrees
G1	52218	26820	0.217	0.105	40.270	9	0.017	9	0	0	0	0	0	0
G3	54710	26379	0.187	0.101	42.891	45	0.082	45	0	0	0	0	0	0
G4	54465	28485	0.265	0.108	38.728	4	0.007	4	0	0	0	0	0	0
G6	86400	32763	0.268	0.155	30.624	20	0.023	20	0	0	0	0	0	0
G8	53395	27014	0.194	0.112	36.708	1	0.002	0	1	0	0	0	0	0
G9	54865	27539	0.261	0.153	41.457	12	0.022	11	1	0	0	0	0	0
G10	64933	30589	0.247	0.141	34.809	10	0.015	9	1	0	0	0	0	0
G24	86400	28570	0.220	0.105	37.410	64	0.074	64	0	0	0	0	0	0
G25	86400	27367	0.221	0.112	41.167	5	0.006	4	1	0	0	0	0	0
G26	54288	30724	0.231	0.126	32.770	20	0.037	19	1	0	0	0	0	0
G27	54013	28512	0.254	0.123	37.904	7	0.013	7	0	0	0	0	0	0
G30	52280	27388	0.255	0.118	40.457	11	0.021	11	0	0	0	0	0	0
G32	86400	31217	0.256	0.165	31.118	16	0.019	15	1	0	0	0	0	0

Figure A.3.13: Septentrio analysis output file: GPS C5Q signal, detailed results overview

Galileo

PRN	n C1C Observations	n Epochs with Multipath Estimates	RMS Multipath [meters]	Weighted RMS Multipath [meters]	Average Sat. Elevation Angle [degrees]	n Slip Periods	Slip/Obs Ratio [%]	n Slip Periods Elevation Angle 0–10 degrees	n Slip Periods Elevation Angle 10–20 degrees	n Slip Periods Elevation Angle 20–30 degrees	n Slip Periods Elevation Angle 30–40 degrees	n Slip Periods Elevation Angle 40–50 degrees	n Slip Periods Elevation Angle >50 degrees	n Slip Periods Elevation Angle NaN degrees
E1	64914	40941	0.276	0.156	37.324	3	0.005	1	2	0	0	0	0	0
E2	48962	17462	0.337	0.111	21.326	5	0.010	3	2	0	0	0	0	0
E3	66958	21269	0.290	0.147	26.388	1	0.001	1	0	0	0	0	0	0
E4	69770	34290	0.280	0.140	38.831	9	0.013	6	3	0	0	0	0	0
E5	71090	32403	0.287	0.143	27.622	1	0.001	1	0	0	0	0	0	0
E7	49711	23588	0.291	0.147	40.570	2	0.004	2	0	0	0	0	0	0
E8	61006	20428	0.222	0.141	32.674	1	0.002	1	0	0	0	0	0	0
E9	71193	32533	0.268	0.123	33.056	15	0.021	13	2	0	0	0	0	0
E11	86400	21204	0.304	0.170	24.874	6	0.007	6	0	0	0	0	0	0
E12	51036	28720	0.280	0.161	33.460	1	0.002	1	0	0	0	0	0	0
E13	68752	36130	0.216	0.130	39.934	2	0.003	2	0	0	0	0	0	0
E14	55426	11980	0.342	0.118	28.896	1	0.002	1	0	0	0	0	0	0
E15	70476	35187	0.235	0.121	38.989	4	0.006	4	0	0	0	0	0	0
E18	44284	4229	0.263	0.149	28.236	1	0.002	1	0	0	0	0	0	0
E20	58446	0	NaN	NaN	NaN	1	0.002	0	0	0	0	0	0	1
E21	66475	44207	0.267	0.143	34.466	1	0.002	1	0	0	0	0	0	0
E24	57652	27934	0.316	0.143	38.954	2	0.003	2	0	0	0	0	0	0
E25	52446	17412	0.338	0.134	21.234	3	0.006	3	0	0	0	0	0	0
E26	58931	30228	0.272	0.126	40.562	6	0.010	4	2	0	0	0	0	0
E27	63086	38799	0.273	0.135	37.975	2	0.003	2	0	0	0	0	0	0
E30	55968	28486	0.218	0.120	37.848	1	0.002	1	0	0	0	0	0	0
E31	63602	36367	0.205	0.136	40.402	1	0.002	1	0	0	0	0	0	0

Figure A.3.14: Septentrio analysis output file: Galileo C1C signal, detailed results overview

PRN	n C5Q Observations	n Epochs with Multipath Estimates	RMS Multipath [meters]	Weighted RMS Multipath [meters]	Average Sat. Elevation Angle [degrees]	n Slip Periods	Slip/Obs Ratio [%]	n Slip Periods Elevation Angle 0–10 degrees	n Slip Periods Elevation Angle 10–20 degrees	n Slip Periods Elevation Angle 20–30 degrees	n Slip Periods Elevation Angle 30–40 degrees	n Slip Periods Elevation Angle 40–50 degrees	n Slip Periods Elevation Angle >50 degrees	n Slip Periods Elevation Angle NaN degrees
E1	65106	40936	0.171	0.100	37.222	4	0.006	3	1	0	0	0	0	0
E2	49116	17448	0.236	0.077	21.289	4	0.008	4	0	0	0	0	0	0
E3	60905	21268	0.242	0.124	25.232	1	0.002	1	0	0	0	0	0	0
E4	69496	34287	0.191	0.086	38.660	7	0.010	5	2	0	0	0	0	0
E5	71089	32398	0.268	0.114	27.536	2	0.003	2	0	0	0	0	0	0
E7	49915	23576	0.202	0.101	40.460	2	0.004	1	0	1	0	0	0	0
E8	61006	20427	0.211	0.115	32.679	1	0.002	1	0	0	0	0	0	0
E9	70030	32524	0.195	0.095	33.510	13	0.019	13	0	0	0	0	0	0
E11	61956	21180	0.229	0.127	25.150	2	0.003	2	0	0	0	0	0	0
E12	50960	28713	0.237	0.122	33.493	1	0.002	1	0	0	0	0	0	0
E13	69436	36118	0.188	0.094	40.520	3	0.004	2	1	0	0	0	0	0
E14	55393	11976	0.265	0.094	28.773	1	0.002	1	0	0	0	0	0	0
E15	70831	35184	0.183	0.090	38.762	4	0.006	4	0	0	0	0	0	0
E18	4527	4227	0.250	0.110	21.094	0	0.000	0	0	0	0	0	0	0
E21	66413	44183	0.256	0.114	34.427	2	0.003	2	0	0	0	0	0	0
E24	57238	27931	0.262	0.104	39.665	3	0.005	2	1	0	0	0	0	0
E25	51060	17407	0.202	0.068	22.091	4	0.008	4	0	0	0	0	0	0
E26	58025	30222	0.180	0.097	39.840	4	0.007	4	0	0	0	0	0	0
E27	63311	38793	0.163	0.112	37.871	3	0.005	3	0	0	0	0	0	0
E30	55910	28452	0.201	0.101	37.583	2	0.004	2	0	0	0	0	0	0
E31	61604	36360	0.191	0.129	41.974	2	0.003	2	0	0	0	0	0	0

Figure A.3.15: Septentrio analysis output file: Galileo C5Q signal, detailed results overview

GLONASS

Sat ID	Frequency Channel	n C1C Observations	n Epochs with Multipath Estimates	RMS Multipath [meters]	Weighted RMS Multipath [meters]	Average Sat. Elevation Angle [degrees]	n Slip Periods	Slip/Obs Ratio [%]	n Slip Periods Elevation Angle 0–10 degrees	n Slip Periods Elevation Angle 10–20 degrees	n Slip Periods Elevation Angle 20–30 degrees	n Slip Periods Elevation Angle 30–40 degrees	n Slip Periods Elevation Angle 40–50 degrees	n Slip Periods Elevation Angle >50 degrees	n Slip Periods Elevation Angle NaN degrees
R1	1	82176	29568	0.497	NaN	NaN	82	0.100	0	0	0	0	0	0	82
R2	−4	58468	30546	0.348	NaN	NaN	66	0.113	0	0	0	0	0	0	66
R3	5	60720	29031	0.532	NaN	NaN	45	0.074	0	0	0	0	0	0	45
R4	6	62309	31969	0.751	NaN	NaN	38	0.061	0	0	0	0	0	0	38
R5	1	82246	29395	0.393	NaN	NaN	15	0.018	0	0	0	0	0	0	15
R6	−4	86398	0	NaN	NaN	NaN	51	0.059	0	0	0	0	0	0	51
R7	5	86400	34565	0.624	0.319	54.954	52	0.060	17	1	0	0	0	0	34
R8	6	85995	31617	0.724	0.313	36.138	123	0.143	112	11	0	0	0	0	0
R9	−2	83383	33547	0.534	0.245	31.752	27	0.032	26	1	0	0	0	0	0
R10	−7	50294	0	NaN	NaN	NaN	12	0.024	0	0	0	0	0	0	12
R11	0	50050	28390	0.391	0.245	34.023	39	0.078	39	0	0	0	0	0	0
R12	−1	50429	25344	0.405	0.239	35.601	43	0.085	43	0	0	0	0	0	0
R13	−2	51086	27069	0.634	0.409	38.676	54	0.106	25	29	0	0	0	0	0
R14	−7	83413	33857	0.409	0.178	35.213	46	0.055	46	0	0	0	0	0	0
R15	0	86400	34774	0.400	0.247	43.052	66	0.076	66	0	0	0	0	0	0
R16	−1	86400	35304	0.420	0.270	41.278	34	0.039	32	2	0	0	0	0	0
R17	4	86400	35793	0.484	0.305	40.388	49	0.057	49	0	0	0	0	0	0
R18	−3	86400	34620	0.366	0.242	39.362	55	0.064	55	0	0	0	0	0	0
R19	3	81951	30565	0.794	0.468	38.440	69	0.084	59	9	0	0	0	0	1
R20	2	57405	30537	0.741	0.410	37.686	33	0.057	33	0	0	0	0	0	0
R21	4	55241	30461	0.608	0.265	37.169	20	0.036	20	0	0	0	0	0	0
R22	−3	52438	15068	0.438	0.206	37.939	40	0.076	39	1	0	0	0	0	0
R23	3	82900	30538	0.622	0.309	33.110	62	0.075	60	2	0	0	0	0	0
R24	2	86400	27965	0.461	0.365	34.810	100	0.116	61	39	0	0	0	0	0

Figure A.3.16: Septentrio analysis output file: GLONASS C1C signal, detailed results overview

Sat ID	Frequency Channel	n C2C Observations	n Epochs with Multipath Estimates	RMS Multipath [meters]	Weighted RMS Multipath [meters]	Average Sat. Elevation Angle [degrees]	n Slip Periods	Slip/Obs Ratio [%]	n Slip Periods Elevation Angle 0–10 degrees	n Slip Periods Elevation Angle 10–20 degrees	n Slip Periods Elevation Angle 20–30 degrees	n Slip Periods Elevation Angle 30–40 degrees	n Slip Periods Elevation Angle 40–50 degrees	n Slip Periods Elevation Angle >50 degrees	n Slip Periods Elevation Angle NaN degrees
R1	1	81943	29556	0.626	NaN	NaN	84	0.103	0	0	0	0	0	0	84
R2	−4	58313	30544	0.373	NaN	NaN	31	0.053	0	0	0	0	0	0	31
R3	5	60181	29025	0.392	NaN	NaN	12	0.020	0	0	0	0	0	0	12
R4	6	62072	31965	0.406	NaN	NaN	6	0.010	0	0	0	0	0	0	6
R5	1	82237	29392	0.345	NaN	NaN	13	0.016	0	0	0	0	0	0	13
R7	5	86400	34561	0.487	0.202	55.803	53	0.061	9	1	0	0	0	0	43
R8	6	85613	31604	0.434	0.225	36.863	82	0.096	76	6	0	0	0	0	0
R9	−2	83367	33542	0.402	0.190	31.879	30	0.036	30	0	0	0	0	0	0
R11	0	49728	28388	0.393	0.218	34.690	28	0.056	27	1	0	0	0	0	0
R12	−1	46178	25334	0.344	0.201	38.201	40	0.087	40	0	0	0	0	0	0
R13	−2	50075	27039	0.609	0.391	39.814	33	0.066	26	7	0	0	0	0	0
R14	−7	83278	33847	0.434	0.189	35.615	43	0.052	43	0	0	0	0	0	0
R15	0	86400	34767	0.334	0.203	43.780	67	0.078	66	1	0	0	0	0	0
R16	−1	86400	35300	0.544	0.336	41.699	46	0.053	43	3	0	0	0	0	0
R17	4	86400	35791	0.338	0.213	40.384	38	0.044	38	0	0	0	0	0	0
R18	−3	86400	34613	0.345	0.205	39.601	51	0.059	49	1	1	0	0	0	0
R19	3	81845	30541	0.474	0.275	38.257	54	0.066	51	3	0	0	0	0	0
R20	2	57405	30528	0.389	0.211	37.479	26	0.045	26	0	0	0	0	0	0
R21	4	54875	30456	0.408	0.197	37.534	18	0.033	18	0	0	0	0	0	0
R22	−3	38889	15059	0.433	0.202	26.248	26	0.067	22	4	0	0	0	0	0
R23	3	82503	30518	0.644	0.377	34.506	64	0.078	62	2	0	0	0	0	0
R24	2	86400	27896	0.932	0.710	36.269	38	0.044	11	24	3	0	0	0	0

Figure A.3.17: Septentrio analysis output file: GLONASS C2C signal, detailed results overview

BeiDou

PRN	n C2I Observations	n Epochs with Multipath Estimates	RMS Multipath [meters]	Weighted RMS Multipath [meters]	Average Sat. Elevation Angle [degrees]	n Slip Periods	Slip/Obs Ratio [%]	n Slip Periods Elevation Angle 0–10 degrees	n Slip Periods Elevation Angle 10–20 degrees	n Slip Periods Elevation Angle 20–30 degrees	n Slip Periods Elevation Angle 30–40 degrees	n Slip Periods Elevation Angle 40–50 degrees	n Slip Periods Elevation Angle >50 degrees	n Slip Periods Elevation Angle NaN degrees
C5	42270	42255	0.456	0.177	34.870	7	0.017	0	7	0	0	0	0	0
C12	4060	3265	0.588	0.278	19.755	2	0.049	0	2	0	0	0	0	0
C13	20322	18003	0.331	0.169	28.377	13	0.064	7	6	0	0	0	0	0
C19	1109	0	NaN	NaN	7.523	0	0.000	0	0	0	0	0	0	0
C21	17002	0	NaN	NaN	41.168	3	0.018	3	0	0	0	0	0	0
C22	10225	0	NaN	NaN	40.694	3	0.029	3	0	0	0	0	0	0
C24	4345	0	NaN	NaN	19.859	2	0.046	2	0	0	0	0	0	0

Figure A.3.18: Septentrio analysis output file: BeiDou C2I signal, detailed results overview

PRN	n C7I Observations	n Epochs with Multipath Estimates	RMS Multipath [meters]	Weighted RMS Multipath [meters]	Average Sat. Elevation Angle [degrees]	n Slip Periods	Slip/Obs Ratio [%]	n Slip Periods Elevation Angle 0–10 degrees	n Slip Periods Elevation Angle 10–20 degrees	n Slip Periods Elevation Angle 20–30 degrees	n Slip Periods Elevation Angle 30–40 degrees	n Slip Periods Elevation Angle 40–50 degrees	n Slip Periods Elevation Angle >50 degrees	n Slip Periods Elevation Angle NaN degrees
C5	42270	42255	0.281	0.112	34.870	0	0.000	0	0	0	0	0	0	0
C12	4247	3265	0.284	0.141	19.104	0	0.000	0	0	0	0	0	0	0
C13	20462	17996	0.311	0.190	28.497	25	0.122	15	10	0	0	0	0	0

Figure A.3.19: Septentrio analysis output file: BeiDou C7I signal, detailed results overview

A.3.5 Plotted Results

GPS

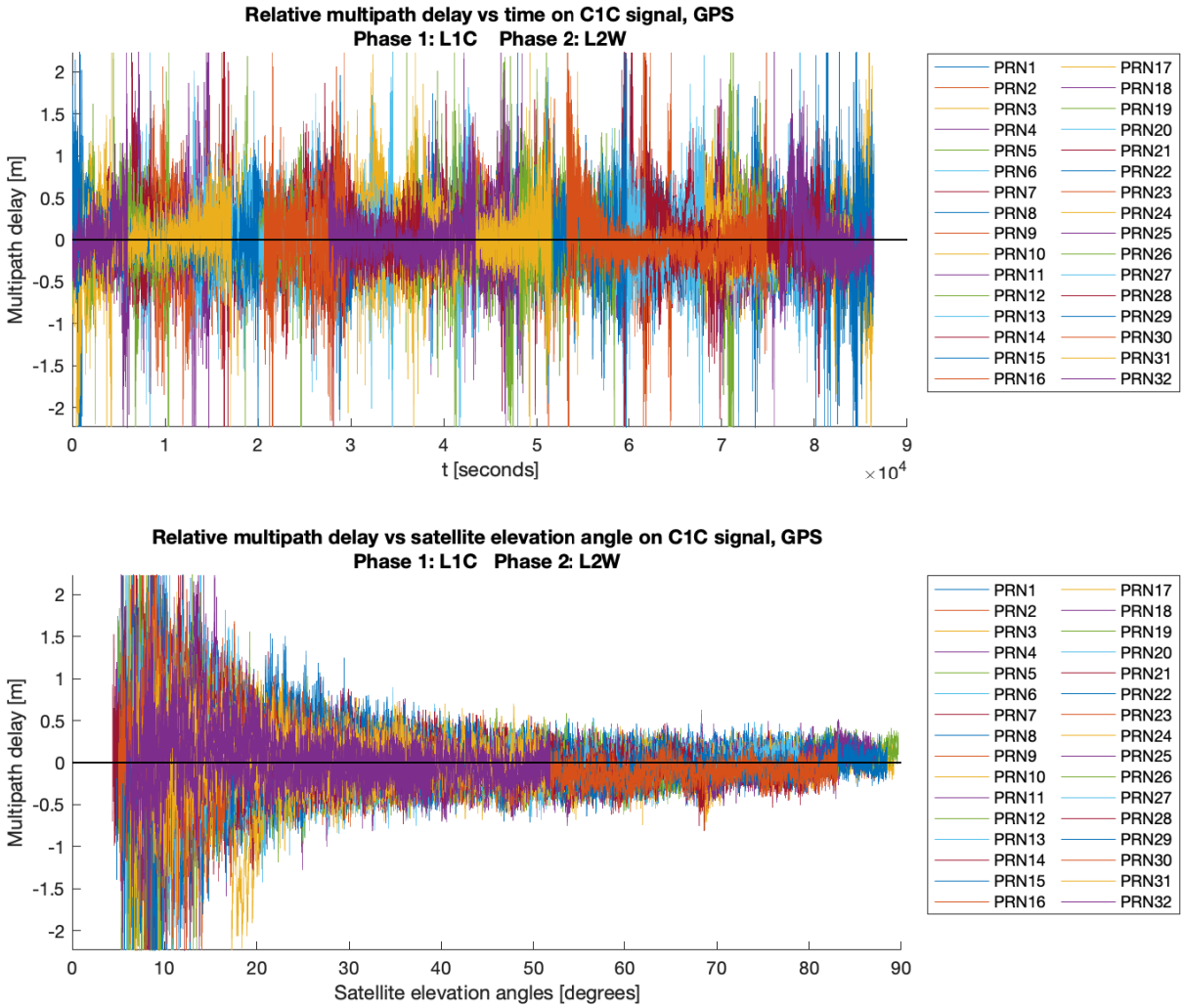

Figure A.3.20: Septentrio analysis results graph: GPS C1C signal, multipath effect vs. time and vs. satellite elevation angle. Graph has been cropped along y axis.

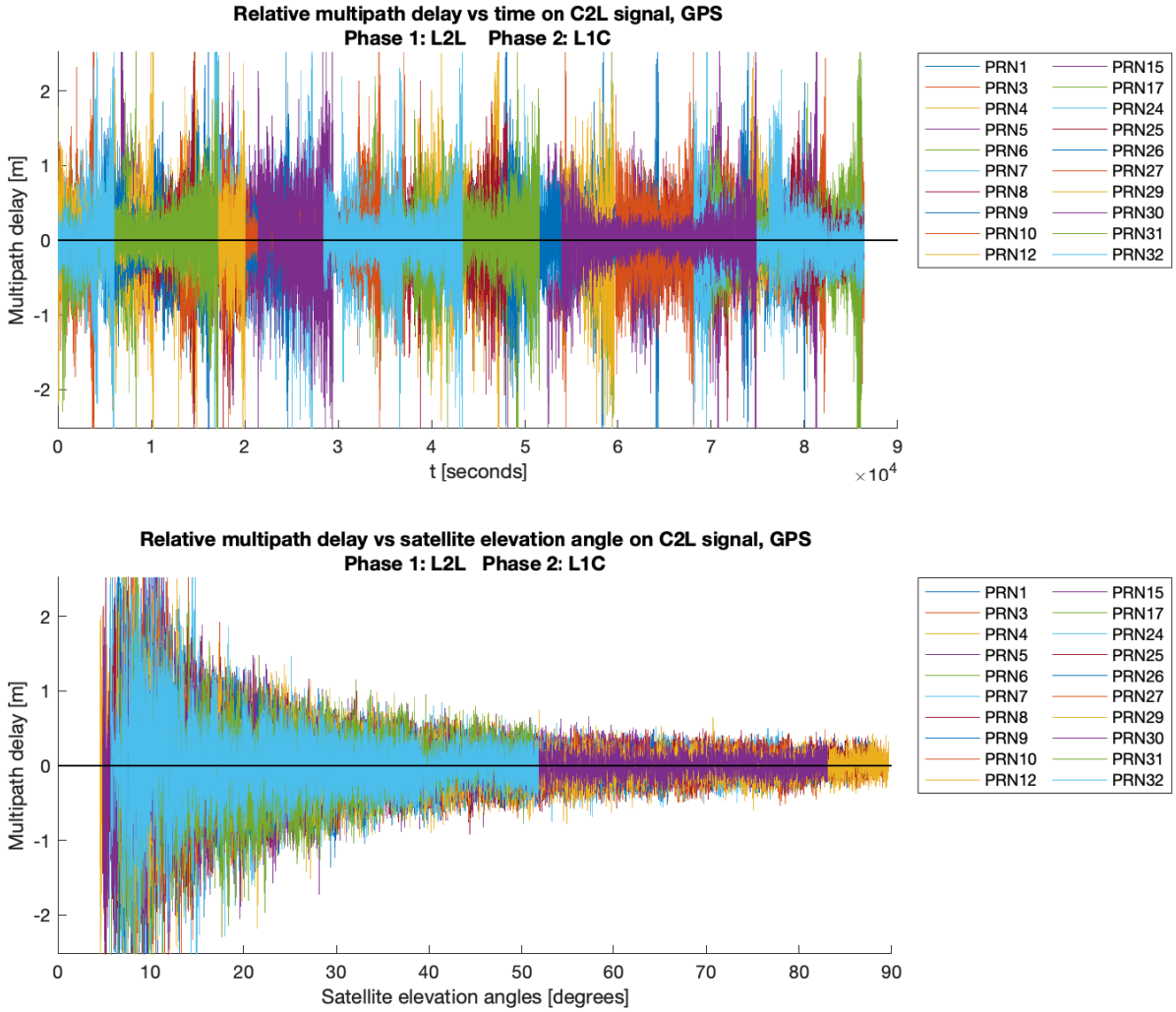

Figure A.3.21: Septentrio analysis results graph: GPS C2L signal, multipath effect vs. time and vs. satellite elevation angle. Graph has been cropped along y axis.

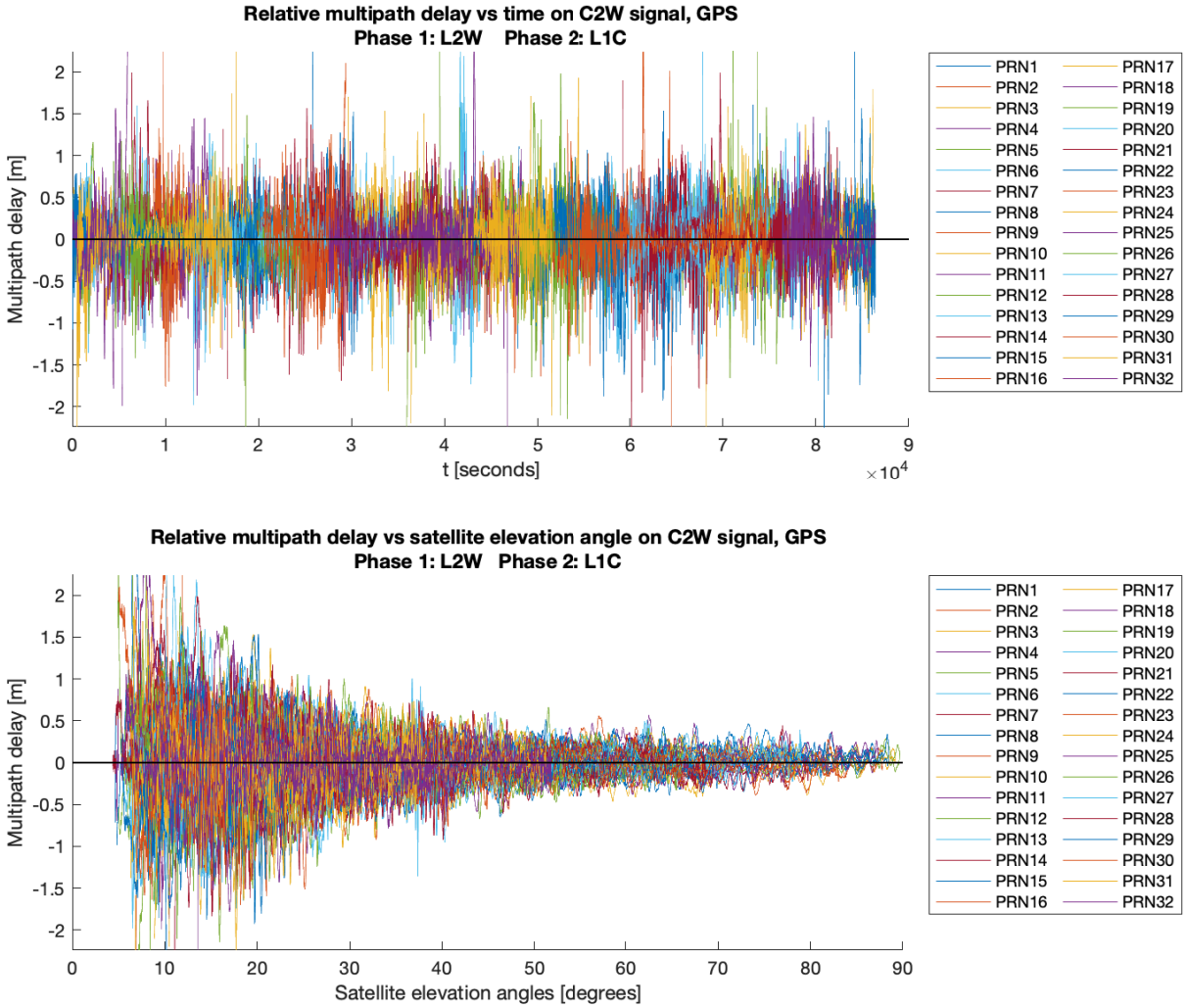

Figure A.3.22: Septentrio analysis results graph: GPS C2W signal, multipath effect vs. time and vs. satellite elevation angle. Graph has been cropped along y axis.

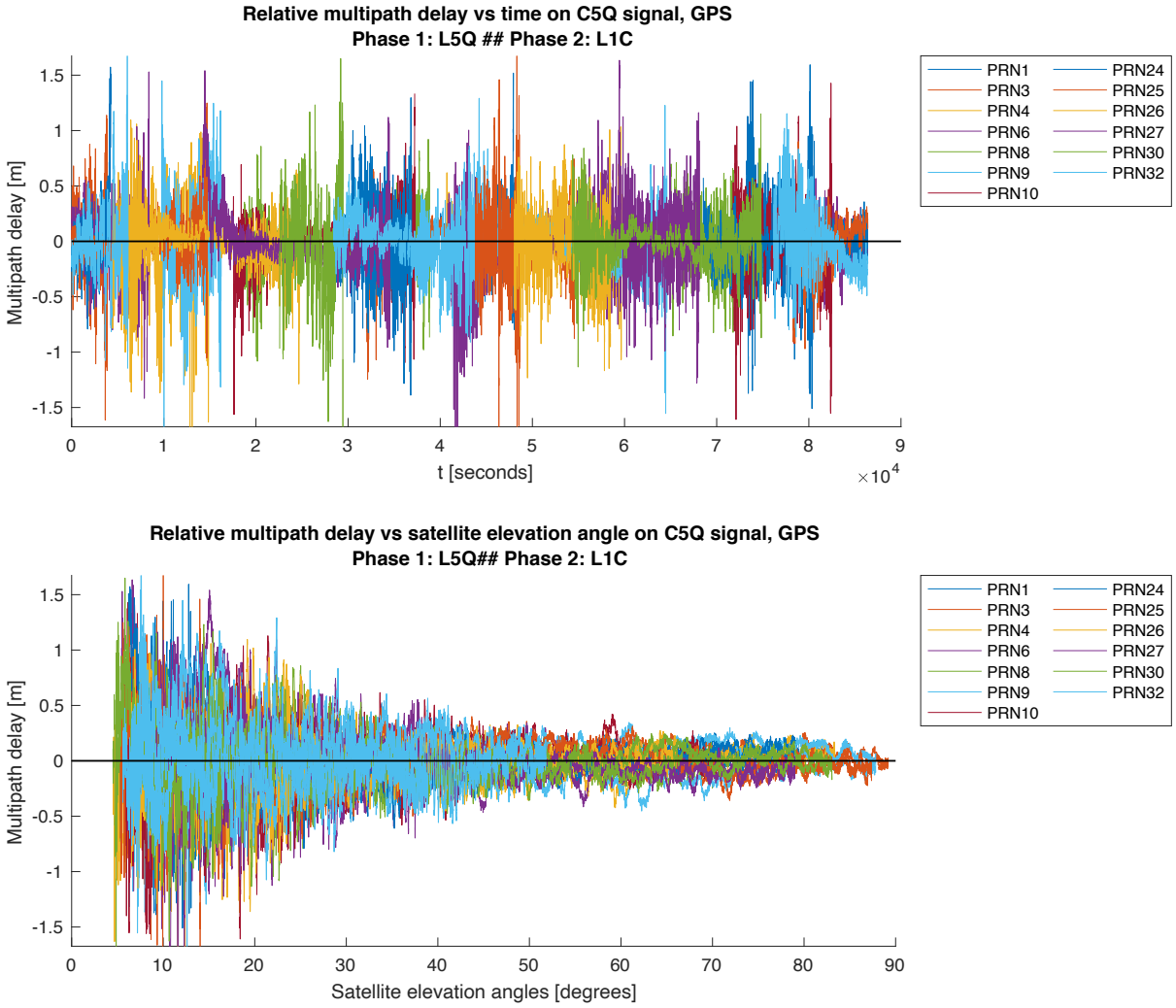

Figure A.3.23: Septentrio analysis results graph: GPS C5Q signal, multipath effect vs. time and vs. satellite elevation angle. Graph has been cropped along y axis.

Galileo

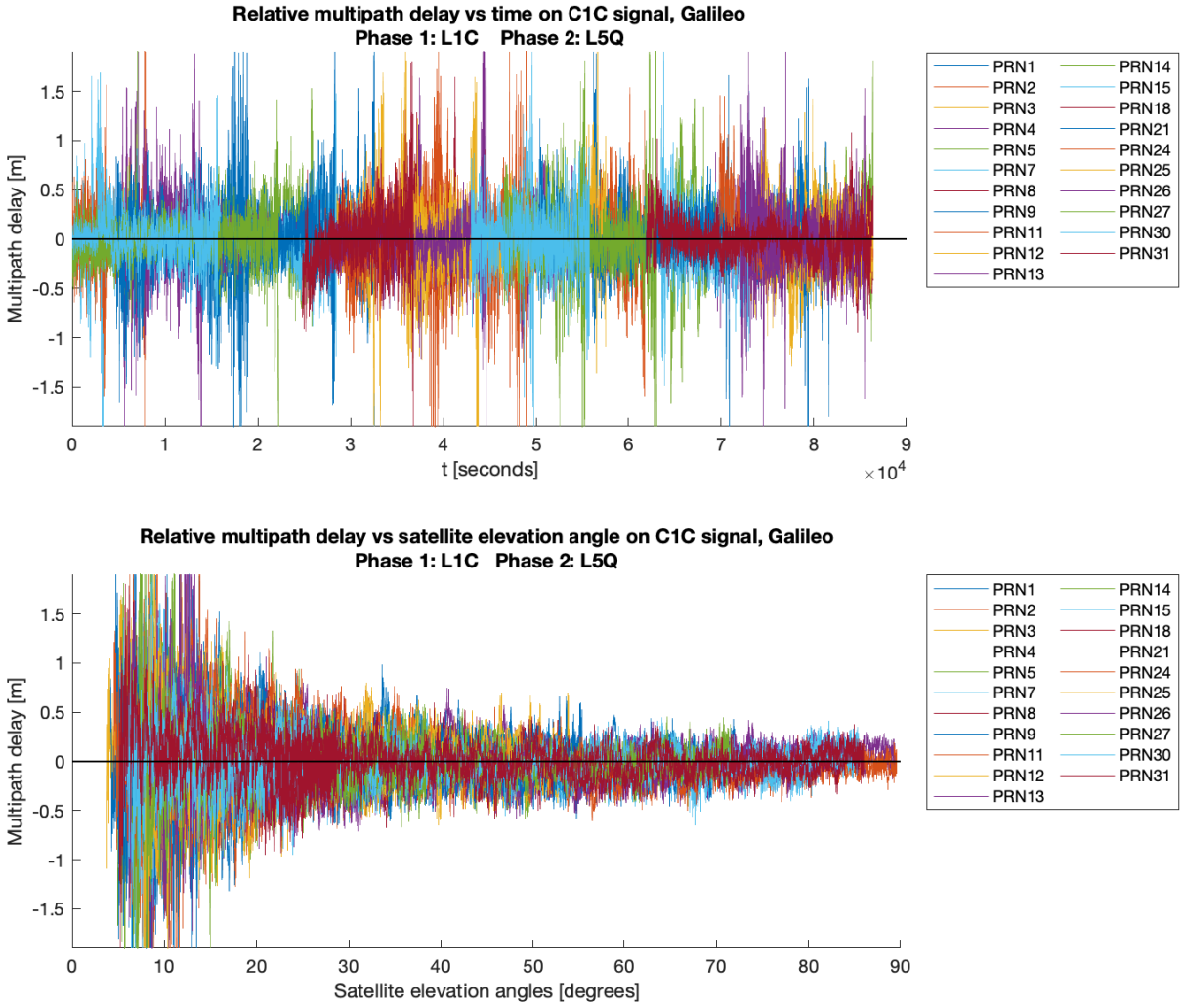

Figure A.3.24: Septentrio analysis results graph: Galileo C1C signal, multipath effect vs. time and vs. satellite elevation angle. Graph has been cropped along y axis.

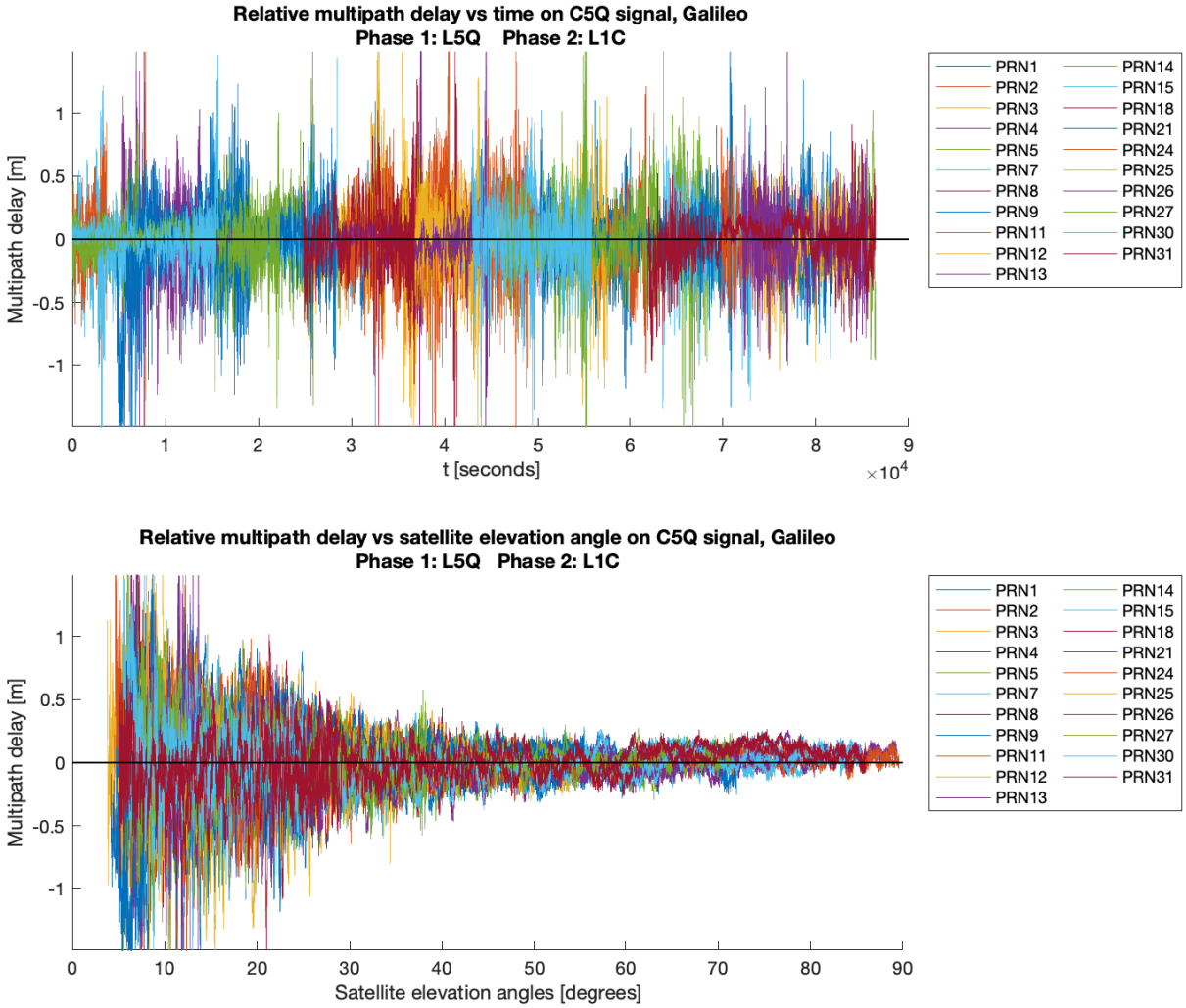

Figure A.3.25: Septentrio analysis results graph: Galileo C5Q signal, multipath effect vs. time and vs. satellite elevation angle. Graph has been cropped along y axis.

GLONASS

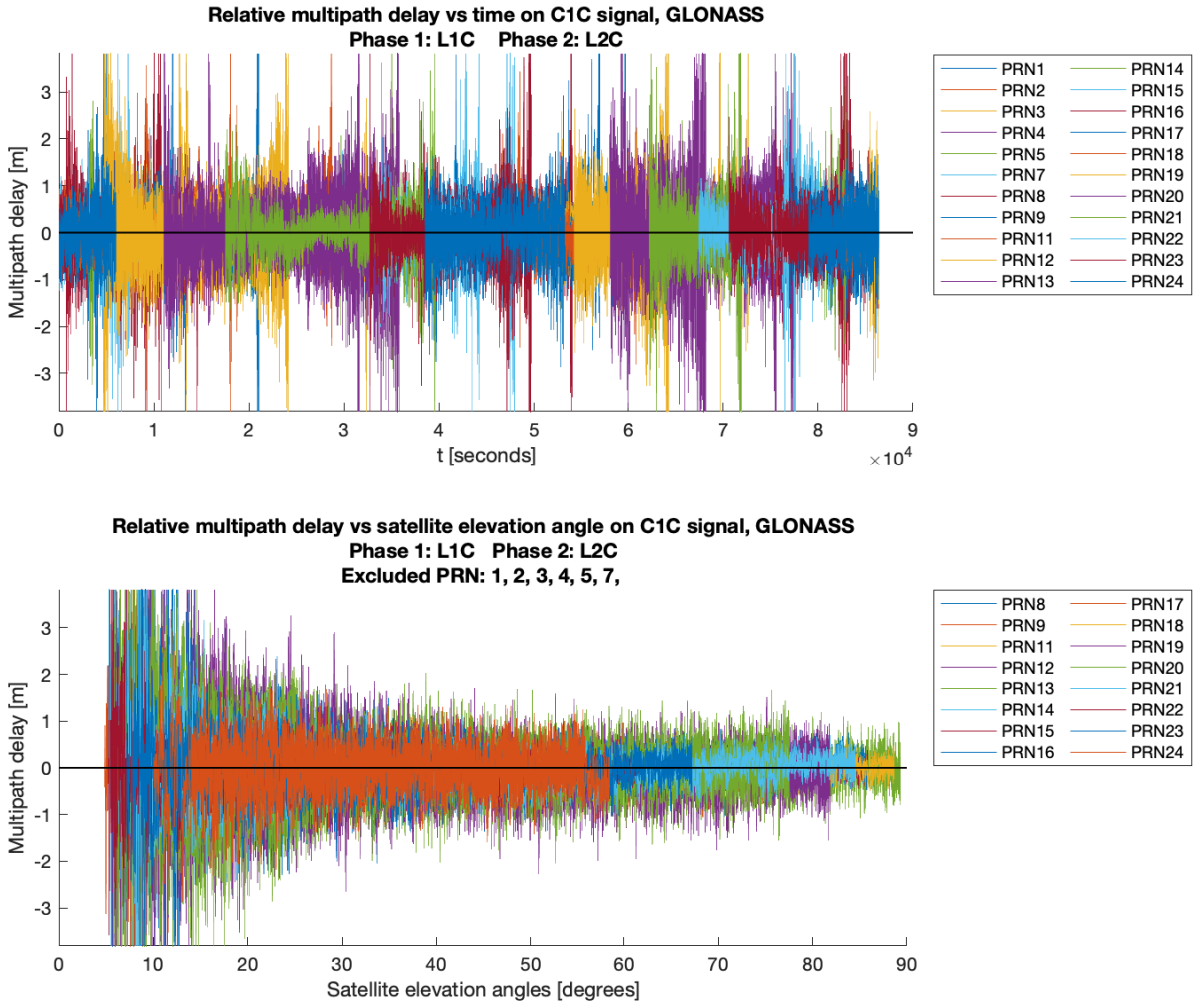

Figure A.3.26: Septentrio analysis results graph: GLONASS C1C signal, multipath effect vs. time and vs. satellite elevation angle. Graph has been cropped along y axis.

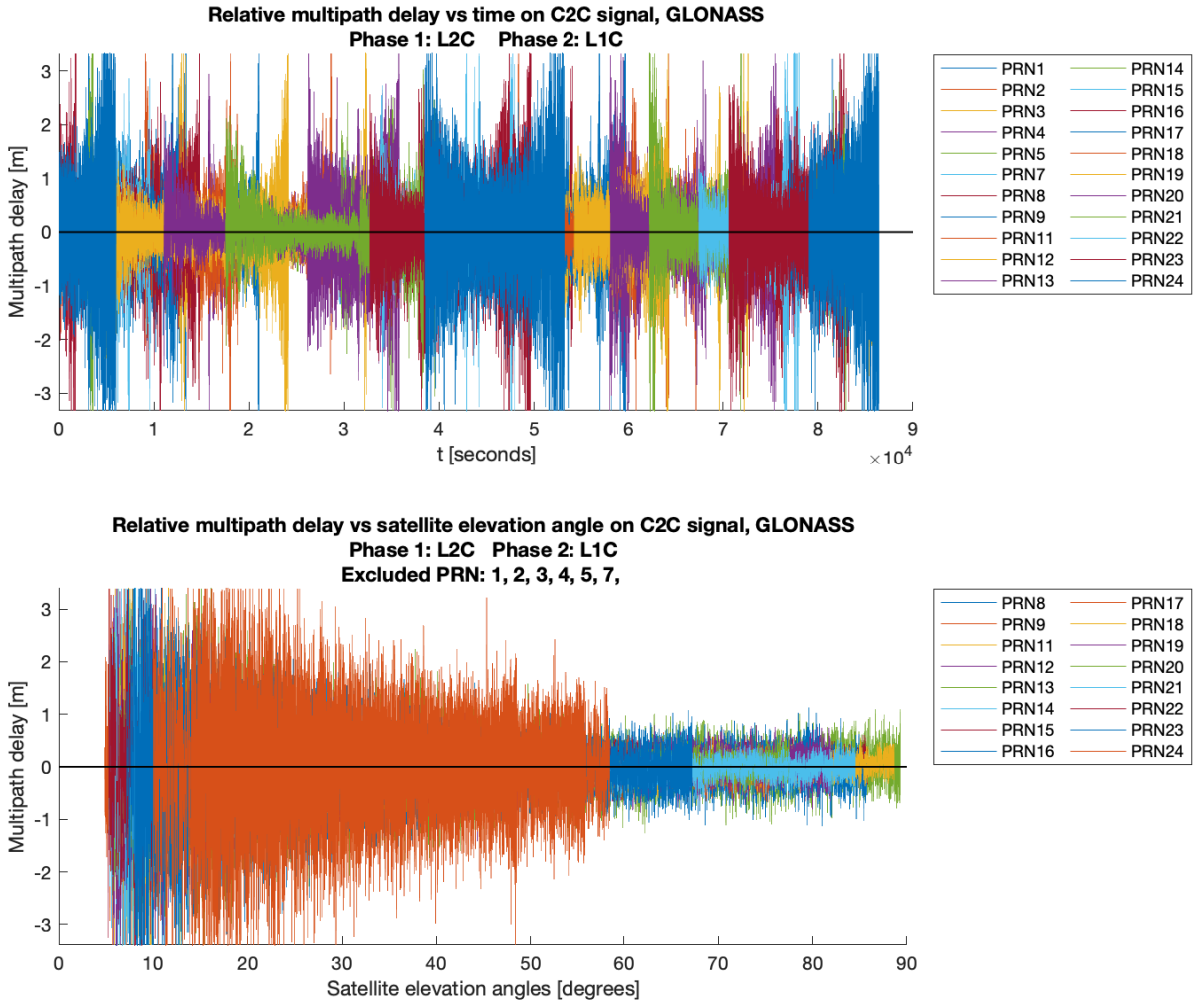

Figure A.3.27: Septentrio analysis results graph: GLONASS C2C signal, multipath effect vs. time and vs. satellite elevation angle. Graph has been cropped along y axis.

BeiDou

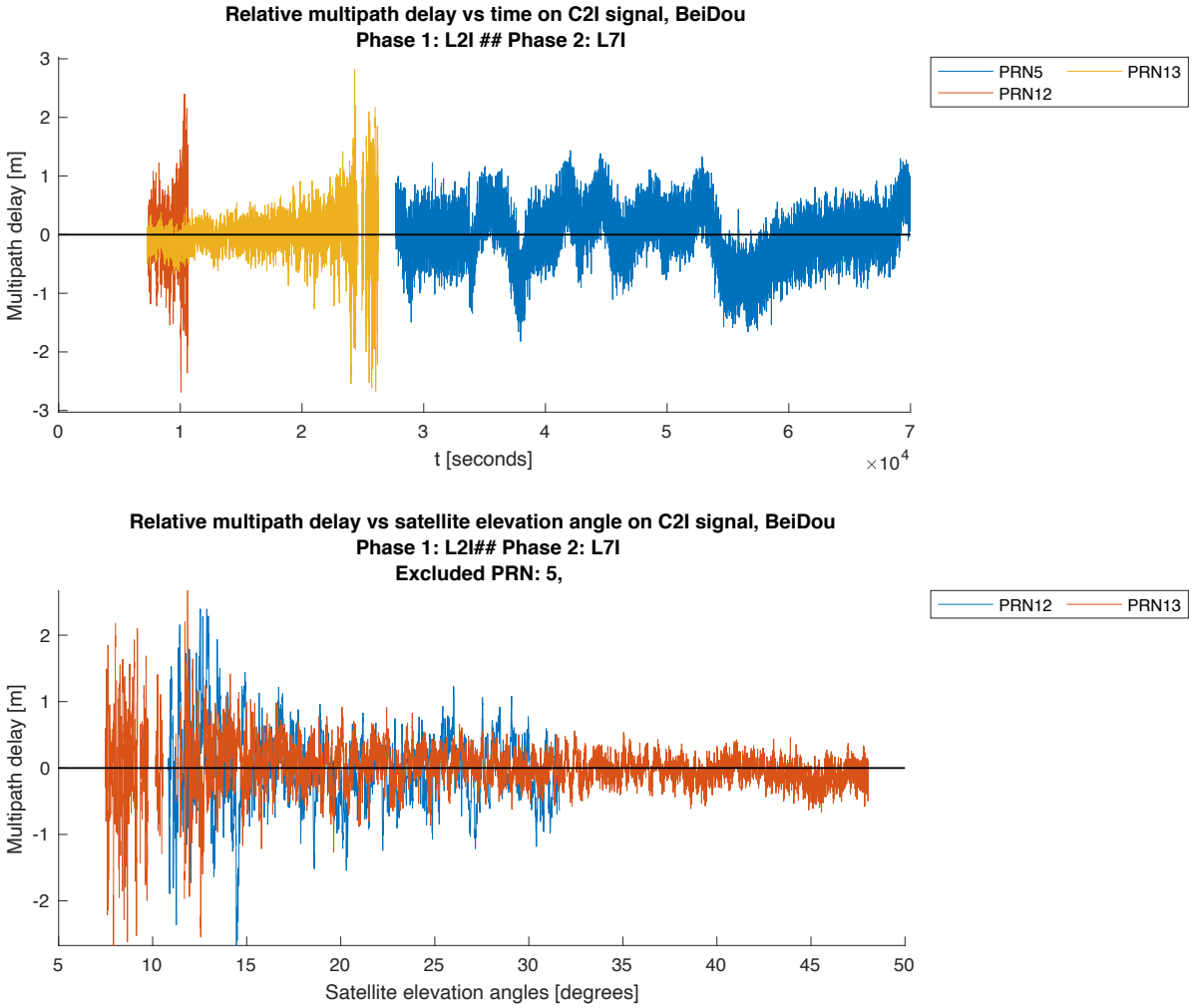

Figure A.3.28: Septentrio analysis results graph: BeiDou C2I signal, multipath effect vs. time and vs. satellite elevation angle. Graph has been cropped along y axis.

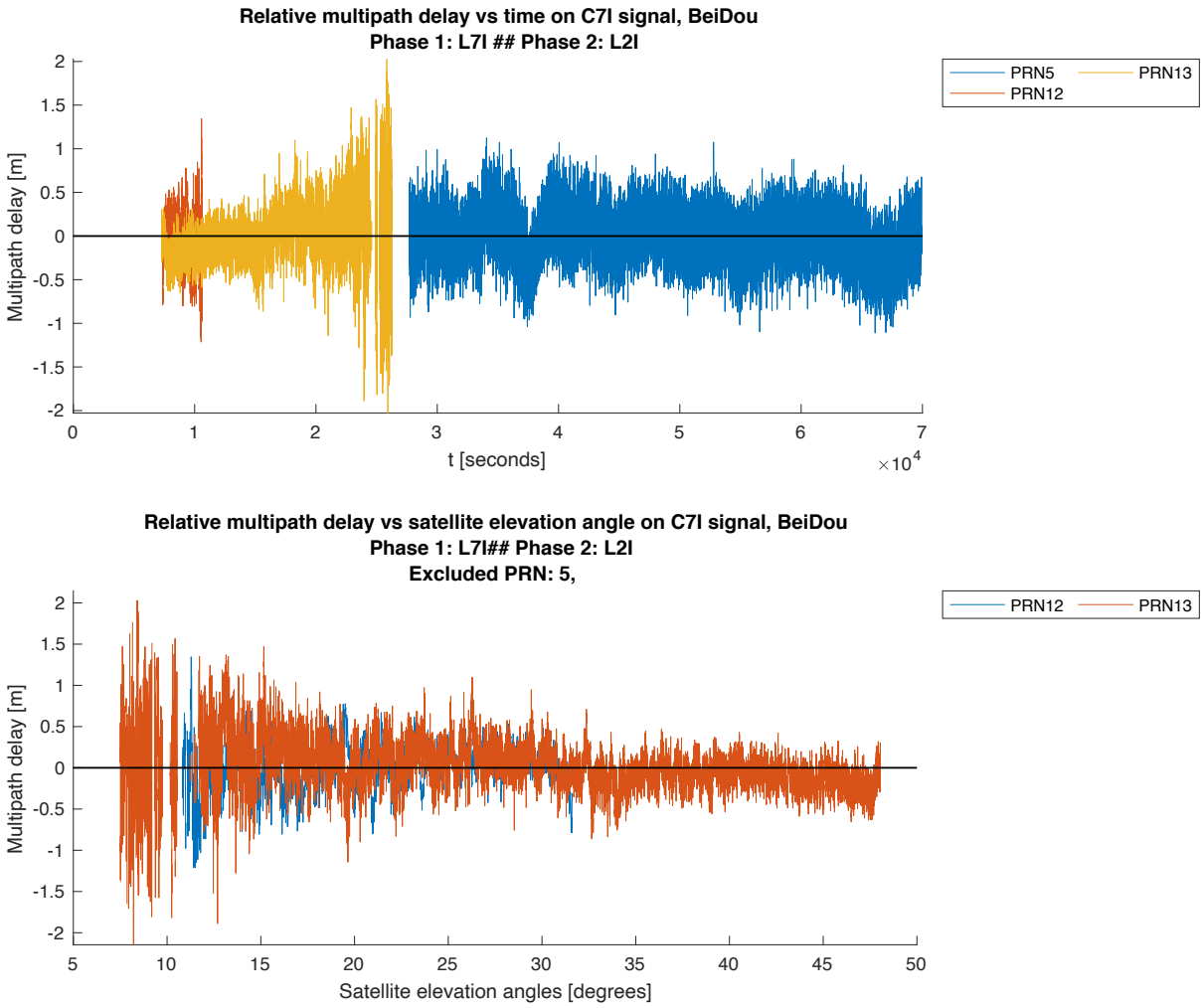

Figure A.3.29: Septentrio analysis results graph: BeiDou C7I signal, multipath effect vs. time and vs. satellite elevation angle. Graph has been cropped along y axis.

A.4 Trimble NETR5

A.4.1 Header

```
GNSS Receiver Quality Check 2020
Software version: 1.00
Last software version release: 02/06/2020

Software developed by Bjørn-Eirik Roald
Norwegian University of Life Sciences(NMBU)

RINEX observation filename:      FLO100XXX_R_20200901200_01D_01S_MO.rnx
RINEX version:                   3.04
RINEX converting program:        cnvtToRINEX 3.13.0
Marker name:                     FLO1
Receiver type:                   TRIMBLE NETR5
Date of observation start:       2020/3/30 12:20:0.00
Date of observation end:         2020/3/31 12:19:59.00
Observation interval [seconds]:  1
Number of receiver clock jumps:  0
Average clock jumps interval:    00:00:00 (std: 0.00 seconds)

Critical cycle slip limits [m/s]:
- Ionospheric delay:             0.067
- Phase-code combination:        6.667

GNSS systems presents in RINEX observation file:
- GPS
- GLONASS


User-specified contend included in output file
- Include overview of observations for each satellite:          Yes
- Include compact summary of analysis estimates:                Yes
- Include detailed summary of analysis
   estimates, including for each individual satellite:          Yes
- Include information about "Loss-of-Lock"
   indicators in detailed summary:                              No
```

Figure A.4.1: Trimble analysis output file: Header

A.4.2 Observation Overview

GPS Observation overview

PRN	L1 Observations	L2 Observations	L5 Observations
G1	C1C	C2X	C5X
G2	C1C	C2W	
G3	C1C	C2X	C5X
G4	C1C	C2X	C5X
G5	C1C	C2X	
G6	C1C	C2X	C5X
G7	C1C	C2X	
G8	C1C	C2X	C5X
G9	C1C	C2X	C5X
G10	C1C	C2X	C5X
G11	C1C	C2W	
G12	C1C	C2X	
G13	C1C	C2W	
G14	C1C	C2W	
G15	C1C	C2X	
G16	C1C	C2W	
G17	C1C	C2X	
G19	C1C	C2W	
G20	C1C	C2W	
G21	C1C	C2W	
G22	C1C	C2W	
G24	C1C	C2X	C5X
G25	C1C	C2X	C5X
G26	C1C	C2X	C5X
G27	C1C	C2X	C5X
G28	C1C	C2W	
G29	C1C	C2X	
G30	C1C	C2X	C5X
G31	C1C	C2X	
G32	C1C	C2X	C5X

Figure A.4.2: Trimble analysis output file: GPS observation overview

GLONASS Observation overview

Sat ID	Frequency Channel	G1 Observations	G2 Observations	G3 Observations	G1a Observations	G2a Observations
R1	1	C1C,C1P	C2P			
R2	-4	C1C,C1P	C2P			
R3	5	C1C,C1P	C2P			
R4	6	C1C,C1P	C2P			
R5	1	C1C,C1P	C2P			
R6	-4	C1C,C1P				
R7	5	C1C,C1P	C2P			
R8	6	C1C,C1P	C2P			
R9	-2	C1C,C1P	C2P			
R10	-7	C1C,C1P				
R11	0	C1C,C1P	C2P			
R12	-1	C1C,C1P	C2P			
R13	-2	C1C,C1P	C2P			
R14	-7	C1C,C1P	C2P			
R15	0	C1C,C1P	C2P			
R16	-1	C1C,C1P	C2P			
R17	4	C1C,C1P	C2P			
R18	-3	C1C,C1P	C2P			
R21	4	C1C,C1P	C2P			
R22	-3	C1C,C1P	C2P			
R23	3	C1C,C1P	C2P			
R24	2	C1C,C1P	C2P			

Figure A.4.3: Trimble analysis output file: GLONASS observation overview

A.4.3 Compressed Results Overview

GPS ANALYSIS SUMMARY

	C1C	C2W	C2X	C5X
RMS multipath[meters]	0.511	0.381	0.311	0.342
Weighted RMS multipath[meters]	0.384	0.367	0.246	0.280
N ambiguity slips periods	4380	32	3025	2014
N slip periods, elevation angle > 10 degrees	4071	31	2774	1854
N slip periods, elevation angle < 10 degrees	294	1	243	154
N slip periods, elevation angle not computed	15	0	8	6
Ratio of N slip periods/N obs epochs [%]	0.220	0.008	0.231	0.244

Figure A.4.4: Trimble analysis output file: GPS compressed results overview

GLONASS ANALYSIS SUMMARY

	C1C	C1P	C2P
RMS multipath[meters]	0.691	0.532	0.576
Weighted RMS multipath[meters]	0.553	0.425	0.495
N ambiguity slips periods	1519	1465	1125
N slip periods, elevation angle > 10 degrees	842	820	698
N slip periods, elevation angle < 10 degrees	107	103	90
N slip periods, elevation angle not computed	570	542	337
Ratio of N slip periods/N obs epochs [%]	0.103	0.099	0.084

Figure A.4.5: Trimble analysis output file: GLONASS compressed results overview

A.4.4 Detailed Results Overview

GPS

PRN	n C1C Observations	n Epochs with Multipath Estimates	RMS Multipath [meters]	Weighted RMS Multipath [meters]	Average Sat. Elevation Angle [degrees]	n Slip Periods	Slip/Obs Ratio [%]	n Slip Periods Elevation Angle 0–10 degrees	n Slip Periods Elevation Angle 10–20 degrees	n Slip Periods Elevation Angle 20–30 degrees	n Slip Periods Elevation Angle 30–40 degrees	n Slip Periods Elevation Angle 40–50 degrees	n Slip Periods Elevation Angle >50 degrees	n Slip Periods Elevation Angle NaN degrees
G1	52365	22021	0.511	0.391	45.773	199	0.380	0	167	30	1	0	0	1
G2	86400	0	NaN	NaN	32.535	132	0.153	0	130	2	0	0	0	0
G3	51319	18916	0.447	0.407	54.398	55	0.107	0	48	6	0	0	0	1
G4	52854	24709	0.545	0.386	42.542	230	0.435	0	218	11	0	0	0	1
G5	61422	26482	0.525	0.412	34.714	72	0.117	0	57	14	0	0	0	1
G6	86400	26190	0.511	0.429	35.029	115	0.133	0	103	12	0	0	0	0
G7	52517	27017	0.539	0.367	39.872	108	0.206	0	101	6	0	0	0	1
G8	51920	23915	0.541	0.395	39.756	194	0.374	0	134	59	0	0	0	1
G9	52102	22209	0.510	0.389	47.355	220	0.422	29	168	20	2	0	0	1
G10	63332	28117	0.515	0.360	36.501	122	0.193	43	79	0	0	0	0	0
G11	51342	0	NaN	NaN	44.998	126	0.245	0	124	2	0	0	0	0
G12	86400	24301	0.490	0.330	45.687	165	0.191	27	137	1	0	0	0	0
G13	58246	0	NaN	NaN	44.920	167	0.287	0	156	10	0	0	0	1
G14	86400	0	NaN	NaN	36.098	103	0.119	0	67	36	0	0	0	0
G15	61502	26006	0.542	0.359	35.571	133	0.216	0	130	3	0	0	0	0
G16	50934	0	NaN	NaN	37.557	117	0.230	0	83	33	0	0	0	1
G17	51696	29871	0.514	0.395	32.888	166	0.321	14	140	11	0	0	0	1
G19	86400	0	NaN	NaN	34.291	114	0.132	1	111	2	0	0	0	0
G20	62762	0	NaN	NaN	36.032	118	0.188	12	81	24	1	0	0	0
G21	60479	0	NaN	NaN	42.435	175	0.289	0	162	12	0	0	0	1
G22	86400	0	NaN	NaN	45.741	183	0.212	38	143	2	0	0	0	0
G24	86400	18908	0.435	0.385	50.928	35	0.041	0	19	16	0	0	0	0
G25	86400	19902	0.423	0.373	52.071	78	0.090	34	39	5	0	0	0	0
G26	50178	22409	0.537	0.403	39.681	208	0.415	0	78	129	0	0	0	1
G27	53287	23195	0.497	0.360	43.248	191	0.358	0	184	5	1	0	0	1
G28	49735	0	NaN	NaN	39.110	120	0.241	0	96	23	0	0	0	1
G29	86400	24700	0.512	0.353	44.605	183	0.212	4	175	4	0	0	0	0
G30	52581	22007	0.507	0.387	46.023	211	0.401	0	205	5	0	0	0	1
G31	86400	28878	0.537	0.412	31.995	179	0.207	44	127	8	0	0	0	0
G32	86400	30633	0.504	0.369	31.620	161	0.186	48	112	1	0	0	0	0

Figure A.4.6: Trimble analysis output file: GPS C1C signal, detailed results overview

PRN	n C2W Observations	n Epochs with Multipath Estimates	RMS Multipath [meters]	Weighted RMS Multipath [meters]	Average Sat. Elevation Angle [degrees]	n Slip Periods	Slip/Obs Ratio [%]	n Slip Periods Elevation Angle 0–10 degrees	n Slip Periods Elevation Angle 10–20 degrees	n Slip Periods Elevation Angle 20–30 degrees	n Slip Periods Elevation Angle 30–40 degrees	n Slip Periods Elevation Angle 40–50 degrees	n Slip Periods Elevation Angle >50 degrees	n Slip Periods Elevation Angle NaN degrees
G2	86400	22042	0.426	0.376	37.661	6	0.007	0	3	3	0	0	0	0
G11	13222	13221	0.284	0.284	57.359	2	0.015	0	0	0	2	0	0	0
G13	14887	14886	0.404	0.402	57.592	2	0.013	0	0	1	1	0	0	0
G14	86400	16900	0.443	0.438	41.692	4	0.005	0	1	2	1	0	0	0
G16	13021	13020	0.438	0.438	49.902	2	0.015	0	0	2	0	0	0	0
G19	86387	21201	0.345	0.318	39.351	6	0.007	1	2	3	0	0	0	0
G20	56852	14990	0.417	0.398	45.802	4	0.007	0	1	1	2	0	0	0
G21	14852	14851	0.358	0.358	59.049	2	0.013	0	0	0	2	0	0	0
G22	17482	17480	0.336	0.329	57.897	2	0.011	0	0	2	0	0	0	0
G28	11834	11833	0.279	0.279	55.388	2	0.017	0	0	0	1	1	0	0

Figure A.4.7: Trimble analysis output file: GPS C2W signal, detailed results overview

PRN	n C2X Observations	n Epochs with Multipath Estimates	RMS Multipath [meters]	Weighted RMS Multipath [meters]	Average Sat. Elevation Angle [degrees]	n Slip Periods	Slip/Obs Ratio [%]	n Slip Periods Elevation Angle 0–10 degrees	n Slip Periods Elevation Angle 10–20 degrees	n Slip Periods Elevation Angle 20–30 degrees	n Slip Periods Elevation Angle 30–40 degrees	n Slip Periods Elevation Angle 40–50 degrees	n Slip Periods Elevation Angle >50 degrees	n Slip Periods Elevation Angle NaN degrees
G1	52360	22021	0.288	0.239	45.794	199	0.380	0	168	30	1	0	0	0
G3	51319	18916	0.269	0.252	54.417	55	0.107	0	48	6	0	0	0	1
G4	52854	24709	0.300	0.227	42.564	230	0.435	0	218	11	0	0	0	1
G5	61422	26482	0.335	0.274	34.714	72	0.117	0	57	14	0	0	0	1
G6	86400	26190	0.297	0.261	35.036	115	0.133	0	103	12	0	0	0	0
G7	52517	27017	0.346	0.242	39.877	108	0.206	0	101	6	0	0	0	1
G8	51920	23915	0.300	0.240	39.760	194	0.374	0	134	59	0	0	0	1
G9	52102	22209	0.309	0.245	47.376	220	0.422	29	168	20	2	0	0	1
G10	63326	28117	0.314	0.236	36.505	122	0.193	43	79	0	0	0	0	0
G12	86400	24301	0.313	0.234	45.702	165	0.191	27	137	1	0	0	0	0
G15	61496	26006	0.352	0.245	35.576	133	0.216	0	130	3	0	0	0	0
G17	51690	29871	0.321	0.258	32.900	166	0.321	14	141	11	0	0	0	0
G24	86400	18908	0.255	0.238	50.928	35	0.041	0	19	16	0	0	0	0
G25	86400	19902	0.267	0.242	52.089	78	0.090	34	39	5	0	0	0	0
G26	50178	22409	0.298	0.244	39.681	208	0.415	0	78	129	0	0	0	1
G27	53287	23195	0.284	0.227	43.248	191	0.358	0	184	5	1	0	0	1
G29	86400	24700	0.342	0.249	44.626	183	0.212	4	175	4	0	0	0	0
G30	52575	22007	0.303	0.243	46.073	211	0.401	0	206	5	0	0	0	0
G31	86400	28878	0.329	0.262	32.005	179	0.207	44	127	8	0	0	0	0
G32	86400	30633	0.319	0.250	31.630	161	0.186	48	112	1	0	0	0	0

Figure A.4.8: Trimble analysis output file: GPS C2X signal, detailed results overview

PRN	n C5X Observations	n Epochs with Multipath Estimates	RMS Multipath [meters]	Weighted RMS Multipath [meters]	Average Sat. Elevation Angle [degrees]	n Slip Periods	Slip/Obs Ratio [%]	n Slip Periods Elevation Angle 0–10 degrees	n Slip Periods Elevation Angle 10–20 degrees	n Slip Periods Elevation Angle 20–30 degrees	n Slip Periods Elevation Angle 30–40 degrees	n Slip Periods Elevation Angle 40–50 degrees	n Slip Periods Elevation Angle >50 degrees	n Slip Periods Elevation Angle NaN degrees
G1	52364	22027	0.304	0.243	45.779	199	0.380	0	168	30	1	0	0	0
G3	51319	18925	0.296	0.279	54.402	55	0.107	0	48	6	0	0	0	1
G4	52854	24703	0.357	0.259	42.548	230	0.435	0	218	11	0	0	0	1
G6	86400	26193	0.393	0.341	35.030	115	0.133	0	103	12	0	0	0	0
G8	51920	23903	0.335	0.264	39.757	194	0.374	0	134	59	0	0	0	1
G9	52102	22201	0.343	0.294	47.361	220	0.422	29	168	20	2	0	0	1
G10	63330	28096	0.375	0.288	36.527	117	0.185	43	74	0	0	0	0	0
G24	86400	18907	0.273	0.253	50.928	35	0.041	0	19	16	0	0	0	0
G25	86400	19904	0.303	0.277	52.075	78	0.090	34	39	5	0	0	0	0
G26	50178	22404	0.340	0.281	39.681	208	0.415	0	78	129	0	0	0	1
G27	53287	23179	0.319	0.244	43.248	191	0.358	0	184	5	1	0	0	1
G30	52579	22018	0.355	0.281	46.037	211	0.401	0	206	5	0	0	0	0
G32	86400	30627	0.376	0.299	31.623	161	0.186	48	112	1	0	0	0	0

Figure A.4.9: Trimble analysis output file: GPS C5X signal, detailed results overview

GLONASS

Sat ID	Frequency Channel	n C1C Observations	n Epochs with Multipath Estimates	RMS Multipath [meters]	Weighted RMS Multipath [meters]	Average Sat. Elevation Angle [degrees]	n Slip Periods	Slip/Obs Ratio [%]	n Slip Periods Elevation Angle 0–10 degrees	n Slip Periods Elevation Angle 10–20 degrees	n Slip Periods Elevation Angle 20–30 degrees	n Slip Periods Elevation Angle 30–40 degrees	n Slip Periods Elevation Angle 40–50 degrees	n Slip Periods Elevation Angle >50 degrees	n Slip Periods Elevation Angle NaN degrees
R1	1	49252	18045	0.692	NaN	NaN	80	0.162	0	0	0	0	0	0	80
R2	−4	56074	26084	0.696	NaN	NaN	92	0.164	0	0	0	0	0	0	92
R3	5	58587	25860	0.658	NaN	NaN	54	0.092	0	0	0	0	0	0	54
R4	6	59681	27150	0.678	NaN	NaN	39	0.065	0	0	0	0	0	0	39
R5	1	61977	28747	0.638	NaN	NaN	56	0.090	0	0	0	0	0	0	56
R6	−4	83556	0	NaN	NaN	NaN	160	0.191	0	0	0	0	0	0	160
R7	5	86400	29810	0.702	0.516	61.498	66	0.076	6	29	3	0	0	0	28
R8	6	81962	23947	0.815	0.636	44.490	117	0.143	0	66	50	0	0	0	1
R9	−2	82262	28340	0.725	0.540	35.590	105	0.128	17	85	2	0	0	0	1
R10	−7	48548	0	NaN	NaN	NaN	53	0.109	0	0	0	0	0	0	53
R11	0	48146	26541	0.649	0.518	36.776	21	0.044	2	13	3	2	0	0	1
R12	−1	48751	26747	0.666	0.506	38.686	41	0.084	17	20	3	0	0	0	1
R13	−2	10706	10442	0.915	0.915	65.936	54	0.504	0	0	0	30	9	14	1
R14	−7	82976	31474	0.751	0.456	37.761	53	0.064	25	28	0	0	0	0	0
R15	0	86400	31808	0.617	0.445	46.720	41	0.047	16	22	3	0	0	0	0
R16	−1	86400	23350	0.696	0.644	53.463	22	0.025	0	17	5	0	0	0	0
R17	4	86400	33056	0.631	0.517	43.060	45	0.052	5	40	0	0	0	0	0
R18	−3	85763	31547	0.673	0.548	42.464	48	0.056	2	38	7	0	0	0	1
R21	4	51755	24582	0.686	0.506	43.287	40	0.077	10	24	5	0	0	0	1
R22	−3	50886	26173	0.692	0.510	40.650	147	0.289	4	102	36	4	0	0	1
R23	3	82202	24634	0.639	0.541	38.047	45	0.055	3	36	6	0	0	0	0
R24	2	86020	16443	0.734	0.734	41.625	140	0.163	0	39	94	7	0	0	0

Figure A.4.10: Trimble analysis output file: GLONASS C1C signal, detailed results overview

Sat ID	Frequency Channel	n C1P Observations	n Epochs with Multipath Estimates	RMS Multipath [meters]	Weighted RMS Multipath [meters]	Average Sat. Elevation Angle [degrees]	n Slip Periods	Slip/Obs Ratio [%]	n Slip Periods Elevation Angle 0–10 degrees	n Slip Periods Elevation Angle 10–20 degrees	n Slip Periods Elevation Angle 20–30 degrees	n Slip Periods Elevation Angle 30–40 degrees	n Slip Periods Elevation Angle 40–50 degrees	n Slip Periods Elevation Angle >50 degrees	n Slip Periods Elevation Angle NaN degrees
R1	1	49252	18047	0.521	NaN	NaN	78	0.158	0	0	0	0	0	0	78
R2	−4	56052	26105	0.529	NaN	NaN	83	0.148	0	0	0	0	0	0	83
R3	5	58586	25875	0.507	NaN	NaN	51	0.087	0	0	0	0	0	0	51
R4	6	59671	27163	0.519	NaN	NaN	37	0.062	0	0	0	0	0	0	37
R5	1	61976	28760	0.535	NaN	NaN	52	0.084	0	0	0	0	0	0	52
R6	−4	83556	0	NaN	NaN	NaN	156	0.187	0	0	0	0	0	0	156
R7	5	86400	29825	0.576	0.413	61.525	63	0.073	6	27	3	0	0	0	27
R8	6	81962	23956	0.596	0.472	44.561	110	0.134	0	61	48	0	0	0	1
R9	−2	82262	28379	0.531	0.408	35.704	85	0.103	10	71	3	0	0	0	1
R10	−7	48548	0	NaN	NaN	NaN	54	0.111	0	0	0	0	0	0	54
R11	0	48146	26538	0.527	0.420	36.791	22	0.046	2	14	3	2	0	0	1
R12	−1	48750	26728	0.524	0.408	38.781	48	0.098	23	22	3	0	0	0	0
R13	−2	10706	10432	0.550	0.550	66.052	56	0.523	0	0	0	32	10	13	1
R14	−7	82976	31468	0.595	0.378	37.817	53	0.064	24	29	0	0	0	0	0
R15	0	86400	31816	0.507	0.374	46.734	42	0.049	16	23	3	0	0	0	0
R16	−1	86400	23346	0.472	0.440	53.585	28	0.032	0	23	5	0	0	0	0
R17	4	86400	33060	0.510	0.425	43.074	43	0.050	4	39	0	0	0	0	0
R18	−3	85763	31558	0.515	0.423	42.486	47	0.055	1	41	5	0	0	0	0
R21	4	51754	24591	0.551	0.408	43.298	40	0.077	10	24	6	0	0	0	0
R22	−3	50880	26245	0.519	0.386	40.705	131	0.257	4	95	32	0	0	0	0
R23	3	82202	24638	0.520	0.444	38.051	45	0.055	3	36	6	0	0	0	0
R24	2	86020	16443	0.527	0.527	41.708	141	0.164	0	41	93	7	0	0	0

Figure A.4.11: Trimble analysis output file: GLONASS C1P signal, detailed results overview

Sat ID	Frequency Channel	n C2P Observations	n Epochs with Multipath Estimates	RMS Multipath [meters]	Weighted RMS Multipath [meters]	Average Sat. Elevation Angle [degrees]	n Slip Periods	Slip/Obs Ratio [%]	n Slip Periods Elevation Angle 0–10 degrees	n Slip Periods Elevation Angle 10–20 degrees	n Slip Periods Elevation Angle 20–30 degrees	n Slip Periods Elevation Angle 30–40 degrees	n Slip Periods Elevation Angle 40–50 degrees	n Slip Periods Elevation Angle >50 degrees	n Slip Periods Elevation Angle NaN degrees
R1	1	48925	18045	0.596	NaN	NaN	63	0.129	0	0	0	0	0	0	63
R2	−4	56054	26084	0.474	NaN	NaN	80	0.143	0	0	0	0	0	0	80
R3	5	58412	25860	0.459	NaN	NaN	55	0.094	0	0	0	0	0	0	55
R4	6	59671	27150	0.503	NaN	NaN	56	0.094	0	0	0	0	0	0	56
R5	1	61972	28747	0.461	NaN	NaN	52	0.084	0	0	0	0	0	0	52
R7	5	86400	29810	0.509	0.369	61.531	62	0.072	5	27	3	0	0	0	27
R8	6	81962	23947	0.513	0.399	44.561	112	0.137	0	62	49	0	0	0	1
R9	−2	82262	28340	0.500	0.389	35.709	80	0.097	8	69	2	0	0	0	1
R11	0	48146	26541	0.486	0.376	36.819	21	0.044	2	13	3	2	0	0	1
R12	−1	48746	26747	0.494	0.378	38.793	44	0.090	20	21	3	0	0	0	0
R13	−2	10706	10442	0.371	0.371	66.054	53	0.495	0	0	0	30	9	13	1
R14	−7	82976	31474	0.595	0.386	37.885	50	0.060	22	28	0	0	0	0	0
R15	0	86400	31808	0.462	0.342	46.775	39	0.045	13	23	3	0	0	0	0
R16	−1	86400	23350	0.380	0.355	53.728	17	0.020	0	13	4	0	0	0	0
R17	4	86400	33056	0.439	0.372	43.086	42	0.049	4	38	0	0	0	0	0
R18	−3	85753	31547	0.466	0.398	42.504	46	0.054	1	40	5	0	0	0	0
R21	4	51750	24582	0.538	0.377	43.304	40	0.077	10	24	6	0	0	0	0
R22	−3	50881	26173	0.508	0.379	40.721	130	0.255	4	94	32	0	0	0	0
R23	3	81847	24634	0.966	0.686	39.599	38	0.046	1	29	8	0	0	0	0
R24	2	83799	16443	1.418	1.418	47.471	45	0.054	0	6	30	7	2	0	0

Figure A.4.12: Trimble analysis output file: GLONASS C2P signal, detailed results overview

A.4.5 Plotted Results

GPS

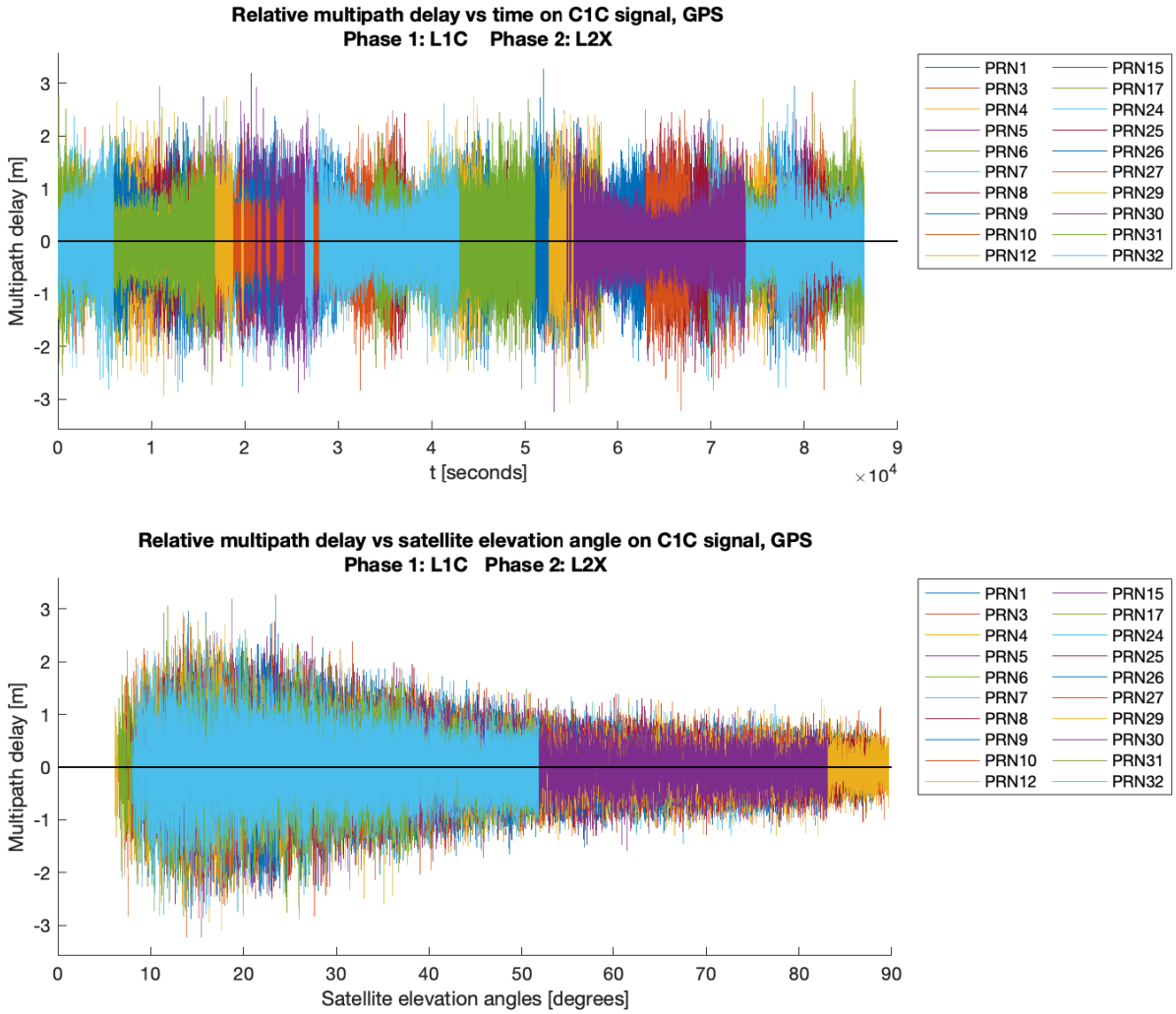

Figure A.4.13: Trimble analysis results graph: GPS C1C signal, multipath effect vs. time and vs. satellite elevation angle. Graph has been cropped along y axis.

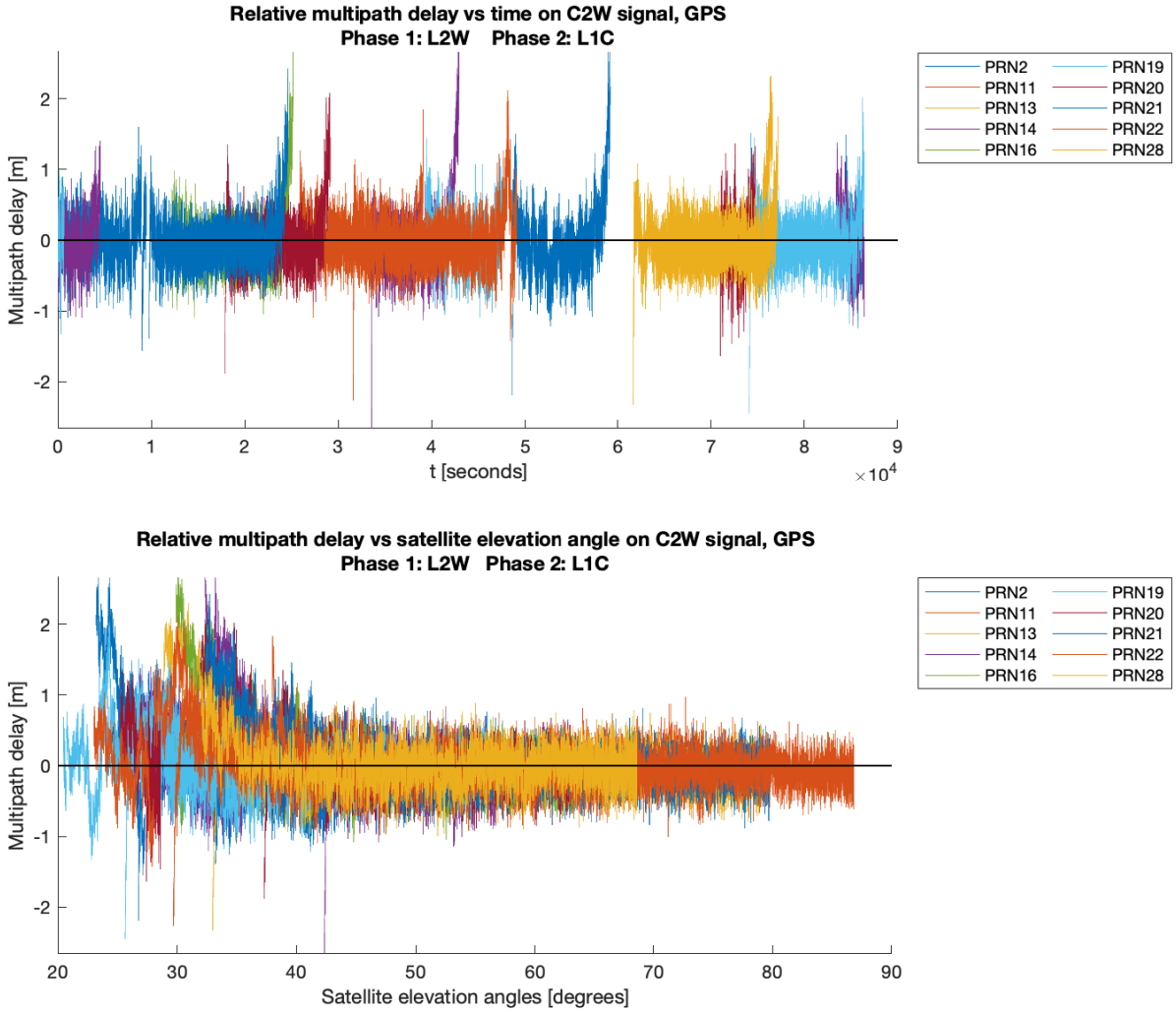

Figure A.4.14: Trimble analysis results graph: GPS C2W signal, multipath effect vs. time and vs. satellite elevation angle. Graph has been cropped along y axis.

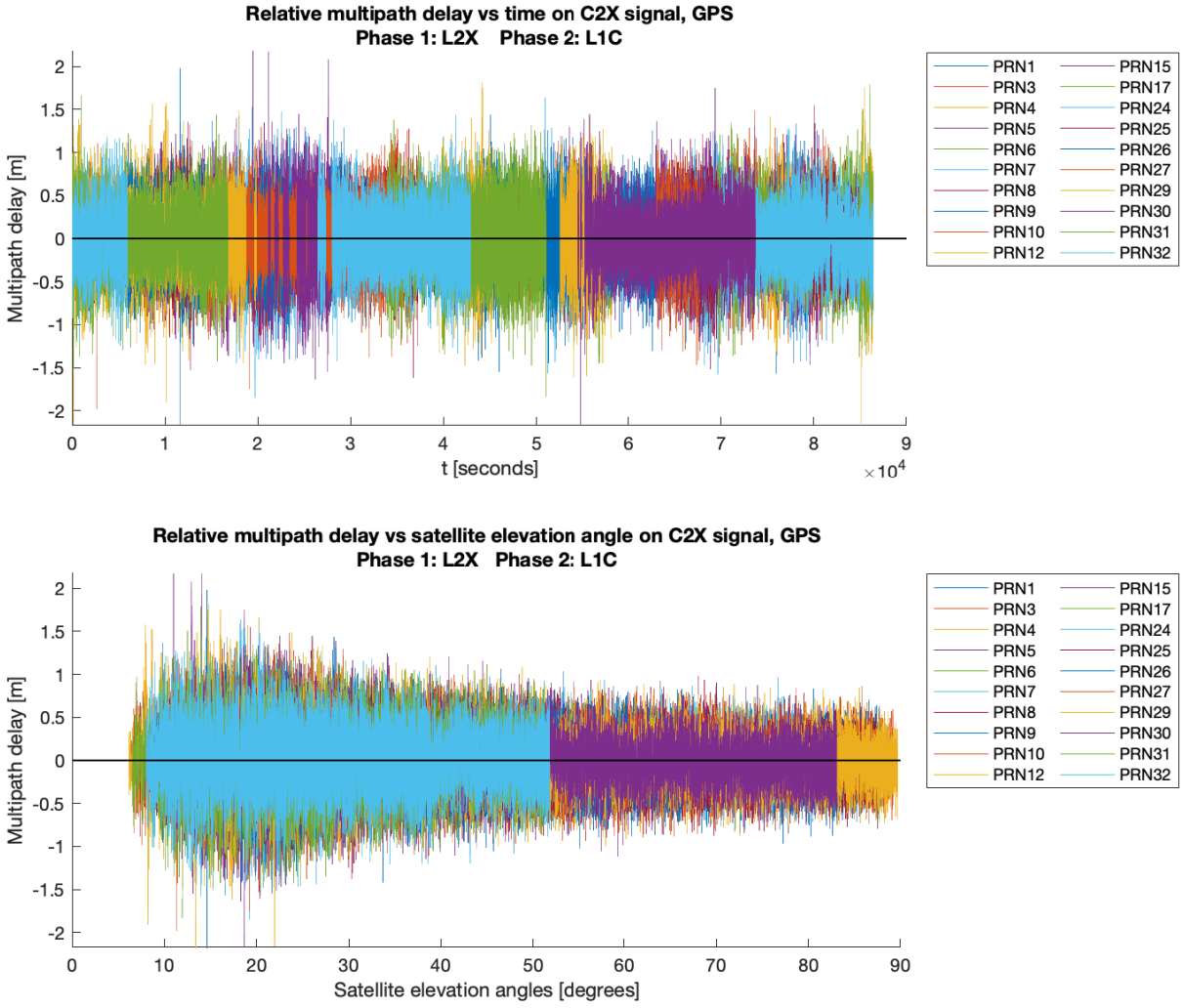

Figure A.4.15: Trimble analysis results graph: GPS C2X signal, multipath effect vs. time and vs. satellite elevation angle. Graph has been cropped along y axis.

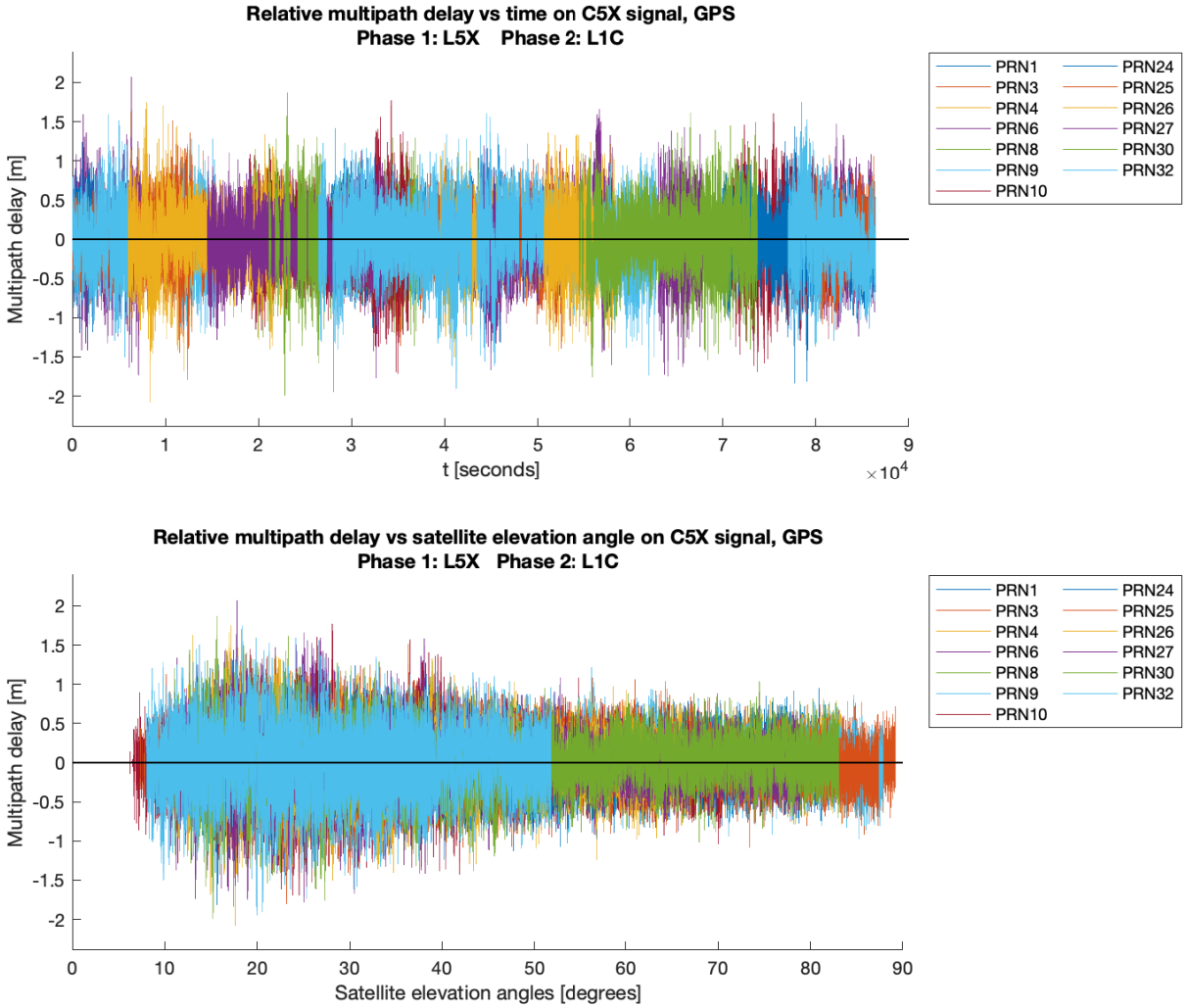

Figure A.4.16: Trimble analysis results graph: GPS C5X signal, multipath effect vs. time and vs. satellite elevation angle. Graph has been cropped along y axis.

GLONASS

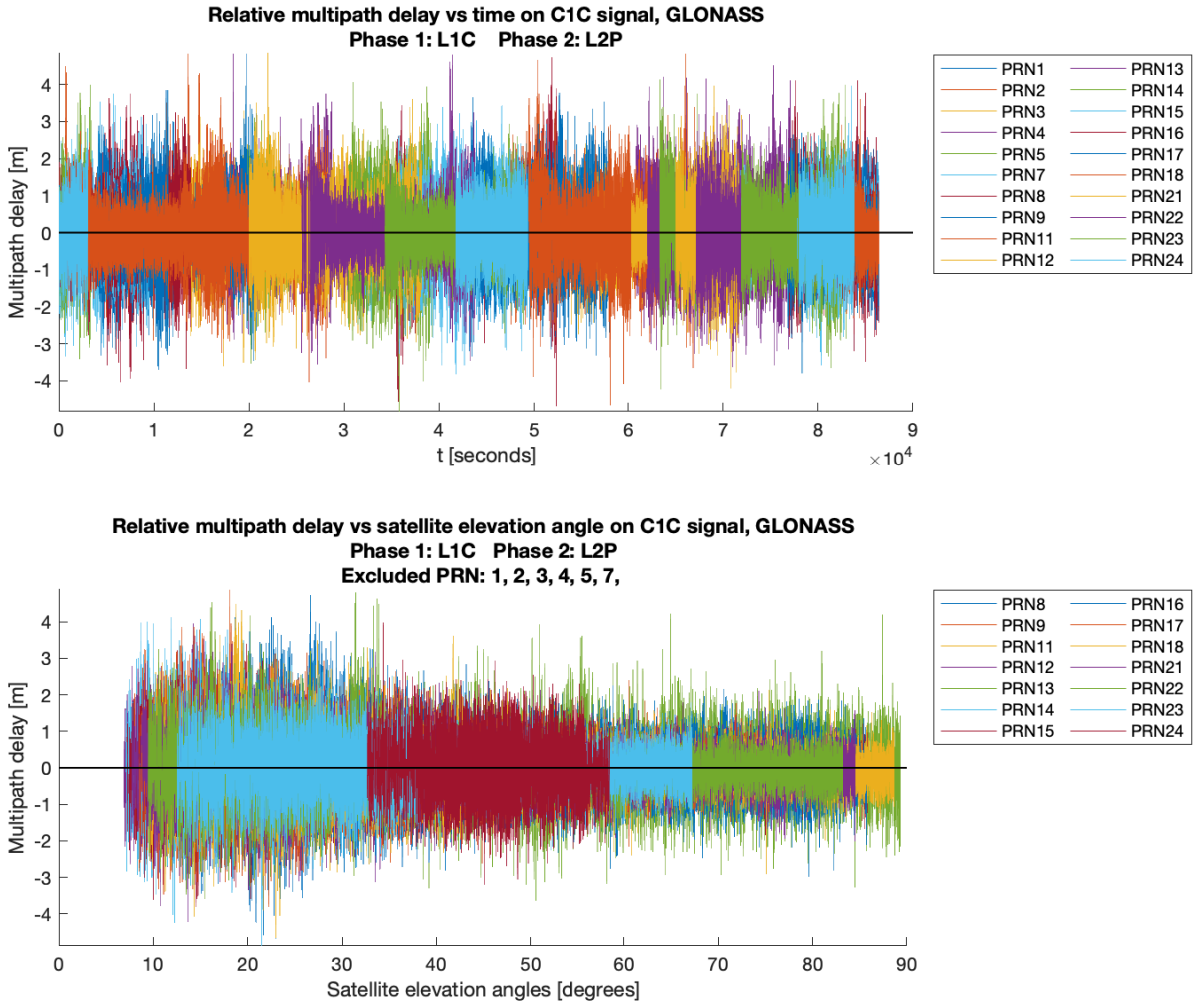

Figure A.4.17: Trimble analysis results graph: GLONASS C1C signal, multipath effect vs. time and vs. satellite elevation angle. Graph has been cropped along y axis.

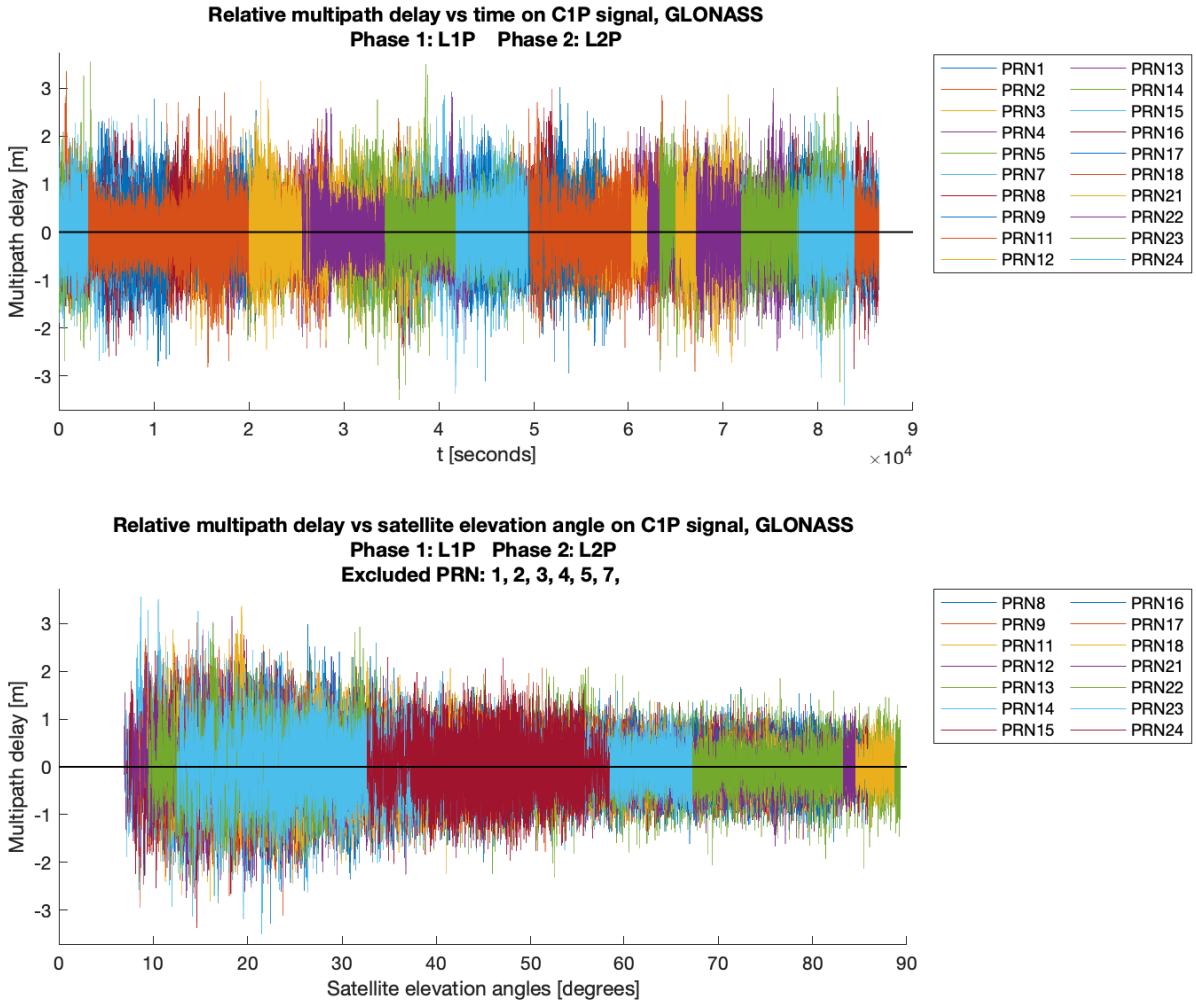

Figure A.4.18: Trimble analysis results graph: GLONASS C1P signal, multipath effect vs. time and vs. satellite elevation angle. Graph has been cropped along y axis.

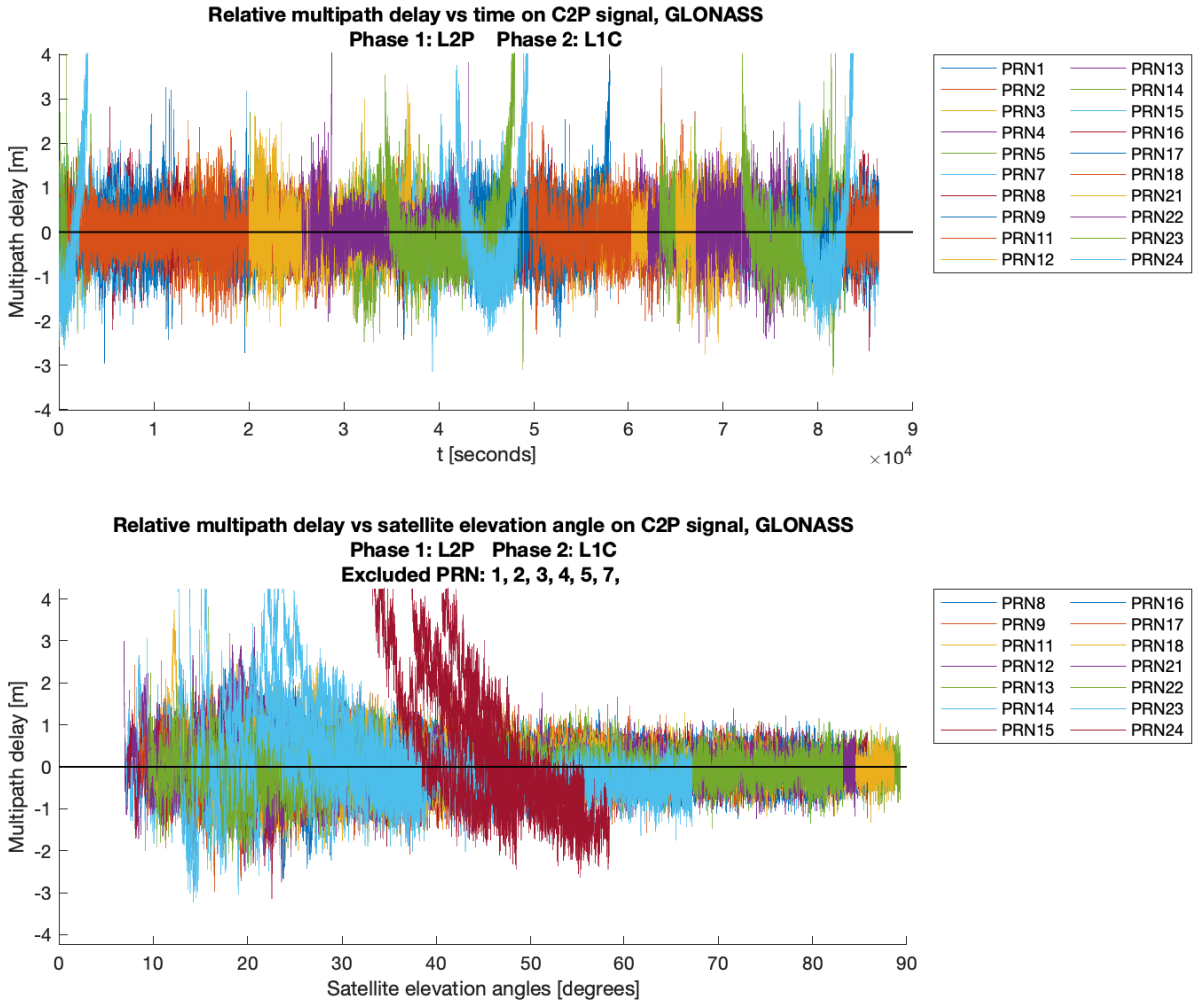

Figure A.4.19: Trimble analysis results graph: GLONASS C2P signal, multipath effect vs. time and vs. satellite elevation angle. Graph has been cropped along y axis.

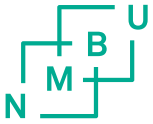

Norges miljø- og biovitenskapelige universitet
Noregs miljø- og biovitskapelege universitet
Norwegian University of Life Sciences

Postboks 5003
NO-1432 Ås
Norway